The Effect of Pulsed Bipolar Plasma Electrolytic Oxidation Coatings on the Mechanical Properties of Open Cell Aluminium Foams

Taha Abdulla

Thesis Submitted for the Degree of Doctor of Philosophy

Department of Materials Science and Engineering

January 2013

Preface

This thesis is submitted in partial fulfilment of the degree of doctor of philosophy in advanced metallurgy. The thesis contains work carried out from 2008 to 2012, and has been made solely by the author. Some of the information in this thesis, however, is taken from the research of others to provide support and/or comparison with the data in the present work. To the best of my knowledge, clear references to these sources have in all cases been provided. It should be noted that part of this work itself been published in articles which can be found as follows:

T. Abdulla, A. Yerokhin, R. Goodall, 2011. Effect of Plasma Electrolytic Oxidation coating on the specific strength of open-cell aluminium foams. Materials and Design: (32) 3742–3749.

T. Abdulla, A. Yerokhin, R. Goodall, 2011. Elastic Response of Plasma Electrolytic Oxidation Coated Open Cell Aluminium Foams. Proceedings of the 7th International Conference on Porous Metals and Metallic Foams (563-568), MetFoam, 18 – 21 September, 2011 in Busan, South Korea.

Abstract

Metal foams have attracted wide range of interest from researchers and industries because of their unique combinations of properties. Of particular interest, open cell metallic foams have good weight-specific mechanical properties, and improvements could make these materials highly desirable for lightweight structural and energy absorption applications. These properties could potentially be increased for open cell foams by treatments affecting their large surface areas. The effect could be very significant, especially when the dominant deformation mode is bending of the foam struts, as the coating will be located away from the neutral bending axis of these struts maximizing its effect. This has been previously found after the application of surface treatments, such as electroplating. The technique of Plasma Electrolytic Oxidation (PEO) is another process that shows an even greater effect on foam specific mechanical properties.

In this work, Plasma Electrolytic Oxidation (PEO) coating treatment is applied to open celled aluminium foams with different structures, aiming to improve the mechanical and weight-specific properties of the hybrid material. Open cell aluminium foams of different types, both investment cast (Duocel foam) and replicated (produced in the laboratory) have been produced and PEO coated using a range of different processing parameters. Two pore sizes of Duocel aluminium foam (measured as 2.2 mm and 2.5 mm average pore diameter) with porosity of 90–91%, and a single pore size (1.6 mm diameter) of the pure aluminium replicated foam with porosity around 60–64% have been examined.

The PEO treatment of foams was carried out in the pulsed bipolar current mode, with a range of processing times (20, 40, 60 and 80 minutes), pulse frequencies (50 to 6250 Hz) and duty cycles (different ON/OFF waveform ratios). These processing parameters were explored in the present work in four different stages of investigation, as will be explained in detail later. The mechanical properties (yield stress, specific strength, Young's modulus and energy absorption) of the coated foams produced are assessed experimentally, both in tension and compression, and simple models developed to describe the elastic behaviour, based on either the Gibson-Ashby model of foams as a regular cellular array, or the Markaki-Clyne model of randomly intersecting fibres are used to make predictions to compare to

these results. Complimentary characterisation was carried out using SEM, EDX, XRD and nanoindentation techniques to understand the nature of PEO coatings on foams (including coating thickness, growth rate, mechanical properties, porosity, elemental and phase compositions), and the effect this has on mechanical properties. Thereby, the process can be optimised to improve the mechanical performance of the foams.

It was demonstrated that PEO coatings can be successfully applied to open cell foams (of low and high level of porosity) and the coating penetrates completely into the structure up to several millimetres depth, with thickness diminishing with depth. The presence of this coating is of benefit for uniaxial mechanical properties as well as specific foam properties. PEO pulse frequency influences coating thickness, porosity and the measured mechanical properties. The major effect on coating hardness and elastic modulus as well as on the strength and stiffness of the coated foams is associated with the volume fraction of porosity within the coating. The effect of using different duty cycles (associated with the ON and OFF times in each cycle in the current pulse frequency used) results in different coating morphology, thickness, distribution and deposition rate. Very fast coating growth rate has been shown to be not always beneficial, whereas low coating growth rate may be useful for the formation of good quality coatings (containing fewer microcracks and possibly lower intrinsic stresses), with potential for a very even distribution into the foam internal structure.

An assessment based on strength increase ($\Delta\sigma$) and density increase ($\Delta\rho$) of the coated foams shows that the benefits of the application of PEO coatings to metal foams are greater than those shown in other metal foams coated by different techniques. The primary reason for this is that the oxide ceramic coatings formed on foams have low density, excellent mechanical properties and good adhesion to the substrate. These properties have been improved for foams by the PEO optimization process carried out in the present work.

Acknowledgments

Table of Contents

Chapter 1: Introduction

1.1. Introduction

Metal foams (metallic structures containing high levels of porosity) have many interesting and unusual properties, which make them potential candidates for innovative designs. These include some structural applications, making use of the high specific mechanical properties of foams. These properties could potentially be increased for open cell foams (where pores are connected together and to the outside environment), by treatments affecting their large surface area. This would be expected considering the common assumption that deformation occurs by bending of foam struts. As the coating is at the beam surfaces (where the strain is highest) even a thin film can have a significant effect, provided that the coating material has a high strength and modulus, and the deposition mechanism allows strong and uniform adhesion.

This has been shown to be the case with some coatings, including a thin surface coating (of the order of hundreds of nanometres, being a reaction layer on aluminium foam processed by replication, formed during the dissolution step), and also with thicker coatings applied by electrodeposition (e.g. Ni, Ni-Fe and Ni-W alloy on aluminium foams to thicknesses of 25-400 μm [1-4]). In this work an alternative coating on a different type of foam is investigated.

Foams can be produced from many different metals, using many processes. Amongst these, good control of the structure may be achieved in investment casting-based routes and the replication process [5, 6]; both of these give open celled foams, but with very different structures and will be the type of foams used in this work. The Plasma Electrolytic Oxidation (PEO) coating process can fulfil the requirements for having coating materials with high hardness and modulus as well as a very high interfacial bond strength with the bulk metal [7].

The aim of this project is to examine the effect of the Plasma Electrolytic Oxidation process on the mechanical behaviour of aluminium foams with low and high levels of porosity processed by these two methods. The examination include investigating the effect of coating processing parameters on coating microstructures and distribution

within the foams and the effect it has on mechanical properties, and how these parameters are affected by the structure of the foams and the coating deposition parameters. This will help to assess if the process will be effective in improving the foams performance for varies types of mechanical applications.

This thesis consists of seven chapters, which can be summarized as follows: Initially there is a brief introduction which outlines the objectives of the research. A literature review is presented on the subject areas of both metallic foams and the Plasma Electrolytic Oxidation processes. The experimental procedures used for the processing of open cell aluminium foams, PEO coating processing of the foam samples, mechanical testing and coating characterization methods are explained in detail. This experimental work on PEO processing of metal foams was carried out in four different stages. The results and discussion obtained from the experimental work in stages 1 and 2 are presented first, with the discussion of the results obtained from the experimental work carried out in stages 3 and 4 presented together. Whenever possible, comparison with the other work from the literature on different coated foams was made. Finally, the fundamental conclusions extracted from this investigation are presented.

Chapter 2: Metal Foam Processing and Properties

2.1. Some Definitions

Metallic foams are metals containing large volume fraction of pores, usually greater than 50% of the total volume. When these pores are sealed off with gas or air trapped inside them, the foam is called closed-cell foam, whereas when these pores are open or connected to each other, allowing gases or fluids to flow through them, then the foam is termed open-cell foam. The existence of such elements (the pores) is what makes these materials special, as result of this they are light weight, giving them excellent specific mechanical properties, they can be permeable to fluids and often have unusual properties, making them suitable for applications such as structural panels, for heat transfer, sound, and energy absorption during impact. Other than pores, metallic foams contain three structural elements called struts, nodes and cell walls, all of which represent the metal part of the whole foam volume.
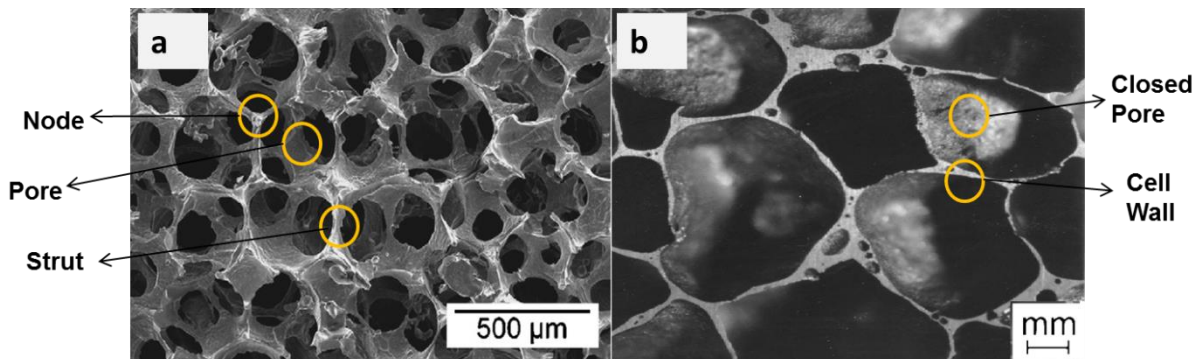
Figure 2.1 – Micrographs showing, a) open cell aluminium foams made by replication with pore diameter of 400 µm and relative density of 0.1, and b) closed cell foam (Alporas), with pore diameter of 2-5 mm. Foam pore, strut, node, and cell wall are clearly marked [8, 9].

The first two of these exist in open cell foams and a foam cell is created when different struts are joined together through nodes, as seen in figure 2.1.a, where these structural elements are indicated. The latter element is present in closed cell foams and the foam pores are enclosed by these cell walls such that air or fluid may

be trapped inside them, see figure 2.1.b with indicated areas showing a pore and cell wall. Open and closed cell metallic foams are currently produced from different metals using a range of processing methods. The following sections are concerned with these processing techniques, providing details on different aspects.

2.2. Processing Routes for Open Cell Metal Foams

Production of metal foams was first reported in the early part of the 20th century, and active research on metal foams has been going on since the 1960s, with increasingly intensive work since around the 1980s [10]. Foaming generally has been applied to many different types of materials, including polymers, metals, ceramics and glasses, etc. to obtain porous structures or sponges [5], and a number of techniques have been developed to produce foams from these different types of solids. More specifically for metals, techniques used to produce metal foams (with both open and closed cells) can be categorized into four different types; these are liquid metal route (e.g. the replication technique, described later), solid metal route (e.g. powder metallurgy techniques, also described later), metal vapor and metal ions routes (e.g. metal deposition techniques described in a later section). This classification is made according to the state of metal before the foam is produced [5, 11-13]. As noted by Banhart and Ashby et al. [1-3], each of these mentioned techniques is specifically used for foaming certain types of metal to produce foam with certain structure, i.e. a particular range of cell shape, cell size and relative densities.

In the following sections, the main foam processing methods are discussed, concentrating on open cell metal foam (as foam must be for coating process to be effective). The ability to control foam structure and to process wide range of metals are the two main objectives sought by many researchers and manufacturers considering foam processing. Recent developments in processes that allow greater control of the processing of advanced alloys are in particular highlighted.

2.2.1. Liquid State Processing Routes

2.2.1.1. Replication Processing

For metallic foams, the replication technique (infiltration of molten metal into a porous preform which is later removed) is amongst several processing techniques that have been developed to date to produce open cell metal foams from liquid. This technique only yields open-cell foams, but can give very different structures (e.g. controlled cell sizes and densities [6, 14, 15]). The process was used in the early attempts to produce aluminum foams, and its usage and development have been continuous ever since [6].

The following is a summary of the major steps in most replication processes, as seen in figure 2.2 below:

- Space holder material (e.g. NaCl particles) are classified by size and compacted to form an open-pore preform.
- Molten metal (e.g. aluminium) is infiltrated under a pressure of argon gas.
- After solidification of the composite, the space holder is removed, usually by fluid dissolution, thermal decomposition or by air blast, to produce open-cell metallic foam.
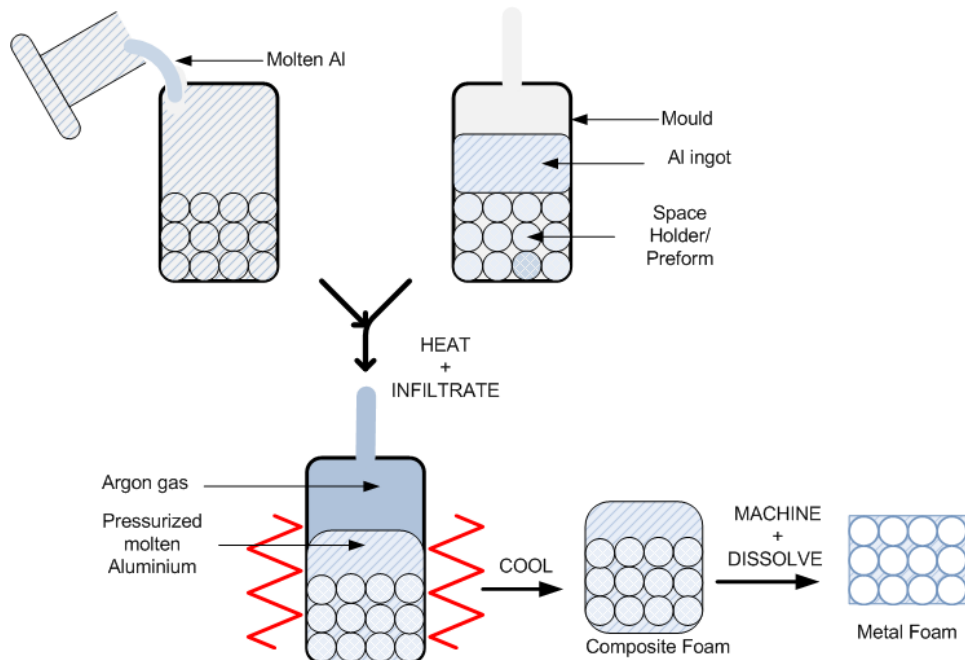
Figure 2.2 – Replication processes for production of open cell metallic foams.

Numerous metals and their alloys have been processed by the replication method to produce metallic foams with tailored structures, with examples being reported for aluminium 99.99Al wt.% and its alloys [8, 16, 17], sliver-copper alloy; 72Ag–28Cu wt. % [18], tin-lead alloy with 50Sn– 50Pb wt.% [19], magnesium 99.98 Mg wt.% [20, 21], zinc alloy 77Zn–22Al–1Cu wt.% alloy [22], copper alloy; 75.9Cu–16.1Zn–7.9Al wt.% [23, 24], brass 57Cu–39.4Zn–3Pb–0.3Sn–0.3Fe wt.% [25] and very recently the replication process was exploited for the fabrication of non-metallic material being mesophase pitch-derived open-pore carbon foams [26]. In all of these processing examples, the success of infiltrating molten metal into a leachable perform requires that the space holder used is strong enough during infiltration to resist force or deformation, has a higher melting point than the infiltrated metal (with no reaction between the two), and has the ability to be removed by shaking or dissolving in a liquid (e.g. water) [6]. The properties of the space holder are therefore crucial in this part of processing. Space holders based on table salt (i.e. NaCl) are the least expensive and most widely used for the replication process [16, 17, 19, 22, 27]. The major advantages of using NaCl particles are the easy of removal after infiltration with molten metals and the ability to control the foam cell size and shape, which can be achieved by sieving particles to certain sizes which are then processed loose or by sintering or cold pressing of (generally fine) NaCl particles to make a preform of controlled density [28, 29]. One limitation of this technique is encountered when using NaCl particles with sizes of > 1mm. This may result in the particles cracking rather than deforming during a cold pressing stage or having a very low sintering rate if this method is used. There is also an issue of the time being longer for dissolving the salt from larger foam samples. However these limitations were resolved by Goodall and Mortensen [30, 31], who developed a version of the process based on a 'dough' paste, by mixing finely ground salt, flour and water, with the salt being the major component.

Figure 2.3 - The flexibility offered by the dough-based replication process in making different shapes and sizes from a paste made by mixing of salt, flour and water [30]. Spacers made in this process can also be easily dissolved in water.

The mixture, which eventually turns into a paste, can be shaped by hand or by other standard food shaping equipment into a range of different shapes and sizes, as seen in figure 2.3. Dissolution of these space holders is made in water and has been found to be quicker than dissolving normal salt due to the fine porosity incorporated within the individual spheres.

The replication processes mentioned above make use of the lower melting point of the infiltrated metals/alloys (it is generally possible to process metals at up to 750 °C for salt preform [6]), as compared to that of NaCl, 810°C [32]. The melting point of the NaCl may, however, be considered relatively low, especially when considering other metals and alloys of technological interest (e.g. copper and its alloys). To overcome this, workers have used alternative space holders that can cope with higher melting point metals. For instance, magnesium sulphate $MgSO_4$, seen in figure 2.4, was used as the space holder for processing of an Ag-Cu alloy with melting point of 779 °C. The $MgSO_4$ can be easily dissolved in water, or can be thermally decomposed at 927 °C [18].
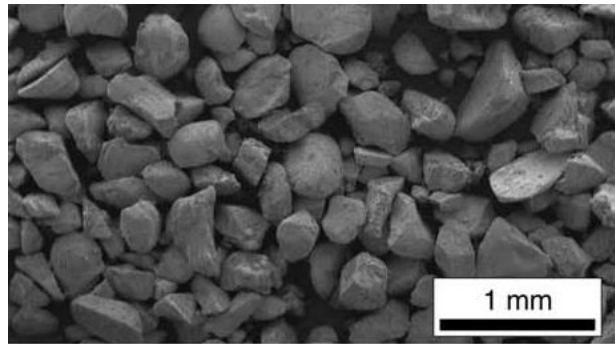
Figure 2.4 - SEM micrograph of MgSO$_4$ particles with irregular shape, having an average size of 300 µm [18], used as space holder for Ag-Cu foam.

For higher processing temperatures of around 975 °C, sintered fluoride salt (BaF$_2$) was used as space holder for processing open cell Zr-based bulk metallic glass foam [33], using commercial alloy Vit106 (Zr$_{57}$Nb$_5$Cu$_{15.4}$Ni$_{12.6}$Al$_{10}$). The advantage of this refractory salt is its high melting point (1368 °C), which allows some degree of flexibility for processing other high melting point alloys. After infiltration, removal of the fluoride salt is achieved by dissolving in 2M nitric acid for 16h. A new study on open cell Zr-based metallic foam reported an improved processing method, using sintered (at 600 °C for 2h and the cooled to 200 °C) NaCl as space holder for their replication process [34].

Recent publications have also shown increased interest in using space holders with even higher melting points to those mentioned previously; that is silica gel particles (SiO$_2$), see figure 2.5, [23-25]. These SiO$_2$ particles offer significant advantages, having a high melting point of around 1600 °C, being chemically stable during interaction with molten metal, and allowing the production of metal foam with regular and spherical pore shape. It has been reported that infiltration of pure Pb, Ag and Cu, as well as for shape memory alloy CuZnAl, PbSb and PbSn alloys into SiO$_2$ preforms was successful, producing different foams [23-25].
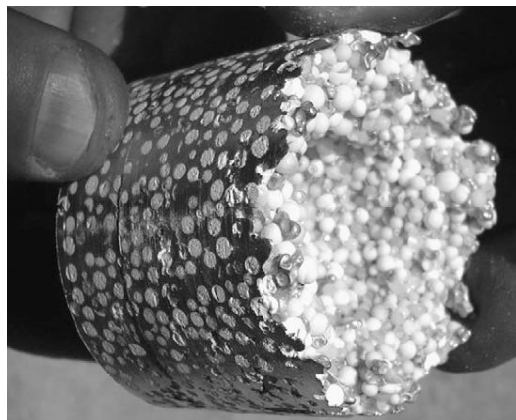
Figure 2.5 - Composite precursor to a metal foam (Cu-based metal infiltrated into SiO_2 Silica Gel preform), with regular spherical shape pores, before machining and removal of silica particles [25].

Dissolution of these particles remains a drawback in their usage, since it is carried out in HF (hydrofluoric acid) solution, which is a highly corrosive acid that requires extreme safety precautions in use.

Research on developing space holder materials went even further to include those suitable for processing of nickel superalloys using the replication process. Recent work has been carried out to investigate the processing of Ni-base alloy J5 (Ni-22.5Mo-12.5Cr-1Ti-0.5Mn-0.1Al-0.1Y, in wt.%), using the replication process [35] to produce open cell foams. The new space holder used in this process was sodium aluminate $NaAlO_2$, see figure 2.6, which has melting point of 1650 °C, higher than that of the J5 alloy (melting point of 1350 °C [35]).
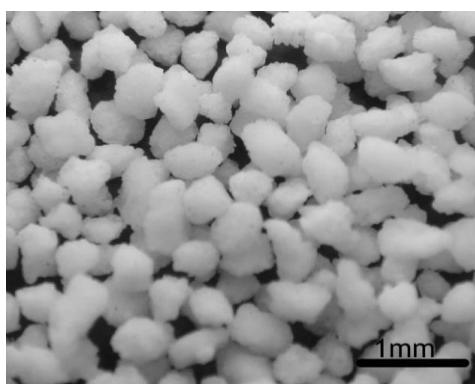
Figure 2.6 – Sodium aluminate $NaAlO_2$ particles with sizes ranging between 355 - 500 µm used as spacer in the replication process of open cell Ni-alloy foam [35].

These space holders are dissolved faster in 10 % HCl (hydrochloric acid) solution than in water, due to formation of tacky hydroxide phases on hydration which are slow to dissolve.

2.2.1.2. Investment Casting

The investment casting method starts with using an open cell polymer foam as the first precursor, which is infiltrated with a slurry that is heat resistant (e.g. a ceramic suspension; mixture of mullite). After drying the slurry, the polymer foam is then removed by a heat treatment, forming a negative mould. The molten metal is cast into this second precursor, and replicates the original polymer foam structure. After removing the mould (e.g. by water spray), the final structure of the foam is formed. This processing route is used for foaming aluminium and its alloys, magnesium and copper [5, 12]. A good example of foams made in this processing technique is Duocel foam, which is commercially produced by ERG Materials and Aerospace Corporation, Oakland, California [5]. Currently, different grades of Duocel foams are available which range from 5-40 PPI (pore per inch); corresponding to 1 - 5 mm pore sizes [12]. The foam structure and morphology produced are controlled by manipulating the polymer precursor, which means that different densities, as low as 0.135, and different structures can be made. Typical Duocel foam structure is illustrated in figure 2.7. This type of low density foam is used in different applications with examples being as heat exchange media, core structural materials and silencers etc. [5] .
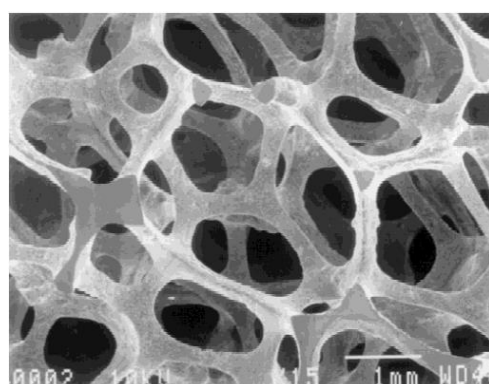
Figure 2.7 – SEM image of typical Duocel foam structure with relative density of 0.075 (20PPI), showing morphology that is produced by the investment casting process [36].

Although this processing method provides high accuracy of the foam structure produced, its limitation to castable metals and alloys with relatively low melting point, and requirement for removing the mould with minimum damage to the foam structure may be considered drawbacks of the process [5, 12].

2.2.2. Solid State Processing Routes

Recent publications have also shown increased interest in the sintering-dissolution technique (also sometimes called the powder metallurgical route or powder-based replication method) for the production of metallic foams. This technique is based on mixing and compacting metal powders with a specific space holder. As is the case in the replication process, different space holder materials have been investigated, with a typical example again being NaCl [37, 38] used to produce aluminium and copper foams. Carbamide granules, see figure 2.8, have also been used in the processing of both aluminium [39, 40] and pure titanium foams [41] and more recently starch, see figure 2.9, an organic polymer, was used as space holder for the fabrication of open cell titanium foam [42].

Figure 2.8 - An image of spherical carbamide $(NH_2)_2CO$ granules with sizes ranging from 1 - 5 mm, used as space holder in powder metallurgy route for processing of aluminium foams [39]. Carbamide granules were removed by dissolving in a water bath after compaction and before sintering.

It can be seen that the selection of these materials is mostly controlled by their chemical stability so that the chosen material does not interact with the metal of which the foam will be made. This is because carbamide granules have a melting

point of around 133.3 °C, much lower than that required for sintering of aluminium and titanium 680 and 1200 °C respectively [39, 41]. For this method requiring a space holder that can withstand these higher processing temperatures is not an issue, but rather it is the stability and ease of removal that may be more essential.
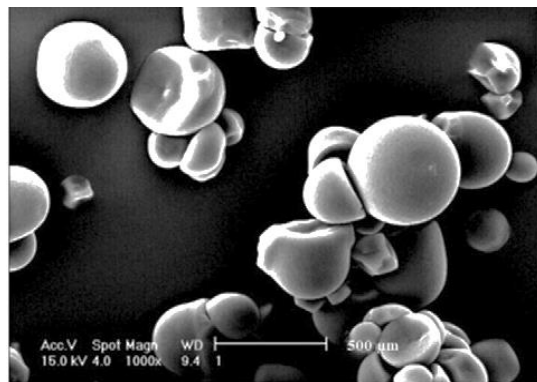
Figure 2.9 - SEM image of spherical starch powders with sizes ranging from 100 - 400 μm, used as space holder in powder metallurgy route processing of titanium foams. Starch powders were removed thermally [42], during the first stage of the sintering heat treatment at 450 °C.

A different version of the dough-based process, reported by Mortensen and Goodall [30], has been investigated by Jinnapat and Kennedy [43-45] who used aluminium alloy powder (Al–1 wt. % Mg–0.5 wt. % Si–0.2 wt. % Cu) to make the foam. This study uses spherical salt beads, with sizes ranging between 0.5–3 mm as seen in figure 2.10.a, as a space holder during the powder-based replication processing of open cell aluminium foams. These beads are made of a mixture of flour, water and salt which are mixed, heated in oil at 80 °C while being stirred together. Porous beads (16 % porosity, see figure 2.10.b), are then formed and subsequently sintered to create a preform.

After mixing the space holder and metal powder, the resultant composite material is then pressed together. Removal of the space holder can be done before sintering [39, 40], and in this case the remaining porous material is sintered at high temperature, below the melting point of the metal powder. Dissolution can also be carried out after complete sintering of the whole composite foam [37, 45] or during

the sintering stage [42]. Removing the space holder from the composite foam produced leaves an open pore metallic structure.
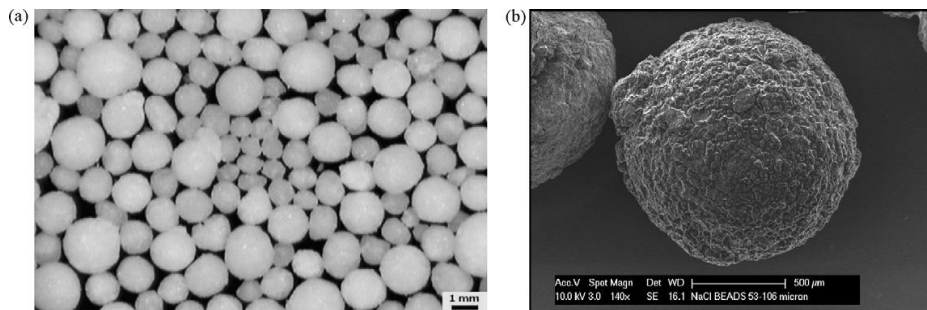
Figure 2.10 – Salt beads made by flour-based paste disintegrated in oil a) with a modal size of 1 - 1.4 mm and b) magnified SEM image of a porous salt bead. Beads/aluminium powder compact is sintered at 650 °C and dissolution of the salt beads is carried out in still water at approximately 60 °C for 30 minutes [45].

2.2.3. Vapor/Ionic State Processing Routes

Vapour, chemical vapour deposition or electrodeposition processing route of foams begins when metal is allowed to condense or is electrodeposited on a precursor (e.g. polymer). After coating, the precursor can be removed by thermal treatment, and the same shape of the foam as the precursor, but with hollow struts is produced. More specifically, in the metal vapour deposition process polyurethane foam can be used as a precursor, which defines the shape of the foam to be made. One example of this process is used by Inco limited where nickel carbonyl gas, $Ni (CO)_4$, is allowed to decompose on the precursor at a temperature of around 120 °C under vacuum. Ni coating deposited on the precursor will grow to a certain thickness on all of the polymeric foam surface area, with the thickness varying depending on the density of the coating and exposure time [5]. The precursor can then be removed by heat and chemical treatment, so that porous hollow nickel foam is produced. This procedure is usually used for production of foams made from high melting point pure metals, such as nickel or titanium foams [5, 12]. Because of the hollow structure produced, this method produces open cell foams with the lowest relative densities (0.02 - 0.05) as compared to other foams produced in different methods. Nickel foam made in this

way is available today branded as Incofoam or similar products from other suppliers. It has been found that it is difficult to process alloys by these methods [12]. However, Douglas et al. used the electron beam-directed vapour deposition (EM-DVD) method to deposit Inconel alloy 625 (Nickel-based superalloy with chemical composition of Ni–21.3 Cr–8.8 Mo–3.9 Nb–0.13 Al– 0.19 Ti wt%) on open cell polyurethane foam [46], with the results seen in figure 2.11.
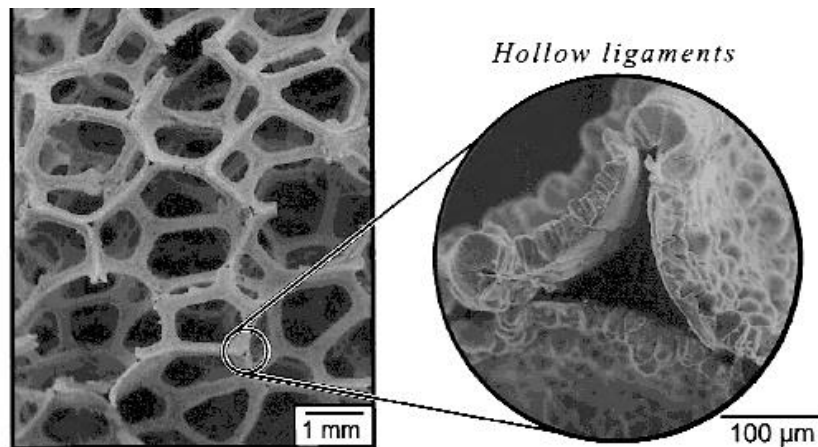
Figure 2.11 – An image of hollow strut nickel-based superalloy foam made by EB-DVD method, with magnified SEM image of hollow ligament after removal of the polymeric precursor. Image after ref. [46]. The hollow ligament foam structure shown is typical of other foams made by vapour/ionic state route.

After removal of the precursor, which was carried out by heat treatment under vacuum, a sintering process is required to reduce the porosity of the deposited coating as well as to increase the integrity of the porous structure.

An alternative method for metal deposition on a precursor is to use electro-deposition. This can be achieved by immersion of a polymeric foam with a thin layer of a conductive coating into an ionic solution where the metal is deposited by electroless plating or electrodeposition. The precursor is removed by a similar process to the metal vapour deposition method (i.e. thermally) [5, 12, 47]. Nickel, nickel-chromium and copper can be used in this process. Retimet (made in Britain), Celmet (made in Japan) and Recemet (made in Holland) are the currently available grades of metallic foams made in this process [5].

It can be concluded that open cell metallic foams or sponges can be produced using many different manufacturing routes. It is also seen that in the replication and powder metallurgy processing routes, a range of space holder materials have been used, each with its own advantages and limitations. The selection of these materials is generally based on their melting point, environmental impacts, ease of removal after infiltration or sintering, ability to obtain different sizes and shapes, and the price of these materials can also play a role. It is essential to note that open cell foams produced by these methods have therefore a range of different densities and structure/morphologies, depending on the manufacturing route. These characteristics and properties are summarized in table 2.1.

Table 2.1 – Properties of different open cell metallic foams processed by different methods reported in the literature.

Processing Method	Space Holder	Metal	Porosity (%)	Pore Size (mm)	σ_y (MPa)	E (GPa)	Ref.
Replication	NaCl	Al, Al alloy	57 - 90	0.075 - 5	0.1 – 23	0.1 – 8.5	[8, 16, 17]
		Sn-Pb	58 – 68.6	1.6 - 4	2.9 - 5	-	[19]
		Zr- Vit 1	65	0.5 - 1	30	-	[34]
		Zn-Al-Cu	52.8 – 67.5	2.3 – 6.6	2.8 – 48.6	1.9 - 22.3	[22]
	NaCl Dough/ Paste	Al	86 - 88	1 - 7	-	-	[30, 31]
	MgSO$_4$	Ag-Cu	50 - 64	0.3	10 - 33	5 - 12	[18]
	BaF$_2$	Zr- Vit 106	78 - 85	0.25	-	-	[33]
	SiO$_2$	SMAs	62- 75	2 - 3.2	15 - 25	3	[23-25]
	NaAlO$_2$	Ni-J5 alloy	52.6 - 56	0.355 – 0.5	119	44	[35]
Powder Metallurgy	NaCl	Al, Cu	45 - 83	0.3 - 1	2.5 - 20	-	[37, 38]
	Carbamide Granules	Al	40 - 85	1 - 5	6 – 12.4	0.07 – 0.3	[39, 40]
	Starch	Ti	64 -79	100 - 300	23 - 41	1.6 – 3.7	[42]
	Salt Beads	Al	67 - 87	0.5 – 3.1	0.27 – 5.1	0.46	[43-45]
Investment Casting		Al, Cu, Mg	88 - 97	1 - 5	1.24 – 2.5	0.1 – 0.65	[5, 12, 13, 48]
Electro/vapour Deposition	Polymer	Ni, Cu	86 - 97	0.5 – 3.2	0.6	-	[5, 12, 13, 46]

2.3. Summary of Processing Routes of Closed Cell Foams

Closed cell foams are the second type of metallic foams which are available today, and because it is beyond the scope of this work, only a summary of some commercially available processing routes is provided to illustrate the differences in structures made. As discussed earlier, the cells of this type of foam are closed or sealed off and so it can be imagined that bubbles of air are incorporated and distributed within the metal. One way to do this is use a direct foaming method which might involve the injection of gas (air, argon or nitrogen) into molten metal or alloys. Prior to gas injection though, elements such as aluminium oxide, magnesium oxide or silicon carbide may be added to the molten metal to increase its viscosity. This technique is used for processing of e.g. aluminium and its alloys and magnesium foams. It is one of the earliest foam processing methods and large volumes of these closed cell foams are produced by companies e.g. Cymat Aluminium in Canada and by Hydro Aluminium in Norway [5, 12, 13].

An alternative way is to use direct foaming with a blowing agent, which involves mixing of molten metal or alloy with a foaming agent e.g. TiH_2. Under the effect of heat, the blowing agent decomposes and releases the gas required for the foaming process. Control of pressure is required while cooling. This process is used to produce aluminium and magnesium foams [5, 12, 13, 49]. Alporas is one brand name of commercially available closed cell foams made by this method, and it has been reported to be the most homogenous type, with different studies having investigated its properties [50-52]. An example of a cross-sectional image of the foam interior is shown in figure 2.12.
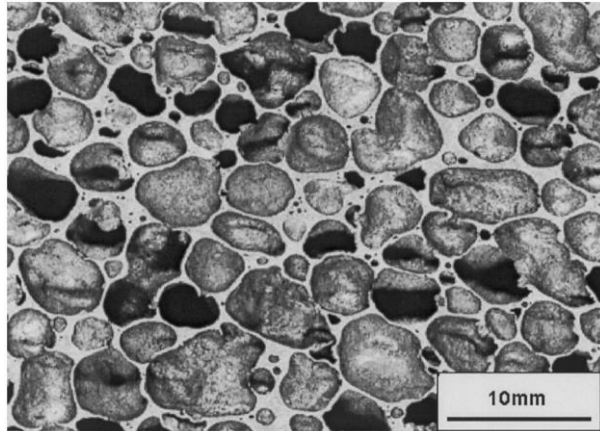
Figure 2.12 – image of ALPORAS closed cell foam made by mixing TiH_2 into aluminium. The sample was provided by Shinko Wire Company Ltd, Japan for the study in ref. [52]. The foam has a relative density 0.08 – 0.1 and average cell size of 4 – 5 mm.

Another method uses solid state metal. Metallic powders are compacted together with a foaming agent; once again TiH_2. Heat treatment at temperatures close to the melting point of the metal and the decomposition point of the blowing agent is then used. Hydrogen is released by the foaming agent, which will expand the foamed material [5, 12, 13]. This method was used for foaming aluminium, zinc, iron, and lead. Other metal alloys can also be foamed but this requires a good knowledge of the appropriate blowing agent and processing parameters. This method was developed at Fraunhofer Institute in Bremen, Germany in 1960 [5].

A further version developed at Cambridge used oxidation of the TiH_2 to delay foaming, allowing it to be mixed with molten metal and solidified in the unfoamed state (later a baking treatment is used to cause foaming)[53]. This process has also been shown to work with calcium carbonate ($CaCO_3$) foaming agent [54].

2.4. The Mechanical Properties of Metal Foams

Metal foams are currently used in a number of areas but there may be other potential applications in which foams could excel. To fully exploit the interesting combination of physical and mechanical properties of foams, we need to understand how they behave mechanically in service and how they can be tested to obtain reliable data. The following sub-sections are concerned with aspects of the deformation

mechanisms involved when foams are subjected to loads and the structural factors that affect their mechanical properties.

2.4.1. Deformation Mechanisms in Metal Foams

When metallic foams are tested in compression or in tension, their behavior can be best explained by identifying three distinct modes of deformation; namely the initial elastic mode, after which the foam cells start to bend plastically, plateau or full plastic deformation mode, and finally the densification or failure mode. Densification takes place when the foam is fully compressed, whereas the failure mode occurs when foam struts break in tension [47]. Figure 2.13 illustrates these deformation modes for foams and some details can be given as follows:

The elastic mode is clearly demonstrated in the compressive and/or tensile stress-strain curve in which the initial linear elasticity occurs at relatively low stresses and strains [47, 55]. The elastic portion in both curves has the same linear shape. The linear–elastic behaviour of foams is characterized by the *Young's modulus E**, and its mechanism vary depending on whether the foam has open or closed cells.
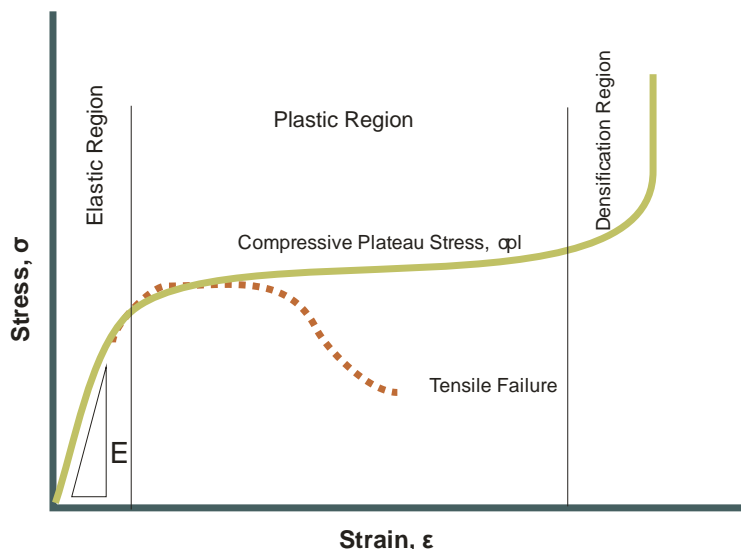
Figure 2.13 – Schematic diagram showing the different deformation regions experienced by metal foams when subjected to compressive or tensile load.

The Young's modulus of open-cell foam is modelled simply by assuming regular structures, for example the cubic array of members of length L and square cross-

section of side t, that was considered by Gibson and Ashby, see figure 2.14.a. When a load is applied, the edges making up the cell bend and deflect by a displacement δ, as seen in figure 2.14.b, [55, 56]. The analysis gives the result that the Young's modulus E^* can be obtained by:

$$\frac{E^*}{E_s} = C_1 \left(\frac{\rho^*}{\rho_s} \right)^2$$ (2.1)

where E^* and ρ^* are the Young's modulus and the density of the foam and E_s and ρ_s are those of the material of which the foam is made. The constant C_1 is normally assumed to be 1, as this value has been previously found to be theoretically suitable for general data on open cell foams [56]. However, different values of C_1 are found to be more appropriate for some types of foam.
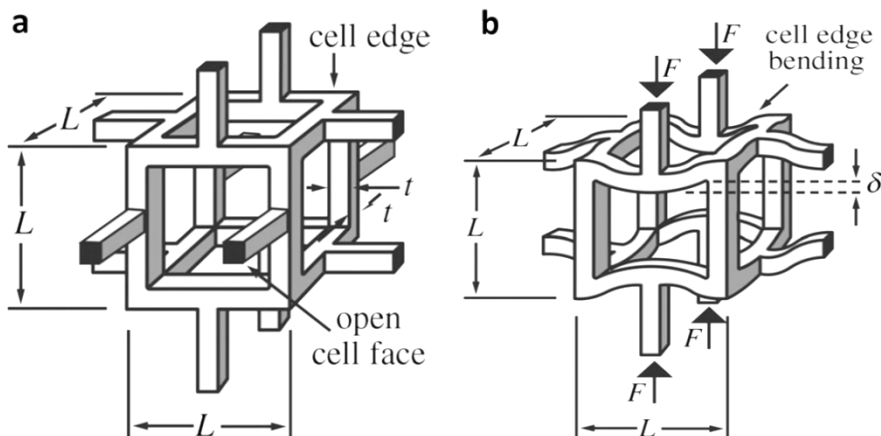
Figure 2.14 – a) An idealized cubic model of open cell foam as proposed by Gibson and Ashby and b) showing cell edge bending when load is applied [55].

For closed cell foams, the expression of Young's modulus is different, and more complex due to the nature of the cell structure. Figure 2.15 below shows modelled closed-cell foam with fraction Φ of the solid contained in the cell edges and the remaining fraction (1-Φ) is represented in the faces.
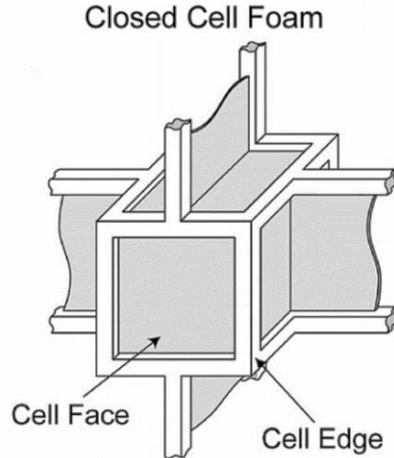
Figure 2.15 - A cubic model for a closed-cell foam, showing cell edges and cell face of a cell of a regular structure proposed by Gibson and Ashby, (image taken from [10]).

The Young's Modulus can be obtained from the sum of three contributions as follows;

1. Bending of the cell edges.
2. Compression of the fluid trapped within the cells; the fluid is usually air, and for metal foams the contribution will usually be negligible.
3. Stretching of the cell faces.

$$\frac{E^*}{E_s} = C_1 \phi^2 \left(\frac{\rho^*}{\rho_s} \right)^2 + C_1 (1 - \phi) \frac{\rho^*}{\rho_s} \qquad (2.2)$$

where ϕ is fraction of solid contained in the cell edges, and the rest of the terms are as previously defined.

At the end of elastic mode, the stress reaches maximum value, which is considered to be the foam compressive strength, and upon further loading the foam cell edges and faces will collapse. This is where plateau-plasticity mode begins. It is a point where stress does not (or will only a little) increase with increasing strain. In compression, the common picture is that the foam's cells collapse by the formation of plastic hinges (metal) as shown in figure 2.16. However, it is different in elastomeric (rubber) foam where the cells collapse by elastic buckling and in brittle foam (ceramic) the failure is only by brittle fracture [9, 47, 55].

The structure then begins to collapse at an approximately constant stress [47] forming what is known to be plateau region and it is to access the properties in this

region that foams are used in applications such as crash protection and energy absorption [12, 47, 48, 55]. In tension, however, the cell edges rotate towards the tensile axis due to the larger strain imposed increasing the stiffness of the structure. This is followed by a yield point after which the stress-strain curve rises and then ends by foam fracture. For both compression and tension, deformation at this stage is not recoverable [47].
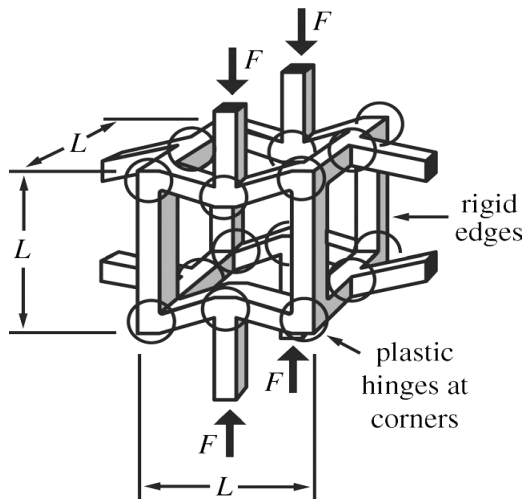
Figure 2.16 - The cell edges deform plastically after yielding and plastic hinges form at the corners of an open cell foam [55].

For open cell foam, the cell edges yield when the force *F* imposed on them exceeds their fully plastic moment. The plastic collapse strength or plateau stress of a foam $\sigma_{pl}{}^*$ estimated by the analysis of the cubic-based Gibson- Ashby structure, is given by [47, 55]:

$$\frac{\sigma_{pl}{}^*}{\sigma_{ys}} = C_2 \left(\frac{\rho^*}{\rho_s} \right)^{\frac{3}{2}}$$

(2.3)

where C_2 has been estimated theoretically, and experimentally and has been found to be 0.3, σ_{ys} is the yield strength of the solid and other terms are as previously defined.

The case with closed-cell foams is always more complex than open-cell foams. It has been proposed that mechanisms such as stretching of the cell faces, bending of the cell edges and the presence of a fluid, usually air, within the cells contribute to the yield strength of the foam [9, 47], although this latter mechanism makes only a small

21

contribution for metal foams, and can usually be assumed to be negligible. From the Gibson-Ashby analysis the collapse strength of closed-cell foams is σ_{pl}* is given by:

$$\frac{\sigma_{pl}^{*}}{\sigma_{ys}} = C_2 \left(\phi \frac{\rho^{*}}{\rho_s} \right)^{\frac{3}{2}} + C_2 \left(1 - \phi \right) \frac{\rho^{*}}{\rho_s} \qquad (2.4)$$

where ϕ is the volume fraction of solid within the cell walls (as opposed to the faces) and all other terms are previously defined.

When foams' cells have collapsed, the whole foam structure will densify during a stage on the stress-strain curve called densification. When densification starts, the stress begins to rise rapidly with increasing strain to a certain limit ε_D beyond which the porosity has been crushed out and the material will behave as dense metal. This limiting strain can be obtained [9, 47] by:

$$\varepsilon_D = 1 - 1.4 \left(\frac{\rho^{*}}{\rho_s} \right) \qquad (2.5)$$

It can be concluded that Gibson and Ashby analysis of foams deformation behaviour depends largely on foams' relative density and the properties of the constituent metal (i.e. stiffness and yield stress of the metal) and that the experimental data backs up the importance of these factors. The constants C_1 and C_2 can be different for different types of foams and are therefore affected by foam processing conditions and hence the exact foam structures. It is also seen that each deformation stage associates with certain mechanism. For example, in the elastic region, the Young's modulus E* has been used to measure the foam stiffness, which is derived from the elastic bending of each individual element or beam within the cell, while in the second region, the plateau, plastic yielding, region, the plastic collapse strength of the foam σ_{pl}* is used as a characteristic value. For metallic foams, the usual picture is that the collapse strength is the stress at which the foam yields and further plastic strain requires little if any increase in the stress (although not all foams behave in this way, as described later). Densification of foam upon compression occurs after relatively large plastic strains and here the foam's behaviour becomes similar to that of fully dense metal, where the stress will increasingly rise with further plastic deformation. It must be

noted, however, that these models find good agreements with the experimental data of most metal foams with examples for open cell foams in [19], and for closed cell foams [57].

2.4.2. Measuring the Mechanical Properties of Metal Foams

As far as the foam mechanical properties are concerned, the yield strength, Young's modulus and energy absorption on crushing are the most common properties measured [10]. It is essential that great care is taken when measuring the mechanical properties of metallic foams in order to get reliable data. This is because metal foams are occasionally subject to some structural deficiencies, caused by the complexity of the processing routes, which can act to reduce the measured properties. For this reason, metal foams with no or with the smallest number of structural defects and homogenous structures are preferred to evaluate their deformation behaviour [15]. Nevertheless, how the values obtained will relate to the properties achievable on real structures must be borne in mind.

Awareness of these testing fundamentals (prior testing basics such as specimen size etc, and post testing analysis such as analysis of stress-strain graphs) are needed, especially for design and development purposes. These aspects are explained in the following sections:

2.4.2.1. Uniaxial Compression and Tensile Tests

According to Ashby et al. [12], prior to compressive or tensile testing of metallic foams some guidelines should be taken into consideration for achieving realistic results. These are specimen shape, size, gripping, greasing of specimens and final measurement. Other testing parameters are summarized in table 2.2 for both compression and tensile tests.

It has been suggested that foam samples with cylindrical or prismatic shape should be used for compression tests. The sample dimensions are to be larger than seven times of its cell size to avoid sample edge effects, with the sample height to length ratio being greater than 1.5 [12].

Table 2.2 – Compression and tensile testing parameters of foams as suggested by Ashby et al. [12], which are considered essential to obtain reliable data.

Testing Parameter	Compression	Tensile
Specimen Shape	Prismatic or cylindrical.	Waisted cylinder or dogbone.
Specimen Size	Seven times the cell size.	Seven times the cell size.
Greasing	Reduce friction, increase σ_c by 25% compared to dry specimen.	Require adhesive bonding, gripping with sandpaper to increase friction.
Displacement	External LVDTs or extensometer.	External LVDTs or extensometer.

The effect of foam specimen length was reported in [58], who found that shorter specimens had an average compressive strength that was higher than that of longer ones. This has been interpreted by the fact that larger specimens are more likely to contain structural defects, which would result in reduced strength and modulus.

The noticeable difference between both types of tests is related to specimen gripping methods. In compression tests, greasing is recommended on faces of the specimen in contact with the loading platens to reduce friction so as to obtain best results, whereas in tensile test friction is required to ensure effective gripping.

2.4.2.2. The Foam Stiffness

Unlike in most dense metals, the elastic properties of metal foams may not be accurately measured from the initial slope of the compressive or tensile stress-strain curve. This is because it is often found that the initial slope is not completely elastic and metallic foams (with open or closed cells) tend to undergo some plastic deformation at, for example, defected pores at very small strains, even in the elastic region, forming as bands [12]. Some of these bands are recoverable when unloaded but many will remain. These permanent micro deformations have been studied by X-ray tomography [59-61], with a reported micro deformation occurring at stresses as low as 0.45 of the plastic yield stress [12], with reported values of 0.11 MPa for Duocel foam, and as small strain as $\varepsilon = 0.009$, in the compression tests of 10 PPI Duocel foam [62].

Ashby et al. [12] suggested that the foam stiffness (characterized by the Young's modulus) is to be determined from the slope of the linear part of an unloading curve,

to ensure there is no effect of plastic deformation. Measuring foam stiffness from the initial slope has been found to give lower estimates of the true value, as result of the initial small permanent deformation. This procedure has been widely adopted for evaluating the stiffness of different metallic and composite (metal/metal and metal/polymer) foams, with the ability to perform more load-unload cycles at different strains which allows the evaluation of the development of Young's modulus with deformation. For example, Aly et al. attempted measuring the stiffness of low density copper and nickel foams from the unloading slopes of tensile tests at different interval strains [63-65], with a representative example shown for copper foam in figure 2.17.
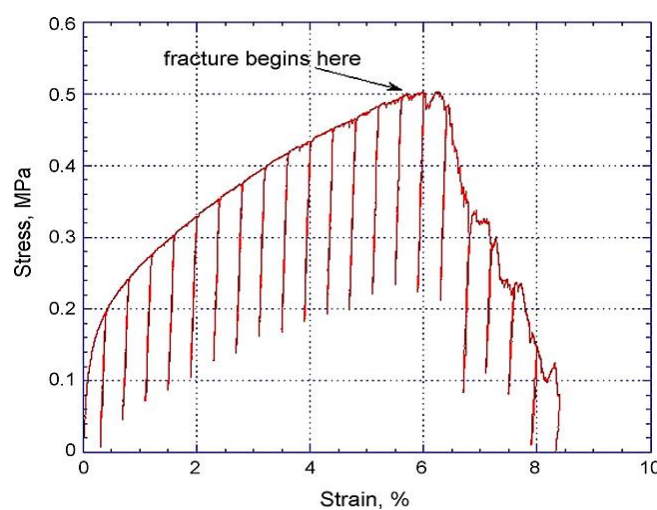
Figure 2.17 - Tensile stress-strain curve of open cell copper foam with porosity of 96%, showing the load-unload cycles made during testing to evaluate the stiffness of the foam at different intervals [65].

Similarly, The stiffness of aluminium foam-polymer hybrid was determined from the unloading slopes of compression tests at different strains [66]. Similar conclusions were drawn by Vendra and Rabiei [67] who determined the elastic modulus of Al-steel composite foam, made from aluminium and hollow steel spheres, from the slope of both loading and unloading curves, and found that the initial loading modulus was lower than that of the initial unloading modulus, see figure 2.18.
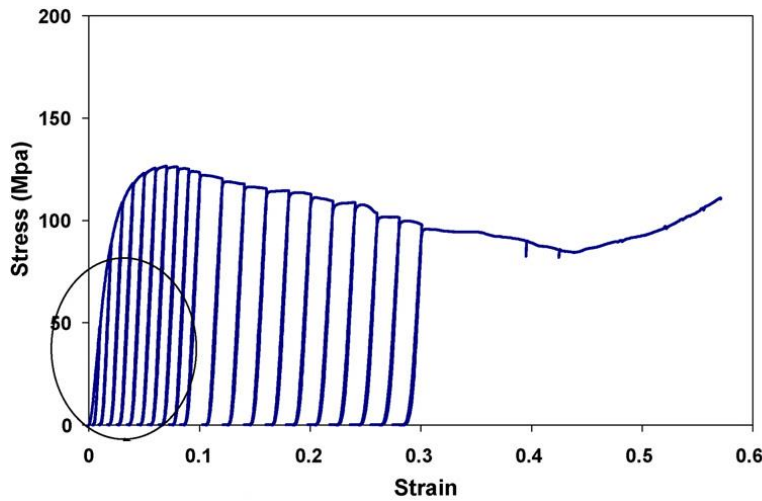
Figure 2.18 - Tensile stress-strain curve of Al-steel composite foam with porosity of 84 %, showing the load-unload cycles made during testing to evaluate the stiffness of the foam at different intervals [67].

This was attributed to the plastic micro-movement of the steel spheres that took place at the initial loading, which resulted in movement towards the optimum packing density of the spheres. Measuring the stiffness from the slope of unloading curves provided more accurate values of the actual modulus of the foam.

Moreover, the foams modulus determined in tension has been found to be 10 % higher than that obtained in compression due to cell anisotropy and rotations. The foam modulus was also found to be affected by the orientation or cell shape of the foam cell, a subject which will be discussed later [12].

2.4.2.3. Foam Yield Stress and Failure Behaviour

The compressive strength of metal foams can be measured from the stress-strain graphs by reading the initial peak stress, usually reached at the end of the pseudo elastic region. However, sometimes these peaks are not clearly shown, and in this case a representative value can be determined by intersecting the initial slope of loading and that of the plateau stress [12]. For more defined procedures, different workers suggested that the yield stress, for metal foams that exhibit power-law hardening behaviour typical of bulk metal [68], is best measured by taking the flow stress at 0.2% plastic deformation [28, 68-72] (an offset yield stress approach). This is made by intersecting the stress-strain curve with a straight line originated at 0.2 %

strain with the same slope as the Young's modulus determined from unloading curves, as seen in figure 2.19.
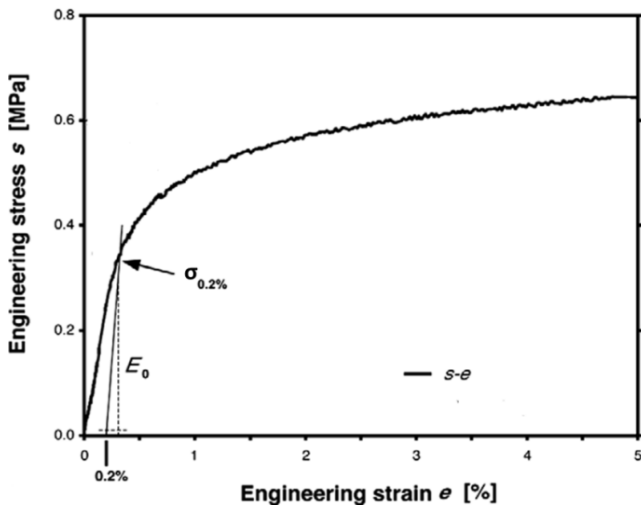
Figure 2.19 - Compressive stress-strain curve of replicated open cell aluminium foam with porosity of 86 %, showing how the yield strength is measured using the flow stress at 0.2 % plastic deformation (after ref. [68]).

In compression, metal foams undergo large plastic deformation after yielding and before full densification, and this is where the foam is exploited in energy absorption applications [12], a subject detailed in the following sub-section.

Theoretically, Gibson and Ashby [9, 47, 55, 56] assumed a foam with a regular cell where struts are located perpendicular to the loading direction and further assumed the only mechanism imposed is bending of these elements. In practice, however, foam struts may plastically buckle, bend or undergo a blend of both mechanisms to determine the deformation behaviour. Many foams, such as Duocel, are stochastic in nature, where most struts are inclined at different angles with respect to the loading direction [62]. As in this case, struts that are aligned or parallel to the compressive loading will undergo plastic buckling whereas those that are aligned at angles will be bent plastically. The study reported in [62] used in-situ and ex-situ examination to investigate the mechanics and mechanisms of deformation behaviour of Duocel foam and found that shorter struts are usually thicker and have larger cross-sections, meaning that their moments of inertia are increased, which affects the foam strength by making them harder to bend. On the other hand, struts at larger angles will impose lower foam strength, and the onset of plastic deformation of an individual strut (as

observed by the appearance of dislocation slip bands) is influenced by defects or porosity, and such struts will act as the weakest link, and foam failure would start from such points [62]. Figure 2.20 shows initially observed dislocation slip bands on the structure of a buckled strut from 10 PPI Duocel foam.
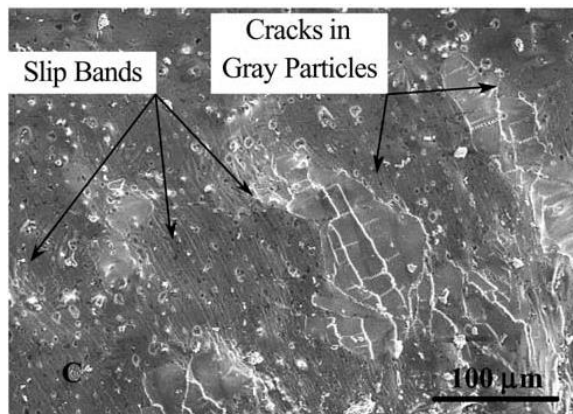
Figure 2.20 – Magnified SEM image from middle region of a strut that deformed by buckling, illustrating slip bands initiated upon deformation and cracks that may grow and propagate to cause strut failure [62].

In tension, by contrast, metallic foams tend to deform plastically after yielding only to a relatively limited strain before they fracture or break. Ashby et al. [12] reported that aluminium foams have relatively low failure strain which is estimated in general to be within the range of 0.2 to 2 %. An example for replicated foam is presented by San Marchi et al. [73] who reported failure strain in tension of around 1 - 2 and 7 % for Al - 12Si and pure (99.99 %) aluminium foams respectively. Amsterdam et al. [74] pointed out that the low strain to failure of metallic foam is mainly associated with weakness of individual struts. In their study, tensile tests were performed on an individual strut made from 6101 Al alloy specifically for the test. Another findings were revealed by Despois et al. [14], in which replicated aluminium foam with low relative density of 0.13, failed at less than 2 % strain in tensile test. Though, foam with higher relative density was in some cases observed to fail at strain as high as 5 %, which still much lower than that experienced in compression [68, 73] (typically strain can reach more than 50 % before densification starts).

Such lower strains to failure of metallic foams are normally experienced in tension and this is partially attributed to the microstructure of metal itself as well as to the

foams morphology, where metallic struts rotate till they are parallel to the loading direction. Struts that are initially aligned with the loading direction will undergo stretching to a limited stain. Further strain causes struts, particularly those containing defects such as porosity or brittle grain boundaries, and surrounded with other rotated and distorted struts, to break. The stress is then redistributed, concentrating again on the weakest neighbouring struts and failure of the entire foam continues with successive failure of struts in the same plane [62, 74]. Amsterdam et al. [74] examined the fracture modes of low density Duocel foam and related the microstructures of struts to the failure behaviour. Two modes of fracture were observed; namely the transgranular ductile mode and intergranular brittle mode. This comprehensive study reported that shear bands initiating in a single grain, followed by necking and failure of strut are the two mechanisms observed in the transgranular fracture mode. Similar ductile transgranular fracture mode has been observed during tensile tests on both copper and nickel foams [64, 65], where slip lines and necking were also detected, see figure 2.21.
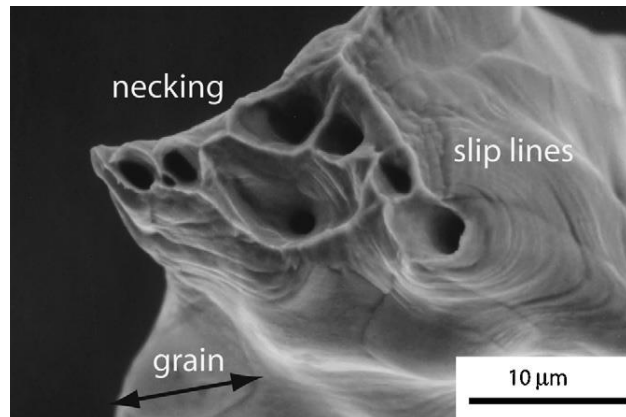
Figure 2.21 – SEM image showing transgranular fracture mode of an individual strut of copper foam after a tensile test [65]. Microstructural features are clearly indicated.

In the brittle intergranular mode, no necking was observed; rather it was the AlFeSi precipitates formed on grain boundaries which made the struts weaker. For aluminium 6xxx alloy, iron (Fe) alloying element (which is frequently present not for desirable effects, but because it is hard to remove) has low solid solubility and form second-phase precipitates (α-AlFeSi and β-AlFeSi) with Si and Al. β-AlFeSi precipitates have low fracture toughness and so crack propagation is favoured due to

less energy being required than for transgranular fracture [74], as seen in figure 2.22 below.
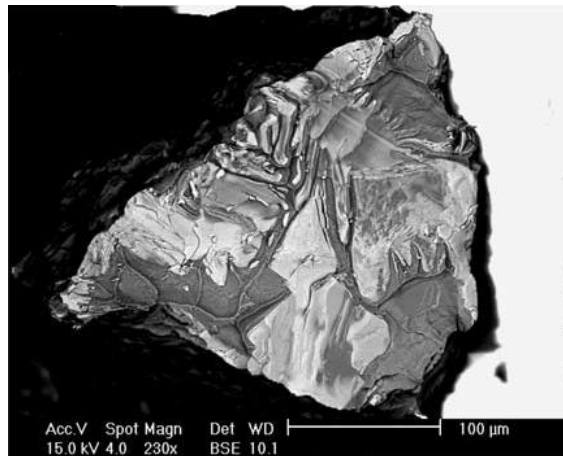
Figure 2.22 – BSE image showing intergranular fracture mode of an individual strut of Duocel foams after tensile test. Different contrast is shown for the present of β-AlFeSi precipitates and possible additional Si. Large surface area has fractured by cleavage of precipitates [74].

This mode of brittle fracture without large necking is comparable to that shown by Al-12Si foam in other work, where the effects of the Si-phase led to foam failure at much lower strain [73]. It is suggested that to increase the fracture toughness of the grain boundary, the content of AlFeSi precipitates should be minimized. This could be done by decreasing the amount of Fe element, by heat treatment or by the addition of other transition elements such as Mn, Cr and Co, all of which are associated with an increase in cost.

It should be noted that the fracture analysis of metallic foams investigated above is directly related to the fracture mode of the individual struts, and the fracture mode of the entire foam body has not been clearly highlighted. Liu [75] emphasized the fracture mode in this respect. It was concluded that the fracture behaviour of the entire nickel foam (as was examined), processed by electrodeposition method explained in section 2.2.3, material is neither fully brittle nor plastic in mode. Moreover, the fracture of the whole nickel foam follows an avulsion mode after limited plastic deformation and the struts fail one after another. The limited deformation of

foam occurs mainly by plastic bending of the struts in the tensile direction, the cell is seen to be elongated to some degree as seen in figure 2.23, plus a small contribution resulting from plastic deformation of the struts and nodes.
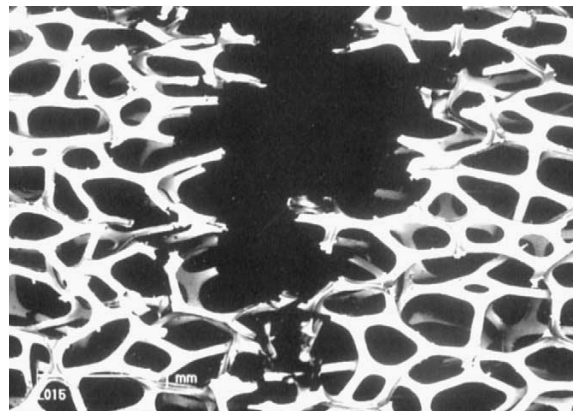
Figure 2.23 – An image showing the fracture behaviour of porous nickel foam showing elongation of metallic struts in the direction of tensile load [75].

2.4.2.4. Energy Absorption of Foams

One of the many attractive mechanical and physical properties potentially offered by metallic foams is the energy that can be absorbed during impact [12]. The increased demands for safety in the automotive industry and the requirements of packaging stimulate a great interest in the energy absorption capability of metal foams [76]. In packaging, for instance, foams can be used as efficient energy absorbers, with the best performance determined by applying different constraints, likely to be either minimum volume or minimum mass. In case where minimum volume is required, designers may consider foams that fulfil equation 2.6 and gives the highest value of the energy absorbed per unit volume W_v. This is the energy absorbed by the foam up to densification strain ε_D, and figure 2.24 shows stress-strain curve with the different parameters of mechanical behaviour of energy absorber foam, following ref [12].
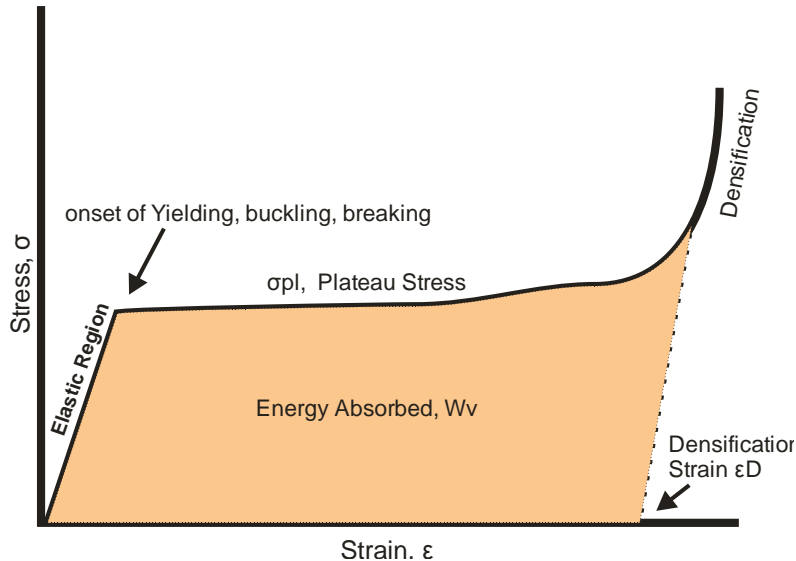
Figure 2.24 – Schematic Stress-strain curve of typical energy absorber porous metal, showing different features of mechanical response under compression, with the energy absorption being obtained under the curve.

$$W_v = \sigma_{pl}\, \varepsilon_D \qquad (2.6)$$

where σ_{pl} is the foam plateau stress, and ε_D is the densification strain, both of which are shown in figure 2.24. On the other hand, if a minimum mass is required for packaging, then foams that have the greatest value of energy absorbed per unit weight, W_w, under equation 2.7 are needed.

$$W_w = \frac{\sigma_{pl}\varepsilon_D}{\rho} \qquad (2.7)$$

For some foams which show slightly different stress-strain curves under compression, equation 2.6 can be modified as suggested by Boonyongmaneerat et al. [1], as follows:

$$U \approx \sigma_y \left(\varepsilon_{max} - 0.5\, \varepsilon_y\right) \qquad (2.8)$$

This model assumes constant stress σ_y after deformation past yield strain ε_y. The value of $(0.5\varepsilon_y)$ has been subtracted from 0.2 total strains; ε_{max} (Eq. 2.8) in ref. [1], which could be done so the model is more representative of the (foam behavior) their

system. Observation of their stress-strain curves shows, prior to the elastic response of the foams, small plastic strains at very low stress at the beginning of deformation, creating small regions which ought to be omitted. ε_y can be estimated using:

$$\varepsilon_y = \sigma_y/E \tag{2.9}$$

where E is the Young's modulus of the foams which can be measured experimentally or predicted using [9]:

$$E = E_s \left(\frac{\rho}{\rho_s}\right)^2 \tag{2.10}$$

.

However, some open cell metal foams show a different stress-strain curve under compression, which is closer to that typical of bulk metals. This is explained by the fact that some metal foams are power-law materials and show work hardening character, where the compressive strength increases gradually with strain [15, 68]. For these types of foams, the potential energy that can be absorbed by the foams can be estimated by integrating the area under the stress-strain curve as follows:

$$W_v = \int_0^{\varepsilon_D} \sigma \, d\varepsilon \tag{2.11}$$

where $d\varepsilon$ is the change in strain, σ is the corresponding stress and other terms are previously defined.

Generally, materials with good strength and ductility are favored for applications in energy absorption sectors and when these properties are combined with low density, the specific properties can be attractive, and their use can be extended to include structural applications (e.g. core materials in sandwich structures). Metallic foams possess these properties and therefore are currently finding an increasing use in wide range of applications, along with ongoing researches to test its suitability for different uses, with examples being as filler materials in aeronautical leading edges [77] and in general crashbox structure, where aluminum foam proved 10 % saving in weight, 30 and 60 % reduction in crashbox length and volume respectively [76] (to be discussed in detail in section 2.7).

2.5. Factors Affecting Mechanical Properties of Metal Foams

Like bulk metals, the mechanical properties of metal foams include their stiffness or Young's modulus, yield strength, ultimate tensile strength, and elongation to failure. These properties can be altered or improved by a number of different factors relating to the foam structure itself or how it has been treated. The effects of these factors on the mechanical behaviour should be carefully understood because this will allow the ability to control the properties to a great extent. Some of the most important effects will now be considered.

2.5.1. The Effects of Cell Size and Shape

Foam structures and cell morphologies depend on production techniques [5, 6, 11-13]. Previous studies showed that the effect of cell size on the mechanical properties of metal foams is insignificant. For instance Gibson and Ashby [47] reported that of all structural parameters cell size has the least effect on mechanical and thermal properties. Instead, cell shape has a much greater influence on foams' properties. Anisotropy of the foam cell shape has been reported to result in 30 % difference in the measured modulus [12]. The properties of foams will be isotropic, (i.e. having the same properties in all directions), if the cells are equiaxed. However, if the cells are more elongated, then the properties depend on whether the direction of the load applied is parallel or perpendicular to the elongated cells. For instance, two tensile tests were carried out on Duocel Al foam specimens by Andrews et al. [48]. The tests were performed parallel and prependicular to the elongated cell axis. For instance, a specimen with ρ =0.193 g cm^{-3} tested parallel to the elongated cell axis showed E = 0.502 GPa whereas a specimen with ρ = 0.19 g cm^{-3} tested prependicular to the elongated cell axis showed E = 0.184 GPa. Similar behaviour was observed in compression tests in terms of the effect of cell shape and orientation on the mechanical properties of aluminium foams. For example, in a study done by Nieh et al. [78], dynamic and quasi-static compressive tests were carried out on aluminium foams with different orientations (morphologies) and densities. It was concluded that the cell size showed a negligible effect on the mechanical properties if the density of the samples remains the same (in some processing methods, changes in cell size and density occur together). However, the cell shape was proved to have

definite effects. For instance, both Young's modulus and yield stress of foam were observed to be different in two orientations. In particular, specimens compressed parallel to elongated cell axis (the longitudinal direction) showed higher Young's modulus and yield stress than those tested prependicular to the elongated cell (the transverse direction) as seen in figure 2.25. below.
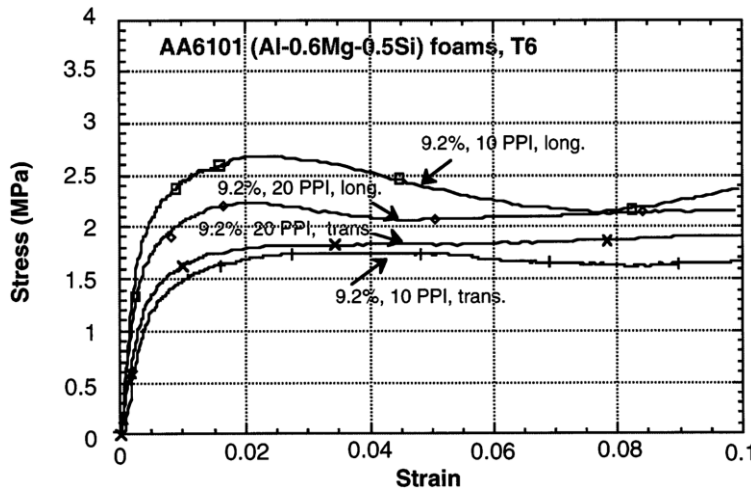
Figure 2.25 - Compressive stress-strain curve for Al6101-T6 foam with different cell orientations [78].

Recent studies, however, have given different findings. These studies have shown that cell size can have an effect of similar magnitude as the relative density on the mechanical behaviour of metal foams. According to Despois et al. [14] , decreasing the pore size from 400 µm to 40 µm in replicated aluminium foams will result in an increase in the work hardening rate and flow stress by a factor of two, as seen in figure 2.26 below. Two reasons may contribute to this size effect, both of which are specific to foams produced by this method. Firstly, formation of dislocations while the Al-NaCl composite was solidifying has been suggested to be the critical cause for such behaviour [3, 14]. This also explains why the effect was not seen in the previous studies, where foams produced in a different method and with different structures (and therefore without this dislocation formation effect).
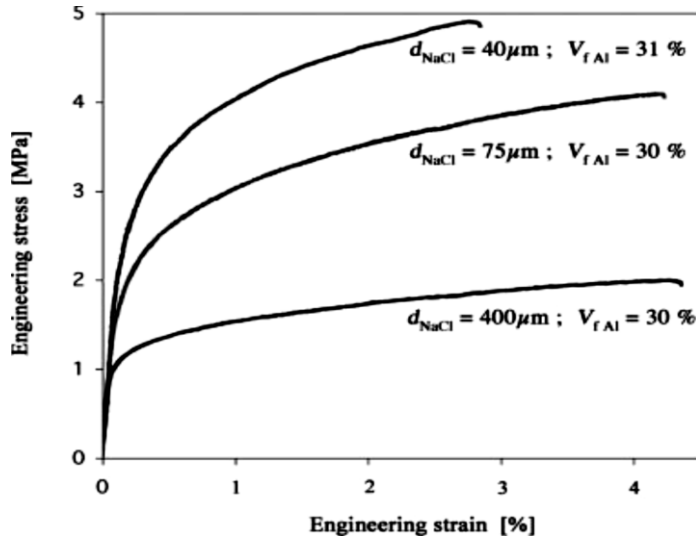
Figure 2.26 – Tensile stress–strain curves of replicated 99.99%pure Al foams, showing the effect of different pore sizes (400, 75, 40 μm) with constant relative density V_f of about 30% [14].

Secondly, decreasing the cell size to e.g. 40 μm can alter the effect on foam surface oxidation processes, in that it increases the volume fraction of the oxide layers during the dissolution step in the replication process. These oxide films can have an effect on the foam mechanical behaviour. The effect exerted by surface oxide on the foam behaviour has been studied in detail [3]. The effect was seen when the pore size is less than 100 μm in diameter.

This size effect observed in [14] should be distinguished from the specimen-pore size effect explained by the model developed by Onck et [79]. This model relates the collapse strength of the foam sample σ_{pl} to its cell size d and width W using the following equation:

$$\frac{\sigma_{pl}}{\sigma_{bulk}} = \frac{(\alpha - 0.5)^2}{\alpha^2} \qquad (2.12)$$

where α, α = W/d, is the ratio of the sample width W to the cell size d, and σ_{bulk} is the stress value in the core of the sample with W→∞. It was indicated that cell edges and faces in the bulk are expected to be much more constrained (i.e. stiffer) than in near the free surfaces. This model tells us that obtaining higher (i.e. more representative of the bulk) σ_{pl} requires larger value of α. This is achieved by using smaller cell size d when the sample dimensions are similar.

Cao et al. [80] reported slightly different observations on open cell aluminium foams made by the infiltration process. It was found that the foams of middle cell size ~ 1.50 mm exhibited higher modulus and strength under both quasi-static and dynamic compression, as seen in the figures 2.27.
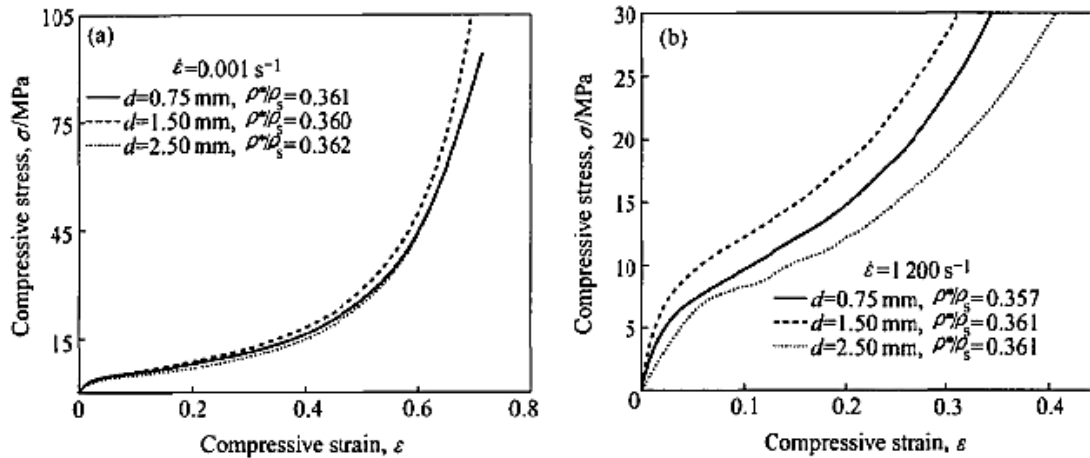
Figure 2.27 - Compressive stress-strain curves of aluminium foams of different cell sizes (0.75, 1.5, 2.5 mm) under quasi-static and dynamic loading with ρ^*/ρ_s = 0.36 ± 0.002, but at different strain rate of 0.001 s^{-1} and 10^3 s^{-1} [80].

In this study, aluminium foam samples with different average cell sizes (0.75 mm, 1.5 mm, and 2.5 mm) and various relative densities (0.36 and 0.41) were studied. It was found that the Young's modulus and yield strength depend on relative density and are strongly affected by cell size. Moreover, when the strain rate is increased from 0.001 s^{-1} up to 10^3 s^{-1}, then the effect of the cell size becomes even stronger on the stiffness and strength of the foam samples. The foam samples with cell size of 1.5 mm and with lower relative density = 0.36, showed more significant strain rate sensitivity, where the strength was increased by more than 110%.

According to [80] , the reported cell size effects on the mechanical behaviour of metal foams are generally contradictive. This is maybe interpreted by the fact that foams can be produced by different methods and with different structures. The more consistent the structures, the better the mechanical properties are. For instance, in the case of foams investigated by [80], the increased strength of foams with 1.5 mm cell size could have been resulted from the regularity and consistency of spheres used in foam production, rather than the absolute cell size. This, in turn, would result

in producing foams with consistent structures. Further investigations have been suggested to explore the mechanisms involved in this cell size effect. This could be practically achieved by using theoretical modelling approaches and numerical methods [80].

2.5.2. The Effects of Relative Density

The relative density is often considered the most important feature in the structure of foams. Relative density of foams is denoted as ρ^*/ρ_s, where ρ^* is the density of the foam, divided by the density of the solid ρ_s [47, 55]. Density of foam can be readily obtained by measuring its mass divided by its volume. Relative density of foam provides measures to the amount of metal relative to the amount of pores in any given foam. For instance, if relative density of a foam is 0.38, then this means that metal occupies 38% of the total volume of that foam. In general foams have relative densities ranging from as low as 0.003 up to 0.4 [47]. According to [58, 81] increasing foam density leads to an increase to foam strength, which is a typical feature for metal foams. A power law function has been established to account for such dependency; stating the fact that the properties of metal foams (i.e. mechanical, thermal and electric conductivity) largely depend on the relative density. The equation is set as follows:

$$K = K_o (\frac{\rho}{\rho o})^m \tag{2.13}$$

K is the property and ρ is the density of foam, whereas K_o and ρ_o are properties and density of bulk metal. The exponent *m* is usually in the range of 1.5 - 1.7. Even so, metal foam samples with very close or similar densities could exhibit variations in their measured properties due to the foam structures heterogeneity i.e. their defects such as regions of lower density, large pores, broken walls or struts etc. Such variations perhaps allow us to question the usefulness of simple equations linking mechanical properties to a single feature of the foam structure (such as the density). The truth is that it is a combination of many features of the foam structure, its treatment and the condition of the base metal that will affect the mechanical behaviour.

Despois et al. [14] found in tension tests that increasing foam density will result in an increase of both Young's modulus and flow stress. Furthermore, Aly [81] found similar findings related to compressive stress and foam density. Moreover, as the density increases the length of the plateau region decreases and the foams will be compressed to densification at lower strains. Figure 2.28 below shows the effect of relative density on tensile stress of replicated Al foams found by Despois et al. [14].
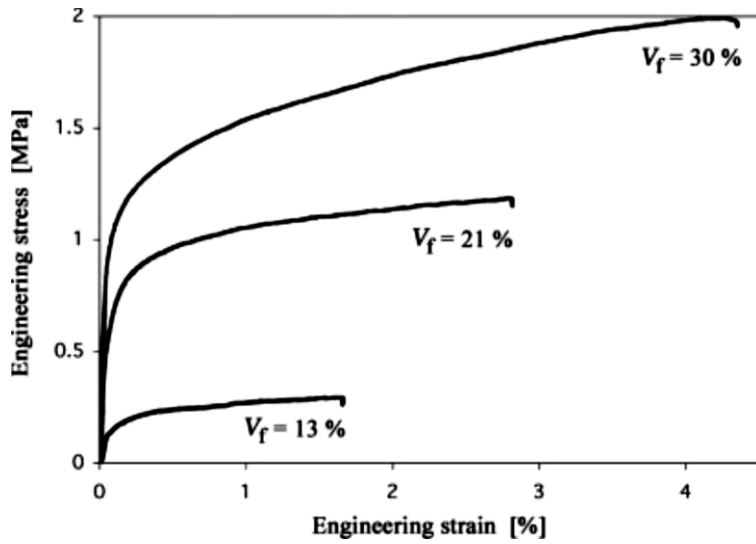
Figure 2.28 – Tensile stress–strain curves of replicated 99.99%pure Al foams, showing the effect of relative density V_f at constant pore size 400 μm [14].

Nieh et al. [78] has also mentioned in his study that density of foam plays the largest role in affecting its properties, stating that foam with higher density will have highest modulus and strength. Gibson and Ashby [47, 55] developed a modelling approach to predict the properties (i.e. the stiffness) of metal foams (open and closed cell). In this model, the stiffness of open cell metal foams depends on the relative density ρ^*/ρ_s, as seen in equation 2.13.

2.5.3. The Effects of Surface Treatments (Coatings)

It is well established that coating any material with another material that has better properties is commonly effective method to improve its mechanical and surface properties [1, 3]. Metal foams have good weight-specific mechanical properties, which could be increased for open cell foams (where pores are connected together

and to the outside environment), by treatments affecting their large specific surface areas. This has been shown to be the case when a surface coating is very thin; of the order of nanometres, being a reaction layer on aluminium foam processed by replication, formed during the dissolution step [3]. The compositions, properties and the effects of the oxide layers are dependent on the leaching medium used. For instance, the oxide formed on aluminium foam when the NaCl preform was dissolved in distilled water consists of an inner hard amorphous alumina layer, a middle soft gelatinous boehmite layer, and outer bayerite crystals, totalling up to 100 nm in thickness. In contrast, the layers formed after dissolution in chromate conversion solution, having thickness of 10 nm, contain no hydroxide but the presence of chromium was detected. The effect of these surface oxides on the foam behaviour has been studied in detail [3], in which an increase in flow stress by a factor of near 5 was seen when dissolving in water. This effect was only observed when the pore size is less than 100 µm in diameter (specifically in 75µm and 26µm), as opposed to the foam sample with 400 µm, where effect is hardly seen (compare figure 2.29.a and 2.29.b below).
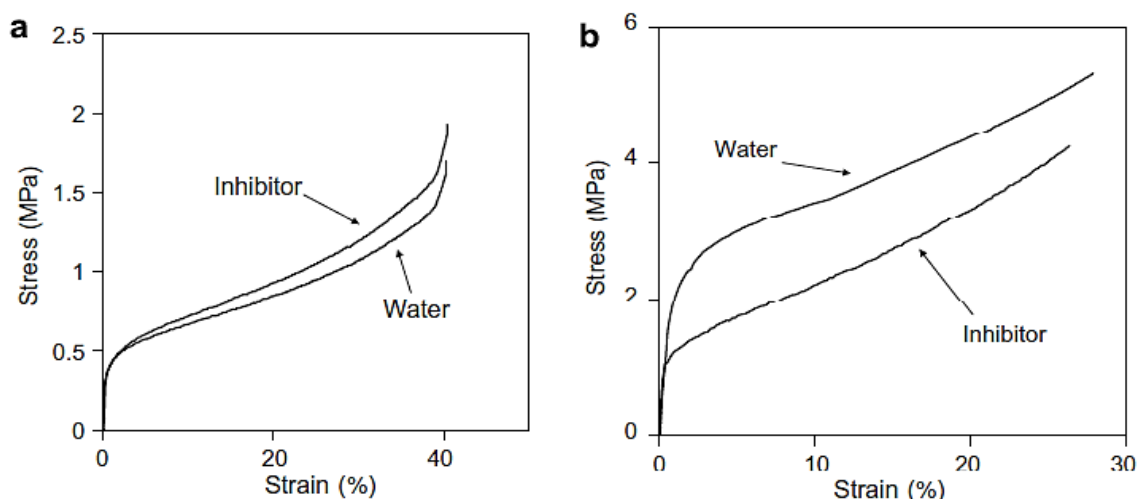
Figure 2.29 - Stress –strain curves for aluminium foams with a) 400 µm pore size and relative density 18 %, and b) 26 µm pore size and relative density of 22 % [3].

Having a very small pore size implies that the struts making the foams are also very small, of the orders of microns, and so the dislocation movements during deformation are disturbed or blocked by these penetrating oxides. The effect could be attributed

to the fact that thicker (e.g.100 nm) oxide layer have the ability to bear more load than the thinner ones (e.g. 10 nm) during deformation, but when compared to the size of strut this does not appear capable of explaining the size of the effect. Other reasoning could be that foams with smaller pore size have larger collapse stress than that for foams with larger pore sizes, as proposed by some studies [58], yet this would not account for the difference between the two surface layers. A reasonable explanation provided by the same study [3] pointed to the effect of a hard and adherent oxide layer on dislocation arrangement underneath the surface layer of the metal (i.e. the image forces felt by the dislocations). This has also been found for passivated aluminium and copper thin films when oxide layer prevent dislocations from exiting the surface [82], resulting in increase in flow stress. The magnitude of such effect on dislocations depends on the structure and thickness of the oxide layer [3, 82], which would explain the plasticity size effect since different oxide layers were formed after using distilled water and conversion solution as leaching media.

Other work on coating of aluminium foams has been carried out by Boonyongmaneerat et al. [1]. In this study, the peak stress of open cell aluminium foam coated with Ni-W alloy (by electrodeposition method similar of that explained in section 2.2.3, but here the initial aluminium foam is not removed) increases with the coating thickness. While foam coated for 1 hour exhibited peak stress of nearly 5 MPa, foam coated for 3 hours showed peak stress of 7 MPa, as compared to uncoated foam with peak stress of nearly 2 MPa. Though this study reported a large increase in foam density especially at higher coating thicknesses e.g. 30 µm, as result of the applied denser coating where densities of the Ni–13W and Ni–20W (at.%) alloys are 10.8 and 11.7 g cm^{-3} respectively.

Similar results relating the increase in peak stress and compressive modulus with coating thickness were obtained by Bouwhius and Lausic [83, 84]. In this study [83], nanocrystalline nickel coating was electrodeposited (as is the case in pervious example) on Duocel foam, where considerable increases in peak stress and Young's modulus were observed with an in the electrodeposited coating thickness, as seen in figure 2.30 below. For instance, the thin coating with thickness of n-Ni = 25.6 µm has resulted in an approximate doubling of the average modulus and peak strength. Moreover, the thick coating with thickness of n-Ni = 72.3 µm had even larger effects, increasing the average Young's modulus by a factor of 3.6, and the peak stress by a factor of 5.2. It is further noticed that stress-strain curves for coated foams show

significant stress drops after reaching the peak stress, which is followed by further increase in stress and the curves became less smooth, as opposed to that shown for uncoated foam, where a ductile behaviour typical for aluminium foams is evidenced.
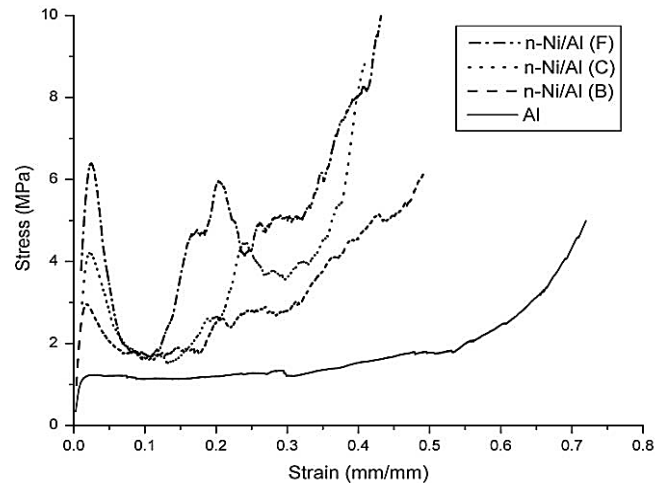
Figure 2.30 - Stress-strain curves of uncoated aluminium foam, foam (B) with nominal coating thickness of t = 25.6 ±1.8 µm, foam (C) with nominal coating thickness t = 39.0 ± 4.8 µm, and foam (F) with nominal coating thickness of t = 72.3 ± 6 µm respectively shown [83].

The drop in stress is explained by the onset of fracture of some coating sleeves, as shown in figure 2.31, located specifically in the middle region of the foam sample. Observations showed that the inner struts receive less coating compared to the outer region (attributed to the foam structure inhibiting the passage of charge and altering the electric field distribution in the electrolyte penetrating the pores), though this is less of a disadvantage for resistance to bending [83].
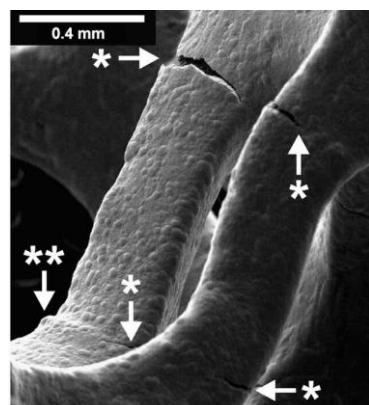
Figure 2.31 – Cracking of a coated strut located in the middle of a foam after peak loading [83].

The strength achieved by coating of metal foams comes from the fact that coating can be applied on the large specific surface area available. As metal foams (at least in their open-cell variants) deform by bending of their struts, each strut acts as a beam. The beam stiffness EI (the resistance of a beam to bending when load is applied) is equivalent to the Young modulus in uniaxial loading. According to the beam theory, the bending moment M applied on a beam is related to the beam stiffness EI and the resulting curvature K of that beam after the load is applied, as follows:

$$M = EI\,K \hspace{4cm} (2.14)$$

It is well established that the most effective way to increase the stiffness of a beam of a fixed materials is by maximizing the value of the second moment of area, I. In conventional structural engineering, this is achieved by using sectional shapes for which most of the sectional area is remote from the neutral axis [2, 83, 85]. This could be similar for coating, in that as the coating is at the beam surfaces (where the strain is highest), even a thin coating on the surface of a strut can have a significant effect, provided that these types of coatings have a high strength and the deposition mechanism allows strong and uniform adhesion with foam struts [1, 83, 86].

2.5.4. Coated Cellular Microtrusses

Hybrid nanocrystalline micro-truss is a type of coated cellular materials that have developed recently. These materials can be produced by electrodepositing nanocrystalline material such as Ni around periodic micro-trusses (regular lattice of small unit cell size) made from metal (i.e. aluminium) or non-metal (i.e. polymer, see figure 2.32 below) [2, 85, 87]. The notion behind this type of material is mainly driven from the need for materials with very low densities accompanied with high strengths. High structural efficiency and ultra-high strength are the main characteristics of these materials, due to the regular truss structure and the good mechanical performance, which is associated with the reduction of the grain size in the material being electrosynthesized, respectively.

Unlike metal foams which have a bending-dominated deformation mechanism, cellular micro-truss materials can be designed to have stretch-dominated deformation

behaviour, a situation where the internal struts deform by compressing or stretching (this is due to the fact that the struts can be positioned precisely and the structure is designed to produce this effect). The design of these hybrid nanocrystalline structures allows the control and enhancement of their load bearing capacity by the strength and adhesion of the electroformed nanocrystalline sleeves.
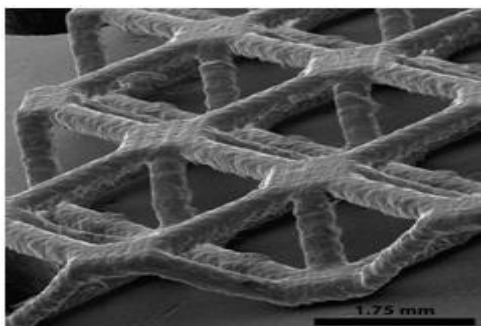
Figure 2.32 - SEM micrograph of an as-deposited nanocrystalline Ni on polymer micro truss [87].

Different mechanisms are involved during deformation of cellular micro-trusses. For instance in an experiment where nanocrystalline hybrid was created by electroforming Ni-Fe on aluminium core [4], a series of load drops took place prior to reaching the peak strength, as demonstrated in figure 2.33. SEM analysis showed the existence of some cracks that had initiated as a result of rotation of the struts before the micro-truss structure buckled.
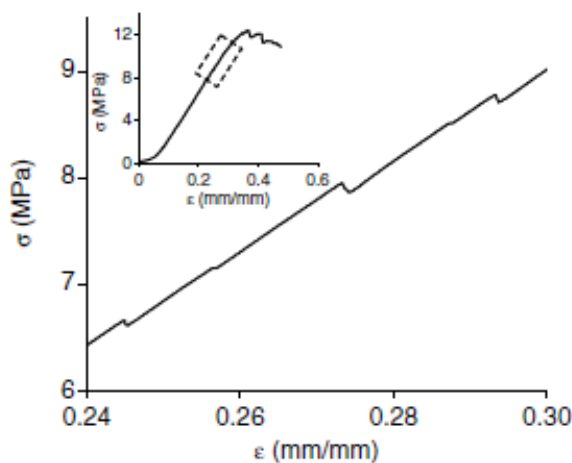
Figure 2.33 - The load drops seen before reaching the peak stress in stress-strain curve of nanocrystalline Ni-Fe/aluminium micro-trusses [4].

However, a different behaviour was seen in the compression of nanocrystalline hybrid of Ni around polymer micro-truss [87]. The analysis of the stress-strain curve showed multiple of load drops that took place after reaching the peak stress as seen in figure 2.34 below. SEM images revealed that the struts under tension experienced continuous factures in the Ni sleeves after the parent micro-trusses had failed.
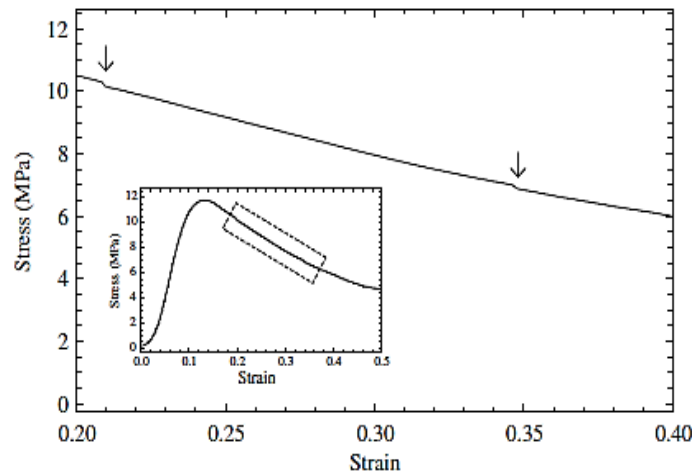
Figure 2.34 - The load drops seen after reaching the peak stress in stress-strain curve of nanocrystalline Ni/polymer micro-trusses [87].

The effect of these ultra- high strength sleeves is seen in the peak strength of the structure. When aluminium is used this is substantially increased by a factor of 12. Several models have been developed in an attempt to predict the mechanical properties of the hybrid micro-truss materials; in particular the elastic modulus and peak stress. However, these models have been found to overpredict the measured values of these properties [86, 87]. Therefore, knockdown factors of α and β are introduced to take into account those overpredictions in the elastic modulus and inelastic buckling behaviour respectively. The overpredictions are attributed to the presence of defects in the real structure of the micro-truss material, along with truss shape irregularity and unsteady initial loading. Furthermore, during deformation the micro-trusses are likely to experience combination of axially and transversely applied loading, conditions which will not be captured by the models developed [86, 87]. Edge effects and the strain absorbed by the Ni sleeves also have a pronounced influence on the measured mechanical properties of the micro-trusses [87]. Under this approach, the elastic modulus E for a pyramidal micro-truss can be written as:

$$E = \alpha E_S(V_{Ni} + V_{polymer})\sin^4\omega \qquad\qquad (2.15)$$

where E_s is the elastic modulus of the individual struts, V_{Ni} and $V_{Polymer}$ are the solid volume fraction of the Ni and the polymer in the strut core, and ω is the strut angle. E_s for the Ni-Polymer strut was estimated using the rule of mixtures approach [87]:

$$Es = f_{Ni}E_{Ni} + (1 - f_{Ni})E_{Polymer} \qquad\qquad (2.16)$$

where f_{Ni} is the fractional Ni strut cross-sectional area, E_{Ni} and $E_{polymer}$ are the elastic moduli of the nanocrystalline Ni and polymer core. This is possible as the struts are considered to be solicited in tension and compression, so the spatial arrangement does not matter. The knockdown factor used in this study was $\alpha = 0.061$, which was obtained by fitting to the experimental data, and the predicted moduli obtained were in good agreement with the experimentally measured properties for different nanocrystalline Ni sleeve thicknesses used. There are other factors that may be considered when using the knockdown factors in the inelastic deformation region; in particular non-uniformity of the micro-truss structures i.e. struts, surface defects and the residual stresses that can be introduced as result of the electrodeposition process [87].

2.6. Modeling Elasticity of Different Porous Structures

This section deals with the predictions of foam mechanical properties, and in particular the foam stiffness. It details some of the existing models that predict the modulus of metal foams, with one example being models which give direct relationship between the foam stiffness and relative density. Other different approaches are also considered, which are based on the elastic response of two different materials combined in a porous structure, to give an understanding of how such response differs from single-material porous structures. This latter type is essentially similar to the material used in the present work, being open cell foams covered with ceramic coatings.

2.6.1. Gibson and Ashby Model

As was explained in section 2.4.1, this simple model was proposed by Gibson and Ashby, and has been used extensively [9, 12, 14, 48, 55, 56, 68, 88] for open cell metal foams. The model is developed by considering the mechanisms by which the foam cell bends, deforms and fails as a result of externally applied loads. The regular configuration assumed for this model is shown in figure 2.14. In this case, the elastic modulus is predicted to exhibit a square dependence on relative density, as follows:

$$\frac{E^*}{E_s} = C_1 \left(\frac{\rho^*}{\rho_s} \right)^2 \tag{2.17}$$

where E^* and ρ^* are the Young's modulus and the density of the foam and E_s and ρ_s are those of the material of which the foam is made. The constant C_1 is often assumed to be 1, as this value has been previously found to be experimentally suitable for general data on open cell metal and polymer foams [9, 10, 55, 56, 89]. However, some workers find this value to be less than 1. For instance, 0.47 has been previously found to be suitable for replicated aluminium foams [15], and is well within the range of 0.1 – 4 experimentally found for different types of open cell metal foams generally [12]. Such differences are commonly attributed to imperfections in the structure of real foam.

2.6.2. Model Based on Beam Stiffness in a Regular Structure

Several workers have used the basic principles of the Gibson-Ashby models (the regular structure of beams and plates, shown in figure 2.35 below, and for example in Chapter 5 of ref. [47]). The core model comes up with a description of the stiffness of the whole system from the stiffness of the individual elements, as determined by beam theory. For such structures, the link between this parameter and the foam stiffness is given by:

$$E_f = \frac{CEI}{L^4} \tag{2.18}$$

where *C* is a constant with theoretically a value close to 1 [24], but in practice often lower, *L* is the cell diameter and *EI* is the beam stiffness.

Bouwhuis et al. [83] used this model but introduce a different parameter to describe the end condition of the beam, B = 192 [12] and, following ref. [83], the equation 2.18 can be re-written as:

$$E_{coating}^{foam} = \alpha \frac{BEI}{2L^4}$$
(2.19)

where α is knockdown factor which accounts for the departure of C from unity, and which has been found to be 0.2 - 0.41 for low density Duocel foam [83, 84], and *B* is the beam end point parameter, and for a fixed end beam loaded at mid-span, and E is the stiffness of the coating, which is taken as 207GPa for Ni for tubular sleeve, or for the metal for an uncoated foam.
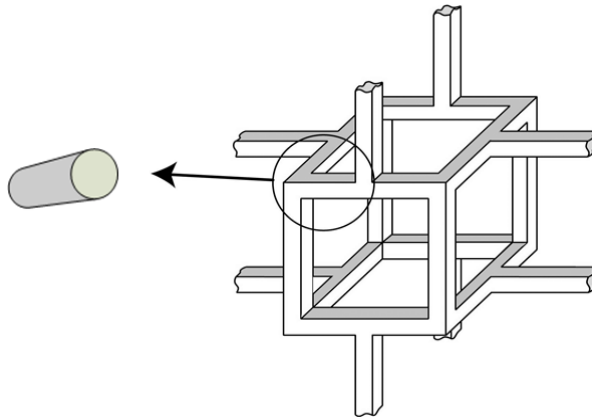
Figure 2.35 – The simplified structure assumed by the Gibson and Ashby model and the circular strut cross-section of the structure as proposed by Bouwhuis et al. [83].

In their study, this equation (2.19) was used to predict the increase in foam stiffness Δ*E* after coating with nanocrystalline Ni of different thicknesses as follows:

$$\Delta E = E_{Ni/Al}^{Foam} - E_{Al}^{Foam}$$
(2.20)

where $E_{Ni/Al}^{foam}$ and E_{Al}^{foam} are the stiffness of hollow tubular foam, part of the structure (consisting of the tubular sleeve of coating) and predicted stiffness of uncoated foam with circular cross-section, as indicated in figure 2.35, both of these are calculated using the same equation (2.19). In each case, the second moment of area I for the nanocrystalline coating sleeve or aluminium strut was calculated as follows:

$$I_{Ni-Al}^{Foam} = \frac{\pi \, ((d+t_{Ni})^4 - d^4)}{64} \tag{2.21}$$

where *d* is the diameter of uncoated foam strut and *t* is the coating thickness.

2.6.3. Model based on Beam Stiffness in a Random Array

A potential drawback of the Gibson-Ashby model is the regular nature of the lattice, different to the majority of actual foam structures which are stochastic in nature. A model that overcomes this was developed by Markaki and Clyne [90], based on a random distribution of uniform fibres bonded together at points, with an example of the basic unit configuration of two fibre segments bonded together at a single point, as seen in figure 2.36 below. Different porosity (ranging from 75 – 95 %) of these brazed metal array fibres can be obtained by changing the volume fraction of the metal fibres and the ratio of the length of a fibre to its diameter (L/D). This model has been found to provide good agreement with the experimental data on the stiffness of the fibre arrays, using tests on a single wires and an assembly of wires bonded together at cross-over points.
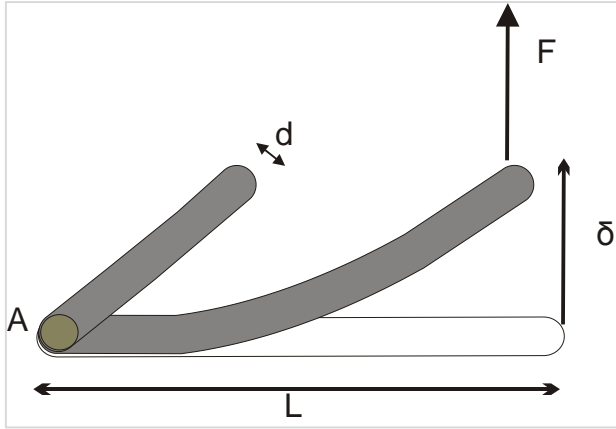
Figure 2.36 – Schematic and simplified drawing of pair of fibers of length L, thickness d, bonded together at point A and its elastic response during an applied load, *F*.

Such a structure is comparable to several types of foam and other porous materials, particularly at lower density, with an example being the Duocel foams.

Following their derivation produces the equation below for the stiffness of the whole array in terms of the beam stiffness of the individual fibre elements:

$$E_f = \frac{9V_f E_S}{32(L/d)^2}$$
(2.22)

where V_f is the volume fraction solid, E_s is the stiffness of the solid materials and other terms are as previously defined.

2.6.4. Hollow Spheres in a Matrix

Syntactic foams are produced when hollow spheres (usually a ceramic) are mixed with a molten metal that is allowed to solidify, forming a metallic matrix around the spheres [91]. This situation is in many ways similar to closed cell foams, but the mechanisms proposed for the potential improvement in mechanical properties of the composite material arise from increasing the stiffness of the foam cell walls, since introducing high volume fraction (up to 35 %) of stiffer hollow spheres to the foamed metal yields a composite cellular solid with sandwich structured cell walls. It is proposed that the walls of the spheres act as the faces of the sandwich while the

dense metal acts as the core, as seen in figure 2.37 below. It is found that these macrostructures affect the foam mechanical properties [91].
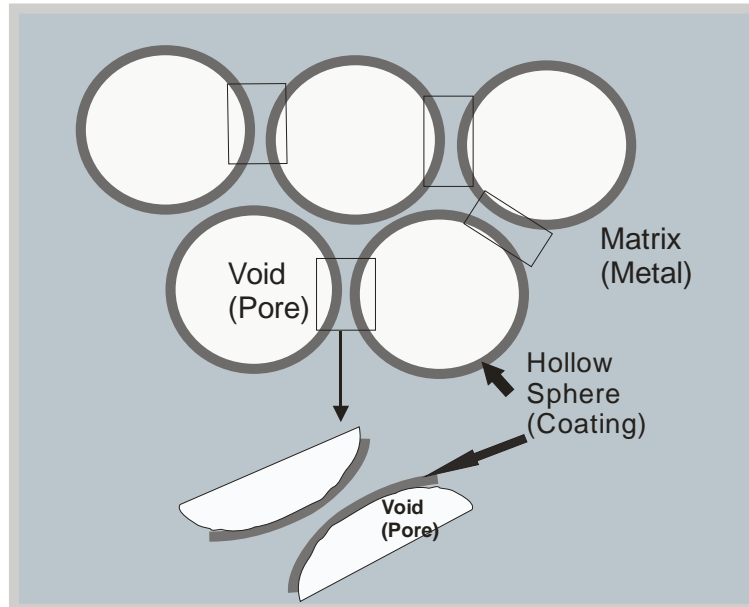
Figure 2.37 – Schematic diagram of a model described in ref.[91] showing composite foam with sandwich beam cell walls (marked in small rectangles). This syntactic foam is made when hollow spheres with thin walls are dispersed into a metal.

This model is developed for syntactic foams and is reported by Huang and Gibson [91], which generalises the stress and displacement fields for a single hollow sphere in a matrix to a dilute dispersion of such spheres (comparing the predictions to experimental results indicates good agreement up to sphere volume fractions of 8%, where interactions between spheres become significant). The elastic modulus of these foams, E_f, is determined using:

$$E_f = \frac{9K_f}{1 + \dfrac{3K_f}{G_f}}$$

(2.23)

where the foam bulk and shear moduli, K_f and G_f are given by:

$$\frac{K_f}{K_0} = \frac{1}{1 - 6\left(\dfrac{1 - \nu_0}{1 - 2\nu_0}\right)C'V_{sphere}} \qquad (2.24)$$

$$\frac{G_f}{G_0} = \frac{1}{1 + 24(1 - \nu_0)C''V_{sphere}} \qquad (2.25)$$

where the subscript *0* relates to bulk properties, ν is the Poisson's ratio, V_{sphere} is the volume fraction of spheres and *C'* and *C"* are dimensionless parameters dependant on the elastic properties and relative geometry of the spheres (radius, wall thickness, etc) which are evaluated numerically by Huang and Gibson to yield values given in [91]

2.7. Applications for Metallic Foams

Metal foams have already been used in a range of applications. However, due to their many useful and unusual properties there may be other potential industrial uses. This section surveys the main types, without going into the detailed design analysis. Foamed metals possess different combined properties and this has been the drive for the increased interest in many applications. For instance, considering an application where weight is the only crucial requirement, then metal foam will not be the only competing material, but if low weight along with heat resistance and energy absorption capabilities are altogether required, then perhaps metal foams are more attractive than other materials [5].

Normally, applications in which metallic foams have been used are linked to typology of the foam; that is if the foams have open or closed cells. For example, certain applications require fluid to be transferred throughout the foamed metal and in this case open cell can be of use. On the other hand, in other applications entirely closed cell foam can have some advantages, as is the case for load-bearing structures. It is also important to choose the appropriate type of metal when deciding to use metallic foam for a certain applications. For instance, aluminium is suitable for lightweight structure but titanium would be more suitable for a bio-medical application. In

summary, structural applications are often appropriate for closed cell foams, whereas for functional applications, open cell foams are the ideal material, as illustrated in figure 2.38 [5, 13]. The selection could be more complex if the foam was expected to fulfil several roles.

2.7.1. Structural applications

Energy absorption is one example; material that exhibits large plastic deformation when subjected to a load of varies speed would the best energy absorber. This is the case in most metallic foams, undergoing large strain at approximately constant stress. It found that metal foams are better than other foamed materials such as polymers due to higher strength, suitable for automobile industry [5, 13]. One example is seen in automobile sector, where the need for passenger safety is of primary importance and impact energy associated with an accident must be absorbed by certain parts of the car body. Metallic foams offer advantages not only as good energy, heat and sound absorbers, but also as lightweight materials, reducing weight and ultimately fuel consumption [12].
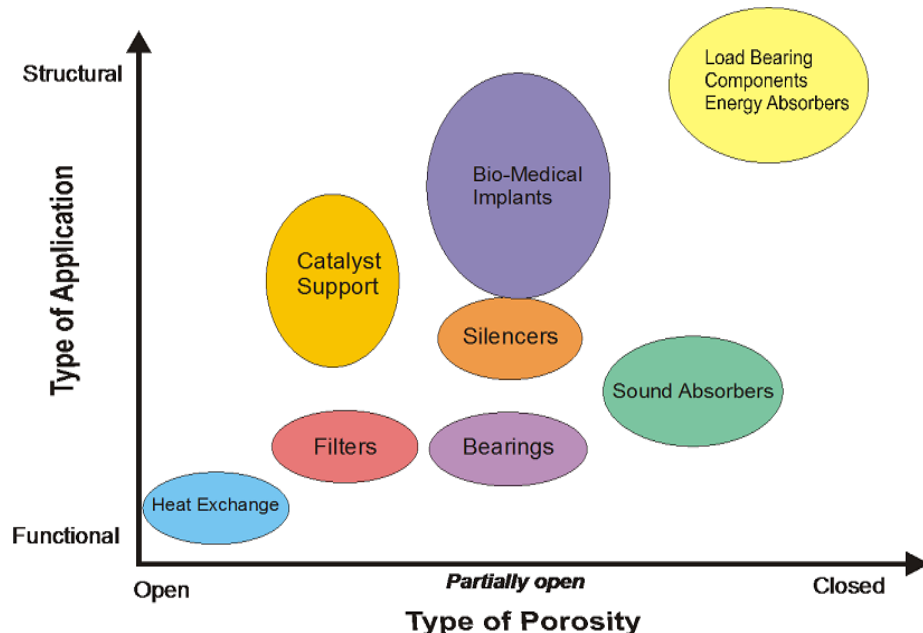
Figure 2.38 – A classification of range of different structural and functional applications in which metallic foams have been or might be used depending on the open or closed cell structures [5].

Other particular structural applications include core sandwich structures, as efficient absorbers for vibration, sound and energy, with the aim to reduce weight, to improve crashworthiness, safety and comfort. Having these properties is needed in many industrial sectors including those in sound control, aerospace industry, ship building, and railway industry, building industry, machine construction and bio-medical sector [12, 47].

2.7.2. Functional applications

Filtration is one example; open cell foam with a range of openness is used as filters. The functionality of filters is to hold back any solid particles or fibres which exist unintentionally in a liquid. The properties required in this application for a given material is to be corrosion resistant, have good mechanical properties, good retention capability at different scales and to be cleaned readily and easily. Metal foams offer these properties with the ability to separate particles and fibres from liquid and gas. Examples of these applications are cleaning of recycled polymer melt and filtration of diesel fumes [5]. However, there are different functional applications. For instance, metal foams are now used as e.g. thermal insulations, heat exchangers, firewalls, catalysts, battery electrodes, magnetic flux conductors [92].

Open cell foams are therefore useful, but may not have the best mechanical properties. Hence, further investigation should be directed to improve their mechanical and physical properties with the aim to focus on processing routes, taking into account the importance of relative density, cell shape and cell sizes which have already been shown to affect foams' mechanical behaviour. The potential applications in impact-absorption systems attract the use of metal foams, with a particular example being aluminum foams. This has been trialled in some of these applications and researches are currently focusing on testing these materials [76, 77, 93], seeking to make use of their combined functional and structural properties, for example having a part that serves a structural role and is also a heat exchanger, fuel store, filler, etc. to optimize this we need to improve the mechanical properties of open cell aluminum foams. As discussed previously, coatings offer one route for achieving this and as a result, coatings can now be considered as new factor which can have an effect on the mechanical and surface properties of these light materials.

Therefore, the mechanical and surface properties of metallic foams can be further improved by applying different types of coatings, using different coating techniques, a fact that has already been reported by several studies [83, 85]. Nevertheless there are many coating techniques available, and it is important that these are all investigated for applicability to metallic foams.

Chapter 3: Plasma Electrolytic Oxidation Coatings

3.1. Introduction

The Plasma Electrolytic Oxidation (PEO) process has been examined on dense metals in a wide range of structures [94, 95], but its application to metallic foams is rather limited [96, 97] meaning that it has not yet been thoroughly investigated. PEO is a plasma-assisted electrochemical surface treatment that is used to convert surfaces of light metals, e.g. Al [98] and its alloys [99], Mg [100], and Ti [101] into hard and well-adhered oxide layers [7]. The process operates at high anodic potentials (typically several hundreds of volts) that trigger numerous microdischarge events at the metal-electrolyte interface, generating high instantaneous temperatures and pressures. Excursions to these extreme conditions alternated with rapid cooling by the surrounding electrolyte significantly affect coating morphology, phase composition and stress state [102] leading to the formation of high-temperature oxide phases, fused ceramic-like structures and crack networks.

PEO coatings on aluminum are usually produced in diluted electrolytes of low electric conductivity. The coatings comprise of a mixture of crystalline phases and amorphous material and consist mainly of two regions [103]: a dense and hard inner region which has increased α-Al$_2$O$_3$ content and a porous outer region containing more γ-Al$_2$O$_3$, plus aluminosilicates and amorphous phases that incorporate some electrolyte species (e.g. Si). Figure 3.1 below shows a cross-sectional backscattered SEM image of PEO coating with a thickness of around 100 µm, formed on an aluminum alloy substrate, exhibiting typical features such as compact inner and more porous outer regions, as well as a network of microcracks including those formed as discharge channels.
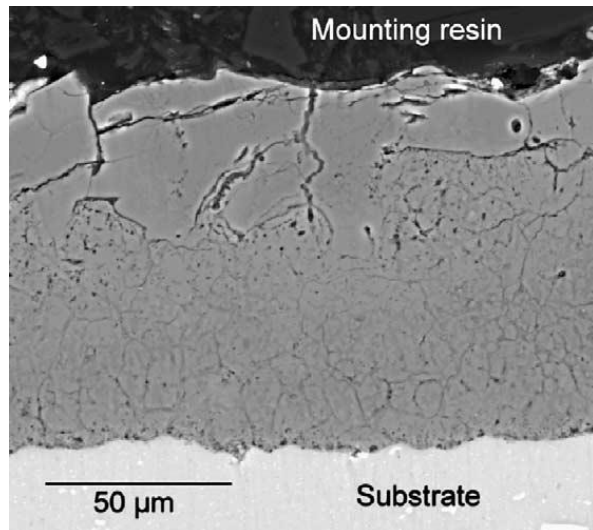
Figure 3.1 – Optical micrograph showing typical PEO coating formed
on aluminum substrate, showing some structural features [104].

Electrolyte composition, treatment time and applied electrical regime (especially current density) are key parameters influencing coating characteristics and properties, including mechanical performance [105]. The content of α-Al$_2$O$_3$ (which is the phase associated with high coating hardness and stiffness) tends to increase with both current density and processing time (which also affects coating thickness) [106, 107] but thicker layers tend to develop coating defects and surface roughness, which can affect the global tensile properties of the coated material [99, 108]. Extensive work has been carried out aiming to refine the coating morphology, e.g. by application of high-frequency pulsed bipolar current waveforms [107].

Uniform PEO coating of metal foams would be expected to be closely associated with the throwing power [109, 110] of the process, which is conventionally maximized in anodizing complex geometry components by arranging electrolyte flow through [95] or using auxiliary electrodes at the inner component surfaces [94]; these would be inefficient for metal foams with fine or high-aspect-ratio porosity. Moreover, additional problems in PEO coating of Al foams may arise due the large Ohmic voltage drops in the electrolyte, caused by the relatively low conductivity (3-6 mS cm^{-1}) of the dilute silicate-alkaline solutions commonly used for production of hard PEO coatings on dense Al components [105]. This can be adjusted by increased electrolyte concentration; however a careful balance is required to maintain coating morphology and growth rates.

3.1. Processing of PEO Coatings

A PEO processing unit consists of an electrolyser, a high power electrical source and electrolyte management system (see figure 3.2). The electrolyser is a bath made of stainless steel which contains the electrolyte, and is often water-cooled. The sample under treatment is connected to the output of the electrical source as one of the electrodes (anode), while being immersed in the bath of electrolyte solution. The stainless steel bath acts as a counter-electrode. High potentials are applied between both electrodes. Different power regimes can be used, which are classified as direct current modes (DC) [111], which may be pulsed unipolar (pulsed DC [112]), and alternating current modes (AC) [94], including pulsed bi-polar [105] with pulse frequencies reaching up to KHz. More details of the differences between the two (DC and AC regimes) will be encountered later in the discussion.

The electrolyser is positioned on an insulating base which is contained in an earthed steel bath. Different attachments may be integrated within the PEO processing unit, such as electrolyte mixing and water cooling arrangements that contain the electrolyte management system, as seen in the schematic diagram in figure 3.2 below.
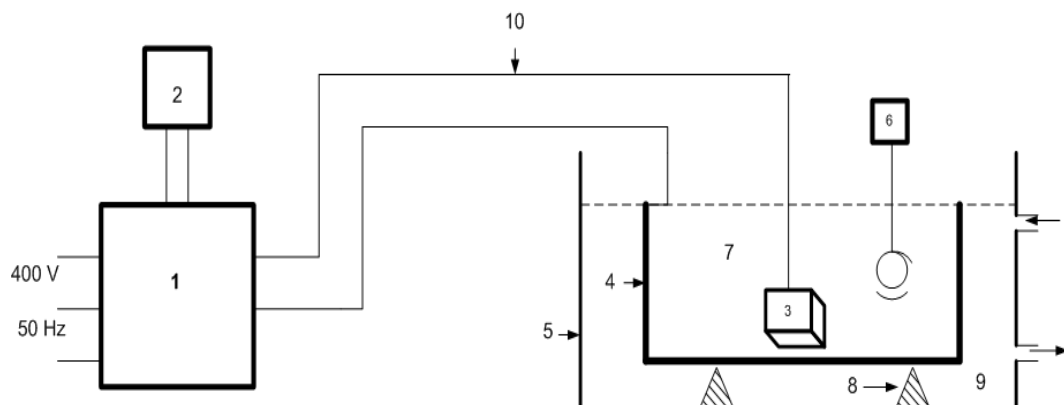
Figure 3.2 – Schematic diagram showing an alternating current PEO coating system with different components; 1- high voltage power supply, 2- control system, 3- treated sample, 4- stainless steel bath, 5- plastic bath, 6- stirring system, 7- electrolyte, 8- insulators, 9- cooled water, 10- connecting wires.

Generally, the PEO process uses much higher voltage (e.g. 400 – 600 V) than that used in conventional anodizing processes (e.g. 50 V). Such higher voltages largely exceed the dielectric breakdown voltage of the anodic film initially formed. This results in the formation of local plasma state, which is observed by the ignition of microdischarges and gas evolution on the metal surface. Microdischarges are mobile and constantly emerging on the metal surface within the electrolyte solution in which different ionic elements such as silica are added in the form of dissolved salts, so that they can be incorporated into the resulting alumina coating [113]. The local instantaneous discharge events (microarcs and sparking events) occur at temperatures as high as 10^3 - 10^4 K and pressures of 10^2 – 10^3 MPa [7, 114]. These extreme conditions cause melting of the metal in the vicinity of oxygen; these high temperatures can also re-melt the oxide in the form of Al_2O_3. The molten material is immediately solidified when it is ejected from the discharge channels to the surface by heat loss to the surrounding electrolyte and this process is continuous in each discharge channel. It is suggested that the electrolyte should be cooled during processing to increase its lifetime in service. Heating above 30 °C may increase the rate of coating deposition, but this will also diminish the active ingredients in the electrolyte [115] and hence how often it can be used.

Cooling of molten metal oxide is also promoted by the metal substrate when coating thickness is not high, so that the middle part of the coating is less affected by these heating/cooling cycles. It is found that the cooling rate can be as fast as 10^8 K s^{-1} [7] which is mainly responsible, along with the discharges, for the formation of certain coating features and defects, including, voids, porosity, flakes and surface roughness [111].

The growth of the oxide coating is mainly attained by two different, yet simultaneous, processes; by an electrochemical reaction process on the discharge-free surfaces of the coated metal and via high temperature reactions caused by discharges. Discharges are responsible for the thermal and chemical conditions at the metal surface, thus playing an important role in formation, composition, and structure and stress state of phases formed.

In light of the discussion above, it is clear that PEO coatings form as a result of different processing conditions, such as high temperature and pressure, along with electrochemical and plasma-chemical reactions. These processes impose the generation of complex internal stresses within the coatings, which affect the coating

microstructure hence the properties. Microcrack formation is the microstructural response of these intrinsic stresses to provide stress relaxation type processes for stabilization of these coatings. While this phenomenon is less seen in more porous coatings, it is promoted in denser coating structures, as explained in detail in the following subsections.

3.2. Properties of PEO Coatings

3.3.1. Coating Microstructures

As PEO coating is formed, the evolving microdischarges continuously affect the annealing, sintering, crystallization and phase transformation in the coating material. It is reported that amorphous phases are formed at the first stage of the coating formation, and upon the following melting, sintering and cooling, transformation is promoted to more crystalline metastable phase of γ-Al_2O_3. Further high temperature heating from the microdischarges leads to final transformation from metastable to more thermodynamically stable α–Al_2O_3 phase, which occurs at temperatures of around 800 – 1200 °C during the process [111]. The existence of these phases within the coating is affected by the heating and cooling cycles. For instance, amorphous and metastable phases (γ-Al_2O_3) largely exist in the regions that experience high cooling rate [114], in particular, the outer surfaces near the electrolyte, the inner region near the substrate and the internal walls of discharge channels. The middle part of the coating experiences lower cooling rate, as compared to the outer and the inner parts, and so transformation is favoured to more compact α–Al_2O_3 crystalline phases, see figure 3.3 below.

The content of alpha alumina phase is increased with increase in coating thickness [105, 112, 116], as result of two different mechanisms. Firstly, as the coating thickness increases, there will be fewer but more energetic, concentrated discharges and as such these strong discharges are accompanied with higher temperature suitable for transformation of gamma to alpha phase. This is further explained by the fact that when the oxide layer is not thick enough (e.g. ≤ 40 µm), as is the case at the beginning of the process, its thermal insulation is weak such that the coating surface

temperature does not exceed that required for transformation to alpha phase occur, since more heat input is transferred through to the metal substrate. In this case γ-Al_2O_3 phase dominates coating microstructures.
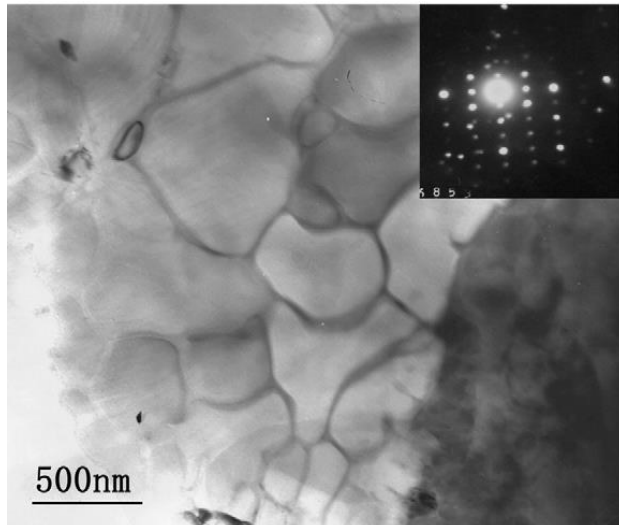
Figure 3.3 - TEM image from the inner part of the coating, showing the inner compact crystal grains with the size of about 500 nm. Also shown is an electron diffraction pattern of the inner structure [103].

However, as coating thickness increases, the thermal input to the substrate reduces, which increases the local gas temperature at the surface. Almost all of the resulting heat is absorbed by the thick coating, allowing less heat to reach the substrate and so transformation of γ→α alumina phase occurs. In other words, phase transformation takes place when the discharges are strong enough to heat the oxide coating to the required temperatures, for a time adequate to allow phase transformation. The estimated time and energy required for melting and phase transition are 0.25 – 5 ms and 18 - 50 kA m^{-2} respectively [116]. Secondly, as coating thickness increases, internal residual stresses will be formed as result of rapid heating and cooling cycles experienced during coating formation, and as such formation of stable and crystalline alpha alumina is favoured for relief of these stresses [105, 112].

It is reported that current density, which depends on the surface area of the treated substrate, plays an important role during the formation of PEO coatings. For instance, the amount of the harder α-Al_2O_3 phase can be increased by increasing the current density, which can reach up to 5 kA m^{-2}, and even more [105]. Moreover,

current density increase results in an increase in coating growth rate with a linear relationship. This is so, especially at the early stage of the coating process with higher energy input into the process. It is known that coating formation is based mainly on the ejected molten alumina from the discharge channels out to the surface, which is then rapidly cooled by the surrounding electrolyte [7]. So higher current density leads to thicker coating quicker, and thicker coating becomes difficult for discharges to penetrate into the substrate which slows the growth process. The reduction in coating growth rate continues till it reaches a stage where it is eventually halted. This means that the effect of current density on coating growth becomes insignificant at later stages of the process.

The effect of substrate chemical composition on phase evolutions of the PEO coatings formed has been investigated. It has been shown that the amount α-Al_2O_3 phase can be substantially increased to reach 60 % or more for coating produced on aluminium containing 4 – 5 % Cu [7]. For instance, a study by Shi-Gange et al. [99] reported formation of PEO coating with a α-Al_2O_3 content of 64±4 %, on copper-containing aluminium alloy (3.8–4.9% Cu) samples. This study found that the highest modulus and hardness on these coatings were 270 GPa and 22 GPa respectively, which are considered to be quite high. On the other hand, higher content of γ-Al_2O_3 phase is mainly formed on magnesium containing aluminium alloys while mullite-based PEO coatings can be obtained on silicon containing alloys [7, 115]. It must be noted, however, that the electrolyte composition is also essential for promoting a specific phase formation. For instance in work [99], sodium aluminate ($NaAlO_2$) used in the solution could be, at least partly, responsible for the formation of more alumina phases, whereas a dilute alkaline solution used in work [115] has been refined with a sodium silicate to promote formation of mullite phase ($3Al_2O_3$–$2SiO_2$). Furthermore, careful selection of the electrolyte concentration is also required, since coatings formed in solution with high concentration of silica have been reported to be thicker, but more porous, which negatively affects the mechanical and tribological properties of these coatings.

As coating growth continues during processing, its surface roughness increases with longer processing times, see figure 3.4. Different structural surface features evolve during the processing. For instance, the diameters of sintered ceramic particles within the coating were measured and found to be in the range of 30 - 50 µm, increasing with the process time [103]. Moreover, porosity at the surface is also affected by

discharge characteristics. It has been found that pore size is increased from ≈ 7 μm to a value of ≈ 20 – 25 μm during the second half of the process cycle (in an investigation with 80 minutes processing time) of the process [116]. This is explained by the fact that discharge channels and the amount of ejected molten oxide become larger as the discharges become fewer and stronger. In other words, stronger discharges have greater energy inputs which causes a larger amount of substrate and its oxide to melt down, and eventually the molten materials is ejected onto the surface, forming larger ceramic particles when it is immediately cooled by the electrolyte.
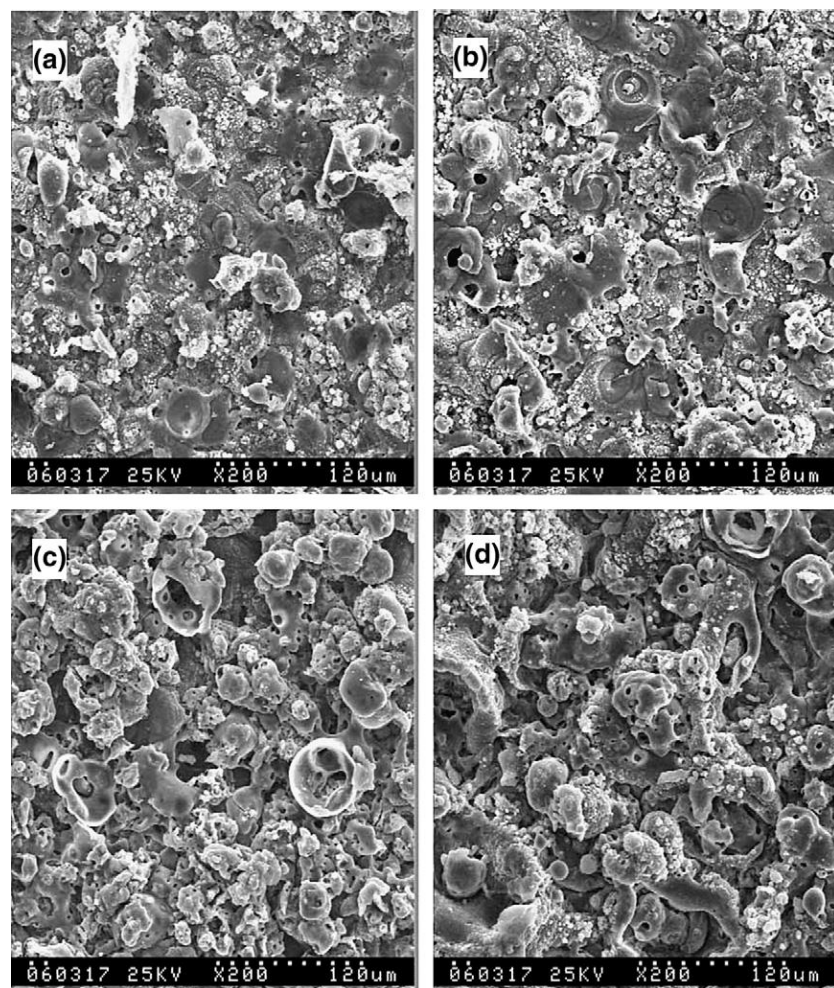
Figure 3.4 - SEM images of PEO coatings formed at different treatment times of a) 60, b) 120, c) 180 and d) 240 minutes. Roughness and ceramic particles can be observed, and their sizes differ in each case, increasing with increasing processing time [103].

The average diameter of the discharge channels (the heat-affected zone around them range between 5 – 50 μm in diameter [7]) increase gradually as the treatment

time progresses, whereas their number decreases. Figure 3.5 shows a discharge channel from which the molten material is ejected, as result of greater energy input. The pore is shown to be surrounded by solidified material and some localised microcracks which may form as result of a rapid cooling by the electrolyte [114].
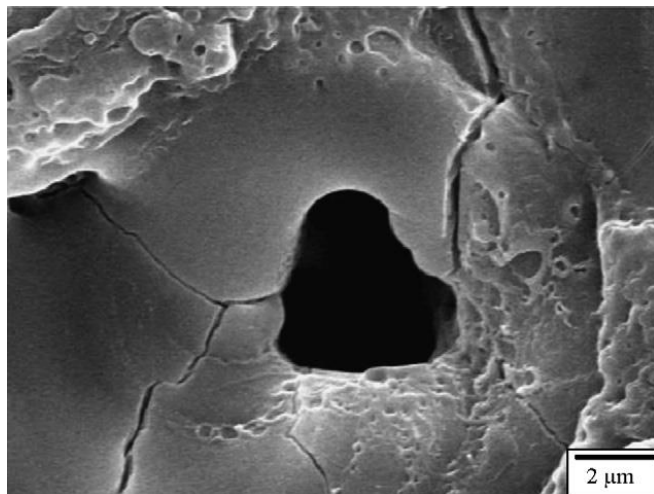
Figure 3.5 – SEM image of a discharge channel; a typical feature of PEO coating processed for 40 minutes at current density of 15 A/dm^2. Such a pore may penetrate the entire coating thickness to the substrate [114].

These different coating transformation processes occur due to electrochemical, high temperature and plasma-assisted chemical reactions, which cause different residual (intrinsic and thermal) stresses that affect coating mechanical properties such as hardness, modulus, wear and corrosion resistance. Residual stresses in PEO coating can cause peeling or cracking of coatings during service; thus these stresses need to be understood if further development based on the coating with fewest structural defects can be established. A comprehensive study on quantifying the residual stress of PEO coating is reported by Khan et al. [112], who found that the mechanical properties of the PEO coating formed are directly affected by these internal stresses (compressive, normal and shear stresses), which may appear as a result of coating formation and growth, thermal effects from the discharges, and phase transformation processes.

The intrinsic (growth) stresses caused by the coating formation and growth occur because the ceramic coating formed has a larger volume than the treated metal. The effects of these internal stresses therefore increase with increase in coating

thickness. In this case, the oxide coating is in compression whilst the metal is in tension. For fatigue and crack resistance, a compressive stress state is better than tensile stress, as the former prevents crack propagation, but too high compressive stresses may harm coating adhesion with the base metal and may lead to cracking between the two.

Thermal stresses can be caused by two mechanisms; firstly, the substrate and its oxide both have different thermal expansion, with an example of aluminium being much higher than that of alumina. Shi-Gang et al. [99] measured the thermal expansion coefficient of both aluminium and PEO coating in a test between 300 – 800 °C, and found values of 24x10^{-6} K^{-1} and 7.38x10^{-6} K^{-1} respectively. This difference clearly indicates that there is thermal stress imposed, which is compressive in nature. Secondly, a temperature gradient across the coating thickness is also responsible for generation of thermal stresses. The degree of impact of this type of stress depends on discharge strength (e.g. how much discharges can cause heating at the interface of electrolyte/coating, at discharge channels, and metal/coating), which is found to be greater in thin coatings. Thirdly, α - γ phase transformation affect coating stress state because alpha alumina has higher density of ~ 3.99 g cm^{-3} with smaller unit cell volume ~ 0.255 nm^3, as compared to gamma alumina with density of 3.60 g cm^{-3} and unit cell size of 0.493 nm^3 [112, 117]. All of these different structural and thermal mechanisms contribute to the formation of internal stresses and their effects increase with increasing coating growth rate and formation temperature. The internal stresses can be direct or shear. Compressive direct stress can be of advantage, since it can increase the effective coating yield stress in tension. But for materials of brittle character, increasing these compressive stresses beyond their failure stresses leads to cracking. For PEO coating, crack formation is perhaps linked to relaxation processes from the intense internal stresses, and its magnitude is higher for denser coating than for more porous coating. Variations in normal stresses measured can be clearly observed, see figure 3.6, with different frequencies and duty cycles. A range of values can be found, with highest normal stress of ~ - 818±47 MPa measured at δ = 0.2 and f = 500 Hz and lowest value of ~ - 111±19 MPa found at δ = 0.8 and f = 5000 Hz.
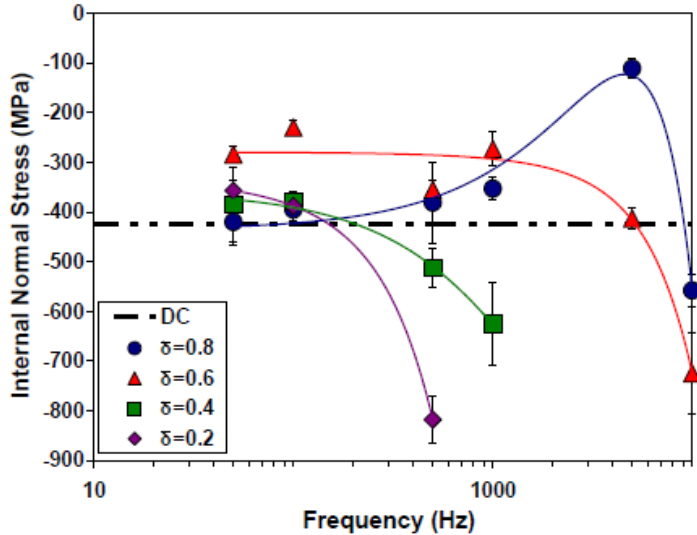
Figure 3.6 – Evolution of normal compressive internal stresses in PEO coatings produced under different frequencies and duty cycles adapted during pulsed unipolar of PEO process [112].

An overall conclusion from the previously reported work may be summarized in that an increase in frequency and a decrease in duty cycle both lead to the formation of thinner coatings, which is generally not favourable as a result of increased compressive normal and shear stresses, which may be due to incorporation of smaller amount of porosity to absorb crack formation as well as the stress gradient being more effective in these thin coatings. Moreover, it should be noted that optimum parameters suggested in the same study were those used for coatings produced at δ = 0.8 and f = 5000 Hz, which offer coating with minimal intrinsic stresses [112]. Nonetheless, as pointed earlier PEO coatings are generally known to contain nets of microcracks and pores which promote stresses relaxation process, and as in such case residual stresses may not be supported and might be ineffective.

3.3.2. Coating Tribological and Mechanical Properties

PEO coatings have been studied under various testing methods to evaluate their physical and mechanical properties. For instance, a comprehensive study on tribological performance of PEO coating is reported by Nie et al. [113]. Different adhesion and tribological friction and wear tests have been performed on range of PEO coating thicknesses, including scratch adhesion, sliding wear, ball-on-plate and

impact tests. In this study, PEO coatings examined had thicknesses of 100, 150 and 250 µm, where the highest measured microhardness was for the thin coating of 100 µm, reaching 2400 HV ($\approx$ 23.5 GPa), which compares well to an average PEO coating hardness value of 2000 HV ($\approx$ 19.6 GPa) reported by Xue et al. [118]. An average value of 120 HV was measured for the bulk aluminium, which is clearly indicative of the large improvements in mechanical and tribological properties of the treated metal substrate. The maximum hardness was reduced as coating thickness increased to 250 µm, and its location within the coating also changed moving away from the coating/substrate interface. For example, the maximum hardness in 100 µm and 250 µm thick coatings was found at 20 and 60 µm distance from the coatings interface respectively. The reduction in hardness in both cases is attributed to a change in phase composition and the porosity [113]. As regards to the location of the maximum hardness at different distances from the interface, this may be because, as explained earlier, the inner regions adjacent to the metal substrate undergo relatively faster cooling which allow formation of moderate hardness phases such as γ–Al_2O_3, unlike the middle denser region which contains larger contents of high temperature phases. Microhardness behaviour for different PEO coatings, being alpha alumina (α–Al_2O_3), gamma alumina (γ–Al_2O_3) and mullite ($Al_6Si_2O_{13}$) as function of coating thickness are shown in figure 3.7.
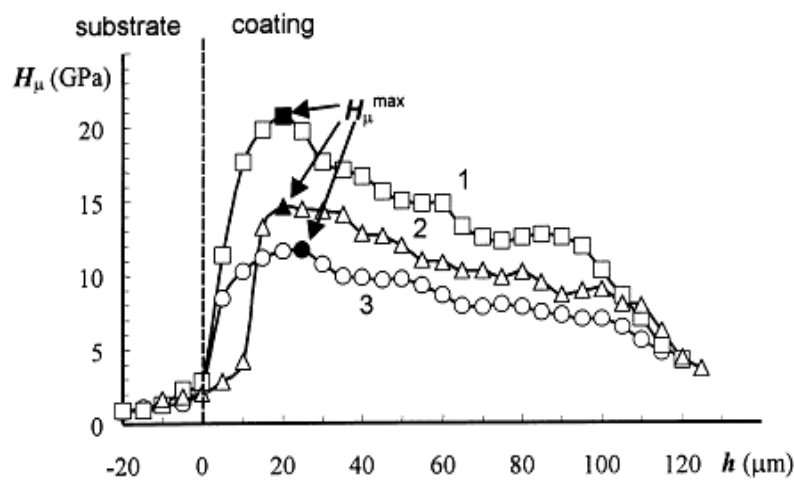
Figure 3.7 – Hardness behaviour showing decrease in hardness in outer porous region and near-substrate inner regions for different PEO coatings based on (1) α–Al_2O_3, (2) γ–Al_2O_3 and (3) $Al_6Si_2O_{13}$ [7].

The highest hardness values found for PEO coating based on α–Al_2O_3 are in the range of 17 – 22 GPa, while lower values found for those based on γ–Al_2O_3 are between 10 – 15 GPa, but much lower values correspond to those found for $Al_6Si_2O_{13}$, with 4 – 9 GPa [7, 99, 111, 115]. These reported PEO hardness values compare favourably to those values offered by conventional anodic alumina with values of 1.2 – 8.5 GPa, and would be expected to give better protection of aluminium alloy substrate with hardness of ≈ 0.69 - 1 GPa [115, 119]. From figure 3.7, it can be seen that, in all cases, the outer and the inner-near the substrate coating regions show lower hardness values than the middle coating regions. While the inner region incorporates fine porosity and softer phases, the outer coating region shows increased levels of coarse porosity and silica-dominated phases which obviously lower the measured hardness. It is suggested that the existence of such porosity can be of benefit to the coating, as it helps reduce brittle failure and relax residual internal and thermal stresses [112], as explained in section 3.3.1. The low hardness and the increased level of porosity in the outer region have been found to increase the wear rate of the coating, and so in many instances these outer porous layers are removed mechanically as a processing step to improve surface properties of the coating [7].

Wear resistance has also been tested on PEO coating on pure aluminium substrate [98]. Wear mechanisms of the ceramic coating appeared as deformation and polishing of microspores and roughness, with signs of local delamination. It can also be seen in figure 3.8 that weight loss of pure aluminium is an order of magnitude higher than that of PEO coating in dry sliding wear test, using a load of 10N in MPX-2000 disk-disk tester against Al_2O_3 sandpaper. This indicates the potential improvement in wear and corrosion resistance of the treated substrate.
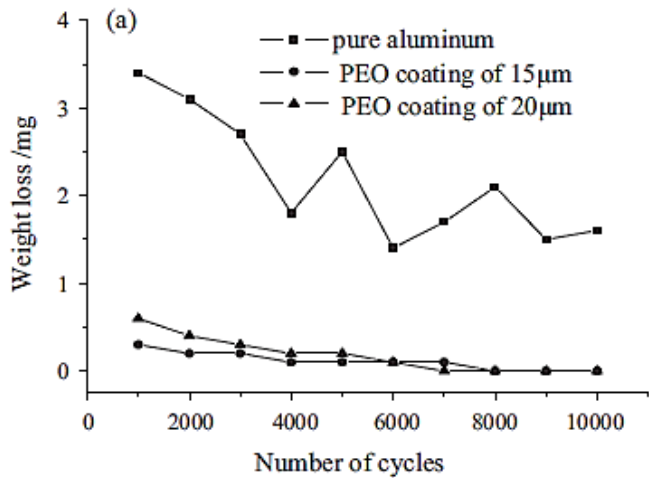
Figure 3.8 – Comparison in weight loss (wear resistance) between PEO coating of two different thicknesses and pure aluminium sample, showing higher wear resistance offered by the PEO coatings which loss small amount of weight after being subjected to 10 N load in rotation disk in dry sliding wear [98].

Another study found in dry wear tests that PEO coatings outperformed the aluminium substrate, with much lower wear values ranging between $10^{-8} – 10^{-9}$ mm^3/Nm, as compared to a value in the range of 10^{-4} mm^3/Nm. In general, the thickest coating of 250 μm showed best performance in load supporting capability in both scratch and sliding tests, while the thinnest coating of 100 μm showed much better capability in impact and low-load sliding wear tests [113].

Bonding between PEO coating and the substrate has been found to be quite significant. The sintering process during the formation of the ceramic coating occurs at extremely high temperatures and pressures, which results in the formation of alumina phases. Xue et al. [118] reported that adhesion of the coating to the aluminium substrate is enhanced because of similarity in lattice (face-centre cubic, fcc) structure between aluminium and gamma alumina phase (usually formed near the coating/metal interface). Metallurgical and interdiffusional bonding created during thermal and plasma-chemical process generates superior interfacial bonding between coating and substrate [7, 113, 118]. Adhesion strength can reach 350 – 380 GPa for thicker coating (e.g. 200 – 250 μm) [7]. EDX analysis from aluminium substrate showed existence of O and Si elements in the region below the interface, which could be an evidence of inward diffusion from the coating [113]. Similarly, it was observed that during Vickers indentation there was no evidence of brittle fracture

or cracking of PEO coating which is also attributed to the excellent coating adhesion to the substrate.

Thermal impact testing has been performed on PEO coatings to investigate the thermal shock resistance [99]. In this study, coated aluminium specimens were heated at ~ 600 °C for 5 minutes, followed by quenching in water. Observation under the optical microscope showed no cracking or peeling off, confirming that the coating has reliable thermal shock resistance and adhesion strength under these conditions. Although the resolution provided by the optical microscope used in this study may not be sufficient, these findings are indicative of the good mechanical and physical properties of the PEO coatings examined.

3.4. PEO Coating on Porous Metals

To date, only few works have been reported on the application of PEO coating to aluminium and titanium foams. Of particular note, an investigation on low density aluminium (Duocel) foams treated with PEO coatings was reported by Dunleavy et al. [96] and another work by Liu et al. [97] studied coating constituents and the effect of this surface treatment on corrosion resistance of coated high density replicated aluminium foams.

In the case of ref.[96], and based on the fact that PEO coating forms partially by the conversion of the substrate to its oxide, estimation of how much metallic material is converted to ceramic coating was carried out. It was found that this can reach as high as 90 % of the metal base, depending on treatment time, largely transforming the metal foam to a ceramic one. In addition, coating morphology was investigated by SEM, in which it is found that typical PEO coating surface features are present, including coating roughness, pores and ceramic particles, indicating that discharge effects such as melting and re-melting of solidified ceramic materials occurred all around the porous body. Figure 3.9 shows metallic struts covered with PEO ceramic coating, along with a magnified image revealing surface porosity and solidified materials (highlighted areas with different colours). In the same study, compression and tensile tests were also performed on coated Duocel foams, where mechanical properties such as fracture energy G_c and deformation behaviour were extracted. The toughness of these coated porous structures was studied and found to be reasonable, with values of G_c ranging from 0.5 – 2.5 kJ m^{-2} depending on the

converted metal fraction. This range of fracture energy values is greater than that of glass, brittle polymers and many ceramics, including alumina, which has values reported ranging between 0.003 - 0.5 kJ/m^2 [96, 120, 121]. The retained fracture toughness of the coated porous aluminium is attributed to the existing coating porosity which would offer less constraint to relatively large plastic deformation undergone by the coated porous metals. It is suggested that these porous metals reinforced with ceramic coatings with such range of values in fracture toughness (few kJ m^{-2}) could be of use in scaffold applications [96].
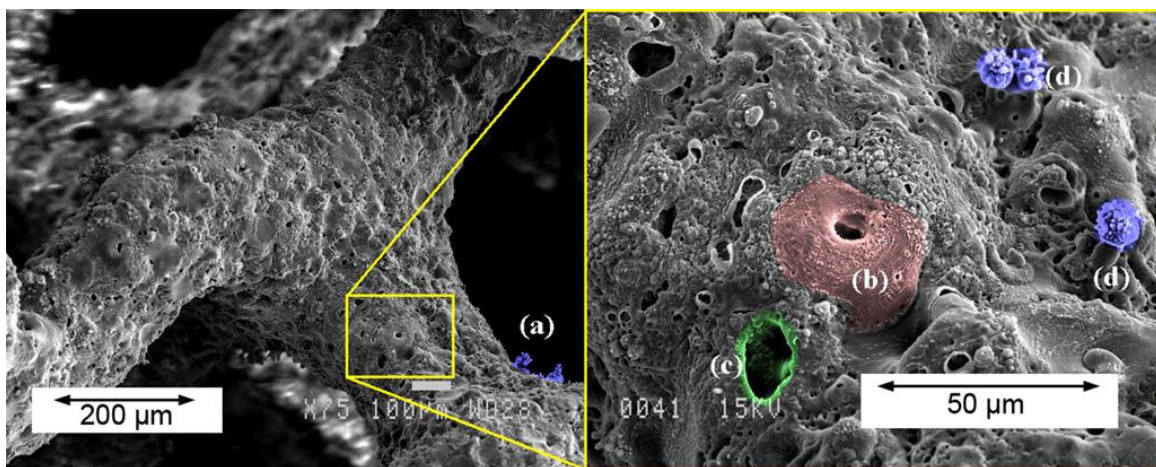
Figure 3.9 – SEM images of (left) Duocel metallic struts enveloped with PEO coating and (right) a magnified image illustrating different coating surface features such as porosity (c and d), solidified ceramic particles (d) and re-solidified pool or crater are also observable [96].

Alternatively, work done in ref [97] addressed coating characterisation as well as corrosion behaviour of the coated replicated foams. As is the case in the previous work, coating microstructure and morphology were found to be similar to those formed on bulk aluminium substrates. EDX analysis showed that Al, O and Si are the main forming elements, with α and γ- Al$_2$O$_3$ phases being the main phase constituents. Figure 3.10 exhibits potentiodynamic polarization curves for both coated and uncoated aluminium foam samples. Highly corrosion resistant materials exhibit high corrosion potential and low corrosion current density [122]. It can be seen that the corrosion current density of the untreated foams is much higher than that of treated foam samples while the corrosion potentials for untreated foam are increased from – 1.55 V to reach – 0.78 V for the treated foams. These results are indicative of

the improvement in corrosion resistance brought about to these coated porous materials [97]. The corrosion resistance can be estimated from using the potentiodynamic polarization curve, using both the corrosion potential and corrosion current recorded during the tests [123].
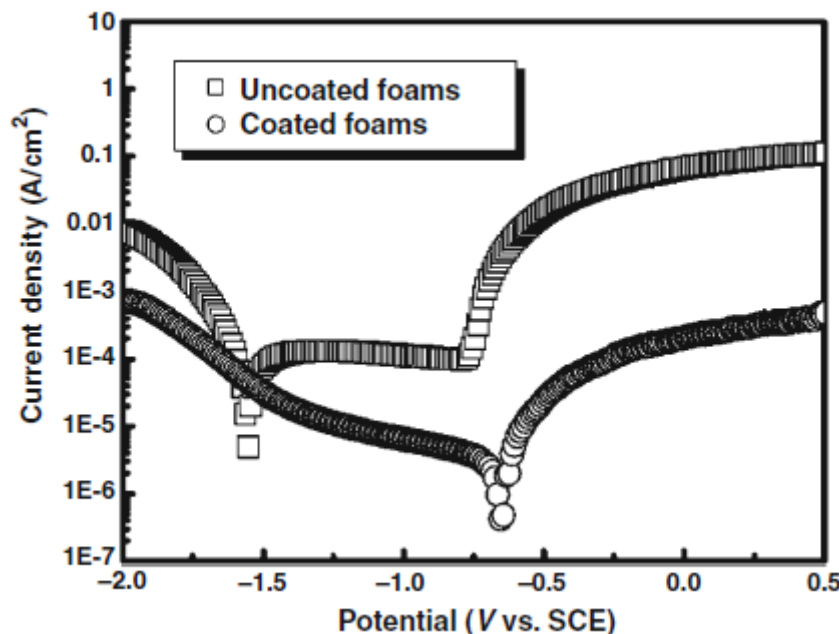
Figure 3.10 – Polarization curves for both treated and untreated replicated aluminium foams samples in corrosion resistance estimation tests where foam samples were immersed in 3.5% NaCl solution using an electrochemical analyser (Versa STAT-3, METEK) [97].

The study also found that the denser inner coating regions played a significant role in preventing the corrosive ions (Cl^-) from penetrating further into the core aluminium, while these ions found their way through the outer porous region [97].

For porous titanium, there is also a limited work concerning the effect of PEO coating [124, 125]. In both studies, modified electrolytes were used to achieve coating of a particular composition, with the aim to improve the biocompatibility and bonding strength between the porous titanium and the living bone tissue after implantation. The former work [124] used NaOH-containing aqueous solution to grow bioactive layers of very small thicknesses (in the range of 65 – 68 nm) on porous titanium having dimensions of 2x5x8 mm. The pore size of these porous bodies is 100 μm and, even so, the coating was found to form on the outer and inner regions. In the

later work [125], bioactive PEO coating was formed in electrolyte containing different elements (Ca, P, Sr,) on open cell titanium foams with different pore sizes (50, 90 and 150 µm). This is clearly an advantage of the PEO process, in which the coating phase and elemental composition can be tailored by adding different elements to the electrolyte. Despite that fact that samples investigated in this study were even smaller (3x3x4 mm), coating penetration into the foam middle part was not complete and coatings were not observed on the inner foam regions for samples with pore size ≤ 90 µm. On the other hand, bioactive PEO coatings were found to form everywhere for foam with pore size larger than 150 µm, as seen in figure 3.11. Moreover, coating thickness reduces from the outer to the inner regions (from 18 to 10 µm).

One finding has been interpreted by the fact that the current density in the middle part of the foam is lower than on the outer regions, and this can have an effect on the formed coating porosity, thickness, elemental and phase composition, which is attributed to the differences in the ionic conductivity (in the electrolyte) in different regions of the foam [125]. This is because ion transport into the foams or porous bodies is dominated by ion distribution and migration with minor effects from fluid flow [124-126].
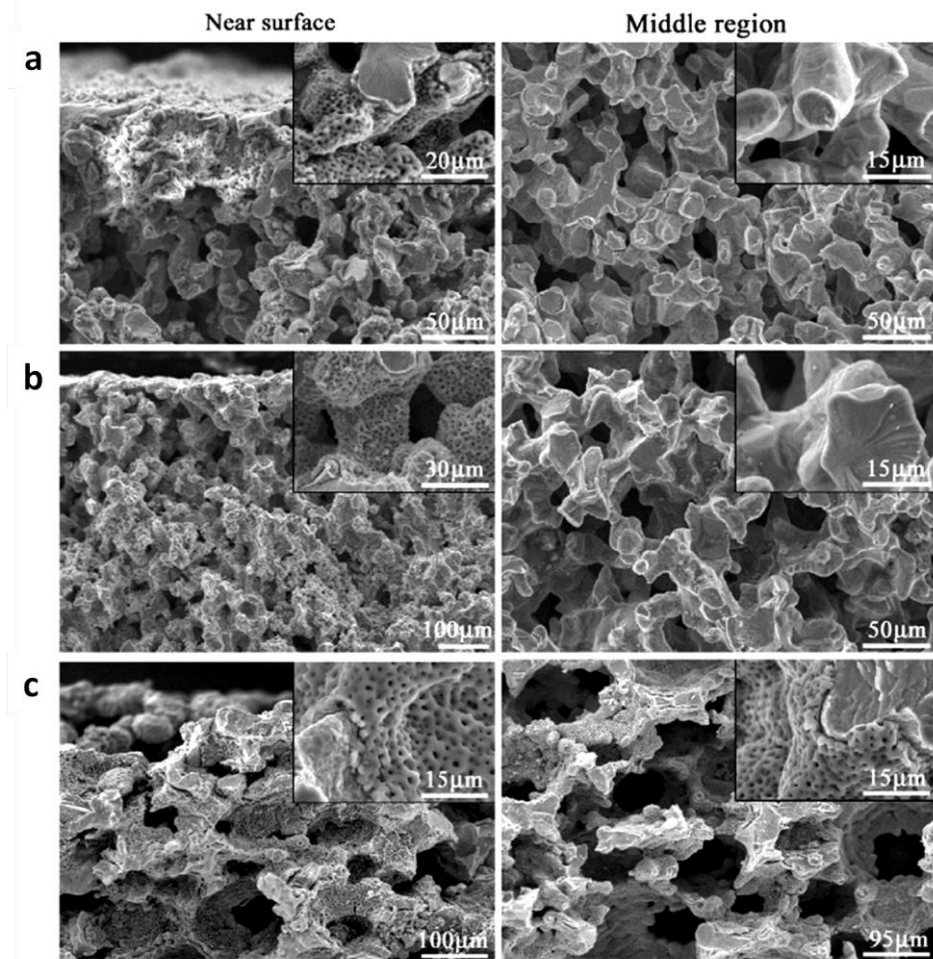
Figure 3.11 – Surface morphologies of three differently PEO coated titanium foams in both the near surface region and the middle region. These fracture surfaces belong to Ti foam samples with pore size of a) 50, b) 90 and c) 150 µm respectively. Note the porous PEO coating forming on the middle region of foam with 150 µm only (see the small magnified images on the top right corner of each image). All foam samples were treated at 400 V for 5 min [125].

It is reported that there is an internal resistance in mass transport between the electrode and the solution [126] and this leads to low current penetration into the electrode as a result of the limited ionic conductivity. This means that the kinetics of the electrochemical reaction are affected by such mass transport resistance. This can be facilitated by increasing the pore size and reducing foam sample thickness [97, 125, 126].

Although these studies have provided some valuable knowledge in the subject of the application of ceramic coatings to metallic foams, no attempts have been made to

further explore the effect of using different current regimes such as using pulsed bipolar current mode, with different pulse frequency and duty cycles. It has been shown that these capabilities allow greater degree of processing control so that optimized processing parameters may be established. Furthermore, as far as the mechanical properties are concerned, the elastic modulus as well as the role of coating damage during deformation of coated foams would be of industrial and research interest and these are some of the objectives of the present work.

Chapter 4: Experimental Procedures

Open cell aluminium foams are widely suggested for use in many different structural and functional applications owing to their inherent properties such as low weight and excellent mechanical properties. However, surface treatments may be used to improve some of these properties and allow enlargement of foam application fields. This Chapter details the materials and techniques used for fabricating open cell aluminium foams, PEO processing of these materials, characterizing the coatings produced and investigating the effects of these PEO coatings on foams mechanical response.

4.1. Materials

In this work two different types of foam were examined; Duocel aluminium foam of low density and pure aluminium foam produced in the laboratory with a higher density. The Duocel material is very open with only slim struts, of roughly circular cross-section (figure 4.1), whereas the higher density replicated structure has much smaller openings between the cells, and much larger dense metal struts (figure 4.2). Similar grades of these replicated aluminium foams are produced by Constellium, and are in the early stage of commercial exploitation.

4.1.1. Duocel Aluminum Foams

Duocel aluminium foams of two pore sizes, 20 and 40 'pores per inch' (PPi) commercial grades, corresponding to an average pore diameter of 2.5 and 2.1 mm respectively (measured by an image analysis method on cross-sections cut through the foam) with relative densities of 9–10% were supplied by the ERG Materials and Aerospace Corporation, Oakland, California. These foams are likely to be made by investment casting technique using 6101-T6 aluminium alloy of chemical composition shown in table 4.1, as provided by the foam supplier. The as-received Duocel foam samples (20PPi and 40PPi types) are shown figure 4.1 below.

Table 4.1 – chemical composition of 6101-T6 aluminium alloy (wt%, Aluminium balance). T6 is the tempering designation of the alloy which means that the alloy is solution heat treated and then artificially aged to achieve good mechanical properties.

Element	Si	Fe	Cu	Mn	Mg	Cr	Zn	Ti	B	Others	
										Each	Total
Wt %	0.3-0.7	0.5	0.1	0.03	0.35-0.8	0.03	0.1	-	0.06	0.03	0.1
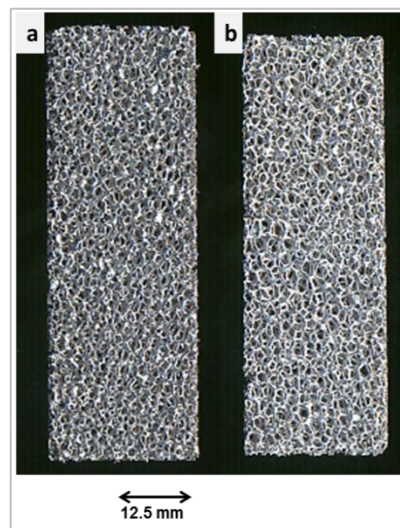
Figure.4.1 - As-received samples of low density Duocel foam of a) 2.2 mm pore size and b) 2.5 mm pore diameter used in this work.

These samples were obtained in blocks of 25×12.5×75 mm and were used at these dimensions for tensile tests. Three batches of Duocel foams were tested in this work. In the first tests, two batches of samples from these materials, 20PPi and 40PPi type, were coated and used for coating thickness characterization and plastic properties measurement. The third batch was of 40PPi type and was used for elastic properties measurement. The nature of the material includes density variations, which could affect properties, and so the density of each sample was verified before coating and those deviating from the mean by more than 0.5 % were removed.

4.1.2. Replicated Aluminum Foams

Pure aluminium foams (wt, 99.8 % Al ingot purchased from William Rowland Limited, UK) were produced in the laboratory at The University of Sheffield, using the NaCl-based replication process [6, 8, 12, 30]. The chemical composition of the aluminium alloy is shown in table 4.2 below, as provided by the supplier.

Table 4.2 – chemical composition of aluminium alloy used for the replication process.

Element	Si	Fe	Cu	Al
Wt. %	0.05 max	0.08 max	0.006	99.8 min

Foams produced by this method have two different pore sizes (measured using the same image analysis procedures as 1.6 and 3.5 mm average pore diameter) and relative density around 36-40 %, which equates to initial porosities ranging between 64 and 60 % respectively. These are very close to the theoretical maximum density achievable with this method, the aim being to obtain a structure as different to that of Duocel as possible. These replicated foam samples (in the form of cylinders and blocks, see figure 4.2 below) were produced using the same technique (replication process), but with two different devices.

Figure 4.2 - High density replicated foam of 1.6mm pore diameter, showing (left) two samples after EDM cutting, and (right) large block of replicated foam before cutting. These samples were tested in compression in this work.

The first equipment used an induction heating to melt the aluminium ingot, whereas in the second equipment a resistance heating is used. These two methods are explained in more detail in the following section with more information about the sample sizes, shapes and how they were cut.

4.2. Processing of Replicated Foams

4.2.1. Replication with Induction Heating

In the first replication method, aluminium ingot (99.8 % Al) was melted within a quartz crucible, with a sub-1 mm diameter hole in the base using induction heating. The molten metal was then forced into a preform of loose NaCl grains (purchased from G.J.W.Titmuss LTD, UK) using an argon gas at a pressure of approximately 1 bar, as seen in figure 4.3 below.
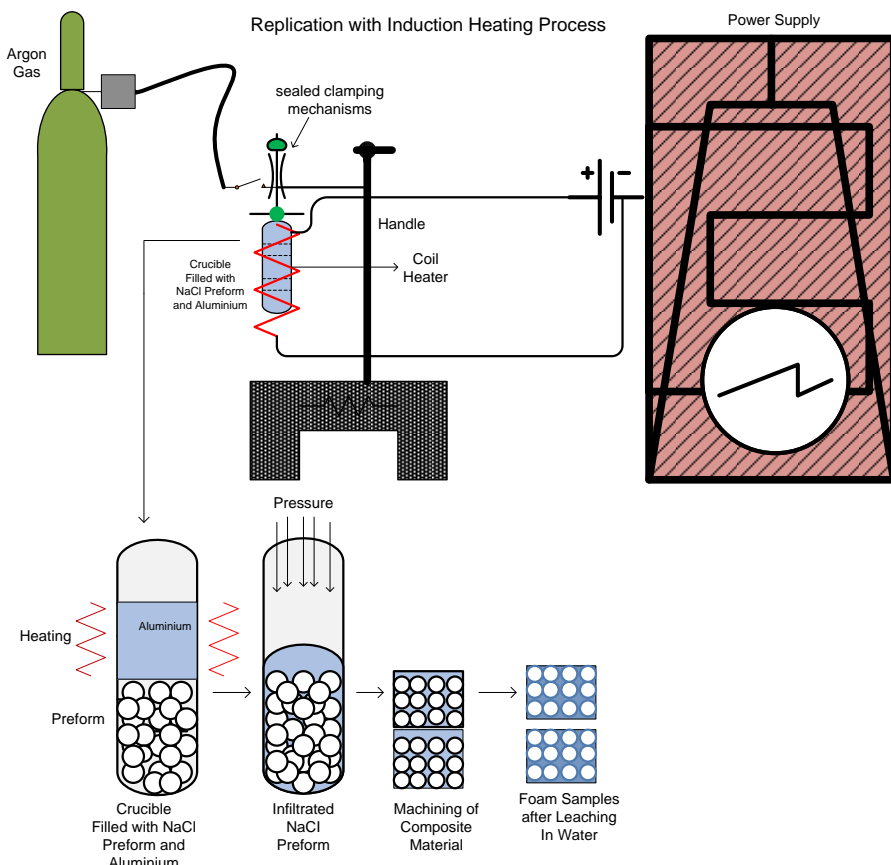
Figure.4.3 - Schematic representation of metal foams rig using induction heating showing elements making up the rig. Schematic images of composite foam within crucible before and after infiltration and foam samples after cutting and leaching in water are also shown.

An average NaCl grain size of 1.6mm was graded through a series of sieves to make the preform. As soon as the molten aluminium is infiltrated into the preform, the composite foam (Al + NaCl) formed is then removed from infiltration equipment and is allowed to cool down in air. After cooling, cylindrical samples of 20 mm diameter and 12 mm height were machined using standard workshop equipment, and immersed in tap water for up to 24 hours to dissolve the salt. Finally, samples were rinsed with distilled water and alcohol to avoid any residual traces of NaCl which could affect the PEO coating process. These samples were examined in the microscope and used for compression tests.

4.2.2. Replication with Resistance Heating

A new infiltration rig allowing much larger sample sizes has been developed during the course of this work and is now being successfully used to produce open-cell aluminium foam. Over 80% of samples tested in this work were manufactured using this technique. In the results it is made clear which processing method was used to produce which samples. In this process, molten aluminium is forced into the NaCl preform with the aid of vacuum and an applied gas pressure. The vacuum system and an argon gas supply are connected to a stainless steel cylinder which is placed inside a furnace during processing. Gas flow regulator and vacuum indicator are installed to control argon gas pressure and vacuum during the process, as seen in the figure 4.4 below.

In this new infiltration method, a stainless steel cylinder of 92, 99 mm internal and external diameters respectively and 150 mm height is used for infiltration process, see figure 4.5 below. To avoid adhesion or reactions between molten aluminium and the inner surface of the cylinder during processing, the cylinder is coated with Boron Nitride spray (supplied by Kennametal Sintec-Group) and loaded with loose NaCl preform with a nominal mean grain diameter of 1.6 mm. Aluminium ingot (99.8 % Al) is then added on top of the salt and the filled cylinder is then closed firmly using graphite gasket (produced by Klinger, UK) rings on the top and bottom parts.
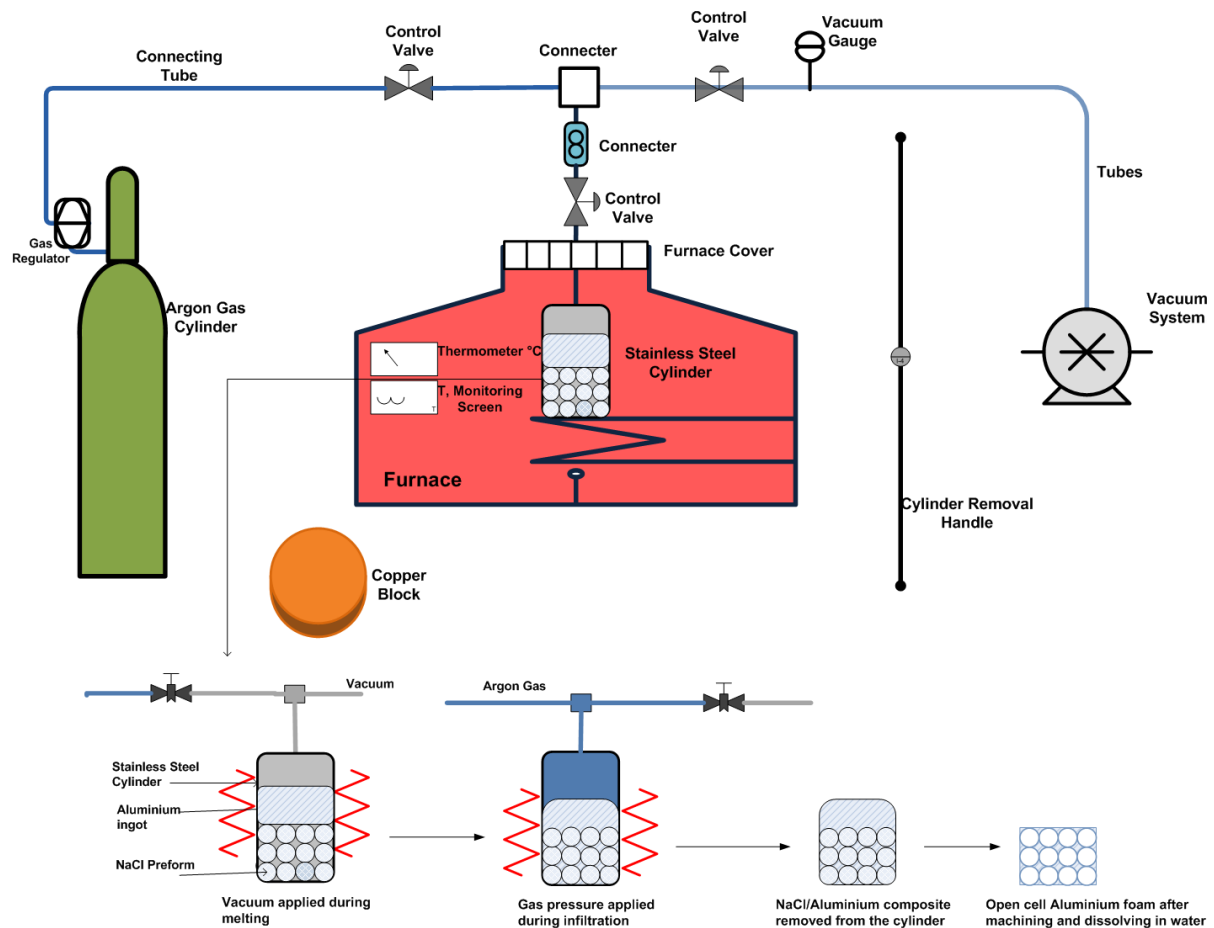
Figure 4.4 - The new infiltration rig in which the molten aluminium is forced into the preform with the aid of vacuum and an applied gas pressure within stainless steel cylinder at 740°C furnace temperature. Control of vacuum and Argon gas pressure inside the stainless steel cylinder are achieved using vacuum indicator, gas regulator and three regulating valves.

After securely closing the cylinder, it is then loaded inside the furnace and a heat-resistant furnace cover is used to close the furnace while allowing a connecting tube to pass out, so that may be connected to the vacuum system and Argon gas bottle using T junctions, control valves and tubes.
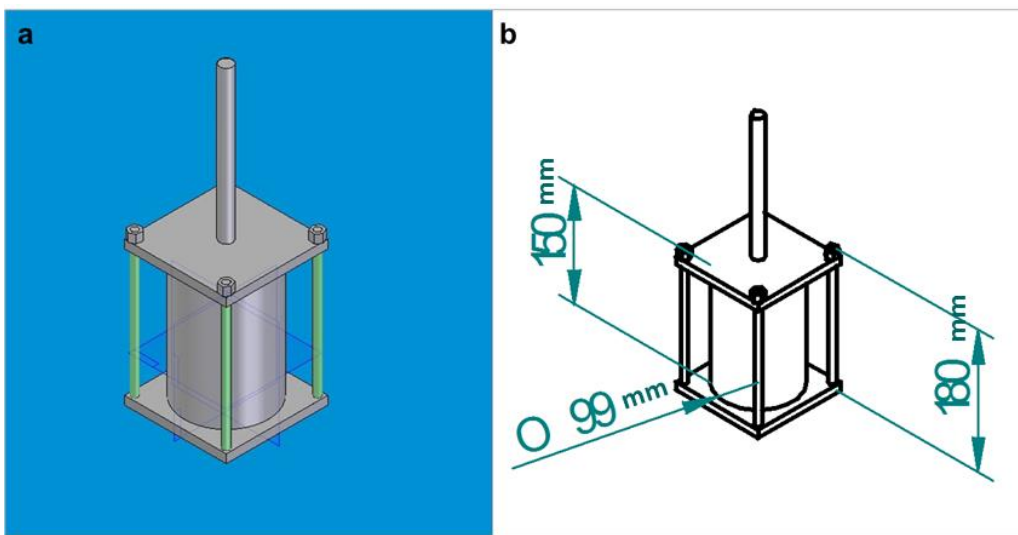
Figure 4.5 - Schematic diagram showing a) the stainless cylinder in which molten aluminium is infiltrated into a NaCl preform, used for infiltration process and b) design drawing is also shown for clarity.

Once all these preparatory steps are made, foam processing can then start with the application of vacuum for 5 minutes, before heating, following the temperature profile shown in figure 4.6 below. Heating of the furnace starts at a rate of 10 °C per minute. The aluminum is melted under a vacuum of approximately 25 Torr through heat transmitted principally by conduction from the chamber wall, since radiation would be expected to have a minor effect at these temperatures.

Maintaining vacuum during the process has been found to be very important to obtain a good result. It was found that the vacuum must be maintained below 30 Torr, although the ideal value should be between 20-25 Torr. If the vacuum reached before heating is above 30 Torr, then this indicates that the sealing is not perfectly secured and that there is leaking of air into the steel cylinder. This can cause problems during melting and infiltration, and should be avoided.
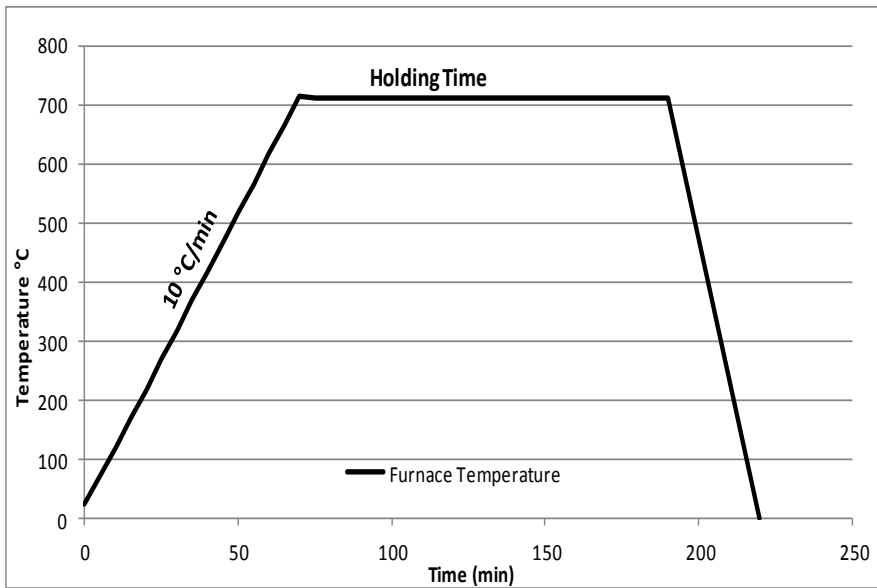
Figure 4.6 - The temperature profile used in the foam processing with heating rate of 10°C/minute. The cooling rate has not been measured, and is shown schematically; this is intended to be as fast as possible, although it may not be as fast as shown here.

A holding time at maximum temperature (e.g. 710°C or 740°C for 2h) is included to allow the heat to transmit through the chamber and to melt the aluminium. Once this holding time is finished, the vacuum is disconnected and argon gas pressure is then allowed to flow in to fill the cylinder, so that the molten aluminium is forced into the salt grain preform. The pressure is applied for only 5 minutes and then the cylinder is taken out at relatively high temperatures (at roughly the same plateau temperature). Increasing the pressure time has no effects on the infiltration process. The removal of the cylinder is carried out using a handle (see figure 4.4) that is specifically designed for this new rig, taking into account the safety of the operators. The hot cylinder is cooled by placing it on a copper block, to allow solidification to proceed from the base upwards, so that solidification shrinkage takes place outside the perform and this will not therefore affect the sample with unwanted extra porosity, and to avoid other solidification defects that could arise as result of slow cooling (for example if the pressure reduces and the aluminium de-wets).

After cooling, a cylindrical sample of 90mm diameter and, typically, 20 to 25 mm height is obtained after rinsing in water to dissolve the salt. This is clearly one advantage of this new technique, where foam samples of larger dimensions can be produced in one experiment. These can then be cut into several smaller samples,

rather than producing each small sample in one experiment. Although, like all foams, foams are still subjected to random variations this aids reproducibility. Figure 4.7 below illustrates the main six steps in the operation of the new rig.
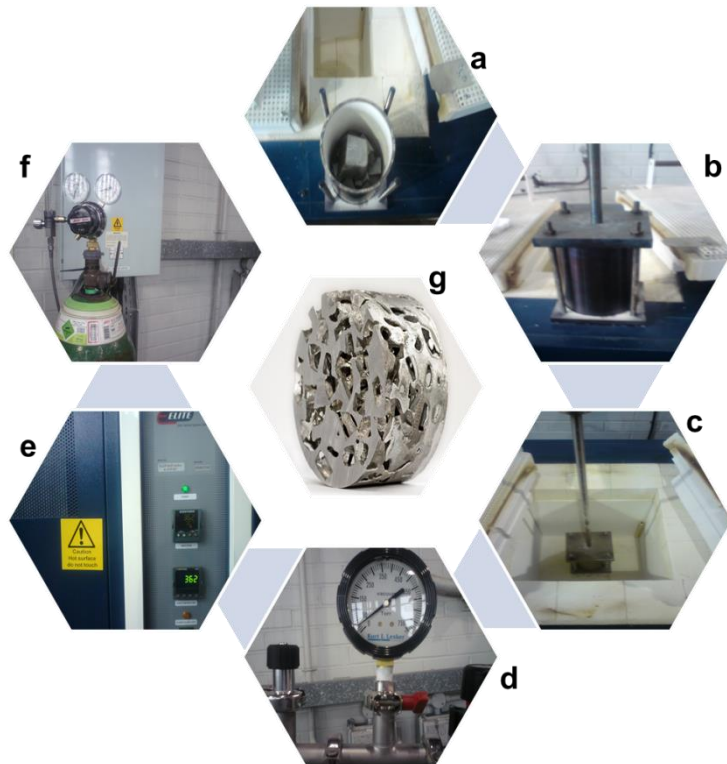
Figure 4.7 - The six steps involved in the foam processing in the new rig with a) loading salt and aluminium ingot into the chamber, b) closing the cylinder firmly, c) loading the filled cylinder inside the furnace, d) vacuum applied, e) temperature raised, f) gas pressure applied, g) foam sample after infiltration.

The open cell aluminium foam specimens obtained with as blocks with an average cell size of 1.6 mm and as cylinders with an average pore diameter of 3.5 mm with porosities ranging between 60-64%, based on measurements made on actual samples. These foam specimens were machined from the large replicated foam blocks, using Electro Discharge Machining (EDM) to avoid any lateral damage to the cell walls due to mechanical loading. Samples are shown in figure 4.8 below. After measuring their densities, which can be readily obtained by measuring foam mass over its volume, these foam samples were PEO processed as detailed below, and subsequently mechanically tested in compression.
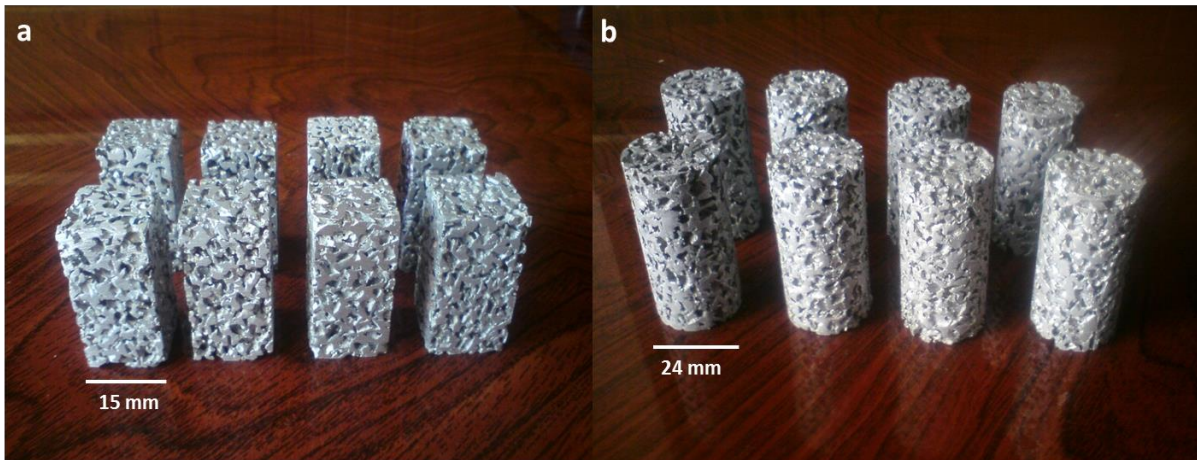
Figure 4.8 - Specimens of open cell aluminium replicated foams with different sizes and shapes (a) blocks and b) cylinders), after EDM cutting (8 specimens were cut from each cylindrical block of foam produced).

4.3. PEO Coatings of Foam Samples

The surface treatment of light metal alloys (e.g. aluminium and it alloys) using Plasma Electrolytic Oxidation coating technique was discussed in detail in chapter 3. This includes processing kinetics, equipment used and coating properties. As discussed earlier, PEO coating characteristics and properties can be affected by a number of processing parameters such as treatment time and electrical regime adopted. Therefore, to investigate the effects of this type of coating on mechanical behaviour of open cell aluminium foams, different PEO coating processing variables were considered in the present work. In the initial PEO processing of foams, treatment time was varied between 20 and 80 minutes. In the second PEO processing batch, the best treatment time that delivered optimum mechanical performance to the foams was taken for further improvement. These treatments were carried out in the pulsed bipolar current mode, with pulse frequency varied between 50 and 6250 Hz. The third batch took even further processing optimisation step by using the best frequency used and investigating the effects of a range of current waveforms (i.e. varying pulse on/off time ratio for both positive and negative bias) to enhance coating characteristics and properties such as thickness, growth rate, crystallinity, hardness and modulus. This ensures optimum enhancement to foams

mechanical and surface properties. Table 4.3 below display the layout of this work and summarizes processing variables which control coating thickness, microstructures, micromechanical properties and growth rates.

Table 4.3 - Different PEO coating processing variables adopted at different stages in this work for coating of open cell aluminium foams. More detail is provided in results chapters.

Optimization Stage	Processing Variables	Treatment	Variations			Invariables
			Processing time (min)			Frequency at 250 Hz
First	**Time**	t_1	20			
		t_2	40			
		t_3	80			
			Pulse frequency (Hz)			Processing time of 40 minutes, (t_2).
Second	**Frequency**	f_1	50			
		f_2	250			
		f_3	1250			
		f_4	6250			
			δ_+^{on} %	δ_-^{on} %	$\delta_{+/-}^{off}$ %	Processing time of 40 minutes / pulse frequency at 250 Hz, ($t_2\,f_2$)
Third	**Duty Cycles**	p_1	32.5	50	17.5	
		p_2	27.5	50	22.5	
		p_3	35	50	15	
		p_4	32.5	25	42.5	
		p_5	32.5	56.25	11.25	
			Processing time (min)			Processing time of 40 minutes / pulse frequency at 250 Hz/ using on/off ratio 4, ($t_2\,f_2\,p_4$)
Fourth	**Duty Cycle, ratio 4, p_4**	t_4	20			
		t_5	60			
		t_6	80			

4.3.1. PEO Procedures

All PEO treatments of foams in this work were carried out in an aqueous electrolyte solution containing 10 g/l Na_2SiO_3, 2 g/l $Na_2P_2O_7$ and 1 g/l KOH, operated at a temperature no higher than 40°C. The PEO processing unit is shown in figure 4.9 below, which shows the main elements making up the unit.
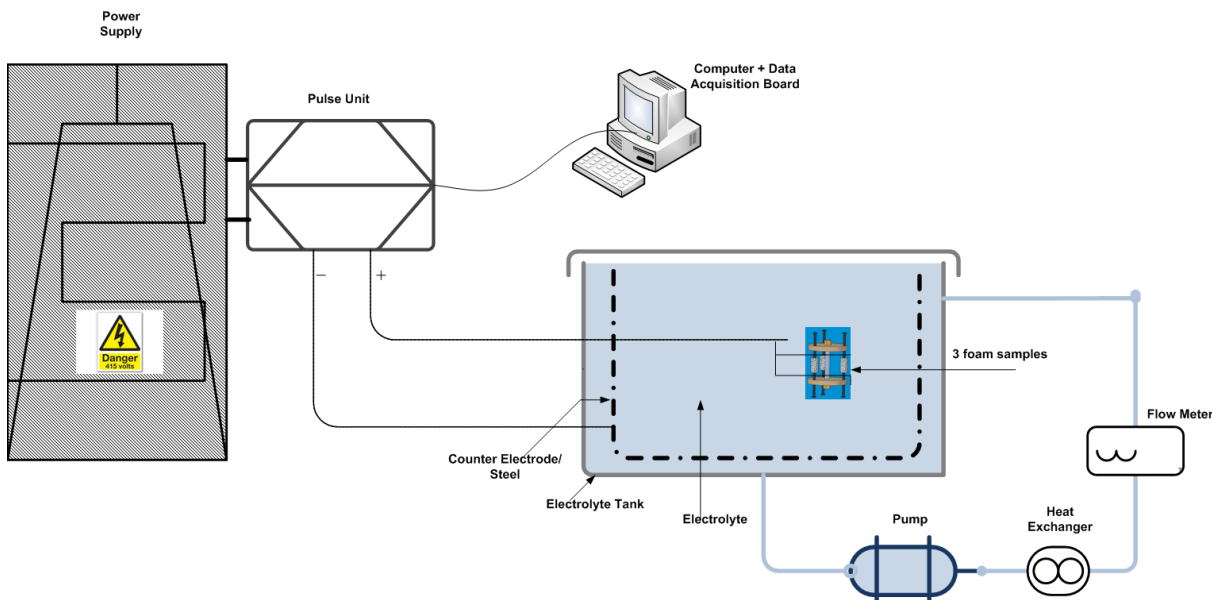
Figure.4.9 - PEO processing unit used in the present work for coating of open cell aluminium foams.

Three samples of each type and pore size of foams were treated for each processing condition, so that two samples will be tested mechanically (compression or tension) and 1 sample will be used for cross-section analysis to study the coating morphology, microstructure (phases present, elemental distribution and microscale coating mechanical properties such as Young's modulus and hardness) and coating thickness distribution with depth. In the first PEO processing attempts on foams, treatment time was varied for 20, 40 and 80 minutes. A rectangular pulse reverse voltage waveform was applied at 37.5 % positive duty cycle and 250 Hz frequency. A stepped potentiostatic regime was maintained, and used with the voltage amplitudes shown in Table 4.4 for the three different treatments. These different treatments were typified as t_1, t_2 and t_3, respectively, to produce PEO coatings with different thickness. The thicknesses generated would be expected to be less than on the reference

samples of dense aluminium using the same conditions, due to the limited throwing power of the process and larger specific surface area.

Table 4.4 - Main parameters of the stepped potentiostatic regime of PEO treatment used in the first part of this work.

Time Step (min)	Voltage amplitude (V)		Treatment		
	U^+	U^-	t_1	t_2	t_3
0 to 20	575	-190	X	X	X
20 to 40	590	-205		X	X
40 to 80	605	-220			X

Furthermore, a special jig (made from plastic to avoid interference with the PEO process) was designed to provide identical conditions for the 3 samples treated simultaneously, as can be seen in figure 4.10 below.
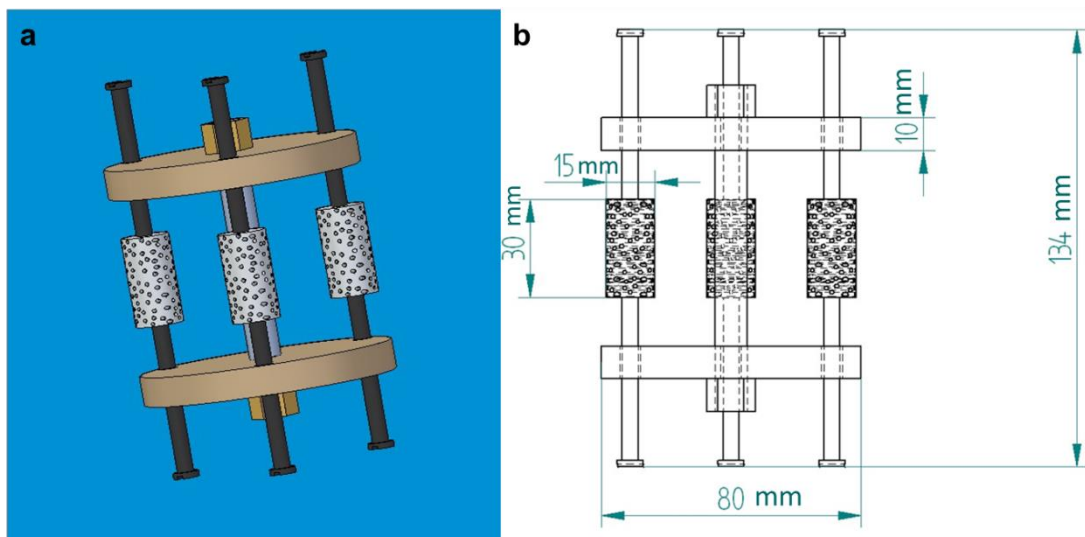
Figure 4.10 - Schematic diagram showing a) the plastic jig used for holding 3 specimens using plastic screws, for each treatment condition and b) design drawing is also shown for clarity.

The three samples held in this jig were wired together using aluminium rods and connected to electrical circuit of the system. This includes immersion of the whole jig with the samples into the electrolyte bath, see figure 4.9. After all PEO treatments carried out in this work, the foam samples were rinsed thoroughly in water and dried with hot air.

4.4. Coating Characterization Methods

In order to understand the behavior of the coated foams it was important to understand the distribution and nature of the coating. Therefore, part of the investigation on the effects of PEO coatings on metal foams behavior was directed to the understanding of coating penetration levels into the foams interior, microstructures and micromechanical properties of these coatings. All of these analyses can be linked to different behavior of the coated foams to envisage the relative benefits brought about to foams mechanical and surface properties. These studies were undertaken in this work utilizing different experimental techniques, which are explained in the following sub-sections.

4.4.1. Optical Microscopy and Eddy Current Thickness Evaluation

To evaluate coating thickness on the reference dense samples as well as the coated foam samples, typical metallographic procedures were used on each cross-section. These cross-sections were cold mounted with epoxy resin under vacuum, and then ground using SiC papers ranging between 120 and 1200 grit. This was followed by polishing steps using 6 and 1micron diamond paste. On the foamed samples and for all coating conditions, polished cross sections examined in the optical microscope were used to measure the coating thickness (normal to the strut surface) at a number of defined locations by distance from the foam surface throughout the sample. Optical images were recorded using digital camera attached to the microscope. For the reference sample, 10 to 15 measurements were made randomly across the surface using an Elcometer 355 modular thickness gauge system equipped with standard No 4 Anodisers probe.

4.4.2. Scanning Electron Microscopy (SEM)

Scanning Electron Microscopy (SEM, JEOL-6400) with an operating voltage of 5 ~ 20kV, was used to carry out a more detailed characterisation of the coating morphology in both the surface plane and cross-section of as-received and fractured PEO-treated samples. The cross-sections for each coating were sputter-coated with

carbon before examination to avoid surface charging (although the foam is conductive the coating is not). Depending on the type of interactions between the high energy electrons (incident beam) with the atoms that form the sample, different signals can be produced by the SEM. These include secondary electrons and backscattered electrons etc. Secondary Electron Imaging (SEI) was used in this work to obtain deep, three-dimensional topographical features useful for understanding microstructures of coating surface at magnification of up to 2,000 X. Backscattered Electron Imaging (BEI) was also used whenever necessary, especially for the purpose of characterizing coating porosity. Because BEI is related to the atomic number (Z), images can provide different contrast with the elements in the sample (which can indicate surface cracks and network of defects) as well as allowing a degree of subsurface imaging.

4.4.3. X-ray Diffraction (XRD)

It is expected that processing parameters can have major influence on microstructures of PEO coatings. As the coating starts to build up during processing, transformation processes take place, and more amorphous phases will transform into crystalline forms, such as α-Al_2O_3 and γ-Al_2O_3. Knowledge of what phases are present and their relative amount is essential in understanding coating effects on foams behaviour. In the present work, the coating phase composition was studied by X-ray Diffraction (XRD) methods using a Siemens D5000 X-ray diffractometer, which is equipped with Cu tube (Cu Kα radiation, $\lambda = 1.54$ Å) and operated at 40 kV and 30 mA. Conventional θ-2θ scans were performed within the range of $2\theta = 20^o$ to 90°, with 0.02^o step size and 4 s time per step. This produces spectra containing peaks at angles characteristic of the crystalline phases present. XRD analysis was carried out on different coatings that were produced under different treatments conditions. Each spectra produced will contain information about the intensity of crystalline phase present, each at specific 2θ scans.

4.4.4. Energy Dispersive X-ray Spectroscopy (EDX)

EDX is a technique that interprets the interactions between a source of high energy electrons and an atomic structure of a given sample. When incident electrons knock out an electron from the inner shells of an atom, a higher energy electron from the outer shells fills the gap left by the ejected electron. The difference in energy associated with higher and lower energy shells will be released as X-rays of specific characteristics of that material. These X-rays can be collected and used for analytical studies on elements or chemical characterization of the sample under study. This is based on the fact that each element has a unique atomic structure, and so the X-rays have characteristic energy.

In this work, elemental composition and spatial distribution3s of elements for the different coatings, produced under different processing parameters, were studied by energy-dispersive X-ray spectroscopy (EDX, INCA software), which was fitted in JEOL-6400 SEM microscope. Major elements such as aluminium, oxygen and silicon are expected to be present at different amounts in each different coating and can form most of coating volume.

4.4.5. Coatings Nanoindentation Tests

To measure PEO coating micromechanical properties, nano-indentation load-displacement behaviour of the different coatings was investigated using Berkovich indenter, with maximum load of 7000µN. This indenter is part of an atomic force microscope (AFM, Dimension^{TM} 3100, supplied by VEECO/BRUKER) which is attached to Triboscope Nanomechanical test instrument (supplied by HYSITRON INC), all of which make up the nanoindentation testing kit. These tests were carried out on each of the coated foams cross-sections (polished transverse sections of different thicknesses, depending on coating processing conditions) using the optical microscope on the system to specifically target the coating. To obtain fine surface preparation, all samples were ground down to 4000 grit sandpaper, and subsequently polished using 6 and 1µm diamond paste. This was followed by polishing with alumina suspension of fine particles of 0.3 micron size. The alumina suspension was diluted with distilled water at 1:3 parts.

When examining the data, a number of indents were not considered valid; this may be the case if indents were made on existing coating defects (e.g. large pores and cracks). Such defects cause the tests to fail and the indenter will be withdrawn as result. This will produce incomplete load-displacement curves, which are easily identified and removed from the analysis. .

All indentation tests were performed following a load-time cycle presented in figure 4.11 below. The indenter was first loaded up to peak load for 5 seconds, held constant for 5 seconds, and finally the indenter was unloaded for another 5 seconds.
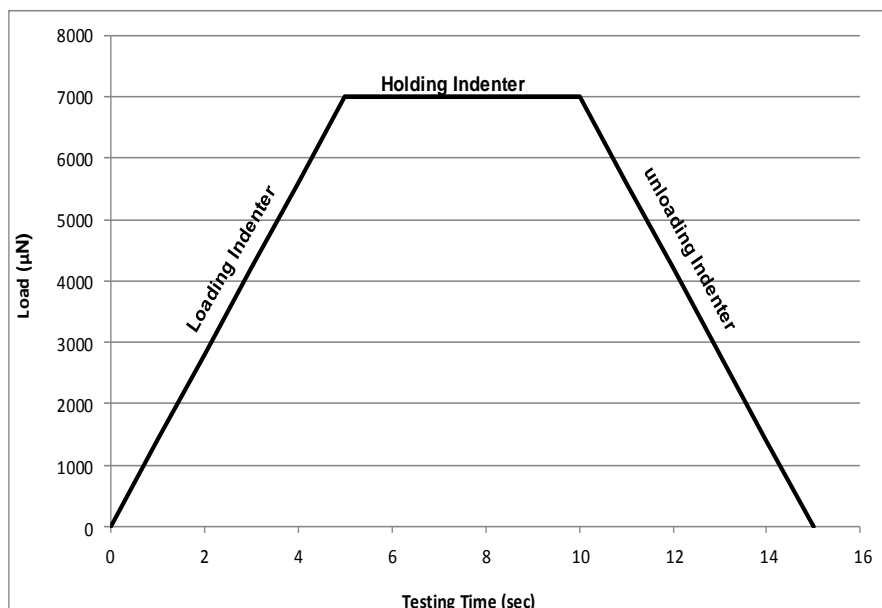
Figure.4.11 - Schematic load-time sequence adapted during each indent; Peak load = 7000μN.

4.4.6. Image Analysis (Pore Size and Strut Thickness)

The mean pore size and strut thickness of foams (Duocel and replicated) were measured using standard methods [127] to obtain the true three dimensional feature size from planar sections. Images used in this analysis were obtained from optical microscopy and a high resolution scanner. To confirm these values, mean pore size and strut thickness of foams were also determined and analysed using ImageJ software. This software is available to the public and has many different capabilities

in calculating and measuring areas, distance and angles and creates density histograms etc.

4.4.7. X-ray Computed Tomography (XCT)

The X-ray microcomputed tomography (XCT) technique is a relatively a new non-destructive technique, allowing an in-depth characterization and analysis using 2-D sectional viewing or 3-D image visualization capability. The X-ray tester consists of x-ray source, a rotating stage for the sample, and an x-ray detector. During the experiment, the specimen is rotated between the stationary x-ray sources and the detector and therefore is being irradiated. This technique was used in this work, using instrument of the Nikon Metrology 225/320 kV Custom Bay. The system was equipped with a 225 kV static multi-metal anode source (Cu, Mo, Ag, and W) with a minimum focal spot size of 3 µm and a PerkinElmer 2000 × 2000 pixels 16-bit amorphous silicon flat panel detector. The scanning was performed with the molybdenum target using a voltage of 80 kV and a current of 100 µA. The acquisition software was Nikon Metrology proprietary software InspectX (version XT 2.2 service pack 5.5). The data acquisition was carried out with an exposure time of 1000 ms, and no filtration. The number of projections was set to 3142 and the number of frames per projection was 1, resulting in an acquisition time of 53 minutes. The correction images were acquired by averaging 128 frames using the exact X-ray conditions as used for the acquisition. To perform a good visualization analysis, a smaller foam specimen (smaller in size than the samples used principally in this work) with a size of 10x10x27 mm was PEO coated using t_2 processing conditions. This part of the thesis was carried out in collaboration with Dr Fabien Léonard, Research Associate - Commercial Access Manager at the Henry Moseley X-ray Imaging Facility, Materials Science Centre at The University of Manchester. The scanning and data analysis was carried out by Dr Léonard, while the coated open cell aluminium specimens were manufactured and processed by the author.

4.5. Mechanical Testing Methods

This part deals with measuring the effect of the ceramic coatings on foams mechanical properties. PEO coatings are known for their high hardness, stiffness and good adhesion to the substrate [7, 111, 112], which would be expected to bring some improvements in surface and mechanical properties of the coated material. In the following sub-sections, details of how the coated and uncoated foams were tested mechanically to systematically investigate coatings effects are given.

4.5.1. Compression Tests

The replicated foam specimens were tested in compression. The coated and uncoated replicated specimens were compressed using Hounsfield, 0038 Model H100KS, a screw driven machine equipped with a 10 kN load cell. Initially, first tests were carried out at a speed of 1mm/ minute, which equates to an initial strain rate of 1.4×10^{-3} s^{-1} for compression of cylindrical specimens. The rest of the tests were executed at a speed of 0.5mm/minute, resulting in an initial strain rate of around 2.8×10^{-4} s^{-1} for compressing block specimens. The experiments were repeated at least twice for all specimen' conditions (coated and uncoated). From the stress-strain curves produced, the values of the yield stress, strain to failure and energy absorption are extracted; the yield stress is calculated using the 0.2 % proof stress.

4.5.2. Tensile Tests

The coated and uncoated specimens of Duocel foams, with 10-15 mm at each end fixed in resin to facilitate gripping, were tested in tension. Two types of tensile tests were done for Duocel samples. The initial tests were performed using the same testing machine for compression tests (Hounsfield, 0038 Model H100KS), with testing speed of 1mm/minute. The purpose of these tests was to measure the plastic properties (yield stress, strain to failure and energy absorption) of coated and uncoated foams. The second set of tensile tests was performed using an MTS tensile test frame, equipped with a 5 kN load cell, and able to perform cyclic loading-unloading to evaluate the elastic modulus at different strains. These tests were

performed at EPFL, Lausanne, by Dr R.Goodall with the assistance of staff from Laboratory for Mechanical Metallurgy. Specimens and grips for holding the specimens during testing were designed and prepared by the author. The experiments were repeated at least twice for all sample conditions. The strains were measured by recording displacement between two extensometers fitted about 20 mm apart on the gauge section of the samples. The crosshead speed was 1 mm/min, which equates to an initial strain rate of around 3.3×10^{-4} s^{-1}. Also, care was taken to align the samples along the tensile axis of the machine, although the grips used allowed rotation in one plane to reduce bending forces. From the stress-strain curves produced, the values of modulus of elasticity at each unloading cycle (found from the unloading slope), the yield stress, ultimate tensile strength and strain to failure are extracted; the yield stress is calculated using the 0.2 % proof stress.

Chapter 5: Processing and Structural Characterization

This chapter provides descriptive detail on the initial foam processing aspects developed during the course of this work, including evaluating the effects of using different plateau times, temperatures and pressures on foam macrostructural parameters such as porosity and density. Post PEO-treatment characterization of replicated, as well as Duocel, foam samples were carried out using Optical Microscopy, SEM, XRD and EDX. Detail of such analysis includes coating thickness variations with depth for both types of foams as well as coating microstructures.

5.1. Engineering Aspects of the Replication Process

During the course of this work, several new aspects of foam production were investigated including installation of a custom-made foam processing rig in the laboratory. This section provides an account of the aspects investigated.

5.1.1. Foam Processing Parameters

The setup, components and operating procedures of the new infiltration rig finally established and used in this work were explained in detail in Chapter 4. Open cell aluminium foams can now be manufactured with the desired cell sizes (in the range of 1 to 3.5mm), cell shapes and with a range of porosities (ranging in this work between 60 and 64%). To arrive at the decision of optimum parameters, several experiments have been carried out, and different gas pressures and operating temperatures have been used in an attempt to find out the optimum processing parameters that could yield aluminium foam with a consistent structure, and also the effect that choices of these parameters might have on the foams made. In the rest of this section, the following notation will be used to describe test conditions: X-Y-Z, where the number X is the dwell temperature (°C), Y is the dwell time (hours) and Z is the infiltration pressure (bar). For instance, processing condition of 710-2-1 would be an infiltration experiment where the dwell was 710°C for 2 hours, and infiltration

was performed with an argon gas pressure of 1 bar. Following other work on processing of foams by replication [6] these are the only variables used which are shown in table 5.1.

Table 5.1 - The processing parameters that have been used in experiments with the processing rig.

Plateau Temperature	Low Temperature 710 ˚C			Medium Temperature 740 ˚C				High Temperature 780 ˚C
Plateau Time	1h	2h	2h	1.5h	2h	2h	2h	2h
Vacuum, Torr	25	20	20	25	20	25	25	25
Pressure, for 5 minutes	1bar	2bar	3bar	1bar	1bar	2bar	3bar	2bar
Aluminium/g	435	450	468	465	485	500	470	480
Salt/g with d ≈1.6mm	255	223	248	225	237	230	240	225
Infiltration %	**0**	**36**	**0**	**29**	**75**	**109**	**23**	**0**
Comments	No melting, low T and short time.	Better melting, large part infiltrated	No melting, no conduction due to small volume of aluminium ingot used	Partial melting, small part infiltrated	Very good structured Foam	Large infiltration, some amount of salt trapped in	Most of molten aluminium squeezed out due to high pressure.	Salt evaporated. Oxidation of aluminium due to very high T

Furthermore, another important factor taken into account is a calculated value of how much free space in the preform was infiltrated with aluminium in each case. For complete infiltration, where all free space was filled, this value would be 100%, although a successful foam does not necessarily require this, rather that the filling of free space must be uniform. It should be noted that because the exact packing efficiency of the salt grains in each case is not known (64% is assumed [128]); this value must be considered an estimate.

Figure 5.1 shows some examples of foam samples that were initially produced under the different conditions using the new infiltration rig.
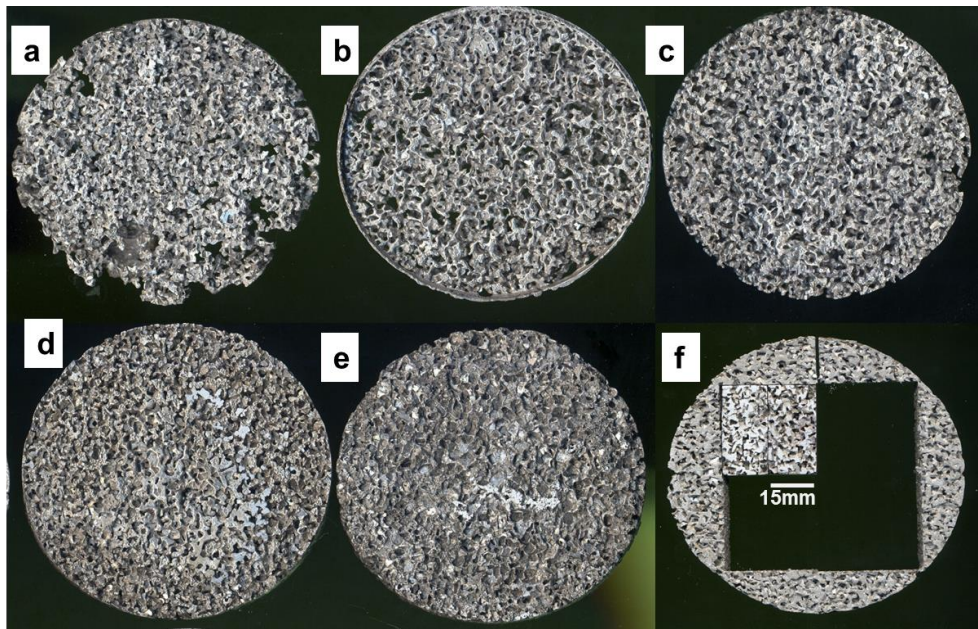
Figure 5.1 - Open-cell aluminium foam block samples produced using different conditions to give different quality foams with different porosities; a) 740-2-3 with 90% porosity, b) 740-1.5-1 with 88% porosity, c) 710-2-2 with 85% porosity, d) 740-2-1with 69% porosity, e) 740-2-2 with 55% porosity and f) foam specimens after EDM cutting of foam block made from 740-2-1 condition.

It can be seen that the processing parameters used (i.e. temperature, time and pressure) allow great control of the foam structure, which provides an opportunity to tailor metal foams with the required porosities. Open-cell aluminium foams produced successfully so far have porosities ranging from 56% to 90% with examples of these foams shown in the above figures. Note that because exact machining of the samples has not been performed on these blocks of samples, the porosities here have been approximately calculated using the volume and weight of the whole block.

5.1.1.1. Effect of Operating Temperature

The processing conditions can be divided according to the three different temperatures that have been used; which are the following:

<u>Low Temperature 710 ˚C</u>

Three different experiments were carried out at this lowest temperature. This is the temperature previously used in replication work (e.g. ref.[8, 29]). In the first experiment, 710-1-1 (with 1 hour plateau time, and 1 bar gas pressure) the

aluminium ingot did not melt. This is thought to be because, although the temperature was sufficient (pure aluminium melts at 660°C [5]), the heat did not have enough time to diffuse through the steel chamber with wall thickness of 7mm into the aluminium. In the second experiment, 710-2-2 (with 2 hour plateau time, and 2 bar gas pressure), a large amount (but not all) of the aluminium ingot was melted, and this allowed 36% of the available space in the NaCl preform to be infiltrated (see figure 5.1-c above). In the third experiment, 710-2-3 (with 2 hour plateau time, and 3 bar gas pressure) the aluminium ingot did not melt. This is thought to be because a smaller volume of aluminium ingot was used and so it was not in contact with the inner wall of steel cylinder during heating. For melting to occur efficiently, conduction must be ensured.

Medium Temperature 740℃

Four experiments were carried out at an intermediate temperature, 740℃. In the first experiment, 740-1.5-1 (with 1.5 hour plateau time, and 1 bar gas pressure) the aluminium ingot was partially melted, and only 29% of the available volume in the NaCl preform was infiltrated (see figure 5.1-b above). This may be as the 1.5h plateau time was also too short for full melting to take place. In the second experiment, 740-2-1(with 2 hours plateau time, and 1 bar gas pressure), a very well structured open-cell foam was produced (see figure 5.1-d above) due to a good melting of the aluminium ingot and an apparently very uniform infiltration of 75% of the available volume. In the third experiment, 740-2-2 (with 2 hours plateau time, and 2 bar gas pressure; the same thermal conditions but higher pressure), melting of the aluminium ingot was once again achieved and the extent of infiltration was much higher, with an apparent value of 109 % of the available space filled (see figure 5.1-e above). This apparently unreasonable result may be explained by the imperfect packing of salt grains or by the existence of some amount of salt trapped within the structure after dissolution. In the fourth experiment 740-2-3 (with 2 hour plateau time, and 3 bar gas pressure), almost all of the molten aluminium was forced out of the cylinder due to the pressure being too high for the sealing method employed, and only a relatively small part of the preform (23.3 % of the available space) was left infiltrated (see figure 5.1-a above).

High Temperature 780℃

Only one experiment was performed at this high temperature, 780-2-2. The furnace was held at 780℃ for 2 hours and with 2 bar gas pressure being applied for infiltration. Due to the high temperature, the salt had begun to evaporate, and had undergone some softening (the melting point of NaCl of 801 °C [30]), such that the porosity in the preform was closed and no infiltration was possible. Also, a high degree of oxidation on the aluminium ingot was observed. For these reasons, it was concluded that 780°C was too high a temperature for infiltration.

5.1.1.2. The Effect of Time and Temperature on Infiltration

From the preceding discussion the effects of time and temperature on the infiltration process begin to emerge. There are some limits imposed due to the thermal environment created in the chamber. For instance, with a low temperature of 710 °C and short time of 1h, melting of the aluminium ingot is not possible because the time is too short for the heat to diffuse through to the aluminium. Also, with a high temperature of 780 °C, the NaCl preform will be evaporated or sintered, which means that infiltration cannot take place.

The processing window that can be established for plateau time and temperature is illustrated in figure 5.2 below; the temperature must be neither too low nor too high, and longer plateau times can assist, although there is the obvious limitation of how long it is convenient for the process to take. The suitable temperature should be 710℃ > T < 750 ℃, but 740℃ has shown the best performance for successful infiltration from those examined.
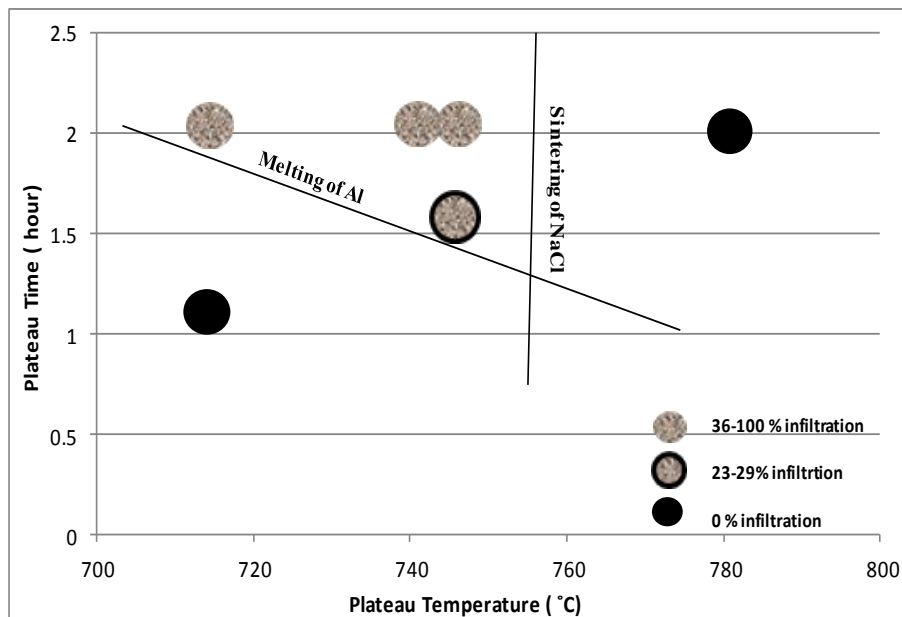
Figure 5.2 - The effect of plateau time and plateau temperature on the infiltration process. Note that lines drawn are for guidance only.

5.1.1.3. The Effect of Pressure on Infiltration

It can be noticed from these experiments that pressure, as well as time and temperature, plays a significant role in the infiltration process, and hence the foam structure produced. It is clear that 3 bar was too high a pressure for the rig, as it drove out a large amount of molten aluminium as demonstrated in the 740-2-3 experiment. Comparison between the pressures used (1, 2 and 3 bars) is made in figure 5.3 below which illustrates the fact that 3 bar pressure has the lowest successful infiltration (in terms of the percentage of the available space in the preform that is filled with metal) at both 710°C and 740°C. If the molten aluminium is quite fluid (as at higher temperatures) then perhaps 1bar pressure could be enough for a successful infiltration, as was seen in 740-2-1 where an infiltration of 75% was achieved. However, 2 bar pressure could also be used for infiltration if a lower temperature (i.e. 710°C) is used as plateau temperature. The latter processing conditions have yielded very open structure aluminium foam.
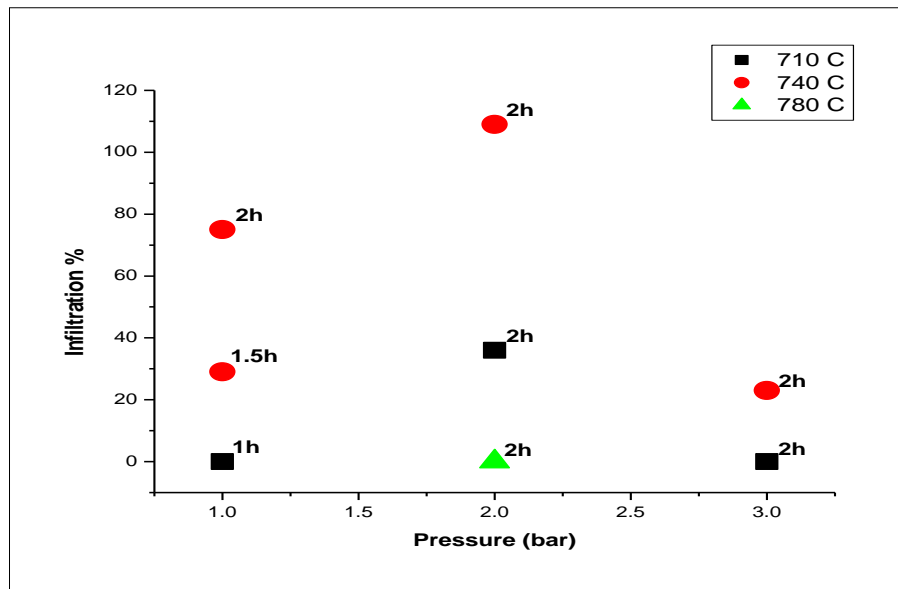
Figure 5.3 - Highlighting the effects of different pressures on the extent of infiltration. Note that the number near each circle indicates the plateau time in hours.

Having explored those foam processing variables, and after repeating several foam production runs to ensure consistency, foam specimens tested in this work were obtained as blocks with dimensions of 15X15X30 mm and cylinders of 24 mm diameter and 48 mm height, taking into account size effects (to respect the approximate rule that specimen dimensions should be ≥ 7 times greater than the pore size [12]), as seen in figure 5.4 below.
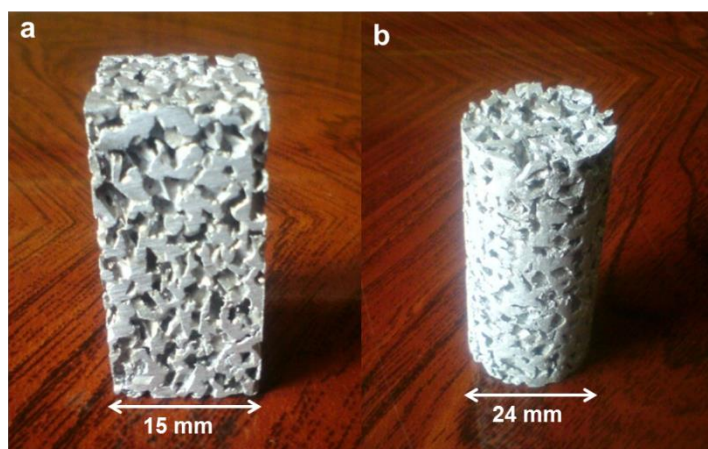
Figure.5.4 - Foam specimens produced using the new infiltration rig with the optimised process, which were obtained as a) blocks of 1.6 mm pore diameter and b) cylinders of 3.5 mm pore diameter, after EDM cutting.

5.2. Characterization of Foam Samples

5.2.1. Replicated Foams

As explained in chapter 2, the relative density of metallic foams has a strong effect on their functional and structural properties. The relative densities as well as the corresponding porosities of foam samples in this work were measured before processing of PEO coatings. In this case, it is done by measuring foam relative density, which can be obtained from quantifying the sample weight and volume (measured by linear dimensions), and dividing it by the density of bulk aluminum (2.7 g cm^{-3} for pure aluminum).

Figure 5.5 below is a histogram showing a frequency distribution of relative densities measured for foam samples. The bins or classes of relative densities are spaced by a class interval of 1%, and it is seen that, despite some scatter in the data, approximately 80% of the foam samples have relative density within 38-40% vol.
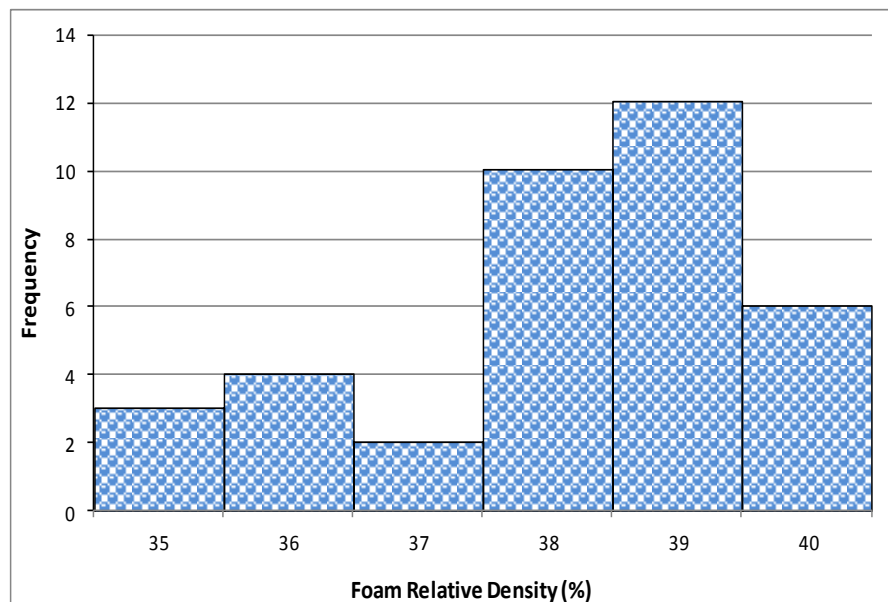
Figure 5.5 - Histogram showing relative density distribution with an average value of 38 ±1.3 % for foam samples made by the replication process.

The corresponding porosities of these foams are presented in figure 5.6, which was calculated as follows:

$$Porosity\ (P) = 1 - \left(\frac{\rho_f}{\rho_s}\right) x\ 100 \qquad\qquad (5.1)$$

where, ρ_f and ρ_s are densities of the foam and bulk aluminum respectively.
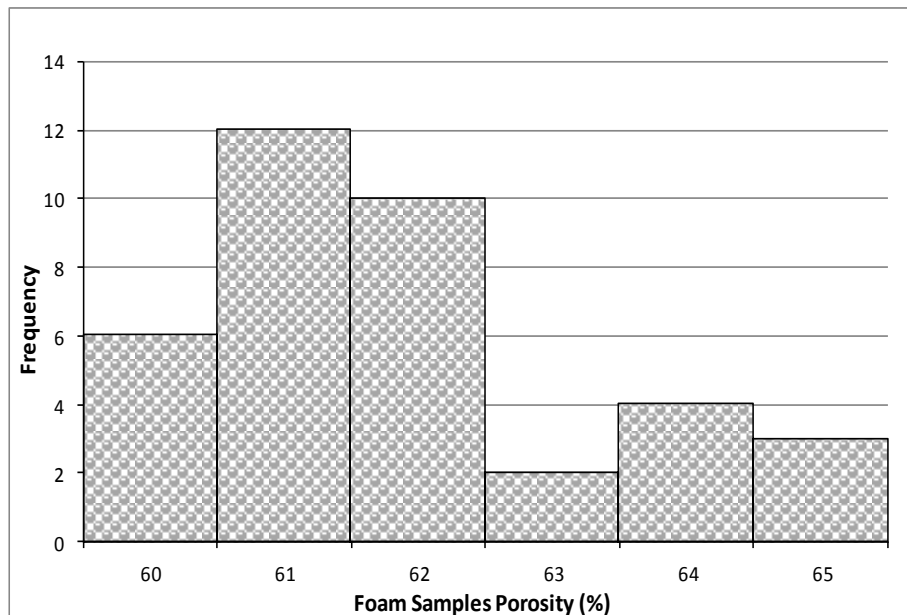
Figure 5.6 – Histogram showing foam sample porosity distribution with an average value of 62±1.4 % for the replicated foams.

The average pore diameter of replicated foams was measured using an image analysis method as follows:

$$L = \frac{4\,V}{S} \qquad\qquad (5.2)$$

$$L = \frac{2}{3}\,d \qquad\qquad (5.3)$$

$$d = \frac{3}{2}\,L \qquad\qquad (5.4)$$

where L is the mean linear intercept (diameter) measured on the section, V and S are the volume and surface area of the pore respectively and d is the true diameter of a pore. An average pore diameter of 1.55 mm was measured using this method whereas an average value of 1.56±0.16 mm was determined via ImageJ software; see section 4.4.6 in Chapter 4 for more detail on this software. It can be seen that these values are comparable with only a small difference, which probably falls within the experimental errors.

5.2.2. Duocel Foams

Duocel foams were also characterized for relative density and pore size. The average relative densities were calculated for all samples tested and were found to be 9.1±0.22 % for 20PPI and 9.5±0.35 for 40PPI. 40PPI type has smaller pores (measured as 2.1 mm) as compared to 20PPI type foam (measured as 2.5 mm), as seen in figure 5.7. The pore sizes of both foams were determined using the same techniques used for replicated foams in section 5.2.1.
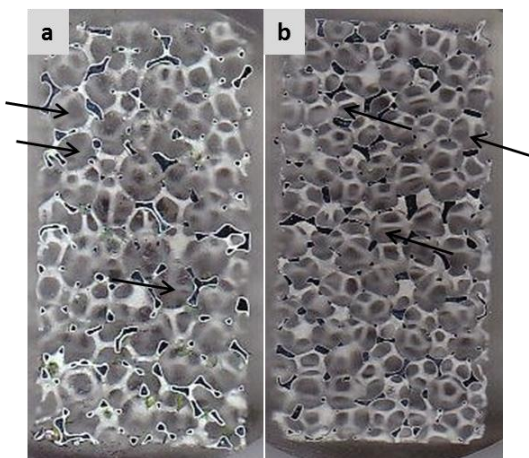
Figure 5.7 – Cross-sections of (a) 20PPi and (b) 40PPi Duocel foams tested in this work, indicating examples of pores (arrowed) that were measured using different methods.

5.3. PEO Coating Penetration and Distribution

PEO coating was applied to foams to allow characterization of coating thickness variations on free surfaces and throughout the treated foams. Also, dense BS 1050 Al alloy coupons of 50 mm in diameter by 5 mm thick were used for reference purposes. These should be very comparable to the replicated foams, made of 99.5 % Al, Duocel foams on the other hand are made of 6101 Al alloy.

As was explained in Chapter 4, in the first PEO processing attempt on replicated foams, Duocel foams and dense reference samples, the treatment time was varied for 20, 40 and 80 minutes. During processing, a rectangular pulse reverse voltage

waveform was applied at 37.5 % positive duty cycle and 250 Hz frequency as seen in figure 5.8 below.
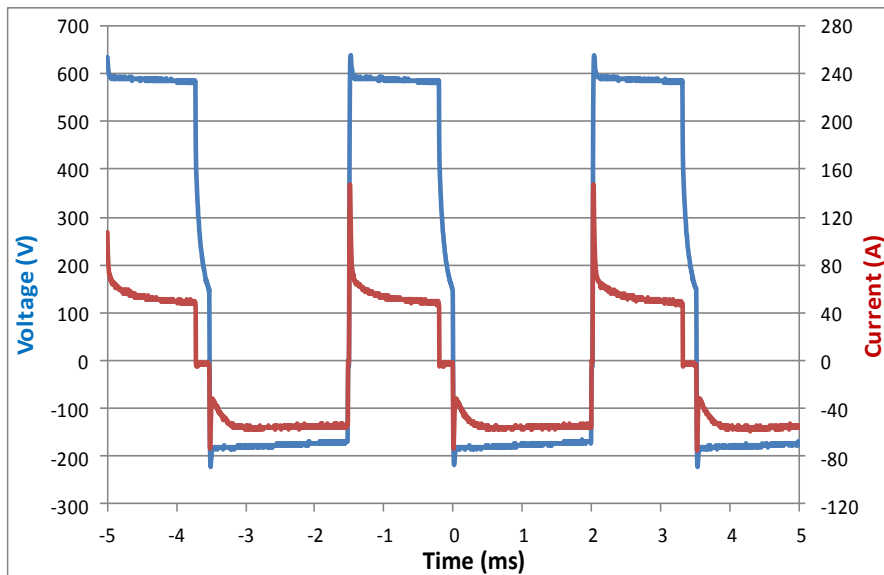
Figure 5.8 - Current and voltage waveforms for a frequency of 250Hz in PBC mode during PEO processing of open cell aluminium foams. Estimation of current magnitude during pulse on time is 56.5 A.

5.3.1. Coatings on Replicated Foams

The variation in sample appearance with the different coatings applied is shown in figure 5.9 for replicated cylindrical samples. The PEO coating thickness distribution in the treated foam specimens was characterized using measurements made from optical micrographs of the polished cross-sections. For all treatments, variations in coating thicknesses were observed with location, with generally thicker coatings being obtained nearer the outer edge of the specimen. Several measurements were taken at different locations across the sample, and average values were found for points the same distance from the specimen surface. The behaviour found was reproducible, and data for replicated foams are presented in Figure 5.10.

The mean thickness of the coatings formed on reference dense samples by treatments t_1, t_2 and t_3 was evaluated as 22.1±3.6 μm, 48.7±7.3 μm and 96.3±11.5 μm, respectively.
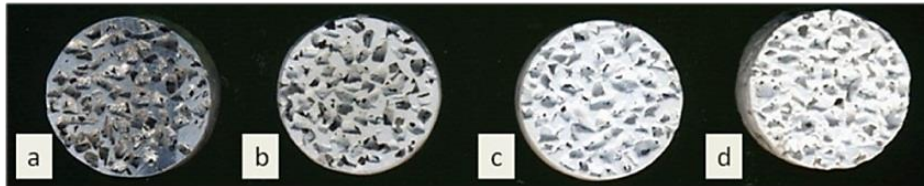
Figure 5.9 - Cylindrical specimens of aluminium foams produced in the laboratory by replication, with a) no coating, and volume averaged PEO coating thicknesses of b) 1.9 µm, c) 13 µm and d) 32 µm, generated by treatments t_1, t_2 and t_3 respectively.

Variation was seen the coating thickness with location in the foams. In order to produce a single representative value of the coating thickness a volume averaged value was determined (i.e. taking into account that, for a cylindrical specimen, more of the material is represented by the measurements made near the surface than near the centre). These values are given in Table 5.2 and in the discussion that follows these are the parameters referred to as the average coating thickness.
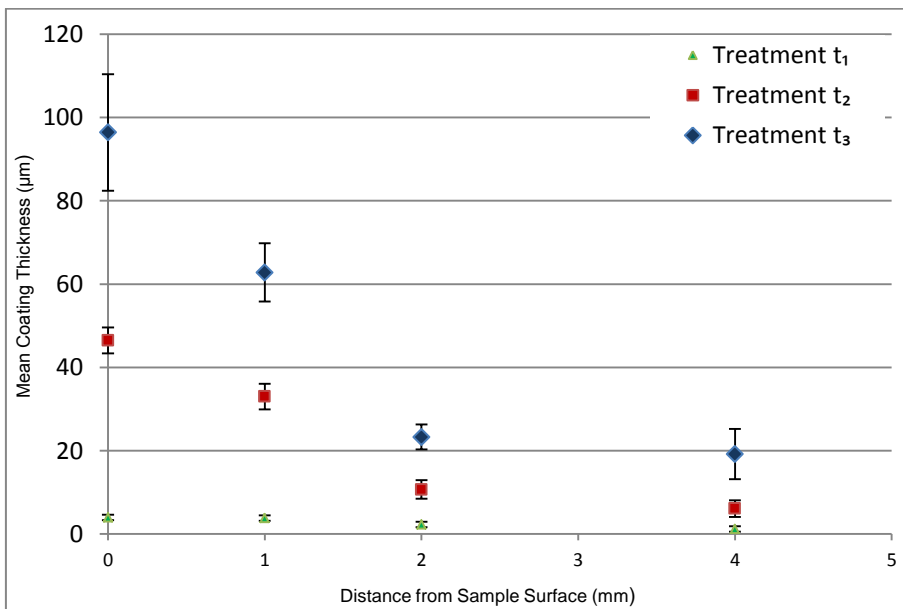
Figure 5.10 – The variation in mean coating thickness with distance from the sample surface for replicated foam after treatments t_1, t_2 and t_3. Error bars represent the standard deviation in results.

It can be seen that treatment t_3 produced considerably thicker coatings (remembering that the potential as well as time are changed between the different treatments), though in all cases there is a sharp reduction in coating thickness in the first 2 mm

from the foam surface. This distance is roughly comparable to the 1.6 mm mean pore diameter, a region which would be expected to be more open to penetration by the electrolyte than the foam interior. Although the decrease with depth is substantial, it should be noted that coating is present throughout the sample at measurable levels. Furthermore, it can be noted that the distribution of coating thicknesses is roughly self-similar for each treatment, at least within the set of data on time-variable PEO coated replicated foams (the same general trend but with different fall off rates was seen when varying other PEO processing variables such as pulse frequency f and on/off ratio δ). For low density, more permeable Duocel foams, there is a tendency for reducing coating obtained towards the centre of the foam structure at longer treatment time i.e. treatment t_3.

This fall off in thickness is in agreement with previous results on electrodeposited coatings on foams [1, 4, 83] and is likely to be for a similar reason; a reduced potential in the centre of the foam and a more limited passage of electrolyte through the foam structure. Also, as expected, the coating thickness, even in the outer regions of the foam, was less than would be expected on dense aluminium coated using the same procedures.

5.3.2. Coatings on Duocel Foams

PEO coatings characterization was carried out for both types of the Duocel aluminium foams (20 and 40 PPI). These foams were Plasma Electrolytic Oxidation coated under similar processing conditions of that used for replicated foams.
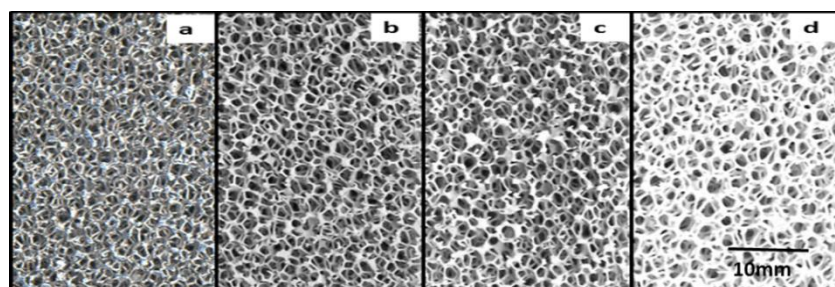
Figure.5.11 – Surface plane for specimens of Duocel aluminium foams with a) no coating, and volume averaged PEO coating thicknesses of b) 10.8 µm, c) 32.0 µm and d) 52.3 µm.

Untreated and PEO processed samples can be distinguished visually in Figure 5.11. The thickness distribution measured for the different PEO treatments of 2.1 mm pore size Duocel foams is presented in Figure 5.12. It should be noted that thickness variations with depth were particularly pronounced in coating with treatment t_3, with generally thicker oxide layers being obtained nearer the outer edge of the specimen. Furthermore, for all coatings, thickness deviations near the edge are smaller, but tend to increase towards the centre of the sample. Nonetheless, there is generally a smaller decrease in the coating thickness formed by treatment t_2 in the foam interior, and almost uniform coating distribution was observed for coating processed under treatment t_1. This behaviour should not be surprising since potential and processing time differ for the treatments, both of which strongly affect coatings produced. These aspects are investigated further, along with the effect of such parameters on coating thickness, structure and properties.
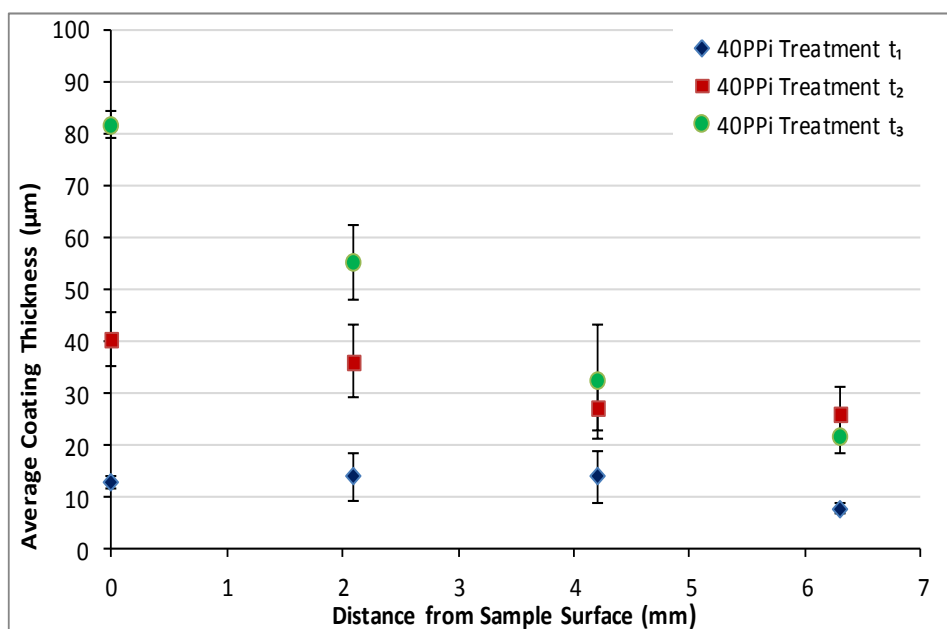
Figure 5.12 - Variation in mean coating thickness with distance from the sample surface for 2.1 mm pore size Duocel foam after treatments t_1, t_2 and t_3. Error bars represent the standard deviation in results.

To evaluate the effect of cell size and hence the openness of foam structures on the penetration and uniformity of coating thicknesses, the coating thickness

characterisation was also carried out for 20PPI Duocel aluminium foams, see figure 5.13 below, treated using similar processing conditions.
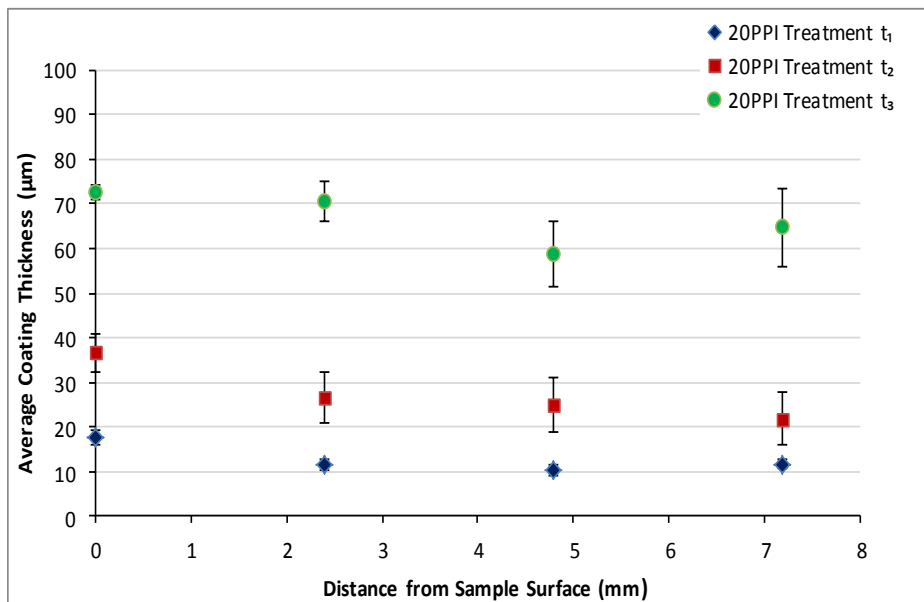
Figure 5.13 - The variation in mean coating thickness with distance from the sample surface for 2.5mm pore size Duocel foam after treatments t_1, t_2 and t_3. Error bars represent the standard deviation in results.

The average coating thickness values for each treatment are presented in Table 5.2, with thickest coating produced by treatment t_3. Coating thickness relative to strut thickness for treatment t_3 can be observed in an optical micrograph in figure 5.14 below.

It was found that coating thicknesses, for each of the three different treatments, are almost uniform throughout. This is in agreement with a previous study [96] of PEO processing of similar grade of Duocel foam, in which it was found that the thickness of the PEO coatings does not vary with depth into the foam structure. Penetration of PEO coating on open cell titanium foams with pore size of 50 μm, 90 μm and 150 μm was investigated in [125]. Despite the change in treatment time and applied voltages, full coating penetration was only observed in the middle region of foams with 150 μm pore size, with variations in coating thickness with depth. For foams with smaller pore size ≤ 90 μm the coating was only found in the outer surfaces. This has more similarities to the results of replicated foams observed here.
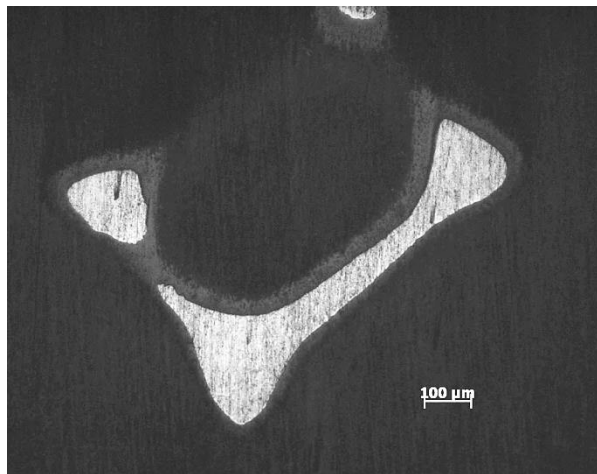
Figure 5.14 - Cross sectional image through a single strut from a 2.5 mm pore diameter Duocel sample, with PEO coating treatment t_3 (68.3 µm volume averaged coating thickness).

This behaviour is likely to be due to the complexity of foam structure itself (closedness versus openness) which may hinder the coating process towards the centre (shielding effects [83]), by both reducing the potential in the centre of the foam and reducing the ease with which material from the solution can be transported in. For the fluid (e.g. electrolyte solution) to flow through the open cell foams, foam permeability needs to be increased, which means that there is less resistance to fluid to flow into the foam structure [129-131]. Foam permeability increases with increasing its porosity, especially when there are large windows between pores (as is the case in 20PPI foams) which could be of an advantage in PEO coating of foams. Despois and Mortensen [129] proposed a model for predicting the permeability K, of replicated open cell aluminium foams, and it has been found that this model agrees well with the experimental results of replicated foams of different pore sizes (0.075 mm and 0.4 mm) and a range of porosities; 60 - 90%, as following:

$$K = \frac{\Delta\, r^2}{\pi} \left[\frac{\Delta - \Delta_0}{3(1 - \Delta_0)} \right]^{3/2} \tag{5.5}$$

where Δ is the measured foam porosity, Δ_0 has been assumed to be 0.64 for random dense packing of monosized spheres and r is the initial average pore radius in a foam. Using this model for the foams of this investigation gives a range of values that fall off towards smaller pores and higher density, as seen in figure 5.15.
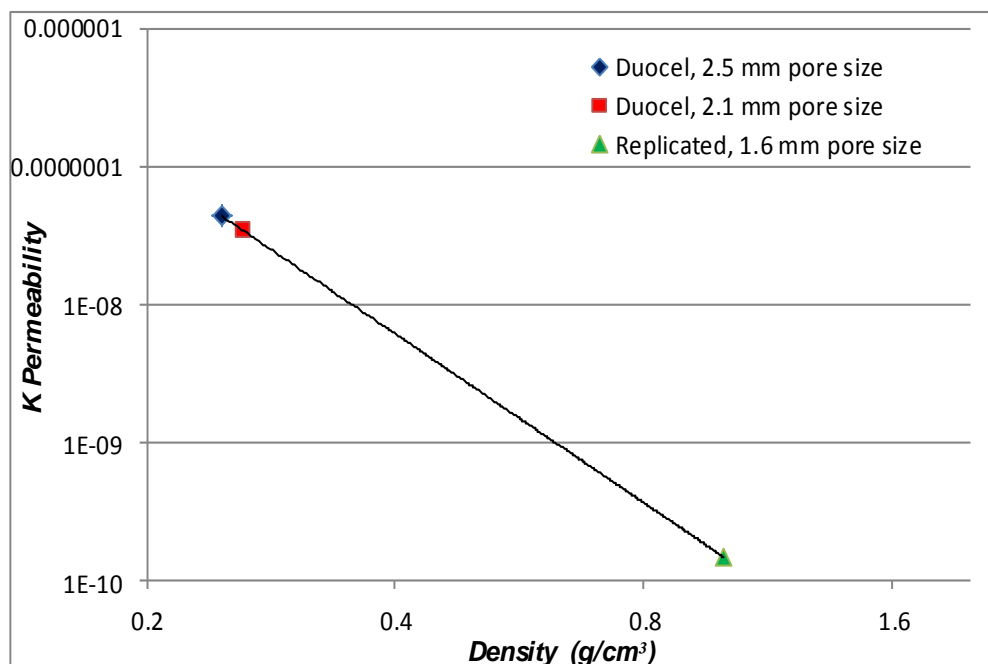
Figure 5.15 – Permeability K calculated suing Eq. 5.5 [129] for the different foams tested in this work, which decreases with decrease in foam pore size and increase in density.

This may be explained by the fact that the windows, connecting between different pores in foams, tend to decrease in size and may close off as the relative density reaches 0.36 [129]. The reduction in permeability K, as discussed above, may be linked to what have been observed for PEO treated foams, specifically for high density replicated foams where impedance to electrolyte circulation is most obvious. Furthermore, there is also an indication that even with higher porosity Duocel foams, coating thickness may vary with depth. This is may be a clear indication that ion transport into foams interior is largely controlled by ion dispersion and diffusion with minor effects from fluid flow [97, 125], thus playing significant role during formation of PEO coating. It has also been shown that ion distribution and diffusion are not uniform and can vary depending on the pore size and the size of the treated porous electrode [125]. Randomly distributed ions lead to uneven current density distribution hence irregular reaction rate in the porous electrode, which can have an effect on the amount of materials being transformed and transferred into foam specimens during formation of PEO coating.

It can further be noted that the overall coating thickness achieved by a specific treatment is higher on sample free edges, and the maximum thickness variation with depth is reduced in the 2.5 mm pore size Duocel samples, where both the surface available for coating and the impedance of the coating process due to the foam structure were less. This may indicate that the precise surface conditions can have a very strong effect on the coating process.

5.3.3. Alternative Estimation of Coating Thickness Formed

The value of volume averaged coating thickness formed on foam struts is required for analytical models predicting foam mechanical properties, where a single value is usually used. Although this has been measured here it is important that it is accurate and to check an alternative measure, based on weight change, can be used. For PEO coating on foams, the coating thickness can be estimated by considering the reaction that is occurring. If we assume the coating to be alumina, Al_2O_3 (a simplification as it will also contain other species such silicates), the increase in mass of the sample must be due to the uptake of oxygen, the number of moles of which, n_O, can be found from:

$$n_O = \frac{\Delta W}{M_O}$$
(5.6)

where ΔW is the increase in weight of the sample and M_O is the molar mass of oxygen. Using this number and the stoichiometry of the reaction, the number of moles of aluminium which are left unconverted, n_{Al}, and the number of moles of alumina that are created, n_{Al2O3} are:

$$n_{Al} = \frac{W_0}{M_{Al}} - \frac{2}{3}n_O$$
(5.7)

$$n_{Al2O3} = \frac{n_O}{3}$$
(5.8)

where W_0 is the mass of the sample before coating and M_{Al} is the molar mass of aluminium. Thus from the weight change the number of moles of each species present after the coating process can be found. If we assume the coating is dense, defect-free Al_2O_3 (another simplification as it will also contains cracks and pores)

then we can use the molar volumes of aluminium and alumina to work out the volume ratio of each present from the number of moles of each that have been produced. If we consider a cylinder with a thin coating, it can be shown by simple geometry that this volume ratio will give a relationship between the radius of the cylinder, *r* (analogous to the strut in the foam) and the thickness of the coating as seen in figure 5.16 below, *t* as follows:

$$t = \frac{Volume\ Coating}{Volume\ Al} \frac{r}{2}$$
(5.9)

The mean diameters of the struts in the replicated foam were measured by optical technique (see Chapter 4, section 4.4.6 for more detail) to be 820 µm, and those in the Duocel foam as 280 µm, and the difference in sample weight before and after coating were recorded, allowing this estimate to be made. The results of this estimate calculation are given in Table 5.2, and these can be compared to the experimental results for coating thickness (minimum and maximum values of coating thickness recorded) and the volume averaged coating thickness to which they should bear some comparison.
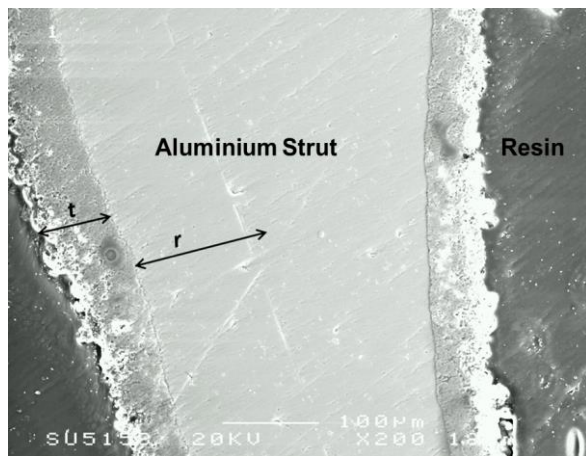
Figure 5.16 - Low magnification SEM image, showing cross-section for in-plane cut of Duocel foam strut enveloped with PEO coating. Estimation of coating thickness can be made based on images of this type of foam structure.

It can be seen that the estimates for Duocel foams compare reasonably well to the actual volume averaged coating thicknesses recorded. The estimates are slightly low,

which is to be expected as it has assumed the coating to be dense alumina, whereas it will actually consist of a range of compounds, and, more importantly, will contain pores and flaws such as cracks, see Figure 5.17.

Table 5.2 – Coating thicknesses estimated from the weight change using equation (5.5) and the measured averaged coating thicknesses for each type of coatings and of foams are also presented.

Foam	Treatment	Measured Averaged Coating Thickness, µm (min/max)		Estimated Coating Thickness, µm
Replicated (1.6 mm pore size)	t_1	1.9	(1.2/4)	9.0
	t_2	13	(6.1/47)	116.6
	t_3	32	(19/96)	241.0
Duocel (2.1 mm pore size)	t_1	10.8	(7/14)	6.4
	t_2	32	(25/40)	12.9
	t_3	52.3	(22/81)	55.4
Duocel (2.5 mm pore size)	t_1	12.5	(9/17)	3.4
	t_2	29	(22/36)	12.0
	t_3	68.3	(60/80)	59.5

All of these will increase the molar volume of the coating, and so the thickness recorded for a given weight increase. This correlation contrasts with the poor comparison between the estimates and the experimental values for the replicated foams. In these experiments the coating is much thinner than predicted. While this could be because the density of the coating is increased, for example by the incorporation of particularly dense species, there is no clear reason why such a significant difference should occur between two different aluminium foams. It is more likely that the deposition of SiO_2 is promoted in the more isolated pores of the replicated foams (which have high density) compared to the lower density, more permeable Duocel foams. Silicate species are usually weakly dissociated, with majority remaining in micellar form [132]. The surface concentration of silicate is therefore less dependent on the electric field and its precipitation occurs mainly due to physical adsorption. This is likely to increase the silicate content in PEO coatings deposited into deep holes and crevices (present in the replicated sample, see Figure 5.8), where electrolyte circulation may be hindered. As in such a situation the silicon

being deposited in the coating comes from the electrolyte, the initial assumption that the weight increase is due to oxygen forming Al_2O_3 is incorrect. EDX results, while displaying a degree of variability between different locations and through the coating thickness, are generally consistent with there being a higher silicon concentration in the replicated coatings, as shown in table 5.3. Such increase in Si content in the coating formed on the replicated foam may also be interpreted by the fact that this coating was thicker than those formed on the Duocel foam (see figure 5.10, 5.12 and 5.13), and as the coating gets thicker, the contents of elements such as Si, O are increased while that of Al is decreased.

Table 5.3 – averaged elements distribution of the PEO coating formed at treatment t_3 on replicated and Duocel foams.

Element, At. %	Coating on Replicated Foam	Coating on Duocel Foam
Aluminium	26.7±0.5	29.5±0.5
Oxygen	62.2±0.1	61.75±0.8
Silicon	11.1±0.4	8.75±0.4
Total	100.00	100.00

The actual scanning areas used for characterizing element compositions of the PEO coatings are shown on the SEM micrographs in figure 5.17. These coatings were produced under treatment t_3 for both replicated and Duocel foams.
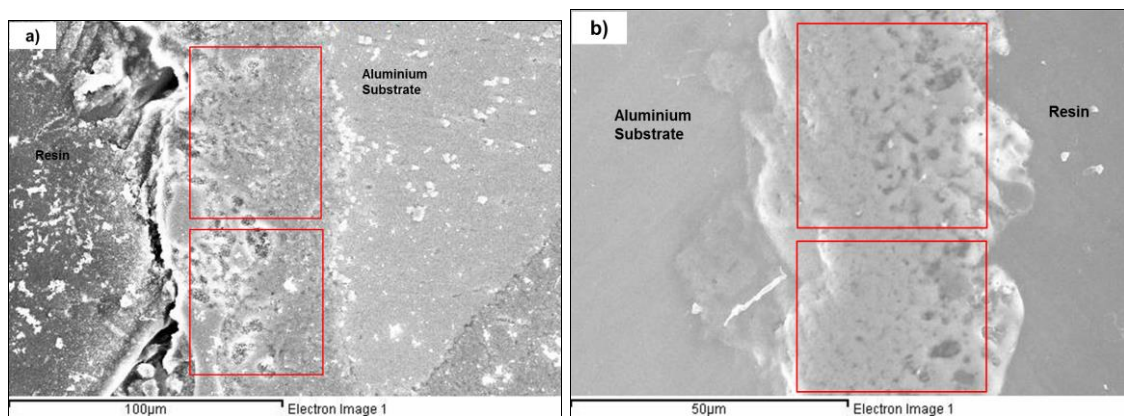
Figure 5.17 – SEM micrographs taken during EDX analysis of PEO coating with treatment t_3 for a) the replicated and b) Duocel foams.

It should be noted that another factor which may contribute to the difference is the complex structure of the replicated foams, where the struts do not approximate well to cylinders, means that the simple estimate developed here may not simulate the true coating distribution very accurately.

5.4. PEO Coating Characterization

5.4.1. SEM Microstructural Analysis

The typical coating morphology seen on the reference dense sample and on foam samples is presented in Figure 5.18. The surface plane image (Fig 5.18.a) reveals a topography characteristic of PEO coatings formed in silicate electrolytes, featuring nodular agglomerates, traces of discharge craters, radial and concentric cracks. In the cross-sectional images, two coating regions with different morphology can be resolved in the reference dense sample (Fig 5.18.b), replicated and Duocel foam coated struts (Fig 5.18.c & d). The rough and porous outer region comprises 30 - 40 % of the coating thickness. This is associated with increased silicate concentration in the electrolyte, which promotes precipitation of porous silicate and aluminosilicate compounds. Thus the coating morphology is compromised to some extent, compared to PEO coatings produced in more diluted silicate-alkaline solutions [105]. However a stable surface passivation state and a steady coating growth are ensured over a wide range of potentials that are expected to be present across the foam surface. The inner coating region features a denser morphology, although some structural defects, e.g. voids, microcracks and traces of discharge channels, can be clearly observed. The effect of coating parameters on coating morphologies, and its effect in turn on the mechanical properties of foams is discussed in detail later.
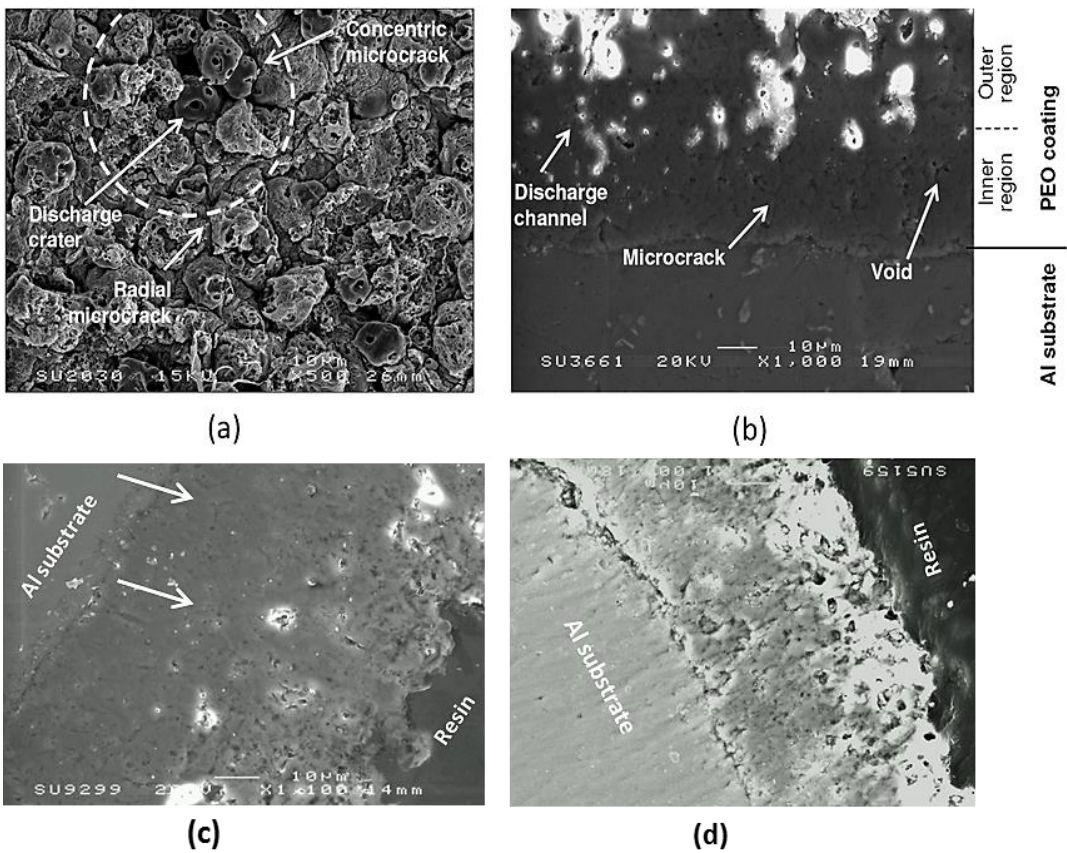
Figure 5.18 – Typical surface plane (a) and cross-sectional (b) SEM images of a PEO coating formed by treatment t_3 on a reference dense Al alloy sample. Defects present in the coating are indicated. Also shown are cross-sectional (c and d) SEM images of PEO coating formed by the same treatment on replicated and Duocel aluminium foam struts, demonstrating (arrowed) similar microcracks and void formation within the coating.

5.4.2. Coating XRD Analysis

The typical phase composition of PEO coatings formed under the process conditions adopted in this work is shown in Figure 5.19 below. The following three main constituents can be distinguished: crystalline alumina, silicate phases and the amorphous component, which is consistent with SEM observations. Alumina phases are common in the inner dense region and represented by α- and γ-Al_2O_3 in approximate proportions of 2:5 (judging by the intensities of the (113) $_α$ and (400) $_γ$ peaks at 43° and 46° 2θ, respectively). The silicate phases are formed mainly by

mullite ($Al_6Si_2O_{13}$) with a minor addition of silica; these (and possibly the amorphous constituent) are abundant in the outer porous region.
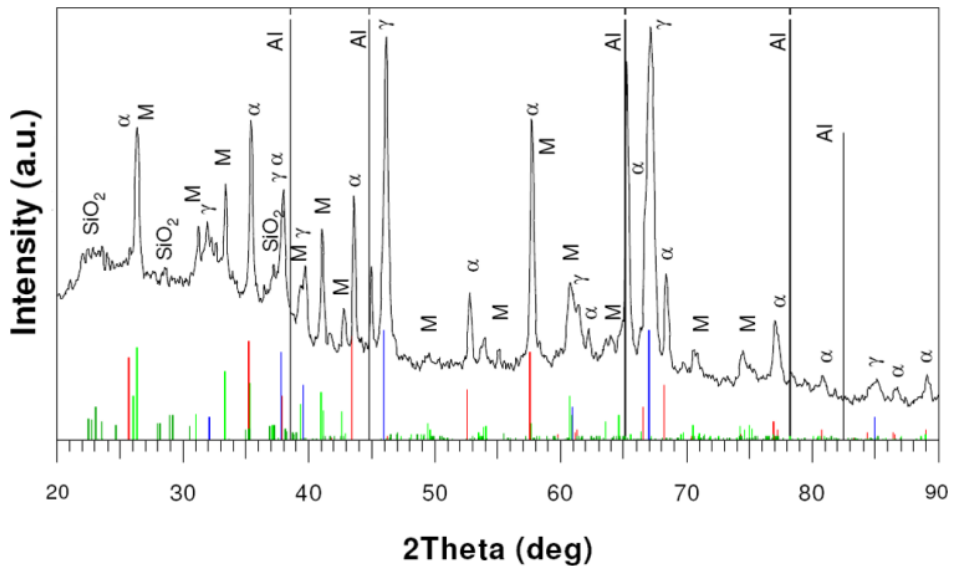
Figure 5.19 - An X-ray diffraction pattern of the PEO coating produced by treatment t_3, on a reference dense Al alloy sample. The phases are identified using the following PDF data: Al – [04-0787]; a – [10-0173]; g – [10-0425]; M – [73-1253]; SiO_2 – [82-1566].

5.5. X-Ray Microcomputed Tomography

The technique of X-ray microcomputed tomography has been previously performed on open and closed cell (Duocel and ALPORAS respectively) aluminium foams [60], ceramic foams made from pure aluminium matrix reinforced with a low volume fraction of spherical ceramic particles [59] and on syntactic foam [61], to investigate the microstructure, deformation modes and damage of the metals during deformation.

In the present work, XCT (X-ray source using Nikon Metrology 225/320 kV Custom Bay) was used to characterize PEO coating distribution into the open cell aluminium foams produced by the new developed infiltration rig shown in figure 4.4, chapter 4. Visualisation has been performed on foam (size of 10x10x27 mm) coated under t_2

condition (see table 4.3), as this condition produced PEO coatings with improved mechanical properties (hardness and modulus) and is shown to improve foam mechanical and specific properties. The contrast is enough to perform an accurate segmentation of the foam and of the coating as seen in figure 5.20. The coating thickness and foam strut thickness were measured and the statistical distributions were obtained.
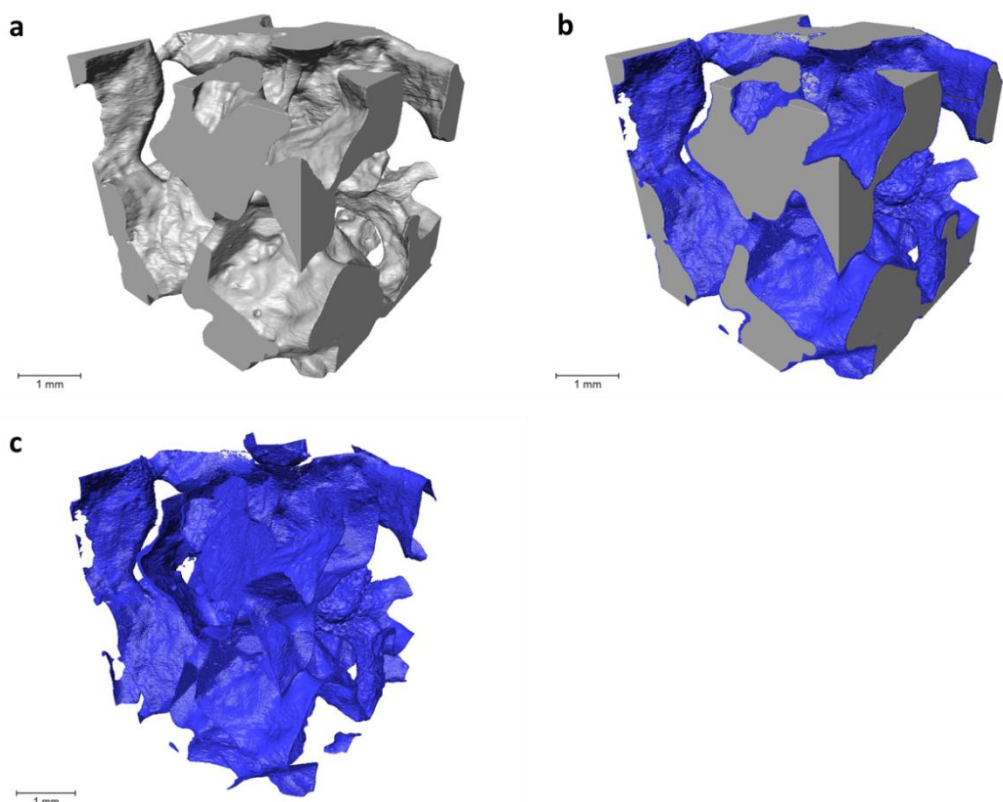
Figure 5.20 – μ-CT reconstructed tomographic 3-D images showing a) the aluminium foam, b) images of both foam and coating, c) PEO coating only while the aluminium structure is removed to reveal the shape and distribution of the coating. The image analysis in this section was carried out by Dr F. Léonard, Research Associate at the Henry Moseley X-ray Imaging Facility at The University of Manchester.

It can be seen from figure 5.20 that PEO coatings can be formed on the inner and outer regions of the foam, but their thickness may vary location. This was confirmed by further 2-D image analysis as shown in figure 5.21, where coating is shown to be distributed everywhere on the foam structure, but the coating thickness may change.
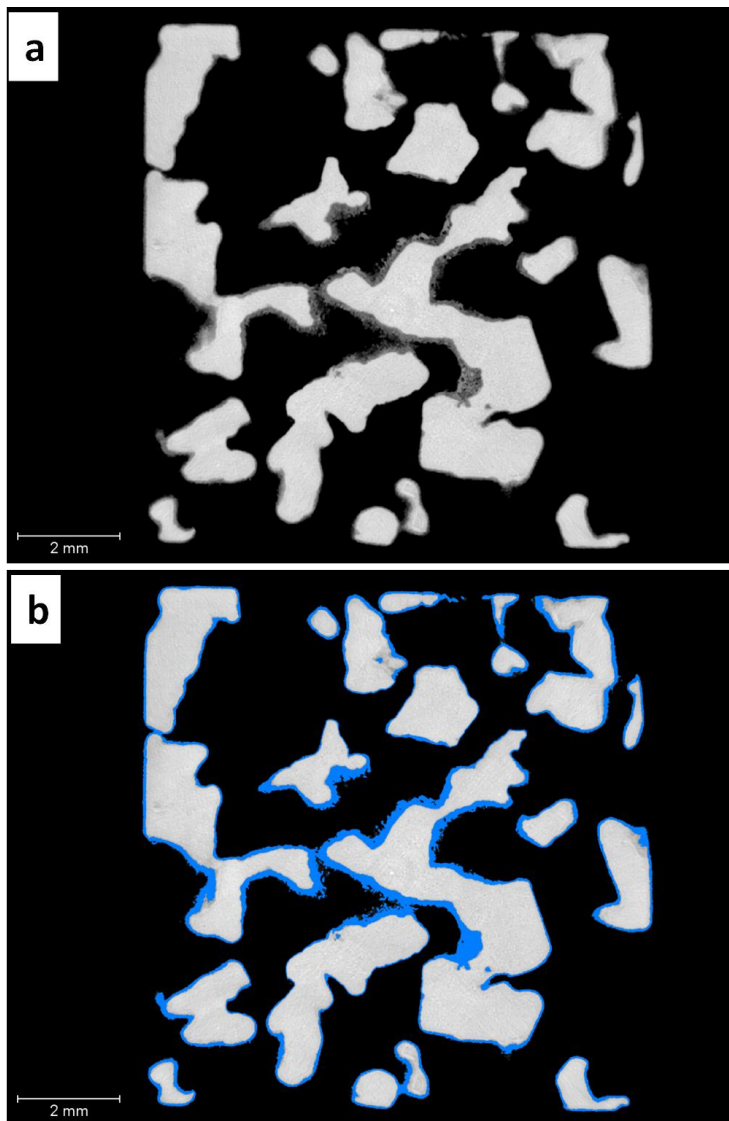
Figure 5.21 – μ-CT extracted tomographic images showing a) 2-D filtered slice of the PEO coated aluminium foam (coating produced by treatment t_2 can be distinguished by the different contrast with the bulk aluminium) and b) coating is labelled relative to the metal, which provides clearer view of both materials.

Statistical distribution analysis using probability density function (PDF) and cumulative distribution function (CDF) analysis are shown in figure 5.22. The figure shows that coating thickness with a minimum value of 8 μm and a maximum value of 680 μm is measured in this sample. The average coating thickness was calculated as 44 ±61 μm, which is still compares reasonably with the average measured values (80 – 90 μm), especially given that the specimen size is smaller than those tested

mechanically (although the very large error indicates the high range of values reported). The variations in coating thickness may be expected due to the change in current density distribution across the specimen. Current density is found to be higher at the edges and corners than in the interior of a sample. The effect of current distribution and the resistances from the electrolyte and the oxide coating formed on coating penetration into the foam middle structure are discussed in more detail later in chapter 7.

The foam strut thickness was found to range between a minimum value of 0.016 mm and a maximum value of 1.65 mm. The maximum value, however, is comparable to the result calculated earlier in this work, using 2D optical image analysis (average value of 1.55 mm). The smaller values measured here can be directly linked to the fact that struts of the replicated foam have random shape cross-sections with elongated edges, and so as the software may measure these areas the average values become smaller.
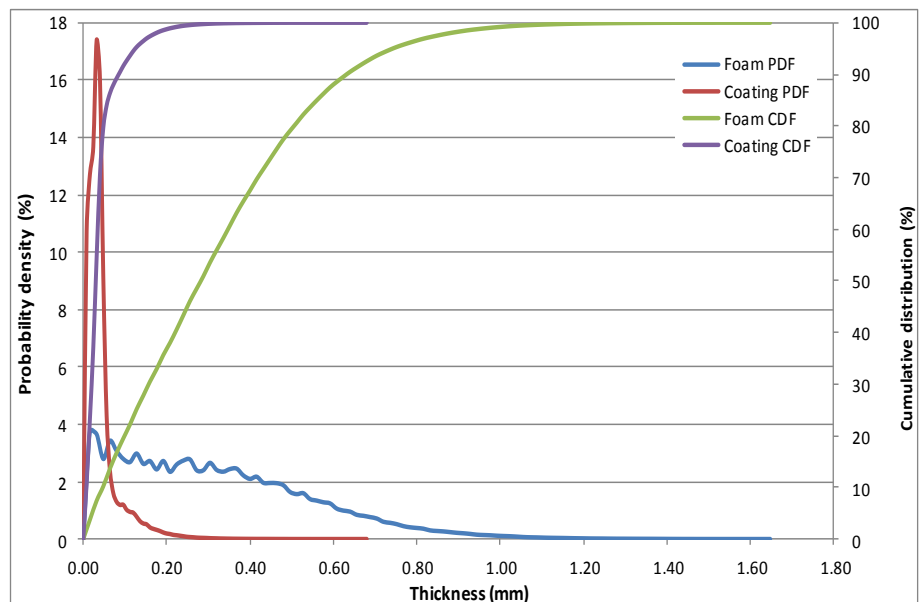
Figure 5.22 – coating thickness and foam strut thickness distribution analysis, using probability density function (PDF) and cumulative distribution function (CDF), % analysis.

Furthermore, the analysis showed that aluminium represents 83.6± 3.4% of the coated foam, while the coating occupies only 16.4 ± 3.4 %. A calculation based on foam density before and after coating for the other PEO coated foam using the same

processing conditions (t_2) showed that aluminium represents 73.4 ± 4 %, while the coating occupies 26.6 ± 4%. These values are reasonably comparable. However, the difference in these values obtained using both micro-computed tomography (MCT) and manual (density measures) calculations could also be related to the difference in the size of the treated foams and coating formed as a result. It can be concluded that MCT can be utilized to understand how coating penetrates into the foam internal structure, knowing that coating procedures should be optimized to avoid significant variation in coating thicknesses. This is essential for the optimisation of coating technique and is discussed in chapter 7.

Chapter 6: Effects of PEO Coatings on Foam Mechanical Properties

This chapter looks specifically into the effects of the PEO processing time, on the overall mechanical properties of the coated foams. As stated in chapter 4, three samples of each type and pore size were treated for 20, 40 and 80 minutes under treatment conditions designated as t_1, t_2 and t_3, respectively (with the principal variable being the processing time, although the voltage also has to be modified as the coatings thickness changes), to produce PEO coatings with different thickness. The PEO coating procedures, coating microstructures and penetration into internal structures of the foams were explained in detail in the previous chapter (Chapter 5). Whenever possible, correlation between effects of coatings behaviour (microstructure and coating penetration/distribution) and foam mechanical properties will be clearly made in this chapter.

6.1. Effects on Foam Elastic Behavior (Stiffness)

To investigate the effects of PEO coatings of various thicknesses on foams elastic behaviour, Duocel aluminium foams with an average pore size of 2.1 mm were processed under the same treatments of t_1, t_2 and t_3, and subsequently tested in tension. These tests were carried out using load-unload cycles at various stages throughout the test to evaluate their Young's modulus more precisely, and the effect of coating damage during deformation on the overall behaviour of coated foam. The mechanical properties obtained for coated foams were compared with uncoated ones.

6.1.1. Effects on Elastic Properties

Representative stress-strain curves for Duocel foams coated under t_1, t_2 and t_3 processing conditions, as compared to uncoated foam are shown in figure 6.1. It can be seen in the stress-strain curve that uncoated aluminium foam exhibits a good

ductile behaviour typical of bulk aluminium. The initial values of Young's modulus, E_o, for the different foams (measured before any damage takes place) can be obtained from the values of E_ε, moduli obtained from the unload cycles at different strains, extrapolated back to zero strain, as suggested by Depois et al. [68].
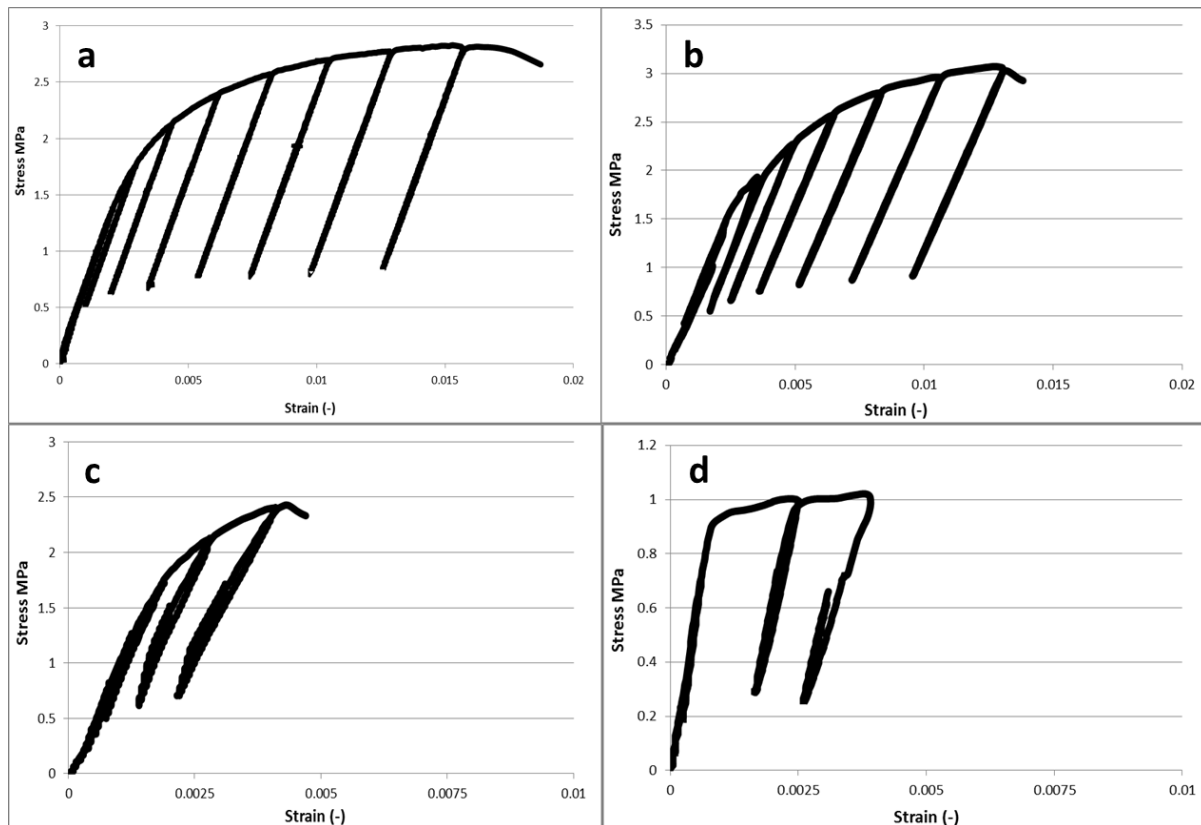
Figure 6.1 - Representative stress-strain curves for a) uncoated Duocel foam as compared to those coated under processing conditions of b) t_1, c) t_2 and d) t_3, after tensile tests.

This value of E_o modulus can be thought of as the initial stiffness of foam before deformation, since even a small amount of deformation could act to reduce this value [68]. These values are shown in the table below with an example of how they can be obtained being illustrated in figure 6.2 for the different foams in the present study. We find that for uncoated Duocel foam the initial value of Young's modulus E_o is 646 MPa. This value of modulus compares well with previous data obtained on similar Duocel foams [48], where the Young's moduli along the elongated cell axis were determined to be 502 and 634 MPa in tension and compression respectively. Other

work [88] reported values for compressive Young's moduli of similar foams with values of 670 MPa.

It is worth noting that, for uncoated foams, elastic moduli have been measured in both gradients of unloads and reloads in each cycle. It was found that the moduli measured were similar in each case (unloads and reloads), a fact which has previously been reported specifically for Duocel foams in [48]. Micro-computed tomography investigation in this earlier work revealed that deformation was occurring uniformly and spread throughout the sample [48].
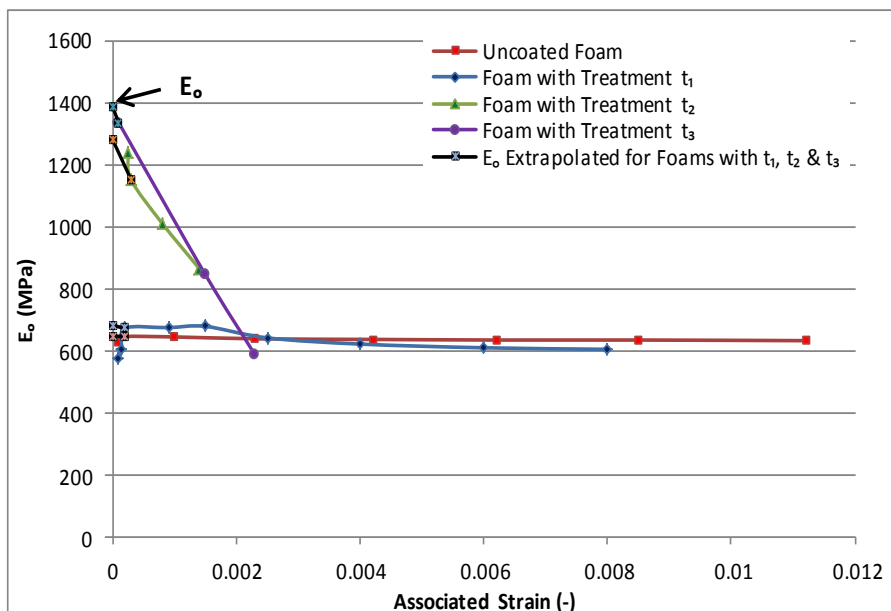
Figure 6.2 – A method suggested in ref [68] for calculating the initial Young's modulus for the different tested foams from stiffness-strain curves for Duocel foams subjected to different treatments.

Similar ductile character was observed in the stress-strain behaviour of foam treated under t_1 condition (having an average coating thickness of 10.8 μm), where coating occupies the smallest volume fraction of the whole material; it would also be expected that the PEO coating has a negligible effect on the core metal at large plastic deformations at this thickness as result of a high level of porosity within it [96]. It is worth noting that, as the uncoated sample and the sample with the thinnest coating both had equal relative density of 10.4%, the improvement in properties with coating are clear, see table 6.1. The stress-strain curves for foams treated under t_2 and t_3 conditions, having thicker coatings of average thicknesses 32.0 and 52.3 μm

respectively, showed smaller strain to failure, which could be, in part, due to a more brittle behaviour during cyclic loading-unloading testing.

Table 6.1 summarizes the results of the initial E_o and mean measured $E\varepsilon$ values of Young's moduli, yield stress, ultimate tensile strength, failure strain and the relative density of the samples before and after coating. The data point to a conclusion that the increased mechanical properties (both plastic and elastic) are more pronounced for the PEO-coated foams with treatments t_1 and t_2. However, for elastic moduli, the values extracted at $\varepsilon = 0$ are increased dramatically for all coatings

Table 6.1 - Average test results for the samples. Relative density is calculated compared to fully dense aluminium.

Treatment	Relative Density		E (MPa)		$\sigma_{0.2}$ (MPa)	UTS (MPa)	ε_f (%)
	Before %	After %	E_o	Average			
0	10.4	10.4	646	636±1.9	2.1	2.8	1.9
t_1	9.8	10.4	680	642±12	2.5	3.1	1.5
t_2	9.2	11.6	1280	1066±82	2.4	2.4	0.45
t_3	9.2	13.9	1385	922±219	1.0	1.1	0.40

The increase in foam properties is attributed to the added ceramic surface layers, which are known to have high modulus (as result of increased content of α-Al_2O_3 phase [7, 116]), and very high interfacial bond strength with the bulk metal (as result of coating growth mechanisms [7, 103]). It is also expected that the hardness of these coating layers will be high, which will have implications for the strength, as examined later.

In structural engineering design, materials with high stiffness and low weight would be attractive for many applications. This means that the weight-specific stiffness is of great interest, which can be calculated by the stiffness divided by the density. The exact criteria vary depending on the coating condition. The weight-specific stiffness can be classified into axial stiffness (E/ρ), bending stiffness ($E^{0.5}/\rho$) or ($E^{0.33}/\rho$) for beam and panel stiffness respectively [12]. It has been proposed that metal foam possesses high values of these properties, and boosting these further will open up more applications in different fields (e.g. as core material for larger sandwich panels or structural material for larger roofing areas). As observed from the results in figure 6.3, which plots the stiffness of all types of foams against the density, it is clearly

seen that coatings can increase the foams axial stiffness, with the highest increase obtained by treatment t_2 with a value higher than 4 GPa Kg^{-1} m^{-3} compared to a value of 2.2 GPa Kg^{-1} m^{-3} when uncoated.
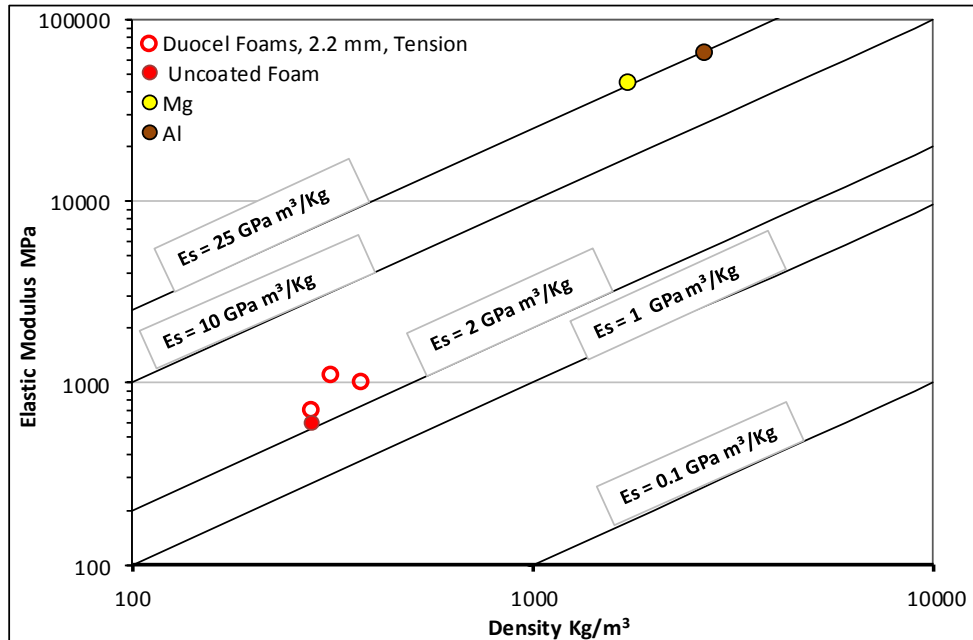
Figure 6.3 - Log–log plot of initial specific stiffness measured for different foam types with different coating treatments against density (E/ρ). Data for specific stiffness for Mg and Al are also included to indicate the relative boost in foams stiffness after coatings.

These values, however, are still lower than some other conventional light metals in dense form, such as Mg and Al, as observed in figure 6.3.

For bending stiffness properties, metal foams usually do better than conventional metals [12]. For instance, metal foams in this work (coated and uncoated) have increased higher values of beam stiffness ($E^{0.5}/\rho$). The highest value obtained was with foams with treatment t_2 of around 0.11 GPa$^{0.5}$ Kg^{-1} m^{-3}), which higher than Al (value of 0.097 GPa$^{0.5}$ Kg^{-1} m^{-3} but little smaller than Mg ~ 0.12 GPa$^{0.5}$ Kg^{-1} m^{-3} For panel bending stiffness ($E^{0.33}/\rho$) property index, foams of the present study have exceeded the dense metals mentioned above, with highest value found with foam with treatment t_2 of around ~ 0.33 GPa$^{0.33}$ Kg^{-1} m^{-3}.

6.1.2. Effect of Coating Damage

It can be clearly seen that the application of PEO coatings to low density aluminium foams can increase their stiffness, but it should be noted that the moduli measured for each coated foam sample undergo a noticeable reduction with strain, most obvious with the thickest coating produced with treatment t_3 (thickness of 52.3µm). It is already established that during PEO processing of aluminium foams, a large fraction of metal, as high as 90 %, may be converted into ceramic coating [96]; this means that the volume of core metal will eventually decrease, and the overall behaviour of the material will be increasingly brittle. The reduction in stiffness with strain may therefore be attributed to internal damage accumulation within the coating itself, similar to behaviour observed in Al -12Si foams [73]. In these foams, the early fracture of brittle Si second phase led to damage accumulation and low failure strains. In the present work, the tensile failure strains of foams with coating thickness >30 µm were 75% lower than that of uncoated foams, likely to be due to damage accumulated within the coating in the initial strain. According to [73], the quantification of the internal damage can be estimated by calculating the reduction of foams' elastic modulus with strain, normalised by the stiffness of undeformed foam E_0 (the initial elastic modulus, see table 6.1). This is characterized by the damage factor, α, which can be obtained from:

$$\alpha = \frac{-1}{E_0} \frac{dE}{d\varepsilon} \qquad\qquad (6.1)$$

The change in strain dε is calculated between ε = 0 and ε at peak stress for the load-unload cycles used to obtain E. It can be seen from figure 6.4 that the reduction in stiffness due to damage is much greater for foams with thicker coatings (32 and 52.3 µm) formed under t_2 and t_3 treatments, as compared to the uncoated foam and the foam with the thin coating (10.8 µm) produced from treatment t_1. This indicates that as coating becomes thicker, the effect of damage within the coating becomes stronger in controlling the overall foam behaviour, despite the initial increase in stiffness. Thicker PEO coatings tend to develop greater defect density (micro cracks and pores), which would lead to a higher damage rate.
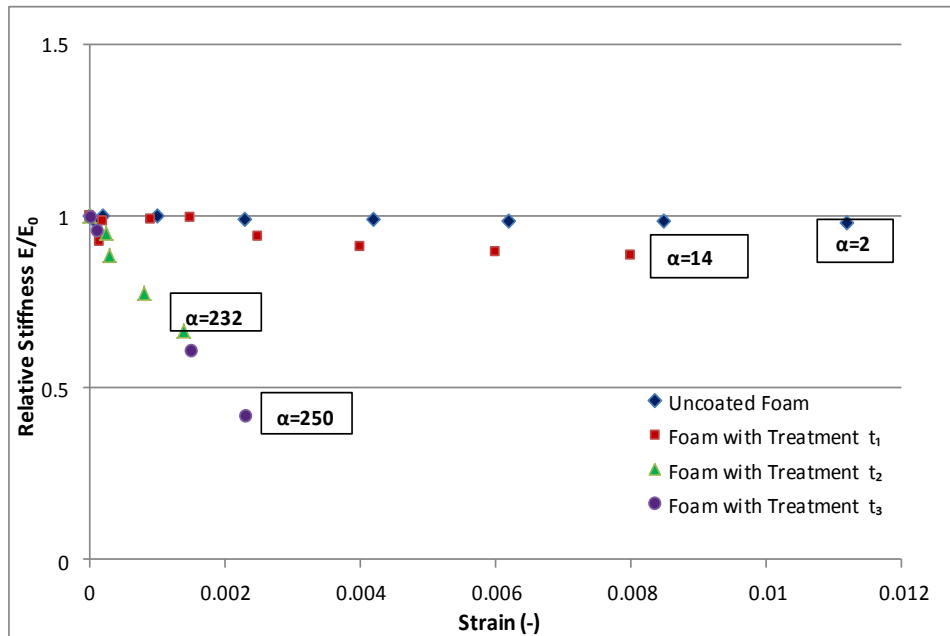
Figure 6.4 - Evolution of elastic modulus during tensile deformation for uncoated and PEO-coated Duocel foams tested in tension. The values of damage factor α were calculated using Eq 6.1.

These values of damage factor α are very high. However, values calculated for the uncoated and foam coated with treatment t_1 in this work (values of 2 and 14 respectively) are comparable to the values found in ref [73], where an average value of $\alpha = 1.3 \pm 0.6$ for pure aluminium foam (showing completely ductile behaviour) and a value of $\alpha = 11.2 \pm 1$ found for Al-12Si foams, which has a small amount of brittle phase. The small differences in such a comparison maybe expected giving that the materials in both cases differ to some extent, but it can be noted that there may be a limit (e.g. in volume or weight of addition) where the effects of inclusions or an addition of stiffer material to another may become substantial. Such effects may become less significant with further addition of inclusions or different materials, with examples seen in the work by Huang and Gibson 1993 [91], where an effective addition of 8 % hollow glass spheres in a polyester resin matrix (composite foam) resulted in improved mechanical properties, and other work by Tonyan and Gibson [133] also reported effective addition of 20 – 50 % volume fraction of polystyrene spheres for strengthening of cement foams.

Furthermore, despite the reduction, strains to failure for different foams in the present study are still within the range of the relatively low tensile failure strains set out for

aluminium foams (typically within the range of 0.2 – 2 % [12]), from 0.002 up to 0.02, as seen in figure 6.4.

6.2. Effect of PEO on Foam Plastic Properties

From the literature on composite materials, it would be expected that the addition of different materials to aluminium foam would also affect the plastic yield and flow behaviour, so these effects are described here.

6.2.1. Effect on Foam Yield Stress

Example stress-strain curves for replicated and Duocel samples with different coating treatments are given in Figure 6.5, and Table 6.2 shows the mean measured values of the yield stresses, the failure strains in tension along with the apparent density changes of the samples after coating. The data show several interesting trends. For instance, the yield strength of the replicated foams may be significantly increased even with the thinnest coating applied in treatment t_1, qualitatively consistent with the results reported for other types of coatings on other open cell aluminium foams [1, 4, 83].

The properties then continue to increase with the thicker coating resulting from treatment t_2, but no increase is detected for treatment t_3 (80 minute processing time). Indeed, there may be a small decrease, but the range of values found in the results means that this cannot be conclusively stated. Direct quantitative comparison between the two foam types is not possible, due to their large density differences and corresponding differences in the properties expected, but it can clearly be seen that the same level of increase is not observed in the Duocel samples. The strength undergoes a small rise followed by a possible decrease with larger coating thicknesses.
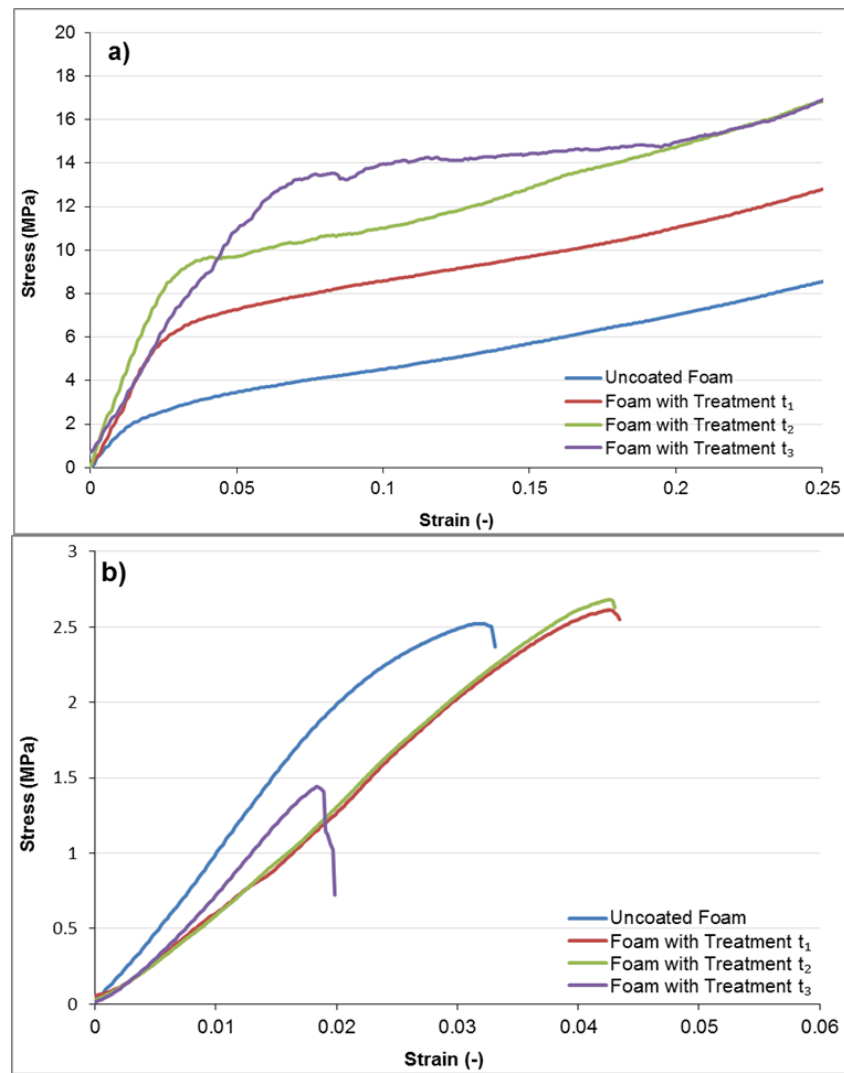
Figure 6.5 – Example stress-strain curves for samples tested in this work with a) replicated foams tested in compression and b) Duocel foams tested in tension.

Table 6.2 – Average test results for the different types of foam when different coatings applied. See the main text and Table 4.2 for details of the coating treatments used. Relative density is calculated compared to fully dense aluminium.

Foam	Treatment	Absolute Density After Coating, g cm^{-3}	Relative Density After Coating, % (%Change)		σ, MPa	ε_f, %
Replicated (1.6 mm pores)	No coating	1.1±0.05	40±2.2	(+0.0)	3.9±1.5	55±0.2
	t_1	1.2±0.02	43±0.8	(+1.2)	6.0±0.2	55±0.2
	t_2	1.4±0.1	53±4.6	(+11)	12±2.5	42±0.3
	t_3	1.6±0.02	59±0.7	(+17)	12±0.4	47±0.1
Duocel (2.1 mm pores)	No coating	0.26±0.01	9.6±0.2	(+0.0)	2.2±0.0	3.5±0.2
	t_1	0.27±0.0	10±0.2	(+0.3)	2.4±0.1	4.3±0.0
	t_2	0.28±0.01	11±0.2	(+1.0)	2.5±0.1	4.1±0.3
	t_3	0.35±0.0	13±0.1	(+3.4)	1.6±0.2	2.5±0.5
Duocel (2.5 mm pores)	No coating	0.25±0.01	9.3±0.3	(+0.0)	2.2±0.1	3.9±0.0
	t_1	0.26±0.01	9.7±0.3	(+0.5)	2.5±0.1	4.1±0.2
	t_2	0.28±0.01	10±0.1	(+1.0)	2.6±0.1	3.8±0.0
	t_3	0.33±0.01	12±0.2	(+3.0)	2.0±0.0	2.0±0.1

The reason for this can be seen by examination of a failed strut with coating produced by treatment t_3 (Figure 6.6). In this image the thickness of the coating relative to the remaining metal in the strut is clearly visible; a large proportion of the strut material has been transformed to coating, as opposed to a failed strut of similar Duocel foam with a coating produced by treatment t_1 (Figure 6.6) where coating thickness is considerably smaller. Furthermore, it is clear that, while the central metal part has undergone plastic deformation, leading to necking, the coating has fractured, although it remains well-adhered to the metal surface, even where this has deformed. Thus, as the coating is formed partly by transformation of the substrate, in the low density Duocel foams the tensile load-supporting capacity of the material is diminished much more rapidly than in the higher density replicated foams. This means that once the metal volume is reduced the overall character of the composite material will be increasingly brittle. Another observation which can be made when looking at the stress strain curves, Figure 6.5, is an indication that the variability of the deformation increases with increasing coating thickness where the curves show a general trend to be less smooth at higher coating thicknesses. This is most obvious in the case of replicated foams, which in this investigation have higher density.
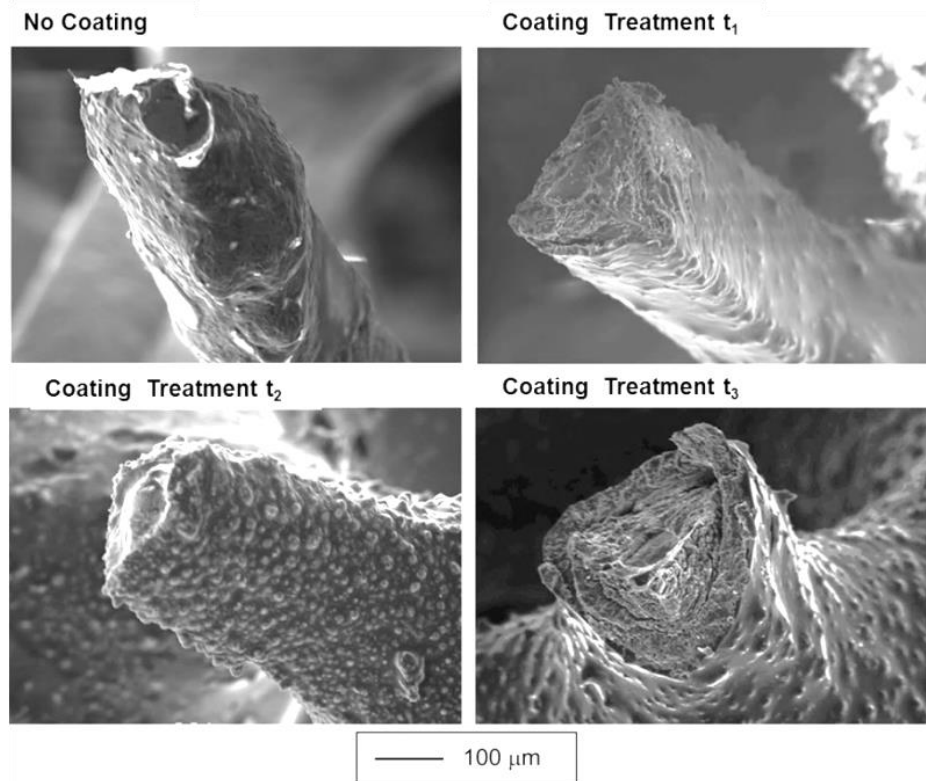
Figure 6.6 – Scanning Electron Microscope (SEM) images comparing struts from the failure surfaces of 2.5 mm pore diameter Duocel samples, with no coating and coating treatments t_1, t_2 and t_3, after tensile testing.

This is consistent with the idea that the foams show an increased proportion of ceramic character as the fraction of coating is increased. As the fracture of ceramic is defect-dependent, it would be expected to be less reproducible from sample to sample. There is less spread in the tensile data on the lower density Duocel foams, although here the effect of the thicker coatings is seen in the reduction of failure stress and strain to failure. This trend will be amplified by the observation made generally in PEO coatings that, as the thickness of the coating increases, the density of defects (microcracks, pores, etc, see figure 5.16 in chapter 5) it contains builds up, and, as failure by fast fracture is dependent on the largest flaw size, this will act to reduce the strength. This increase in defect density could arise from an increase in material disturbance during formation of thicker coatings, as reported previously [104], or as a result of a build-up in residual stresses, as seen in some electrodeposited coatings [87].

6.2.2. Effect on Foam Specific Strength

For use of porous metals in lightweight structural applications, the weight-specific strength is of great interest. As observed from the results in Table 6.2, the coating process does increase the material density, as well as the yield strength, and we must examine how the specific strength varies with coating thickness in order to demonstrate the beneficial effect of a coating on mechanical properties.
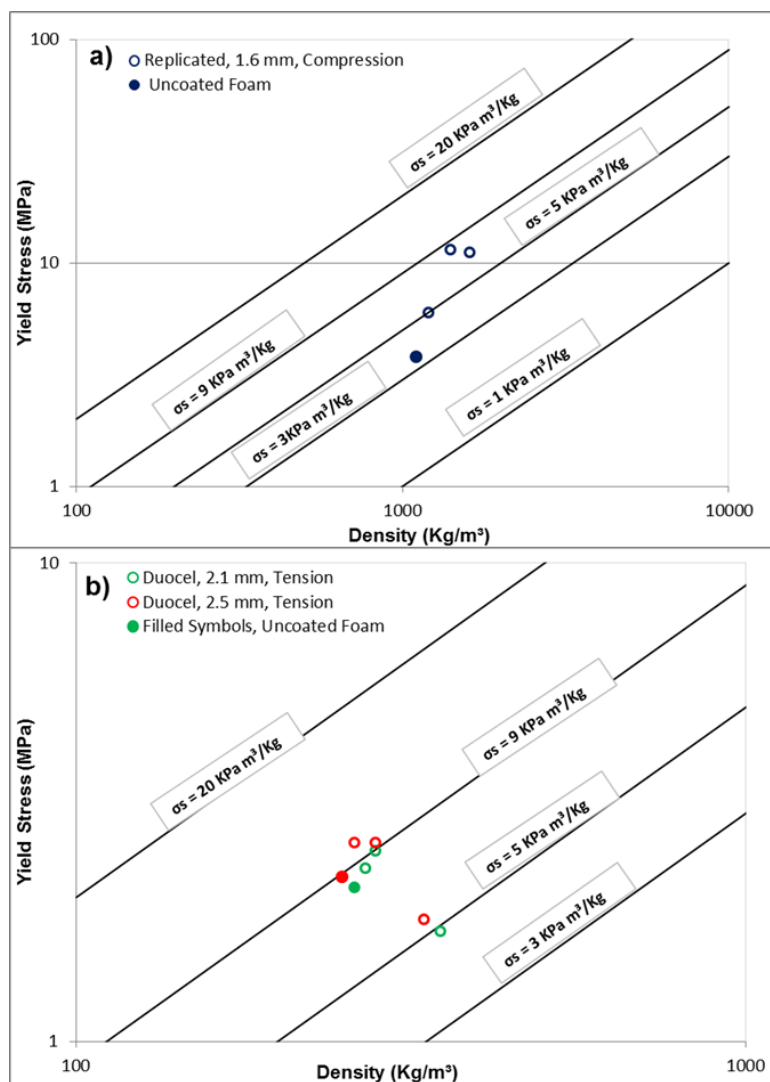
Figure 6.7 – Log-log plot of the mean yield strengths measured for a) replicated foams and b) Duocel foams with different coating treatments against mean density. Lines of equal specific strength (σ_s, yield strength divided by density) are included on the figure to indicate the relative levels of different data points.

A characteristic value for a fixed volume can be calculated by the strength divided by the density (this is similar to the procedure used to create performance indices in materials selection [134]). This is shown in Figure 6.7.a and b, which plots the mean yield strength for samples of each different treatment examined here against the mean density of that type. Also shown on the plot are guidelines of equal specific strength. From the plot it can easily be seen that for the denser replicated foams (see figure 6.7.a), tested in compression, there is a benefit from all coatings, although the highest specific strength is obtained with coating treatment t_2 (8.6 kPa m^{-3} kg^{-1}, compared to a value of 3.6 kPa m^{-3} kg^{-1} when uncoated). For the Duocel samples (see magnified figure 6.7.b), the effect is less, but for coating treatments t_1 and t_2 there is a positive effect where a specific strength of around 9.6 kPa m^{-3} kg^{-1} can be reached, from an initial value of 8.5 kPa m^{-3} kg^{-1}. Note that the uncoated Duocel foams already have a high value of specific strength. Moreover, for both pore sizes examined, coating treatment t_3 produces a lower specific strength, as it increases the density, but does not produce such significant increases in yield strength. It is interesting to note that the specific strength maxima are similar for the two different foam types tested, but given their differing structure, density and test method, this is unlikely to indicate a general law.

6.2.3. Effect on Foam Energy Absorption

The energy absorption capacity of the different foams in the present work was evaluated, and values per unit volume W_v and per unit mass W_w were obtained by integration of the areas under the stress-strain curves [135, 136] (using the Trapezoid Rule) to a strain of 0.3, with an example shown in figure 6.8. Foams in the present study show clear tendency for densification beyond strain of 0.3, and also this value was used in ref.[80] for calculating the energy absorbed by similar types of foam, as follows:

$$W_v = \int_0^{0.3} \sigma \, d\varepsilon \qquad\qquad\qquad (6.2)$$

$$W_w = \int_0^{0.3} \sigma \, d\varepsilon / \rho^* \qquad\qquad\qquad (6.3)$$

where $d\varepsilon$ is the change in strain, σ is the corresponding stress and ρ^* is the actual foam density used to calculate W_w.
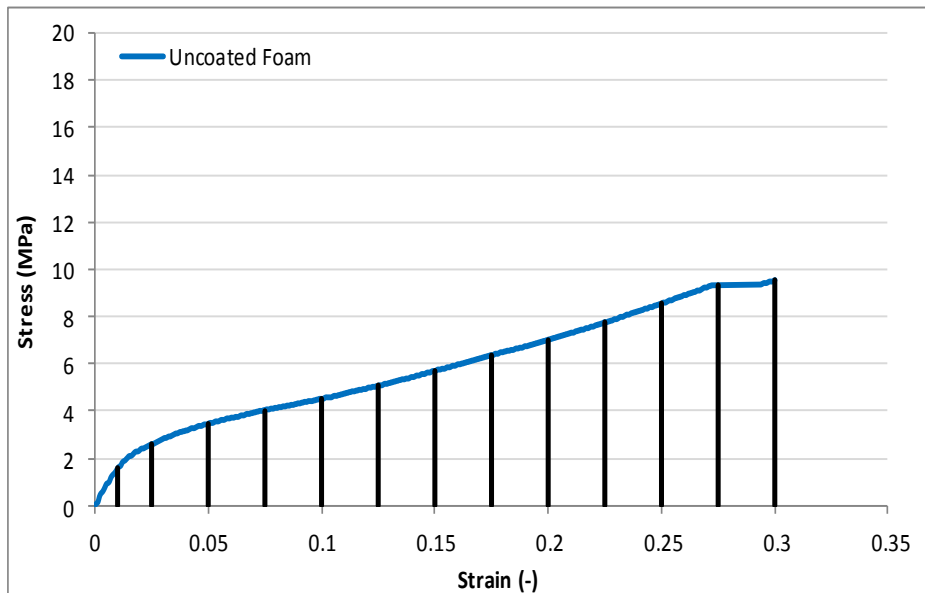
Figure 6.8 – A representative stress-stain curve for uncoated replicated foam tested in compression, showing integration of the area under the curve, using Trapezoid Rule to calculate the energy absorbed per unit volume to a strain of 0.3.

Figure 6.9 below shows the energy that is absorbed by the foams tested in this work, as function of the averaged volume coating thicknesses. Also shown in the same figure the behavior of energy absorption of theoretical foams represented by a curve, using plateau stress $\sigma_{pl/0.25}$ (taken from compressive strength at 25 % strain, as suggested by Ashby et al. [12]) and a densification strain ε_D e.g. 30%, calculated as follows:

$$W_v = \sigma_{pl}\ \varepsilon_D \qquad\qquad\qquad (6.4)$$

As expected from the large increase in strength, PEO coatings showed improved energy and specific energy absorption (calculated from Eq. 6.2 and 6.3) of the foams with different treatments, with the greatest value obtained for foams coated at t_2 condition, as seen in figure 6.9. This is because treatment t_3 brought only a minor improvement in strength, even though the average PEO coating thickness was

increased by a factor of ~ 2.5 as compared to treatment t_2, as seen in table 5.2 in chapter 5.
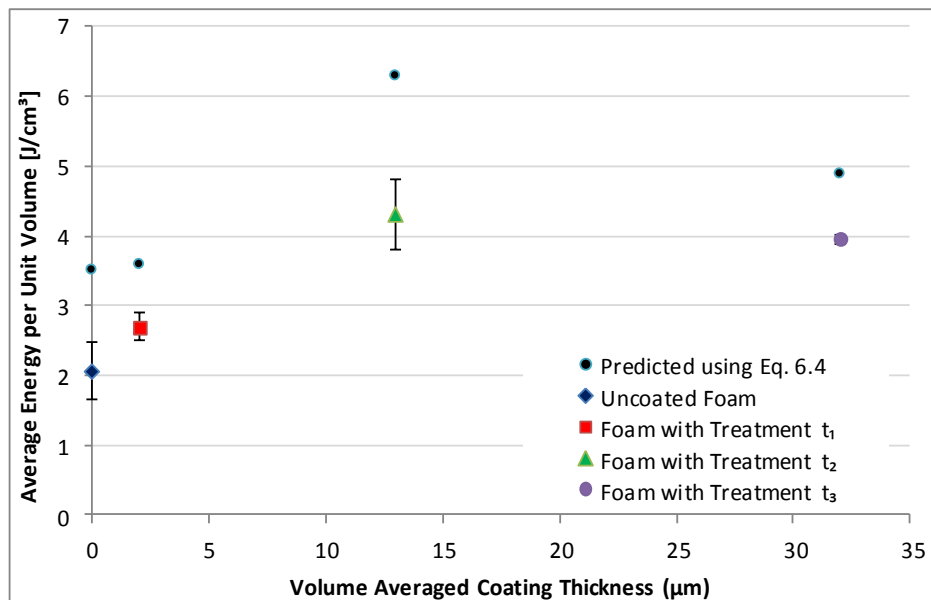
Figure 6.9 - Energy absorbed per unit volume for different aluminium foams during compression to a strain of 0.3. The error bars are standard deviations obtained from double tests. Prediction is shown from a theoretical model using $\sigma_{pl/0.25}$ in Eq. 6.4.

It is seen that the simple theoretical model for the energy absorbed per unit volume of foam showed higher energy than that measured. This is simply due to the fact that using the plateau stress of $\sigma_{pl/0.25}$, when there is work hardening gives a higher values of energy absorbed. Using the plateau stress of $\sigma_{pl/0.25}$ would provide better agreement with metal foams that have long and clear plateau area of the curve (see stress-strain curve for an ideal energy absorber in figure 2.24, Chapter 2). Ashby et al. [12] used the compressive strength at 25% strain for predictions and design analysis on different types of foam (Fraunhofer, Hydro, Alulight Cymat and INCO). However, it has been shown that some metal foams show work hardening character typical of bulk metals [15], where the compressive strength increases gradually with strain with no clear plateau region. Foams in the present work show some degree of work hardening and so using integration of the area under the curve would be more suitable than using the compressive strength at 25 % strain.

Figure 6.10 below illustrates the comparison between the energy absorption capabilities of foams in the present work and of that observed elsewhere by Boonyongmaneerat et al. [1] and Xiao-Qing et al. [80]. In the case of ref.[1] energy absorbed by the low density open cell aluminium foams was increased as result of added Ni-W coatings. However, because of increased content of tungsten in the deposited coatings, which possesses a higher density, the benefits from coatings are reduced due to the large increase in coated foam densities.
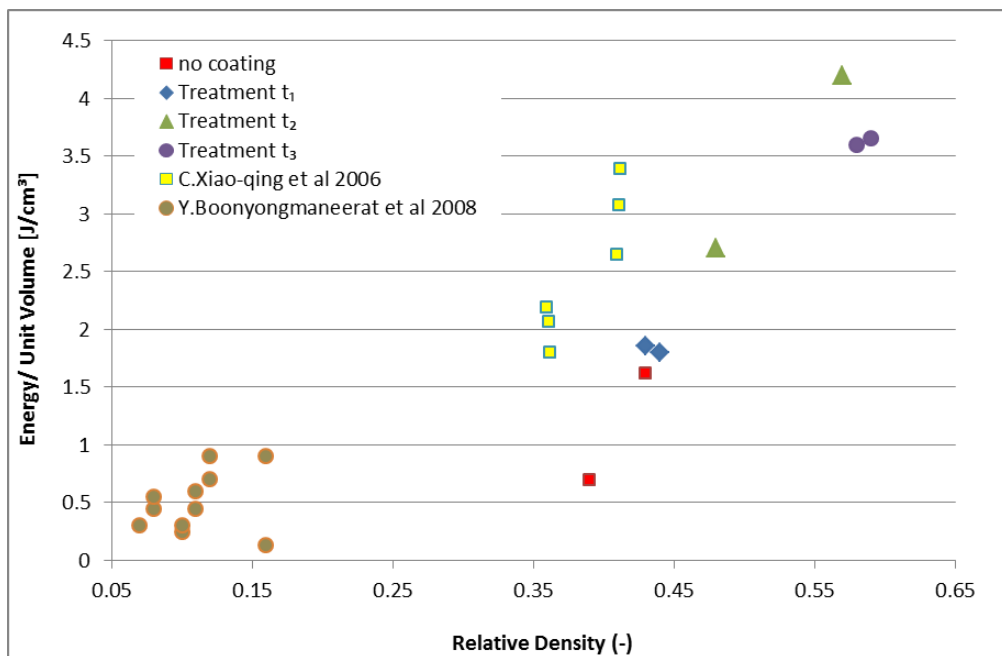
Figure 6.10 – Comparison between experimentally measured data for enegy absorbed per unit volume for different foams tested in this work and other work on similar [80] and different [1] foams.

Foams tested in ref.[80] are more comparable to foams in this study in terms of method of production and the measured foams relative density. The difference being the aluminium alloy from which the foams are made. Aluminium alloy of Al-1.31 Mg-0.25Ca-0.21Ni was used for the fabrication of foams in the work by Xiao-ging et al. [80], whereas 99.8% pure Al was used in this work. Some increase in energy absorption can be observed with the present coated foams with highest values obtained with treatment t_2 condition, averaging at 4.3±0.5 J cm^{-3} for energy absorbed per unit volume, compared to a value for uncoated foam ~ 2.75±0.25 J cm^{-3}, and a value of 3.1±0.4 J cm^{-3} g^{-1} for specific energy absorbed per unit mass calculated from Eq. 6.3.

6.3. Prediction of Coated Foam Properties

In order to explore the beneficial effects of PEO coatings on Duocel foams elastic behaviour, different analytical models have been examined. The theoretical principles of these models are explained in detail in Chapter 2, section 2.6. These models range from some that are easily-derived such as that proposed by Gibson and Ashby, to more complicated modified models which consider the elastic response of 2 phase porous structures. The modifications proposed in the present study have been made to the model of Bouwhuis et al. [83], in which we show the effects of assuming different cross sectional shapes of beam surrounded with coating layers of different thicknesses. We also show that it is possible to modify the model of randomly bonded fibre array developed by Markaki and Clyne [90], by modifying the beam stiffness, EI. Full detail for all of these modifications and their impact is provided in the following sub-sections. The reason for using the two phase porous structure models (models of Bouwhuis et al. [83] and Huang and Gibson [91]) is the fact that they are based on the principle of load partitioning between the phases, so there is the implicit assumption that the coating acts by supporting load itself, and not by affecting the ability of the metal to do so (for example, by affecting image forces felt by dislocations near the surface). For coatings as thick as those examined here, this is the likely mode of action.

6.3.1. Gibson and Ashby Model

As discussed in chapter 2, this model has been found to provide good agreement with experimental data for many open cell metal foams (e.g. [9, 48, 88]), with foam elastic modulus being dependent on square of its relative density and Young's modulus of the parent metal, as follows:

$$\frac{E^*}{E_s} = C_1 \left(\frac{\rho^*}{\rho_s} \right)^2 \qquad\qquad (6.5)$$

The data in the present study are well represented by the model, especially for uncoated foam with relative density of 10.4% with predicted E = 750 MPa. An initial Young's modulus E_0 for the uncoated foam was found to be = 646 MPa, this corresponds to a constant $C_1 = 0.86$, which is well within the range of 0.1 − 4

experimentally found for open cell metal foams generally [12]. Furthermore, it can be noted that the optimum benefits brought by PEO coatings can be clearly seen with the foam with treatment t_2, which has surpassed the expected properties when $C_1=$ 0.86 or 1, as illustrated in figure 6.11 below.
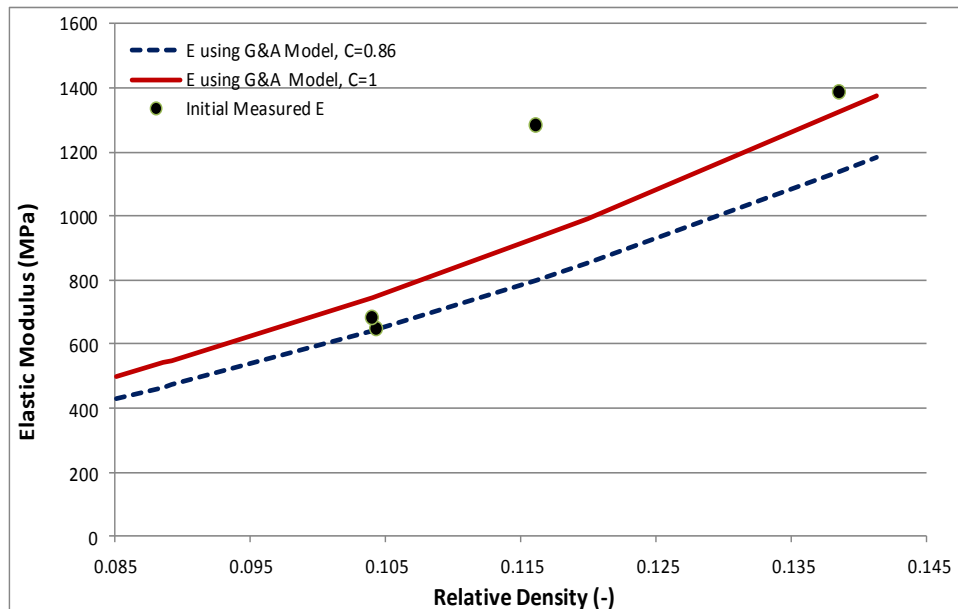
Figure 6.11 - Plots of experimental and predicted foam Young's modulus for uncoated and PEO coated Duocel foams against relative density. Predictions are shown for the Gibson-Ashby (G&A) simple model, using constant C_1=0.86 and 1.

6.3.2. Hollow Spheres in a Matrix

Detail and illustration of this model are presented in chapter 2 (section 2.6.4 and figure 2.37). In this model, it has been suggested that sandwich-like structures can be made between the walls of the spheres and the metal within the syntactic foam (the walls of any two spheres and the metal between them), as seen in figure 2.37. We now examine whether such a strengthening mechanism could be seen for the coated foam in the present work, where the metal struts would be supported by the PEO coatings formed (see for example the SEM images in figure 5.14 and 5.16 in chapter 5), making them ideal structures for resisting bending.

The elastic modulus of these foams, E_f, is determined using:

$$E_f = \frac{9K_f}{1 + \dfrac{3K_f}{G_f}}$$ (6.6)

where the foam bulk and shear moduli, K_f and G_f are given by:

$$\frac{K_f}{K_0} = \frac{1}{1 - 6\left(\dfrac{1-v_0}{1-2v_0}\right)C'V_{sphere}}$$ (6.7)

$$\frac{G_f}{G_0} = \frac{1}{1 + 24(1-v_0)C''V_{sphere}}$$ (6.8)

where the subscript 0 relates to bulk properties, v is the Poisson's ratio, V_{sphere} is the volume fraction of spheres and C' and C'' are dimensionless parameters dependant on the elastic properties and relative geometry of the spheres (radius, wall thickness, etc) which are evaluated numerically by Huang and Gibson to yield values given in ref [91].

6.3.3. Beam Stiffness of Elements in a Regular Structure

As discussed in previously in section 2.6.2, chapter 2, the stiffness of each element or beam makes up the stiffness of the entire regular celled structure (the regular structure of beams shown in figure 6.12 below). In this case, the foam stiffness can be obtained by calculating the beam stiffness EI, provided that constant C and L, the cell diameter, are known, as following:

$$E_f = \frac{CEI}{L^4}$$ (6.9)

Bouwhuis et al. [8] used this type of model and introduce different parameter to describe the end condition of the beam, B = 192 [12, 83], as follows:

$$E_{coating}^{foam} = \alpha \frac{BEI}{2L^4}$$ (6.10)

where α is a knockdown factor which has been found to be 0.41 for low density Duocel foam [83]. In their study, this equation was used to predict the increase in the foam stiffness ΔE after coating with nanocrystalline Ni of different thicknesses. This was achieved by individually calculating the stiffness of the hollow-tube coating foam and subtracting the predicted values from that of core metal foam, using the same equation 6.12 in both cases (see full explanations and equations used to obtain ΔE and I, in section 2.6.2, chapter 2).

In the present study, we propose that as the coating will modify the stiffness of these elements (beams), the effect can be relatively easily incorporated into the predictions of the model once the appropriate geometry is decided on (circular, square and triangular beam cross-sectional shapes are considered), simply by changing the calculation of the beam stiffness, EI. This modification shows that it is possible to predict the stiffness of the entire composite foam.
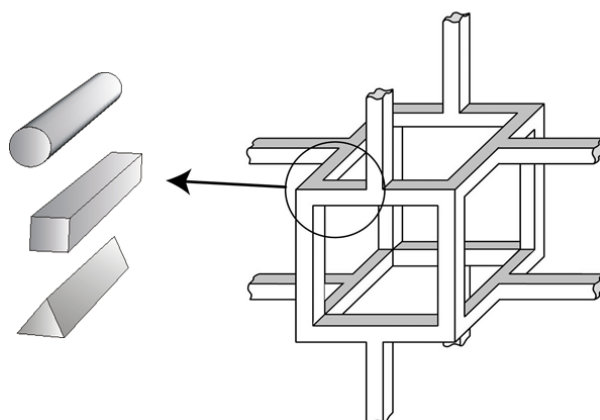
Figure 6.12 – The simplified structure assumed by the Gibson and Ashby model and the circular, square and triangular shape proposed for the strut cross-section of the structure, which are expected to change the resistance of the beams to bending.

Different simple strut shapes, seen in figure 6.12, may be assumed in calculating the beam stiffness. Bouwhuis et al. [83] assume struts to be uniform cylinders coated with a uniform tubular sleeve. In this case the expression for EI from standard beam theory is:

$$EI = E_0 \frac{\pi}{64} d^4 + E_{Coating} \frac{\pi}{64} \left(\left(d + 2t_{Coating} \right)^4 - d^4 \right) \qquad (6.11)$$

where d is the strut diameter, $t_{Coating}$ is the coating thickness and E_0 and $E_{Coating}$ are the bulk material and coating modulus respectively. Similar expressions can be derived for beams with many different cross sections, including those that form squares:

$$EI = E_0 \frac{h^4}{12} + E_{Coating} \frac{h}{12} \left(\left(h + 2t_{Coating} \right)^3 - h^3 \right) \qquad (6.12)$$

and cross sections that form equilateral triangles:

$$EI = E_0 \frac{a^4}{32\sqrt{3}} + E_{Coating} \frac{1}{32\sqrt{3}} \left(\left(a + 2\sqrt{3}t_{Coating} \right)^4 - a^4 \right) \qquad (6.13)$$

where h is the thickness of the square beam, a is the side length of the triangle, and all other terms are as defined previously.

6.3.4. Beam Stiffness of Elements in a Random Structure

As discussed in chapter 2, this model was developed by Markaki and Clyne [90], to measure the stiffness of randomly bonded fibres or beams, seen figure 2.36. Following their derivation produces the equation below for the stiffness of the whole array in terms of the beam stiffness of the individual fibre elements:

$$E_f = \frac{18 V_f EI}{\pi d^2 L^2} \qquad (6.14)$$

where V_f is the volume fraction solid, and other terms are as previously defined. This is analogous to Eqn (6.10) for the Gibson-Ashby structure, and equations such as (6.11), (6.12) and (6.13) may be used to determine the beam stiffness of coated elements of different geometries.

6.3.5. Discussion of Models' Predictions

The predictions of the models introduced above can be confronted with the experimental data generated for the Duocel foams tested in this work (see Table 6.3 and figures 6.13 and 6.14). The model based on hollow spheres in a matrix can be rapidly dismissed, giving as it does predictions for the stiffness of foams with three different thicknesses of coatings generated here (11, 32.2 and 52.2 μm) as 28, 30 and 32.2 GPa (compared to actual values in the range 680 - 1385 MPa, Table 6.1). This is unsurprising as this model is developed for dilute systems (referring to the pores), and the volume fraction porosity in these samples is 90 %, much greater than the 8%, which has been found to be effective for in other studies [91].

To compare data with the other models, it must be decided how to represent the fact that there is a continually varying coating thickness in the PEO coated foams (see, for example figure 5.12, chapter 5). Similar variation was noted in the work of Bouwhuis et al. [83], who, on finding that the variation was most apparent in the direction of testing in their compression tests, used an inverse rule of mixtures approach to combine the predicted properties of different zones. In this study, all predictions were based on using a volume averaged coating thickness generated by measuring coating thicknesses from one sample free surface to the other, across the sample thickness. This was repeated several times across the width of the sample, and the same procedure was carried out for each treatment condition. Using this method, the predictions of each of the models are calculated and results are shown in Table 6.3 and figures 6.13, 6.14 with the experimental data E_o extrapolated for the different Duocel foams (coated and uncoated). In these calculations two values of coating modulus are used. Dense, bulk alumina has been found to have E = 370 GPa [104], but PEO coatings have been investigated by Curran and Clyne [104], using a beam bending method, who found E for PEO coating = 10 - 40 GPa (the difference being attributed to the presence of defects, such as those shown in Figure 5.18, Chapter 5). Nanoindentation tests performed on PEO coating showed a range of values E = 200 - 400 GPa [104] and values between 120 - 400 GPa in Khan et al. [111]. However, it must be noted that during the nanoindentation, the coating is mainly subjected to compressive loading such that the coating material under the indenter tip is compressed, and the existing microcracks is less likely to be effective, since these microcracks would be closed. Also, the nanoindents are highly localised and therefore may miss cracks and porosity, giving an overestimate of the true

stiffness. This may suggest that the coating stiffness may be lower globally [104]. Investigations of nanoindentation of PEO coating by these studies [104, 111] revealed that the existence of different phases such as crystalline alumina (α- and γ-Al_2O_3), amorphous phases and structural defects causes such variance in stiffness and hardness. For this reason the calculations have been performed with $E_{Coating}$ = 370 and 40 GPa to capture the full range of behaviour, and the results are shown in figure 6.13, 6.14 respectively and Table 6.3. The Young's modulus of aluminium alloy, AA6101, is taken to be 69.6 GPa [137], and experimentally measured values of pore size (2.1 mm) and mean strut diameter (0.32 mm) are used.

Looking at Table 6.3, even though it is clear that the predictions shown are lower than the experimentally measured values, all models show similar trends for a continuous increase in Young's modulus with coating thickness. The random Fibre Array model, with all different shapes of cross section beams, gives lower predictions than the Gibson-Ashby model in all cases. Moreover, it can be seen that the models with all different cross-section struts underestimate the true values by a considerable degree when using E coating = 40GPa. However, the predictions based on coating modulus E = 370 GPa are also lower but closer to the true values, as shown in figure 6.13.
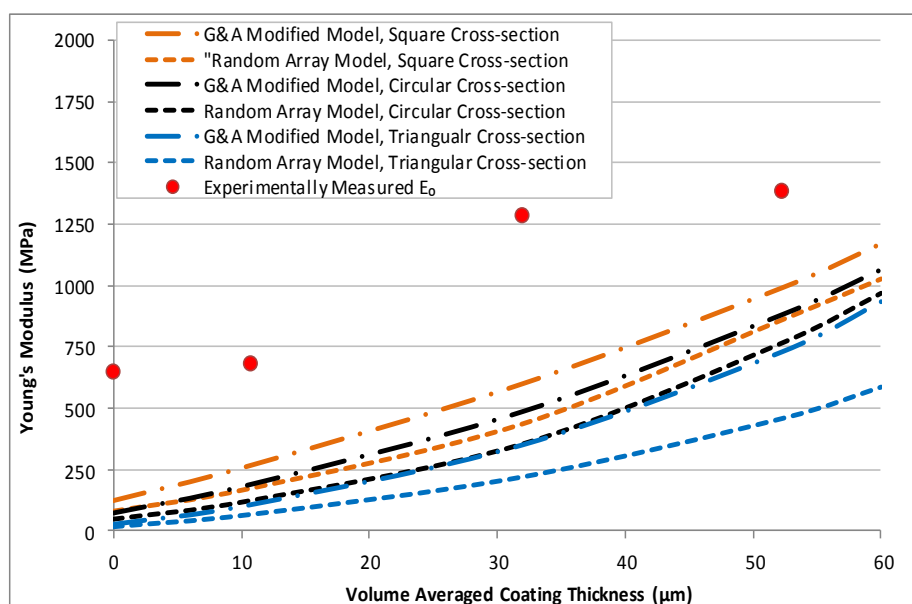
Figure 6.13 – Plot of experimental and predicted foam Young's modulus using E coating of 370 GPa against volume averaged coating. Predictions are shown for the Gibson-Ashby (G&A) and Random Fibre Array models, with different shaped beam cross sections.

Table 6.3 – The experimental results for Young's modulus of Duocel aluminium foams compared with the predictions of the Gibson-Ashby and the random fibre array models with beam stiffness obtained from different cross sectional shapes of strut and coating.

Treatment			None	t_1	t_2	t_3
Coating Thickness (µm)			0	11	32	52.3
Experimental E_o (MPa)			646	680	1280	1385
Predicted E_f (MPa)	$E_{Coating} =$ 370 GPa	Gibson-Ashby (square beam)	122	266	598	990
		Random Array (square beam)	80	174	436	860
		Gibson-Ashby (Circular beam)	72	190	486	881
		Random array (Circular beam)	47	123	354	766
		Gibson-Ashby (triangular beam)	26	107	350	730
		Random Array (triangular beam)	17	67	220	458
	$E_{Coating} =$ 40 GPa	Gibson-Ashby (square beam)	122	138	174	216
		Random Array (sguare beam)	80	90	126	188
		Gibson-Ashby (Circular beam)	72	85	116	159
		Random array (Circular beam)	47	55	84	138
		Gibson-Ashby (triangular beam)	26	35	61	103
		Random Array (triangular beam)	17	23	45	90

It is also seen that the triangular cross section struts produce lower values than cylindrical struts, with square cross sections being the highest. This is evidently due to increase in cross-section area and hence the corresponding increase in the moment of inertia, but it is also interesting to note that beyond this, struts with a non-circular cross section can be more effective for a given weight in resisting bending along certain directions, an effect that has been observed in replicated foams previously [138].

It is also clear that the model of modified Gibson-Ashby gives values that are higher than those given by the model of random array. These predictions can be further looked at, especially considering that the model incorporates the knock-down factor α = 0.41, a constant which account for foams structural defects. This is equivalent to the constant C used in other Gibson-Ashby equations and can vary depending on the foam manufacturing route hence the precise foam structures. As pointed earlier (section 2.6, chapter 2), the constant is often assumed to be 1, as this value has been previously found to be experimentally suitable for general data on open cell metal and polymer foams [9, 10, 55, 56, 89. In order to explore the trends more, particularly the influence of the knock-down factor, using α = 1, the experimental data are compared to the predictions of G&A model using α = 0.41 and 1, with beam stiffness calculated from different cross sectional shapes of strut, using E_c = 370 GPa as shown in the figure 6.14.
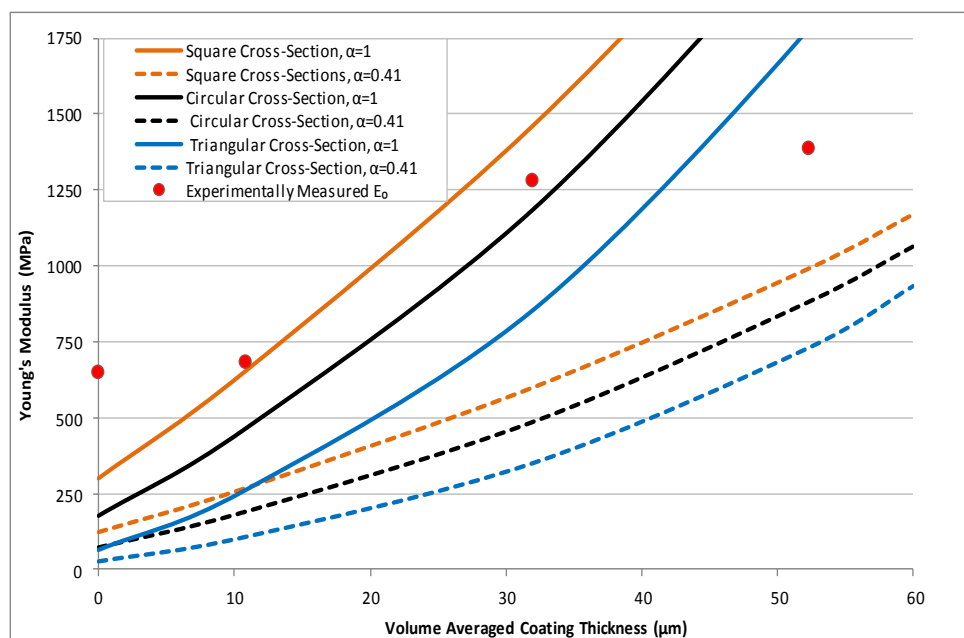
Figure 6.14 – Plot of experimental and predicted foam Young's modulus using the Gibson-Ashby (G&A) model with α = 0.41 and 1, and E coating of 370 GPa against volume averaged coating. Predictions are shown for different shaped beam cross sections.

Looking at the predicted values, the effect of the constant α is clearly seen in the sharp increase in coated foams stiffness, as compared with the uncoated foam. Again, the square and circular cross-section beams both give values that can be

compared with the data for coated foams, but both underestimate the true value of uncoated foams.

Due to the difference in coating thicknesses applied, the non-uniformity of coating distribution within the foams and change coating properties at different thicknesses, the increase in the experimental data in the present work do not follow a specific trend. This perhaps makes the predictions more complicated.

Furthermore, more predications may be required to examine the usefulness of the modified models proposed in this work for predicting the Young's modulus of coated foams. It would be expected that both models with different cross-sectional shapes would give similar trend for similar type of foams with different coating thicknesses, or coatings of a different type. This can be confirmed by making a simple comparison with the data reported by Bouwhuis et al. [83]. In their experiments, aluminium foams with lower density (V_f = 0.072) were coated with nanocrystalline nickel ($E_{Coating}$ = 207 GPa). They also used values of strut thickness of d = 0.2 mm and cell size of L = 1.27 mm. Similar to here, they found a variation in coating thickness throughout the samples, though their experiments showed that the behaviour was dominated by the region with the thinnest coating [83] (a reasonable conclusion as in their experiments the regions of different coating thickness were effectively loaded in series). To calculate the beam stiffness as in the present work, cylindrical and square strut cross sections were used in both models, which are seen as being most appropriate shapes. Figure 6.15, therefore shows the data obtained by Bouwhuis et al. for foam Young's modulus plotted against the thickness of the coating in the mid region of their specimen, compared with the predictions of Eqn (6.14) using the data above, and Eqn (6.10) using the value of α = 0.41 determined in the original work [83]. In both cases Eqn (6.11) and (6.12) are used to determine the beam stiffness. It is seen that using the circular or square cross section beam in the Gibson and Ashby model give the best agreement with the data (the results of the predicted modulus are within the upper and lower bound of the foams Young's moduli obtained from the experiments). Moreover, the fit with the random array model, when using the circular or square cross section shape to estimate the beam stiffness, underestimates the actual experimental values, which could be due to the presence of thicker coating in the outer regions of foam, or that the configuration of the model does not approximate well to the foam structure.
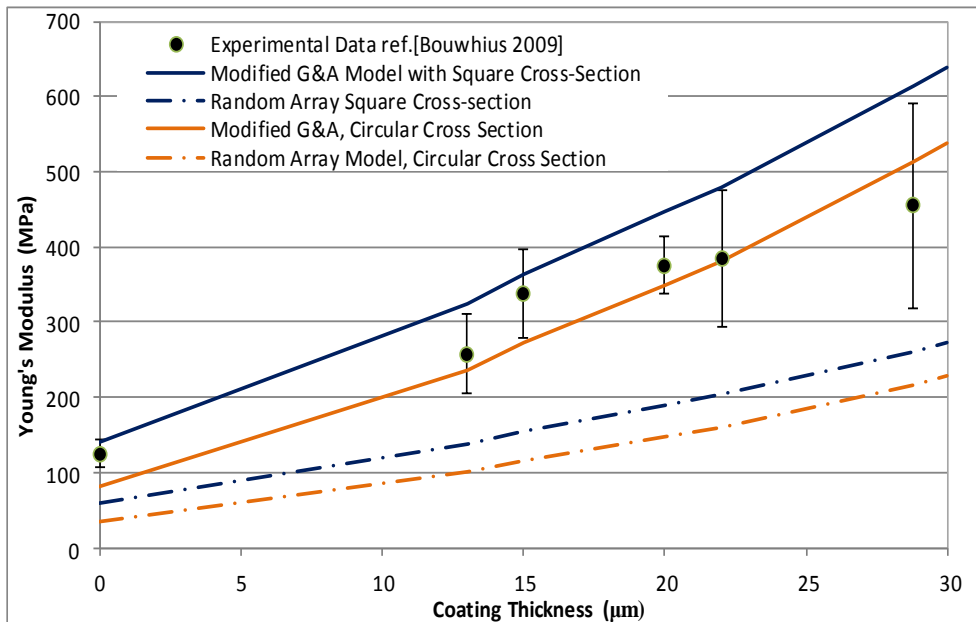
Figure 6.15 – The Young's modulus versus coating thickness data of Bouwhuis et al. [83] for aluminium foams coated with nanocrystalline nickel, and the predictions of the random array and Gibson-Ashby based models given here, for square cross section beams.

It is interesting to note that the Gibson and Ashby model with circular beam cross section provides a reasonable agreement with the experimental results, despite the small underestimation for uncoated foam modulus. When using square beam cross section though, the model predicts well the uncoated foam modulus with slight overestimation for coated foams in some instances (e.g. at 13 and 20 µm coating thickness). This can be linked to the fact that the struts approximate well to cylinders of circular cross-section [83].

Overall, it can be seen that incorporating coatings at different thicknesses on the surface of circular and square cross sectional shape beam can be used for predicting the Young's modulus of low density foams with coatings. We have seen that models based in Gibson and Ashby's regular structure perform better when using α = 1 for PEO coated foams, while using α = 0.41 for both circular and square cross-section beam with give reasonable predictions with the experimental data for Ni-coated foams. The modified random fibre array model has shown to underestimate the experimental data, which can be due to the difference between the model and foam structure. Furthermore, using coating modulus E = 370 GPa has been shown to provide better estimates to the E_o values found for PEO coated foams.

Nonetheless, it must be noted that the stiffness of PEO coating in this work could be lower than the models suggest, as result of the cracks and pores that exist within it, and so values predicted by the models must remain approximations. In fact, it may be that the increase in the foam stiffness is mostly due to the increase in the cross sectional area of the foam struts after the coating is applied, assuming that the modulus of the coating was comparable to that of the struts. As pointed out earlier, the models used here describe the stiffness of the whole porous structure based on the stiffness of the individual elements EI, where E is the elastic modulus and I is the area moment of inertia of the beam cross-section. The model accounts for both the increase in area and the change of material parameters, but as there are two effects occurring; it could be that the effects of each of these changes should be apportioned differently. Even if the coating does not have an elevated modulus, any increase in the cross-sectional area will have major effect on increasing the moment of inertia, I, and hence the bending stiffness (through the relation $I \propto d^4$). Measurements of strut diameters made on different struts from the untreated and foams coated at t_1, t_2 and t_3 conditions showed that there is a small increase in the average strut diameters after coating, averaging at 320±44, 333±37, 350±63 and 355±53 µm respectively. Assuming that the coating layer is dense, such an increase will increase the moment of inertia, I, of the individual struts. Based on these measurements of mean strut diameters, an increase by 17, 43 and 51 % in the area moment of inertia would be estimated respectively for each of the coating conditions. The increases in foam stiffness, E_o, after each coating condition are 5, 98 and 114 % respectively (see table 6.1 for the stiffness of the untreated and foams coated at t_1, t_2 and t_3 conditions).

It can be seen that the increase in cross-sectional area of the individual struts can have an effect on increasing the foams stiffness, however there is not a directly proportional ratio, indicating that it cannot be the only effect. Notably, the increase in the thickest coating case is more significant by a large factor than that predicted for increase in diameter alone. It may also be that a coating with elevated stiffness properties and the increase in cross-sectional area of the coated foam struts both contribute to the improvements seen in the foams elastic, and possibly plastic, properties, especially given that the percentage increase in foams stiffness is shown to be higher than that presented by the increase in the area moment of inertia, I. While it must be acknowledged that the quantitative fit to the experimental data can be sensitive to a number of parameters for which global average values have been

used, such as the cell size and strut width, the models are illustrative in examining the trends.

Chapter 7: Optimization of PEO Process for Metallic Foams

This part of the project focuses mainly on optimizing PEO processes for open cell aluminium foams, based on the initial PEO processing treatment parameters such as bath composition, temperature, and electrical regime (pulsed bipolar). All samples used in this part of the present work have been made using the newly developed infiltration rig shown in figure 4.4, section 4.2.2 in chapter 4. The optimization process begins with selecting the best treatment conditions from the initial work in this research, t_2 condition (see table 4.3), which have brought about the best properties improvements in those foams. This treatment condition was selected for further improvement by carefully and systematically adopting changes in pulse frequencies (f_1, f_2, f_3, and f_4 in stage 2 conditions) and current waveforms (p_1, p_2, p_3, p_4 and p_5 in stage 3 conditions), as detailed in table 4.3, in the experimental procedures section 4.3, chapter 4. In stage 4 conditions, further experiments were carried out on coatings produced under t_2 f_2 p_4 conditions to investigate the effects of different processing times (t_3, t_4 and t_5) on coating deposition rate, microstructure and the effect on foams mechanical properties. Although the selected coating for this final processing condition delivered the smallest deposition rate and coating thickness, it was observed to contain least coating porosity, as compared to the other coatings produced under stage 3 conditions, as will be shown in the following sections.

7.1. Effect of Different Pulse Frequencies

In this second stage of the present work we optimise one PEO coating procedure in which a range of low and high-frequency pulsed bipolar currents were adopted to treat replicated open cell aluminium foams. We use these materials as a basis for understanding the structure of coated foams and their mechanical behaviour.

As detailed in chapter 4, section 4.3, 4 different frequencies were chosen for optimisation; namely 50, 250, 1250 and 6250 Hz. For this part of the project, 12 foam samples produced by the newly developed infiltration rig shown in figure 4.4, in chapter 4, were used. Three samples were treated at each frequency, allowing two samples to be tested in compression and 1 sample to be used for cross-section analysis to study the coating morphology and distribution with depth. The electrolyte conductivity and pH were maintained at 8.53 mS cm^{-1} and 11.52 respectively to ensure sufficient conductance and alkalinity.

Current and voltage waveforms were recorded for each treatment type (f_1, f_2, f_3 and f_4, see table 7.1) and an example for the frequency of 50 Hz (f_1) is shown in figure 7.1, showing the main parameters that can be used to control the waveforms in the positive and negative bias. Estimation of current magnitude during pulse on time for each condition has been found to be 49 A, 56.5 A, 36.5 A and 64 A respectively. For comparison, all current and voltage waveforms for a) 50, b) 250, c) 1250 and d) 6250 Hz in PBC mode during PEO processing of the open cell aluminium foams used in this work are shown in figure 10.1 in the appendix. In all cases, rectangular pulse reverse voltage waveform was applied and 37.5 % positive duty cycle was maintained.

Table 7.1 - Different pulse frequencies used during the second stage of PEO coating processing of open cell aluminium foams. Values for different ON/OFF durations in the positive and negative bias are provided.

Optimization Stage	Processing Variables	Treatment	Variations					Invariables
First	Time		**Processing time (min)**					Frequency at 250 Hz
		t_1	20					
		t_2	40					
		t_3	80					
Second	Pulse Frequency		(Hz)	δ^+_{on} (ms)	δ^+_{off} (ms)	δ^-_{on} (ms)	δ^-_{off} (ms)	Processing time of 40 minutes, (t_2).
		f_1	50	6.5	1	10	2.5	
		f_2	250	1.3	0.2	2	0.5	
		f_3	1250	0.26	0.04	0.4	0.1	
		f_4	6250	0.052	0.008	0.08	0.02	
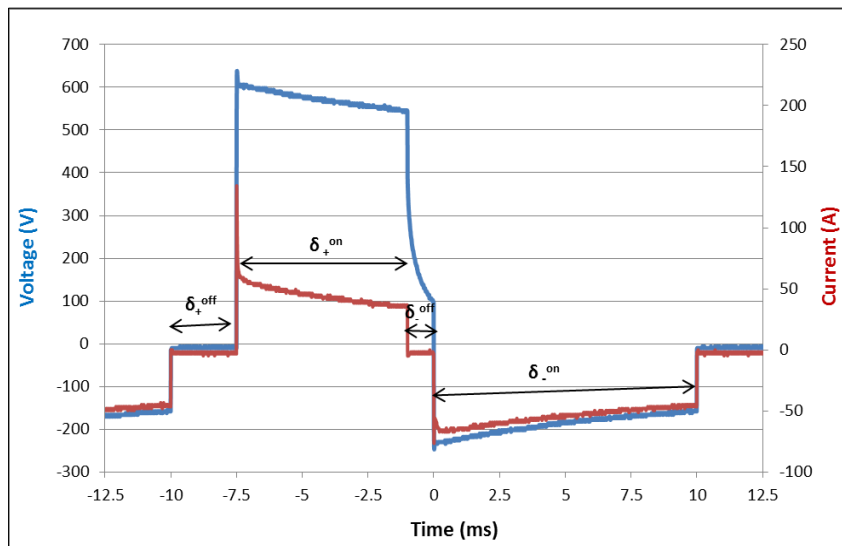
Figure 7.1 - Current and voltage waveforms for frequency of 50Hz in PBC mode during PEO processing of the replicated open cell aluminium foams. Estimation of current magnitude during pulse on time is 49 A.

Investigation of using such range of low and high frequency is achieved by the greater control of current pulse duration ($\delta_{on}^{+/-}$ and $\delta_{off}^{+/-}$) in the positive bias, as shown in table 7.1. Comparison between the differences in sample appearance of untreated foam and those with different coatings formed under different frequencies is shown in figure 7.2 for replicated block shaped samples.
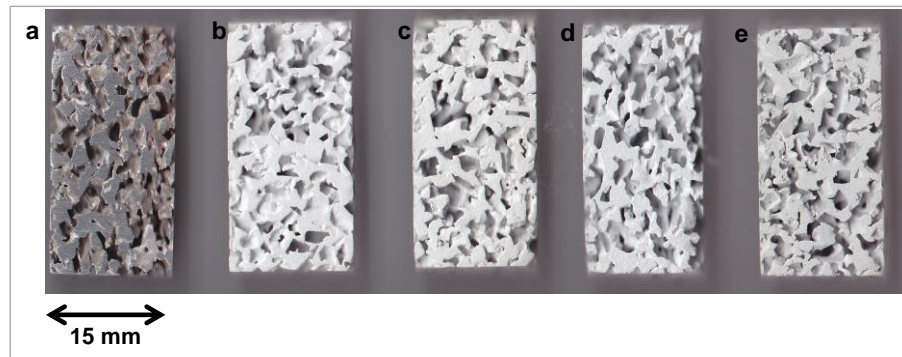
Figure 7.2 - Specimens of aluminium replicated foams with a) no coating, and PEO processed using frequencies at b) 50, c) 250, d) 1250, and e) 6250 Hz respectively.

It is visible that coatings produced at low frequency (f_1 and f_2) are characterized by thicker white layers whereas coatings produced at high frequency (f_3 and f_4) produce relatively grey thinner layers. This is clearly evidence of the effects on coating macro/microstructures that may be experienced during the application of different frequencies during PEO processing of foams.

7.1.1. Effect on Coating Thickness and Distribution

The volume averaged coating thicknesses at the free surface penetrating through to the foam centres for the different frequencies were calculated following the same method described in section 5.3.1, in chapter 5. The coatings produced in all conditions follow similar trend, reducing in thicknesses as coatings enter into foams interior. It can be seen that as the frequency is increased from 50 to 250 Hz, the amount of material being transformed and transferred into foam specimens rises dramatically, resulting in an increase in the average oxide coating thickness from ~ 33 µm to ~ 97 µm. Increasing the frequency to 1250 Hz reduces this effect, producing an average oxide coating of ~ 44 µm thickness, which is ~ 58% smaller

than the previous treatment. Further increase in frequency to 6250 Hz leads to the formation of much thinner coating than all previous coating conditions, averaging at ~ 20 μm.

Based on the initial results, it can be said that the coating distribution uniformity throughout the foam structure is essential for enhanced improvement in foam mechanical performance. Figure 7.3 below show the relative reduction Δt in coating thickness with distance from the sample surface. This was calculated as follows;

$$\Delta t = \frac{t_o}{t_{surface}} \qquad (7.1)$$

where t_o is the actual coating thickness measured and $t_{surface}$ is the thickness found at the free surface of the foam structure. This means that the greater the difference in coating thickness between the outer surface and the inner part of the foam, the smaller Δt will be. It can be observed from the figure that the coating thickness tends to diminish towards the foam interior, but there is generally a large reduction in the first 2 mm of depth for all of the coating conditions, regardless of the actual coating thicknesses measured. Similar behaviour has been observed in the first stage of PEO processing of foams in the present work, and it is most likely to be for similar reasons, especially given that pore size and the porosity are the same. It is also seen that coating thickness tend to be levelled in the last 2 mm distance into the foam middle point i.e. at about 6 mm from the foam surface. An exception to that must be pointed to the coating grown under f_4 condition (f = 6250 Hz), where there has been limitation to the coating penetration into the foam structure. It can be concluded that coating penetration is reduced with an increase in frequency. This is likely to be that at low frequency (e.g. f = 50 Hz), longer continuous pulse ON duration (6 ms and 10 ms in the positive and negative bias, as shown in table 7.1) allows current into the foam interior, despite the resistance encountered. At the same time this can cause disruption or cracking of the oxide layer (see figure 7.4 a), leading to poorer coatings properties. On the other hand, at higher frequency (e.g. f = 6250 Hz), continuous pulse ON time duration is reduced (0.052 and 0.08 ms in the positive and negative bias, as shown in table 7.1) such that it does not allow sufficient time for oxidation process and the current distribution can no longer penetrate into the foam interior.
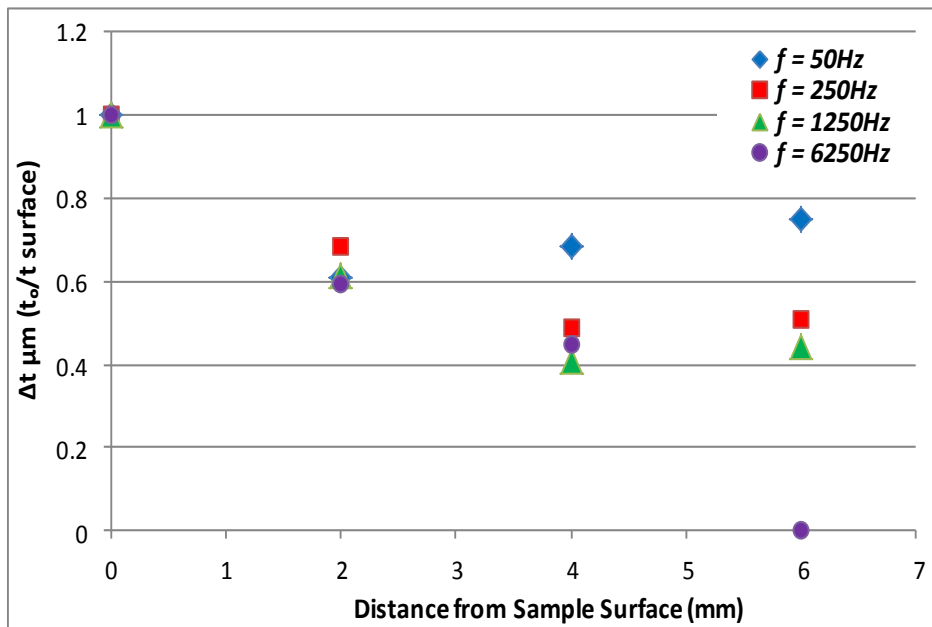
Figure 7.3 - The variation in relative reduction in coating thickness with distance from the sample surface for replicated block samples, after treatments using different frequencies of 50, 250, 1250, and 6250 Hz respectively. The relative reduction in each case is calculated by the actual coating thickness t_o divided by the coating thickness measured at the free surface $t_{surface}$.

The difference in coating thicknesses produced under these low and high frequencies is evidenced in the cross-sectional SEM images shown in figure 7.4. It can be seen that coatings produced at low frequency (f_1 and f_2) are characterized by thicker coatings with both high (f_1) and low levels of porosity (f_2), although in the latter type, porosity is predominantly in the coating outer layer. On the other hand, coatings formed at high frequency (f_3 and f_4) have a relatively thinner (f_4) but denser morphology (f_3), where more silicate has been found and this effect is explained later.
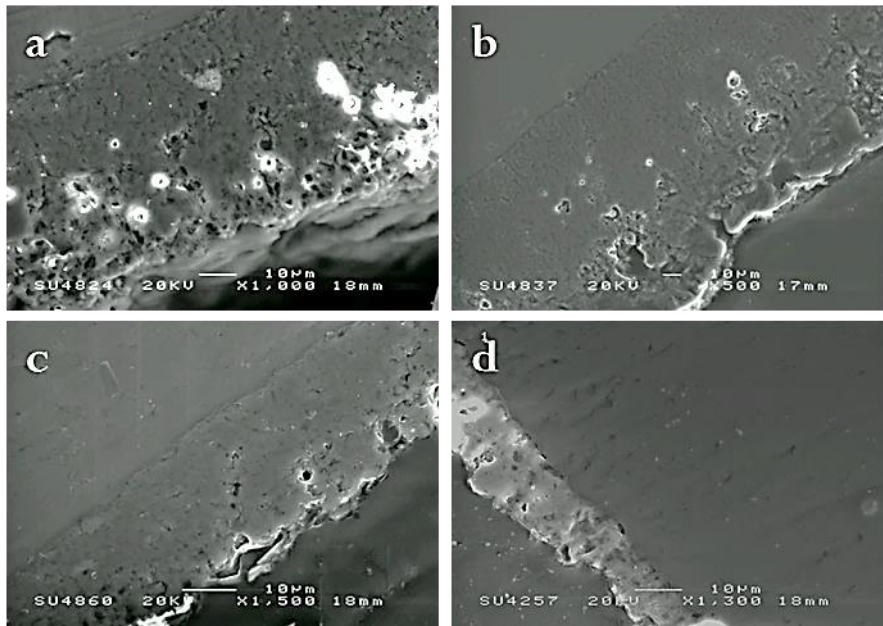
Figure 7.4 - Secondary electron SEM images of a PEO coating formed at frequencies of a) 50, b) 250, c) 1250 and d) 6250Hz on replicated aluminium foam strut cross-sections respectively.

The effect of high frequency (ranging from 0.5 to 10 KHz) pulsed bipolar current regime during PEO coating of bulk Al alloy samples has been investigated previously in detail [105, 116]. These high frequencies produce controlled microdischarges at the metal /electrolyte interface, which are shown to be a very short-lived and highly active. These conditions help reduce the effect of the extreme heating, which would result in the occurrence of long-lived microdischarge events in the direct current regimes, on sample surfaces and increase the rate of material (i.e. the additives) being transported into the samples. For instance, it was found that both optimum coating growth rate and energy consumption can be can be achieved by utilization of high frequency (in the range of 1 to 3 KHz) pulsed bipolar current [105]. Above this frequency range the effect is less and the energy consumption increases dramatically. In the present study, the effect of applying a range of frequencies on porous aluminium samples shows relatively similar behaviour, but here the optimum range is between 250 Hz and 1250 Hz (see figure 7.5). The coating growth rate at the lowest frequency (50 Hz) is slightly higher for dense aluminium alloy samples, but this apparently changes as frequency reaches 250 Hz, where the coating growth rate for aluminium foams exceeds that of dense aluminium.
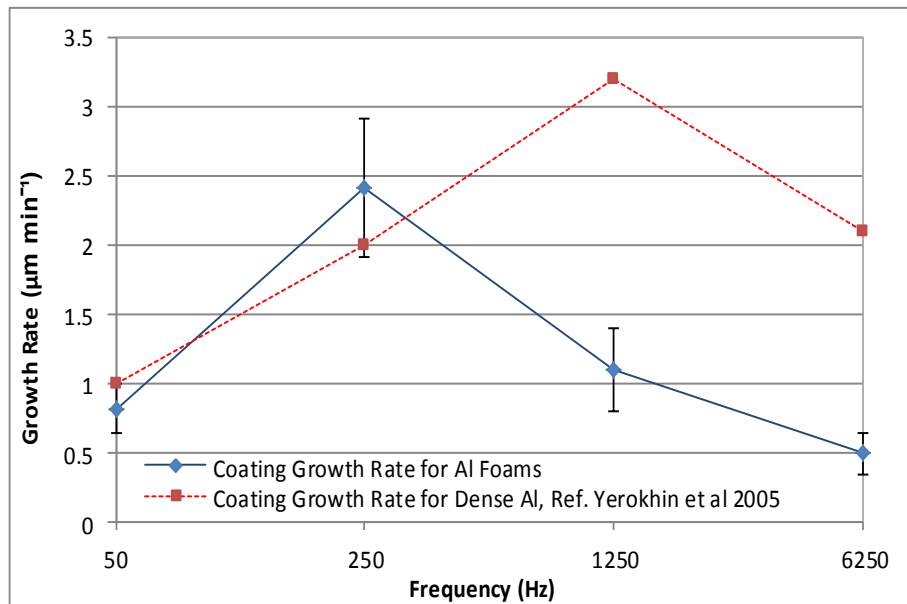
Figure 7.5 - Comparison between effects of frequency on coating growth rate during pulsed bipolar PEO processing of aluminium foams and dense aluminium alloy, ref.[105].

At higher frequencies (1250 – 6250 Hz), the rate of mass transfer is always higher for dense sample, even though in both cases the rate tends to decrease with increasing frequency. Such difference in coating growth rate is expected since foam samples possess larger specific surface in contact with the electrolyte, as compared to dense samples. Also, coating deposition mechanism would be more complicated for porous bodies due to high-aspect-ratio porosity. As mentioned earlier, the characteristic of the current pulse ON durations, which are reduced at higher frequency, and resistances encountered, from the electrolyte, capacitance of the PEO coatings and the shielding effects, all add up in changing the behaviour of current distribution on the treated sample. These factors and their effects are explained in details later.

7.1.2. Effect on Foams Mechanical Properties

Figure 7.6 depicts an example of stress-strain curves for uncoated and foams coated at different frequencies. The average mechanical properties obtained from duplicate tests as well as density changes after coating recorded for the different foams tested are shown in table 7.2.
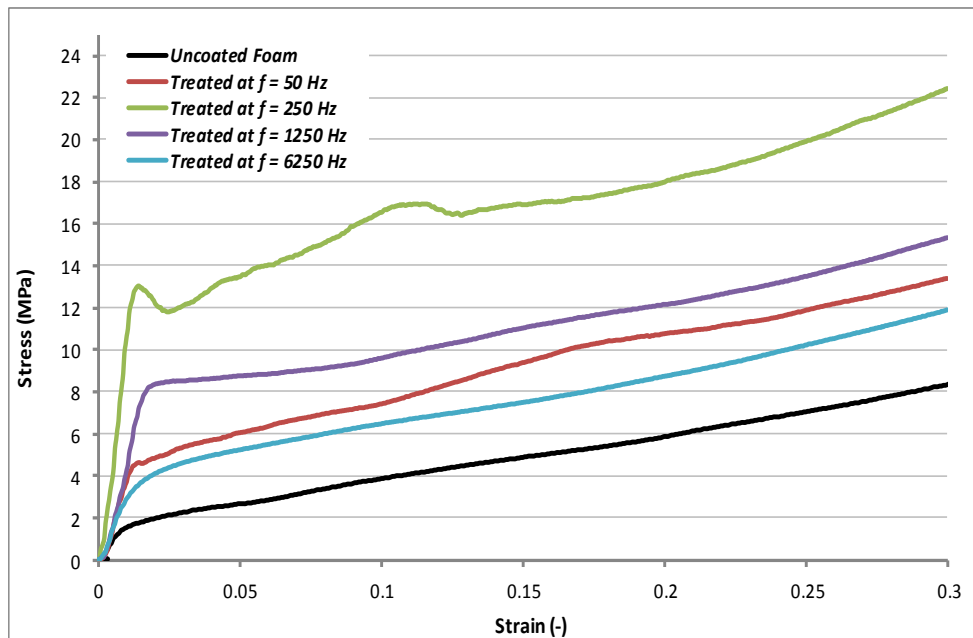
Figure 7.6 - Example stress–strain curves for different PEO coated samples using different pulse frequency, as compare to uncoated sample of replicated foams tested in compression.

Table 7.2 – Average test results for the different types of foam as well as thicknesses of coating applied, absolute density change, and other mechanical properties.

Foam	Frequency (Hz)	Volume Averaged, t (µm)	Absolute Density After Coating, (Change) g cm^{-3}		Yield Stress σ, MPa	Specific Strength σ/ρ, MPa g^{-1} cm^{-3})	Energy Absorbed, W (J/cm^3)
Replicated (1.6 mm pores)	**None**	0	1.04±0.0	(+0.0)	2.2±0.4	2.2	1.74±0.4
	50	32.6	1.15±0.0	(+0.21)	4.2±0.4	3.6	2.5±0.2
	250	96.5	1.46±0.07	(+0.43)	11.1±2	7.6	4.3±0.9
	1250	44	1.13±0.04	(+0.14)	7.1±1.4	6.2	3±0.3
	6250	20	1.08±0.05	(+0.07)	4.0± 0.2	3.6	2.3±0.08

The increase in mechanical properties by different factors (ranging from ~ 2 to 5 factors) can be observed for the processed PEO foams, as compared to the unprocessed one. For comparison, maximum strength increase by a factor of 6 was found for aluminium foams coated with nanocrystalline Ni-W alloy with thickness of ~ 30 µm [1] whereas depositing ~ 72.3 µm thick film of nanocrystalline Ni on aluminium

foams resulted in strength increase by a factor of 5.2 [83]. Another study reported a maximum strength increase by a factor of 10 for periodic aluminium trusses after coating with ~ 400 µm thick layer of Ni-Fe alloys [4]. The latter, however, is somewhat different to typical open cell metal foams which tend to have irregular structures, while these periodic materials have struts which can be positioned precisely and the structure is usually designed to produce better resistance to externally applied loads. These values are comparable to the present study, especially when taking into account that coating mechanisms (since PEO is not a deposited coating, but rather it is a chemical conversion of the parent metal into its oxide) as well as coating thickness formed are not the same (up to average coating thickness of ~ 97 µm in the present study).

Although the coated foams encompass different quantities of ceramic layers and thus are expected to behave differently, the plateau regions follow similar trends where the stress increases slightly as plastic deformation exceeds 25%. This suggests that these ceramic coatings may not have high stiffness and strength (unlike pure dense alumina), and consequently do not restrain the plastic deformation of the ductile aluminium core [96]. This could be due to the presence of a high level of porosity.

The foams treated at f = 250 Hz show slightly different behavior where the curve is less smooth and tends to have some peaks, implying the presence of relatively higher amount of ceramic coating (see density increase in table 7.2), which may exhibit brittle fractures and consequent periodic unloads at some points during deformation.

7.1.3. Investigation of Coating Properties

Complimentary characterization was carried out using XRD, EDX and nanoindentation techniques to investigate phase composition, elemental distribution and mechanical properties of the PEO coatings formed.

Figure 7.7 illustrates the phase composition analysis for the different coatings produced at frequencies of 50, 250, 1250 and 6250 Hz respectively.
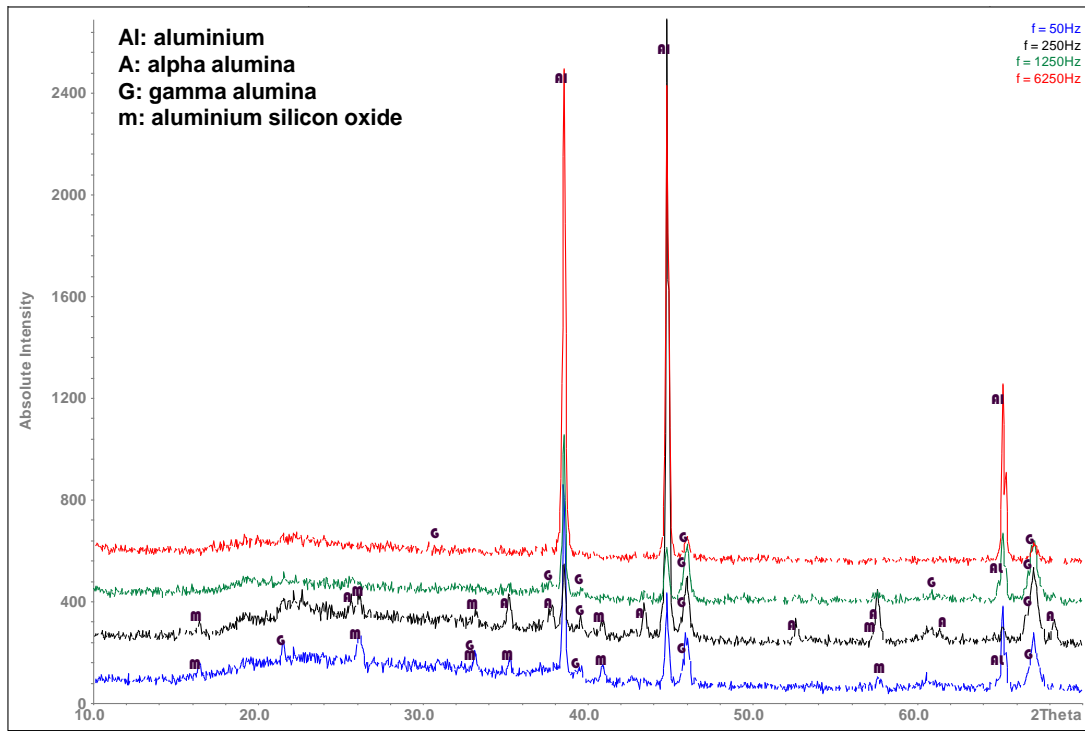
Figure 7.7 - X-ray diffraction patterns of the different PEO coatings produced at frequencies of 50, 250, 1250, 6250Hz on Al foam samples. The phases are identified using the following PDF data: Al – [04-0787]; A – [10-0173]; G– [10-0425]; M – [73-1253].

It can be seen that the coatings consist mainly of α and γ-Al_2O_3, with some traces of aluminum silicon oxide (Al2.35 Si.64 O4.8) found for coatings produced at low frequencies. In fact, the coating grown under f = 250 Hz shows an increased proportion of α-Al_2O_3 phase, as compared to the other coatings. As discussed in section 3.3.1 in chapter 3, thicker coating promotes formation of α-Al_2O_3 phase as a result of the absorbed heat input from the higher temperatures caused by the intensive discharges [7, 105, 116]. Stable α-Al_2O_3 phase is found to be favored for intrinsic stress relaxation processes [112]. Coatings produced at f = 250 Hz are found to be the thickest, with the average value of 96 μm.

The effect of pulse frequencies on the element distribution (at. %) of the different coatings, extracted from the EDX data, are shown in figure 7.8. It is seen that the elemental compositions contain mainly oxygen, aluminum, and silicon. These composition measurements along with the X-ray diffraction analysis clearly indicate that the coatings are composed of metal oxides. The content of oxygen remains unchanged (within the accuracy of the equipment) with the application of different

163

frequencies. The contents of aluminum and silicon vary with the applied frequencies, as seen in figure 7.8. The effect of increased silicon level in coating structures can be observed in this work.
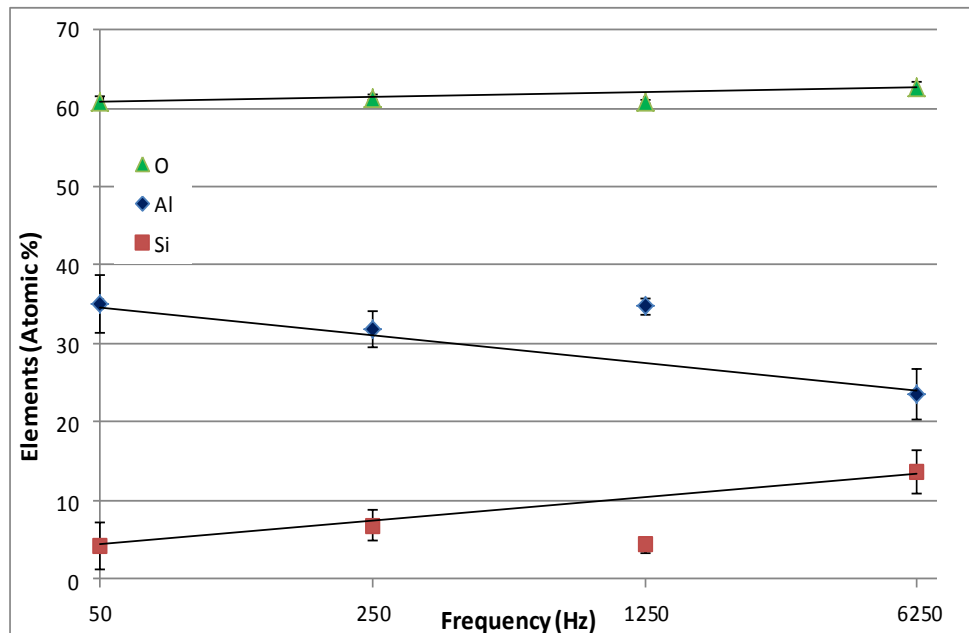
Figure 7.8 - Effect of different applied frequencies on levels of PEO coatings main elements. Note that linear regression lines of best fit are used.

The amount of Si in the coatings increased noticeably with higher frequency used. This effect is predominant for coating produced at f_4 condition (f = 6250 Hz). The increase in Si content may be due to the fact that as the coating gets thicker, aluminium oxidation processes increase the amount of alumina in the coating, and hence the thickness, whereas the Si content, which is expected to form as silicate phases, remain unchanged or only slowly forming due to the adsorption mechanism. Adsorptions, as well as nucleation, are the two predominant formation mechanisms which take place in region (A) shown in, for example, figure 7.32 (for current-voltage characteristics), whereas dissolution, recrystallization and deposition are the mechanisms involved in region (C), after exceeding the breakdown voltage, point (B) shown in the same figure. Therefore in a thinner coating, as is the case for the coating grown under higher frequency of 6250 Hz (volume average thickness of 20 µm), the amount of Si is higher because there is a smaller amount of aluminium

being oxidized, and so the Si is not diluted within the coating as would be otherwise in a thicker coatings.

Nanoindentation tests were carried out on these different coatings (formed under f_1, f_2, f_3 and f_4 conditions) and representative load-displacement curves are shown in figure 7.9. Surface profiles recorded after each indentation test for these coatings (using the indenter tip itself in an atomic force microscope mode) are shown in figure 7.10 which clearly shows different coating morphologies. Marks of the individual indents can be seen in some coatings particularly those containing softer phases, as is the case in coatings produced at frequency of 6250 Hz. Average values for hardness and modulus for all of the different coatings tested are shown in table 7.3.
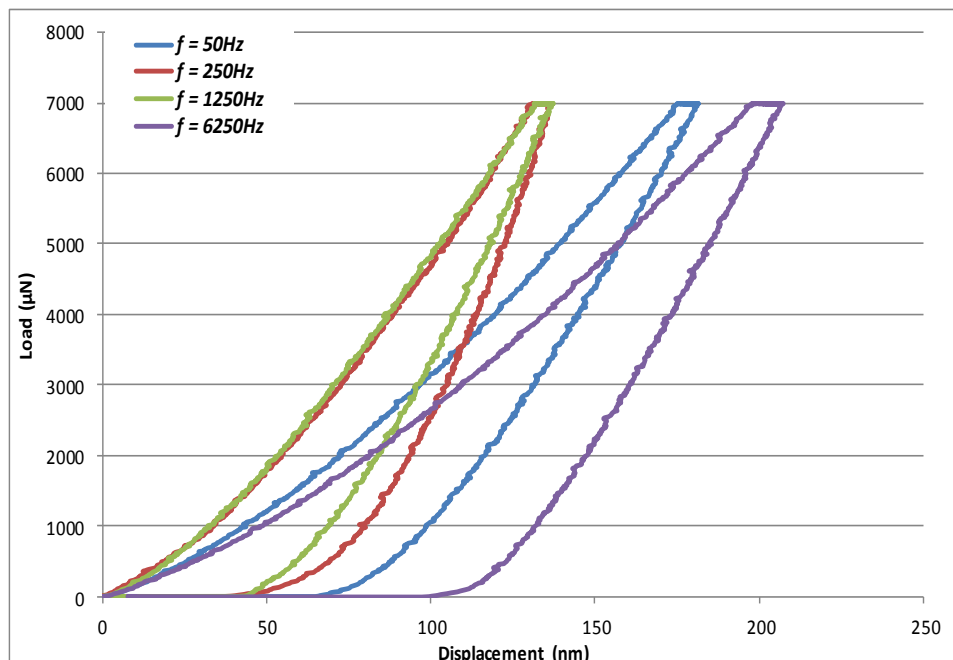
Figure 7.9 - Representative nanoindentation load-displacement curves for different PEO coatings.
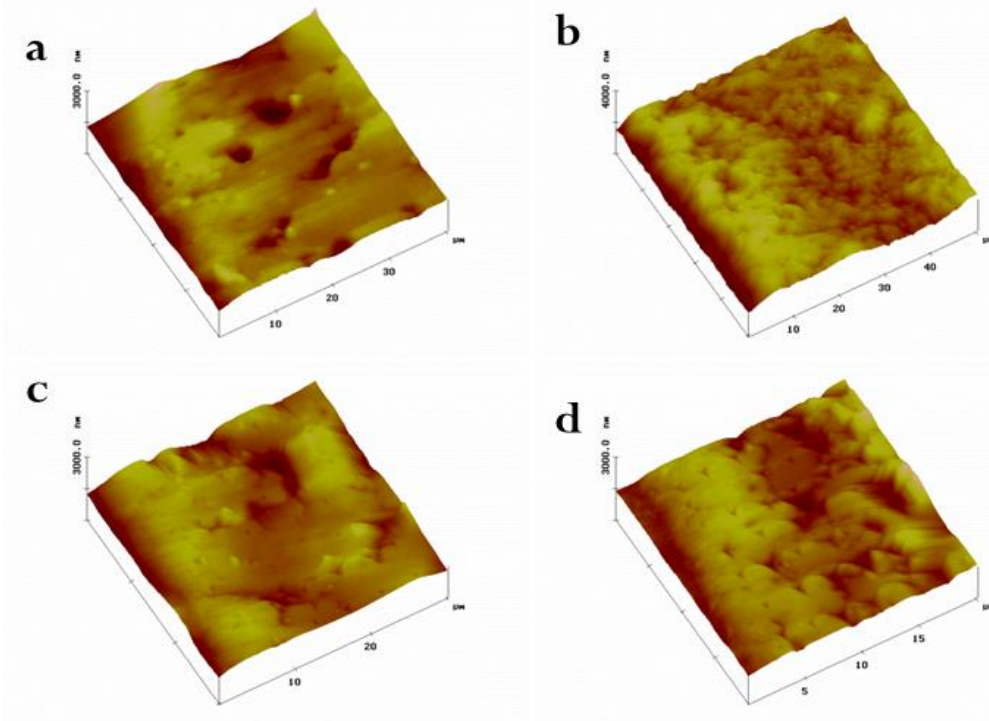
Figure 7.10 – surface profile images for different PEO coatings cross-sections during nanoindentation tests. PEO coatings produced at frequencies of a) 50, b) 250, c) 1250 and d) 6250Hz on Al foam samples.

Table 7.3 – Average values for hardness and modulus (GPa) for all of the different coatings tested.

Coating	Frequency (Hz)	Volume Averaged, t (μm)	Hardness (GPa)	Modulus (GPa)
PEO	50	32.6	9 ± 3	103 ± 29
	250	96.5	11.2 ± 3	153 ± 30
	1250	44	8.7 ± 4	108 ± 33
	6250	20	7 ± 3	85 ± 18

It can be shown that the average hardnesses of 9, 11.2, 8.7, and 7 GPa were found for coatings formed at frequencies of 50, 250, 1250 and 6250 Hz respectively. It can be clearly seen that the measured hardness decreased as the content of silicon increases to high levels, typically above 10 %, in the coatings, see figure 7.8 and table 7.3. The effect on local coating stiffness follows a similar trend, as shown in figure 7.8 and table 7.3.

The average moduli found for these coatings were 103, 153, 108 and 85 GPa respectively. The effect of increased silicon content in the coating was encountered during the investigation of coatings produced in the first processing stage of this work; in particular coatings formed under t_3 conditions. In that coating, the silicon content was found to be in the range of 8.75 - 11.1 at. % and the improvements of foam properties that resulted from treatments t_1 and t_2 were not maintained with treatment t_3, partly because coating produced developed a greater density of porosity and microcracks.

For general interest, although not specifically required for improvement of foam properties, the resilience, defined by (H/E) ratio, of the PEO coatings in the present work is shown in figure 7.11. The increase in coating resilience, shown to be generally slightly higher for coating produced under f_1 condition (50 Hz), is generally favored for improved wear resistance, and this leads to the fact that the effect of coating porosity and microcracks is more pronounced on the coating stiffness than on hardness, as suggested previously [111].
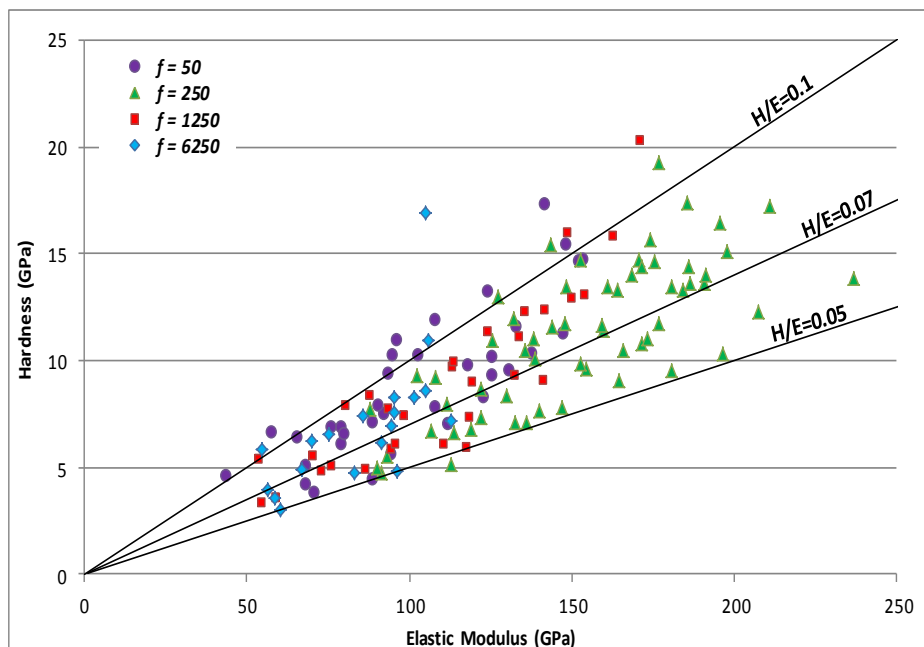
Figure 7.11 – Comparison between the resilience (defined as E/H ratio) of the PEO coatings produced under f_1, f_2, f_3 and f_4 conditions.

A similar effect of higher silicon content on the mechanical properties of PEO coatings was investigated by Kalkanci and Kurnaz [115] who found that the average

hardness and modulus were reduced with increasing silicate concentration in electrolyte (i.e. average hardness reduced from 11.5 to 8.5 GPa). It was also concluded that coatings formed in richer sodium silicate electrolyte were more likely to contain higher level of porosity as result of increase quantity of glassy phases.

For all types of coatings, variations in local stiffness and hardness were observed. This can be interpreted by the existence of the different phases and microstructural features such as pores and networks of microcracks present within the coatings. Four range of indentation data can be distinguished; hard and stiff phases with hardness values between 15 – 20 GPa (likely to be α-Al$_2$O$_3$), less hard phases with hardness values reaching 10 – 15 GPa (likely to be γ-Al$_2$O$_3$), soft phases with characteristic hardness values of 5 - 9 GPa (expected to be amorphous phases) and very low hardness and stiffness regions (microspores and microcracks). Furthermore, it is noticed that hardness and stiffness varies with coating thickness, and both decrease within the outer layers, see figure 7.12 (where stiffness is plotted against the coating thickness, from the interface with the metal. The trend in hardness is similar), where higher level of porosity has been found to exist.
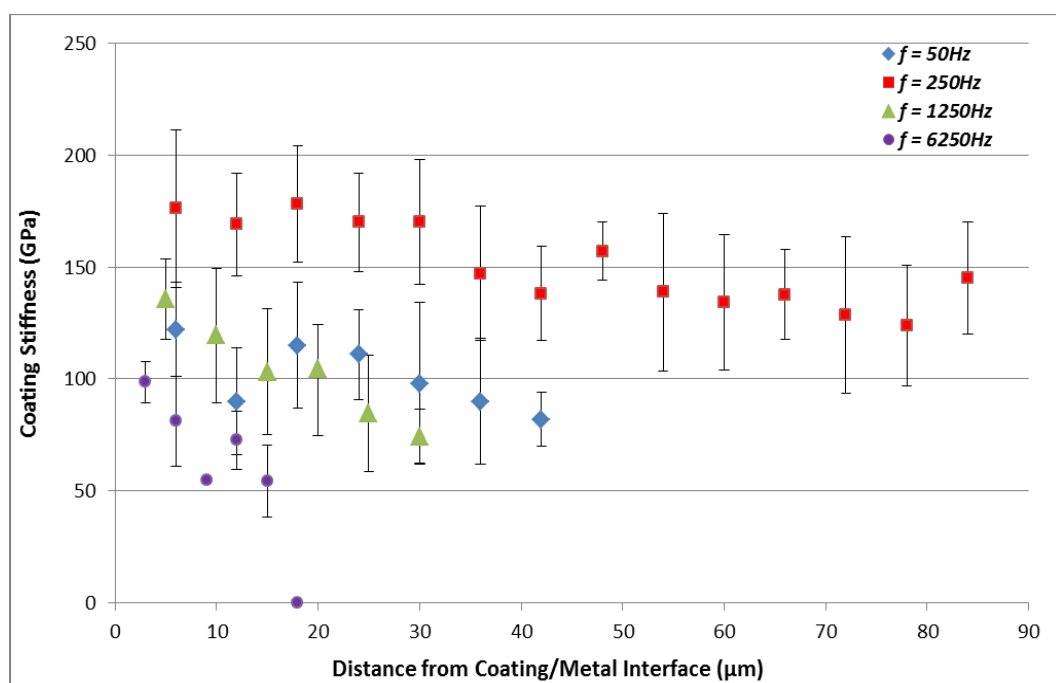
Figure 7.12 - Local stiffness distribution across coating PEO coating thicknesses for the different frequencies used; 50, 250, 1250, 6250Hz respectively.

Characterization of coating porosity (including networks of fine cracks, voids and pores) was carried out on different backscatter SEM images of all coating cross-sections. These images were analysed and pore area calculations were performed using ImageJ software. This software is capable of measuring pore areas (e.g. in μm^2), from which representative pore radii and diameters can be extracted, once a threshold has been applied to the image under investigation. The threshold of an image allows identification of pores to be distinguished as a different phase to the bulk, as seen in figure 7.13 (more images for all different frequencies are presented in the appendix in figure 10.2). It should be noted that the thresholding step is critical to obtain good accuracy, and this was done to get the best visual match with the original images. The summary of results of each image includes counts of each individual pore area measurement, total pore areas and pore volume fractions. Due to the large variations in pore sizes for each coating, representative histograms are shown in figure 7.15 to illustrate such variations, which would be more illustrative than just providing a single averaged value with a large standard deviation.
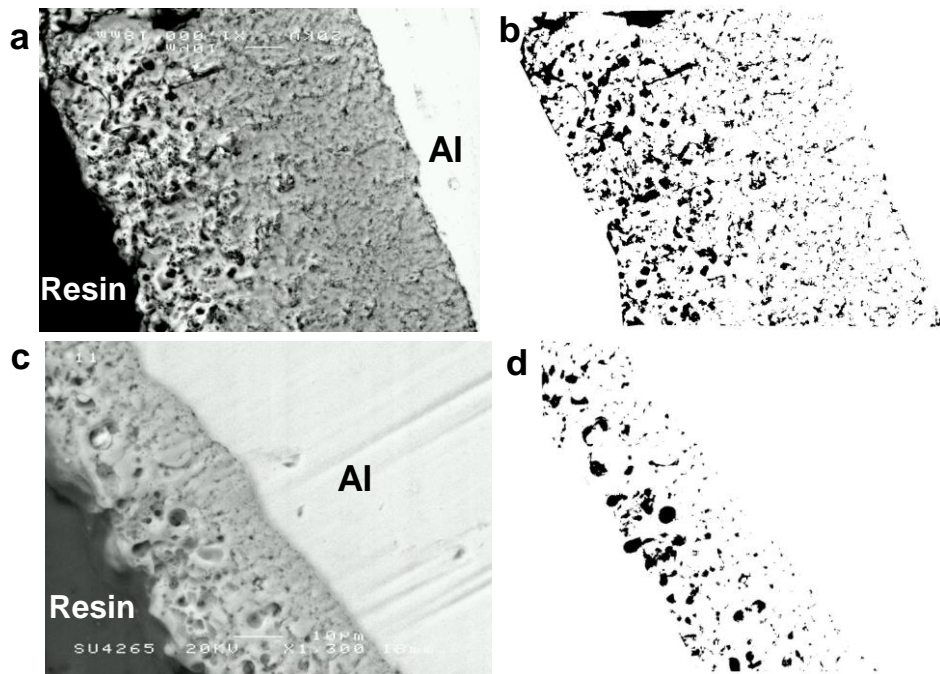
Figure 7.13 - Representative Backscatter SEM images for coatings produced with a) low frequency of 50Hz and c) high frequency of 1250Hz before and after applying threshold to these images (b and d). Pores can be visually seen in Mask images (b and d) produced by the ImageJ software.

Although the coating formed at 50Hz has better average hardness value than those produced at higher frequencies (as show in table 7.3), it might be that this coating contains larger amount of porosity (measured at 15 %, as shown in figure 7.14) than coatings produced at frequencies of 250 and 1250 Hz, which alters the mechanical properties of the coatings, making it weaker. For coating formed at f = 6250 Hz, porosity and Si content were the highest, see figure 7.8 and 7.14, and the fact that aluminum oxidation process is interrupted by the very short pulse ON duration, this could explain why this coating has lowest hardness and modulus, as compare to the others. Despite this, these values of hardness are higher than those measured for conventional anodized coating (~ 4 GPa [139]), and can still provide greater protection to the core material (hardness for aluminum and its alloys ranges from 0.23 to 1 GPa [115, 119].
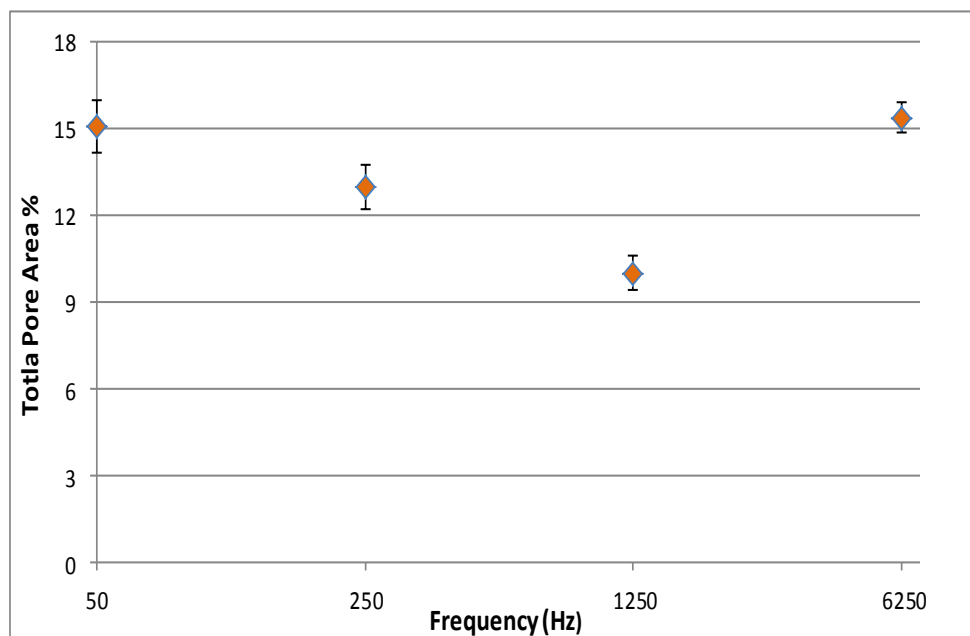
Figure 7.14 - Pore volume fraction quantification for different PEO coatings formed at different frequencies, using ImageJ software. Analysis was carried out on three different backscatter SEM images for each coating produced.

It is seen from the figure 7.15 that the higher frequencies of 1250 and 6250 Hz produced pores with less variation in size across thickness. On the other hand, pores produced by the low frequencies of 50 and 250 Hz vary dramatically in size between

the inner and outer regions of coating. Moreover, the volume fraction of pores relative to the total coating thickness may have more influence during deformation than the size of the individual pores themselves. This is because as the coating thickness increases, cracks propagation becomes important as well as initiation. The present estimation of coating porosity provides values (10 – 15.5 % porosity) that are in agreement with those of a previous study [140], in which a quantification of PEO coating porosity using image analysis found that the coating contained about 13 – 16%.
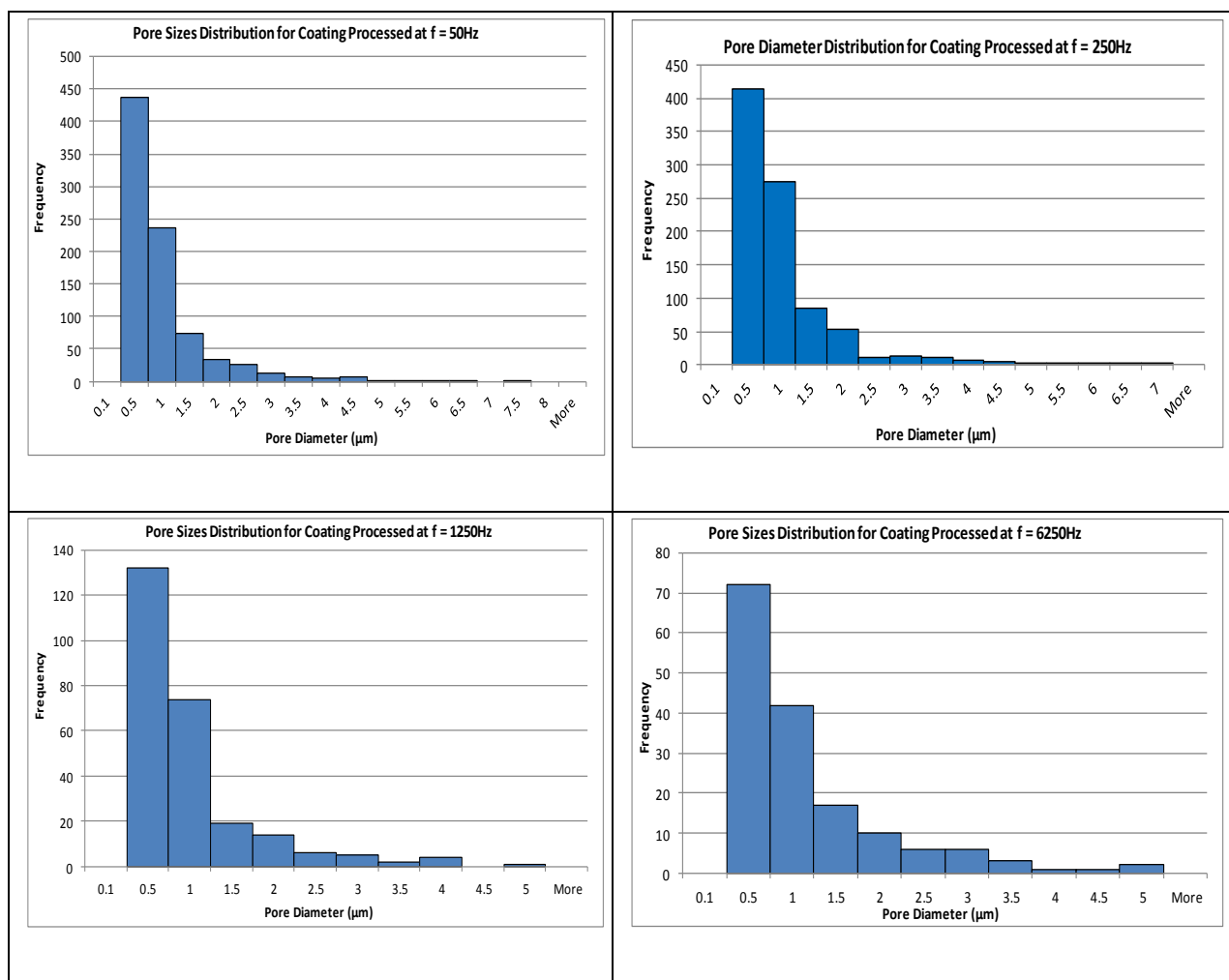
Figure 7.15 - Histograms presenting pore diameters distributions for coatings formed at frequencies of 50, 250, 1250 and 6250Hz on aluminium foams.

7.2. Effect of Different Duty Cycles, p_i

In the third PEO processing stage, see table 7.4, we optimise one processing condition examined in the first and second processing stages (t_2f_2) by using different duty cycles in which pulse ON/OFF times ($\delta^{on/off}$) were adjusted in the positive and negative bias to achieve different ratios, see figure 7.16 and table 7.5. Coatings produced under the selected condition, i.e. t_2f_2, showed improved foam mechanical and specific properties as result of increased proportion of hard $\alpha-Al_2O_3$ present. PEO treatment was carried out in the pulsed bipolar current mode as was detailed in in chapter 4, section 4.3. In this part of the project, 15 foam samples, similar to those presented in figure 7.2, produced by the newly developed infiltration rig shown in figure 4.4, in chapter 4, were used. An example of current and voltage waveform with ON/OFF ratio of p_1 is shown in figure 7.16, where pulse durations, $\delta^{on/off}$, in the positive and negative bias are indicated. Values for pulse durations for the other duty cycles in p_2, p_3, p_4 and p_5 processing conditions are shown in table 7.5. Current transients for duty cycle p_1, p_3, p_4 and p_5 are shown in figure 10.3 in the appendix. Due to the data logging system failure during processing of current and voltage data for p_2 condition, it was not possible to maintain its values. Measurement of electrolyte conductivity yielded 8.82 mS^{-1} and pH = 12.31. As mentioned previously, these measurements are carried out to ensure consistency in electrolyte conductivity (which we aim to be higher than the values of 3 - 6 mS^{-1}) and alkalinity.

Table 7.4 - Different duty cycles used during the third stage of PEO coating processing of open cell aluminium foams. Percentage (%) for different ON/OFF durations in the positive and negative bias is provided for each cycle. Actual times (ms) for these durations are given in table 7.5

Optimization Stage	Processing Variables	Treatment	Variations			Invariables
			Processing time (min)			Frequency at 250 Hz
First	Time	t_1	20			
		t_2	40			
		t_3	80			
			Pulse frequency (Hz)			Processing time of 40 minutes, **(t_2)**.
Second	Frequency	f_1	50			
		f_2	250			
		f_3	1250			
		f_4	6250			
			δ_+^{on} %	δ_-^{on} %	$\delta_{+/-}^{off}$ %	Processing time of 40 minutes / pulse frequency at 250 Hz, ($t_2 f_2$)
Third	Duty Cycles	p_1	32.5	50	17.5	
		p_2	27.5	50	22.5	
		p_3	35	50	15	
		p_4	32.5	25	42.5	
		p_5	32.5	56.25	11.25	

Figure 7.16 - Example of current and voltage waveforms for frequency of 250 Hz in pulsed bipolar current (PBC) mode during PEO processing of open cell aluminum foams. Estimation of current magnitude during pulse on time is 36.5 A.

Table 7.5 – The actual pulse durations δ_{off}^{on} (ms) used during the third processing stage in which a range of different duty cycles were adopted to achieve different ON/OFF ratios.

Optimization Stage	Processing Variables	Treatment	Variations; Pulse Durations				Invariables
			δ_+^{on} (ms)	δ_+^{off} (ms)	δ_-^{on} (ms)	δ_-^{off} (ms)	
Third	**Duty Cycles**	p_1	1.3	0.2	2	0.5	Processing time of 40 minutes / pulse frequency at 250 Hz, $(t_2\,f_2)$
		p_2	1.1	0.4	2	0.5	
		p_3	1.4	0.1	2	0.5	
		p_4	1.3	0.2	0.1	1.5	
		p_5	1.3	0.2	2.25	0.25	

7.2.1. Effect on Coating Thickness and Distribution

Similar trends of coating thickness reducing with depth into the foam interior have been observed for all duty cycles, with only one exception for p_4 duty cycle. It can be seen from figure 7.17 that with p_4 duty cycle, the reduction is negligible with only small decrease that may fall within the experimental error (judging by the difference between the average coating thickness on the surface and that on the middle of the foam, which was found to be 16 μm. For other conditions, the difference can reach 72 – 110 μm).
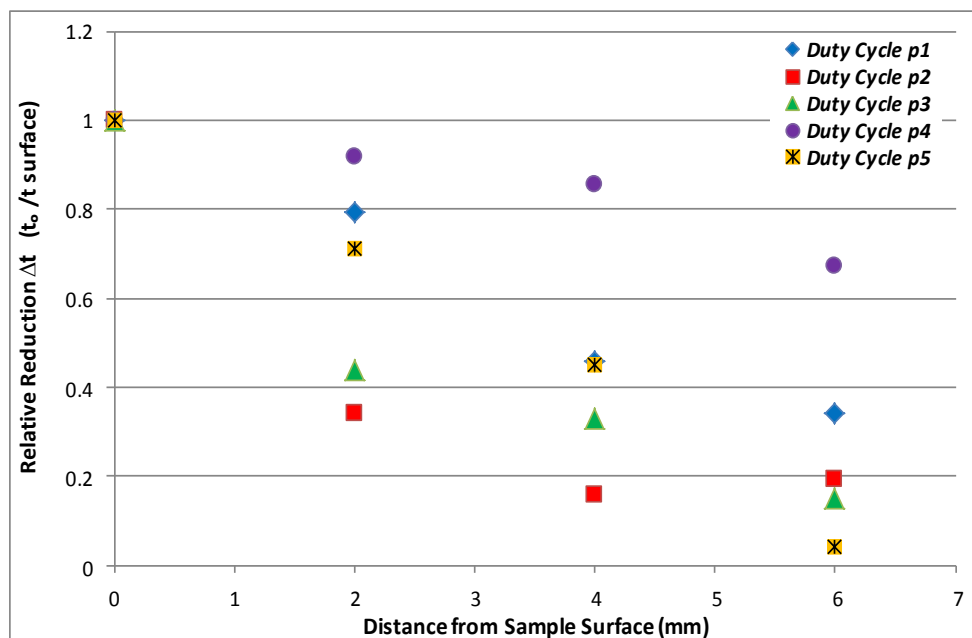
Figure 7.17 - Comparison between effects of using different current waveforms (on/off ratio in positive and negative bias) on relative coating thickness reduction with sample's depth during processing of open cell aluminium foams.

This is due to the fact that during the p_4 duty cycle, longer OFF and shorter ON pulse times were used during the negative bias (set as 1.5 and 0.1 ms respectively). In fact this is the longest OFF pulse time, as compared with the other duty cycles as shown in table 7.5. It is expected that with longer OFF pulse duration, coating thickness and coating growth rate will also be small, and this was the case for p_4 duty cycle. This effect, for p_4 condition, is shown in figure 7.18 for average coating growth rate

calculated for all different duty cycles examined and in table 7.6 for the volume averaged coating thicknesses (average $t = 45$ µm).

The reduction in coating thickness with depth for coating deposition using duty cycle p_1 is reasonable in terms of the average coating thickness measured (average $t = 83$ µm) and coating growth rate, as compared with other values found for the other duty cycles.

The effect on coating distribution of using duty cycles p_2 and p_5 follows almost similar paths, but the distinguishable difference between these two and the other conditions (p_1, p_3 and p_4) lies in the fact that the coatings do not completely penetrate into the middle of foam structure. The low coating penetration for duty cycle p_2 is more pronounced, and so one direct link can be made to relatively long OFF time in the positive bias (0.4 ms), which is the longest OFF time in the positive bias, see table 7.5. It may be that the ionic diffusion processes taking place during processing was interrupted by this longer OFF time, which has also affected the average coating thickness, $t = 60$ µm.

For duty cycle p_5, although the average coating thickness (average $t = 85$ µm) was the highest, the density increase is smaller than that found with treatments p_1, p_2 and p_3, as presented in table 7.6. However, the low coating penetration may be interpreted by the faster coating growth rate (see figure 7.18) on the free surface, as a result of the longest total ON times from both positive and negative bias (measured as 1.3 and 2.25 ms respectively) as shown in table 7.5. This means that the oxide coatings building up on the outer surface quickly provide higher resistance which leads to low current density. The resistance of the oxide layer is influenced by the coating thickness and microstructure. During processing, it was noticed that there were more discharges concentrated on the edges of the samples (outer surfaces).

Although the reduction in coating thickness (Δt) was the highest, coating deposition using duty cycle p_3 showed moderate behavior in terms of average coating thickness (average $t = 70$ µm) and coating growth rate. Coating penetration was found to be complete which is attributed to the longest ON and shortest OFF time (1.4 and 0.1 ms respectively) in the positive bias only, as shown in table 7.5. Again too long pulse ON times will give faster coating growth rate on the foam outer surface and this effect can be reduced when longer ON pulse time is only used for one bias (positive or negative).
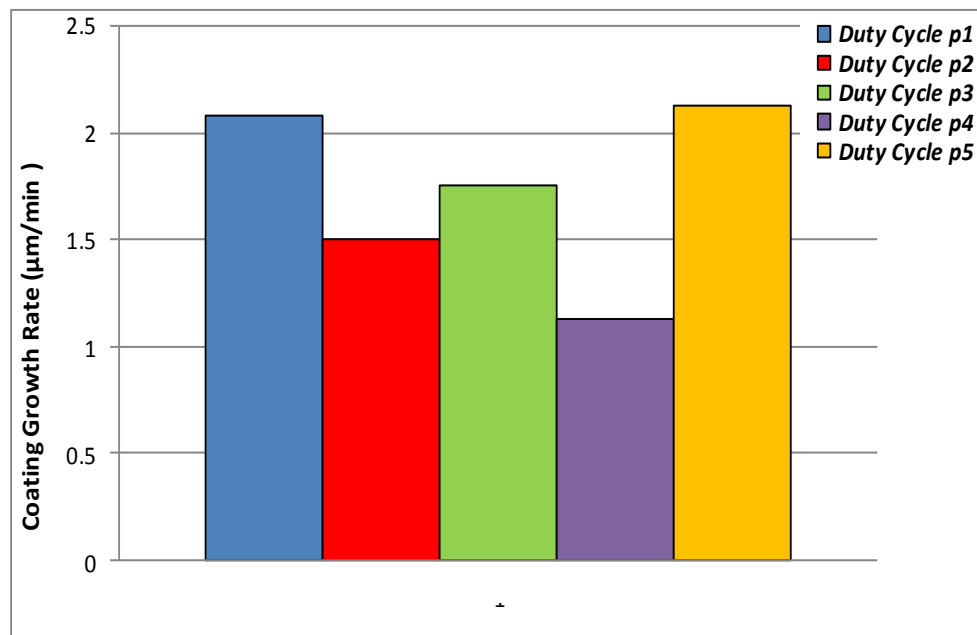
Figure 7.18 - Comparison between effects of using different current waveforms/ duty cycles (on/off ratio in positive and negative bias) on coating growth rate during pulsed bipolar PEO processing of aluminium foams. Error bars represent the standard deviation in results, as coating thickness tends to decrease into foam structure.

7.2.2. Effects on Foams Mechanical Properties

Representative stress-strain curves for uncoated foams and those coated at different duty cycles are shown in figure 7.19. The average mechanical properties obtained from repeated tests for each condition, as well as density changes after coating are shown in table 7.6. The increase in foam mechanical properties (e.g. yield stress and total energy absorption on crushing) is seen for those coated using the range of duty cycles explained earlier (p_1, p_2, p_3, p_4 and p_5).
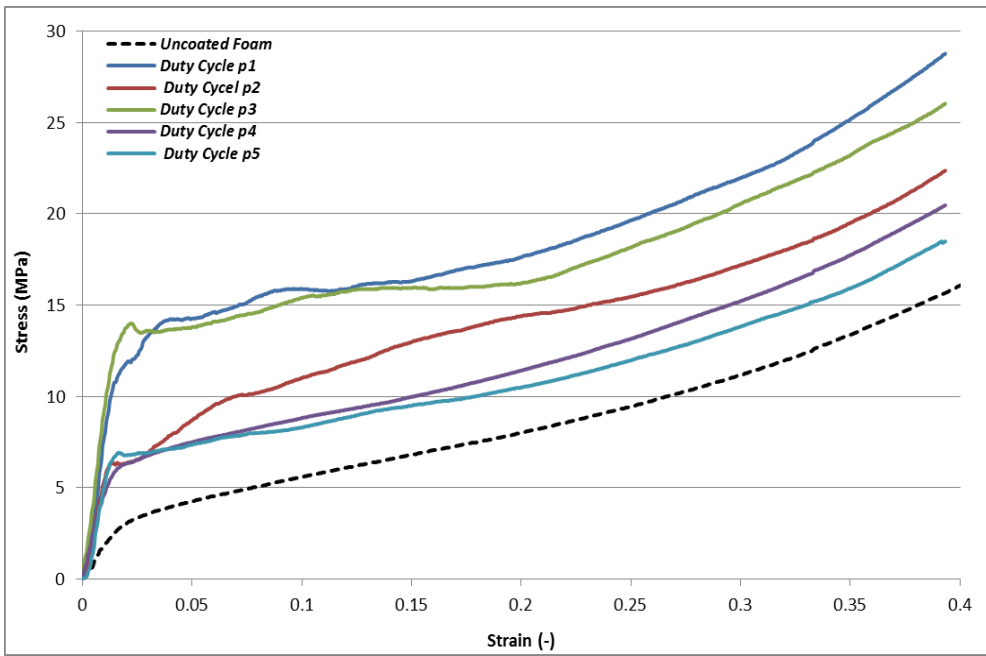
Figure 7.19 - Example stress–strain curves for uncoated and PEO coated samples using different duty cycles (different on/off ratios in positive and negative bias) during PEO treatments of replicated foams tested in compression.

The increase in yield stress for the different foams has been accompanied with some increase in foam densities, and so the specific strength of these foams must be obtained to quantify the benefits of the added ceramic coatings in terms of lightweight structural performance. This is shown in figure 7.20 and it can be seen that the effects vary with the treatment condition but it is observed that the highest improvement in foam strength and specific strength have been achieved with treatments using duty cycles p_1 and p_3. An alternative way to measure the ratio of the increase in foam strength per unit weight of coating is discussed later in detail in section 7.4.

Table 7.6 – Average compression test results for the different types of PEO treated foams as well as thicknesses of coating applied, absolute density change, and other mechanical properties.

Foam	Duty Cycle	Volume Averaged Coating Thickness (µm)	Absolute Density after Coating, (increase) g cm^{-3}		Yield Stress σ, MPa	Energy Absorbed, W (J/cm^3)
Replicated (1.6 mm pores)	No coating	0	1.03±0.0	(+0.0)	2.2±0.4	1.74±0.4
	p_1	83	1.39±0.0	(+0.33)	14.6±0.6	5.0±0.01
	p_2	60	1.26±0.01	(+0.23)	6.5±0.7	3.6±0.5
	p_3	70	1.37±0.01	(+0.34)	11.5±3.5	4.6±0.14
	p_4	45	1.12±0.03	(+0.07)	6.2± 0.25	3.0±0.2
	p_5	85	1.23±0.03	(+0.18)	7± 0.07	3.0±0.03
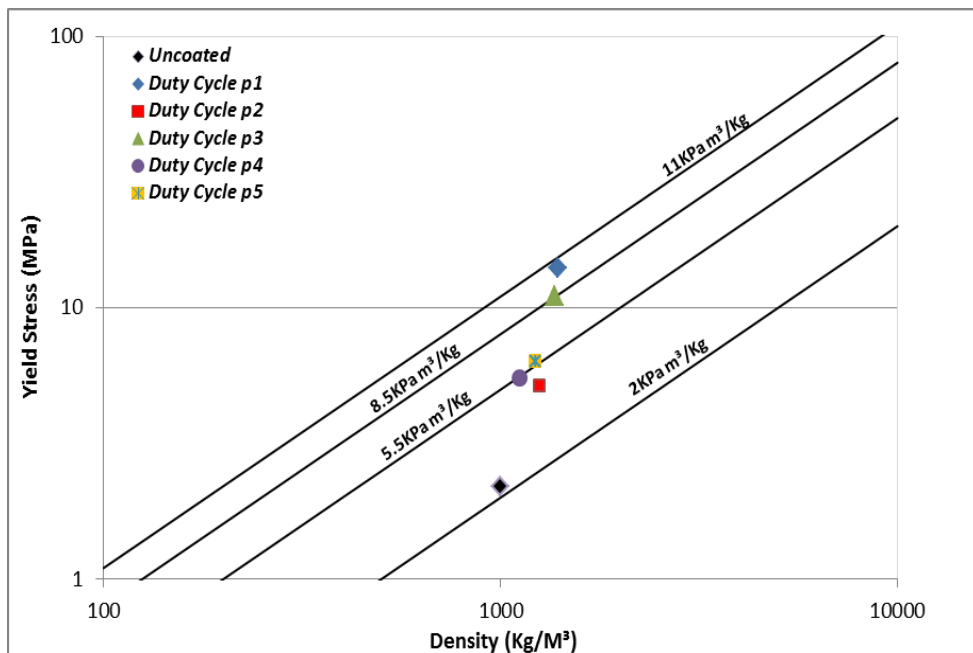
Figure 7.20 - Log–log plot of values of specific strength (mean yield strengths divided by mean density) for different treated and unprocessed foam samples. Lines of equal specific strength (σ$_s$, yield strength divided by density) are included on the figure to indicate the relative levels of different data points.

7.2.3. Investigation of Coating Properties

As is the case for other coatings examined earlier, coatings produced under the different duty cycles were investigated using XRD, EDX and nanoindentation tests.

XRD spectrums taken from the different PEO coatings produced are shown in figure 7.21. It can be seen that alpha and gamma alumina (α and γ-Al_2O_3) are the two main phases present in the different coatings, although mullite phase is also found at small quantities, with the highest level seen for coating formed at duty cycle p_4.
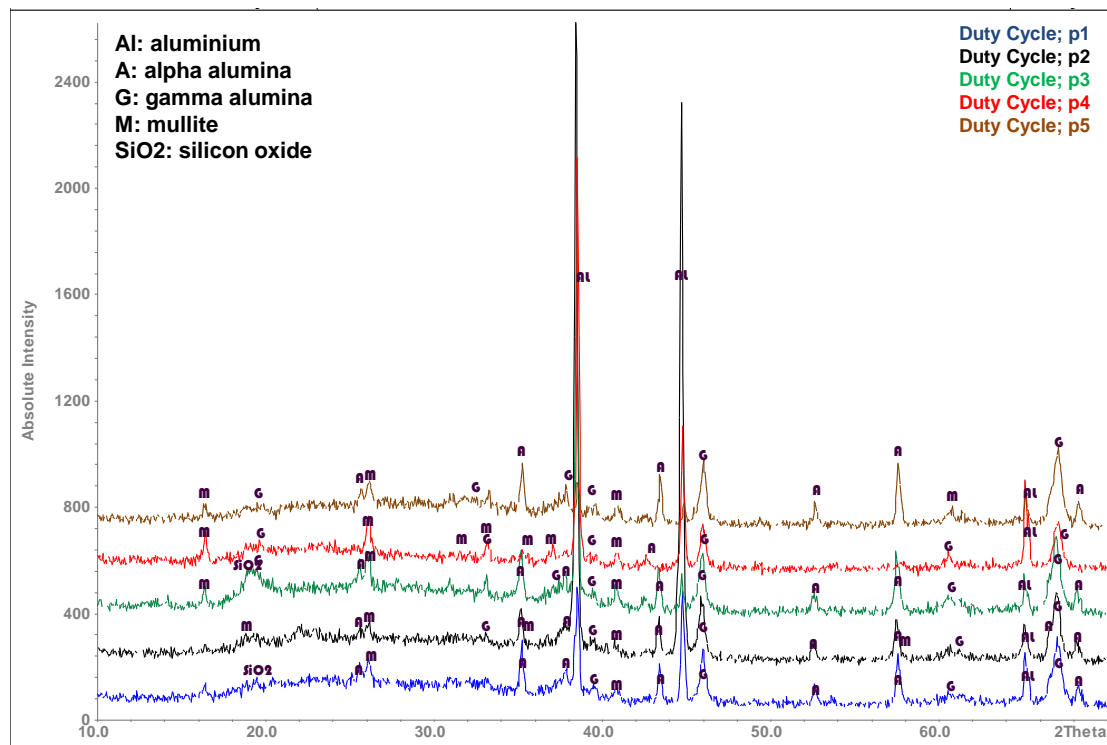
Figure 7.21 - X-rays diffraction patterns of the different PEO coatings produced at frequency of 250 Hz, using different duty cycles (different on/off ratios in positive and negative bias), on Al foam samples. The phases are identified using the following PDF data: Al – [04-0787]; A – [10-0173]; G– [10-0425]; M – [73-1253]; SiO_2 - [18-1170].

The lower peak intensities and the wide background noise levels in the same figure confirm the presence of amorphous phases in the coatings.

EDX analysis was carried out on coatings grown under the different duty cycles. SEM images recorded during EDS mapping of coatings produced under processing conditions of p_1, p_2, p_3, p_4 and p_5 respectively are presented in figure 7.22. The typical scanning areas used for measuring coating elements from each cross-section are shown on the SEM images.
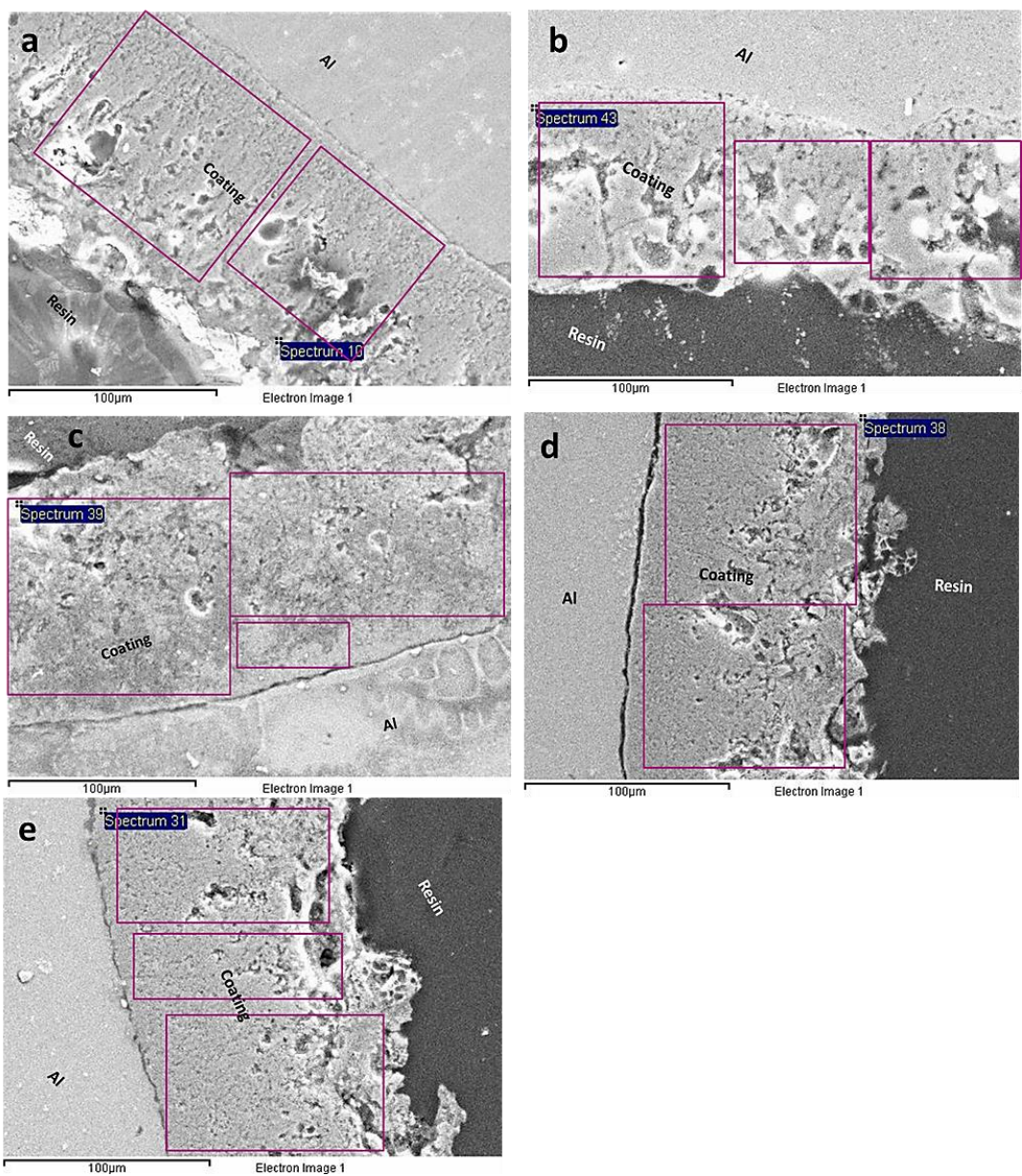
Figure 7.22 - SEM micrographs obtained during the EDS analysis of coating cross-sections produced at frequency of 250Hz but different duty cycles (different on/off ratios in positive and negative bias) of , a) p_1, b) p_2, c) p_3, d) p_4 and e) p_5 on Al foam samples respectively. Boxes indicate typical areas selected for the analysis.

It can be seen from figure 7.23 that there is almost no difference in the elemental distribution of aluminium, oxygen and silicon in each coating. The silicon content in coating produced under p_2 condition varies slightly than the other coatings, but this is within the standard error.
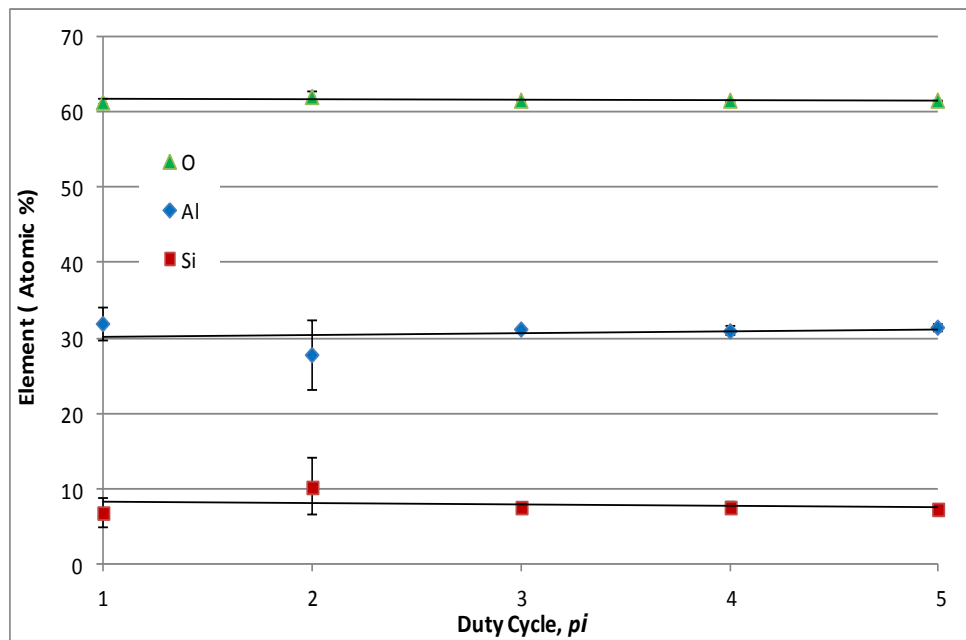
Figure 7.23 - Effect of different waveform ratios on levels of PEO coatings main elements. Current pulse frequency adopted at 250Hz during processing. Note that line of best fit is used.

It is observed that for the coating with higher Si content, the coating quality is reduced and the effect of this trend is reflected in the reduction of the mechanical properties of coated foams, in terms of specific properties (coating and foam). This is more evident with frequency change (i.e. f_4) and likely to be also shown for duty cycle p_2 condition.

The nanoindentation tests were performed on samples of each coating condition. Figure 7.24 shows the measured local elastic modulus and hardness for the different coatings, and the average values are shown in table 7.7.

Table 7.7 – Average values for hardness and modulus (GPa) for all of the different coatings tested.

Coating	Duty Cycle	Volume Averaged, t (μm)	Hardness (GPa)	Modulus (GPa)
PEO	p_1	83	11.2 ± 3	153 ± 33
	p_2	60	7.7 ± 3	84 ± 24
	p_3	70	11.3 ± 3	162 ± 28
	p_4	45	10 ± 2.5	143 ± 22
	p_5	85	11.6 ± 2.8	154 ± 32

The average hardness for these coatings were found to be 11.2, 7.7, 11.3, 10, 11.6 GPa for coatings formed under p_1, p_2, p_3, p_4 and p_5 conditions respectively. The elastic modulus follows a similar trend, averaging at 153, 84, 162, 143 and 154 GPa respectively.
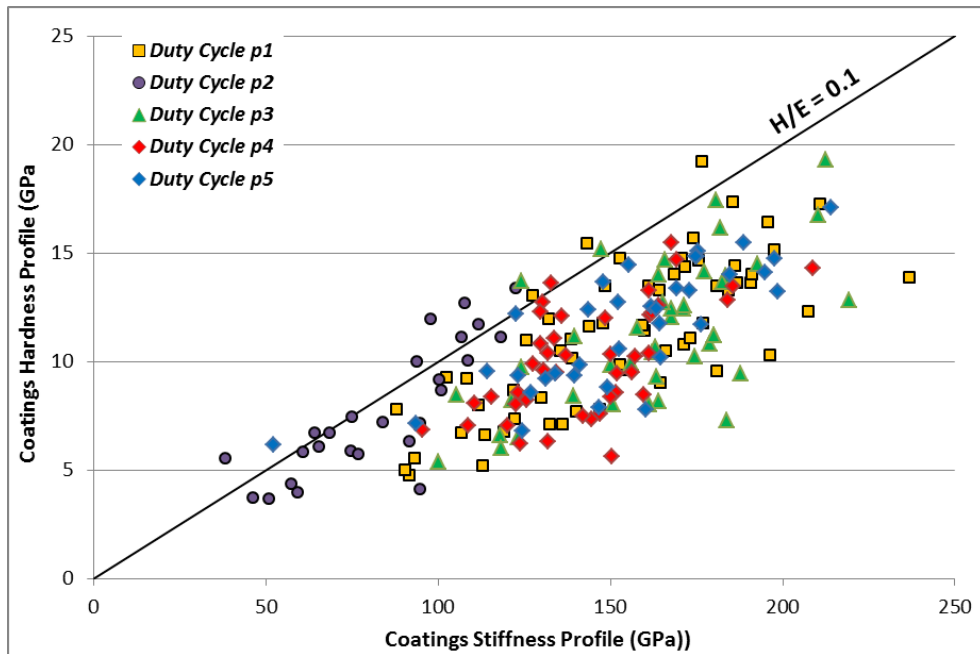
Figure 7.24 - Cross-sectional measurements of coating hardness profiles versus resultant elastic modulus for the different types of coatings produced at frequency of 250 Hz and different duty cycles in the present study. Note that line representing H/E = 0.1 is also shown.

The variation in local hardness and stiffness across coating thicknesses has been observed in other PEO coatings produced in both the present work and in other work [104, 111, 115], and is likely to be for similar reasons; the existence of multi phases present and other microstructural features such as micropores and microcracks.

The coating produced under p_2 condition shows a higher population of larger pores and microcracks (see figure 7.22.b) and seems to have no internal compact coating layer which is present in the coatings grown under p_1, p_3, p_4 and p_5 conditions. Such porosity is expected to affect coating properties giving rise to low hardness and stiffness, as shown in figure 7.24, which influences the coated foam mechanical properties. Even so, the ratio of H/E, typically higher values are favored for wear resistance applications, shows that the effect of such porosity is more pronounced

on stiffness than on hardness. Similar trend of reducing coating stiffness with distance from metal/coating interface, shown for the coatings produced under different frequencies, is seen with the present coatings, as seen in figure 7.25. This confirms that the outer coating layer contains large amount of porosity and structural defects, as compared with the inner compact coating layer.
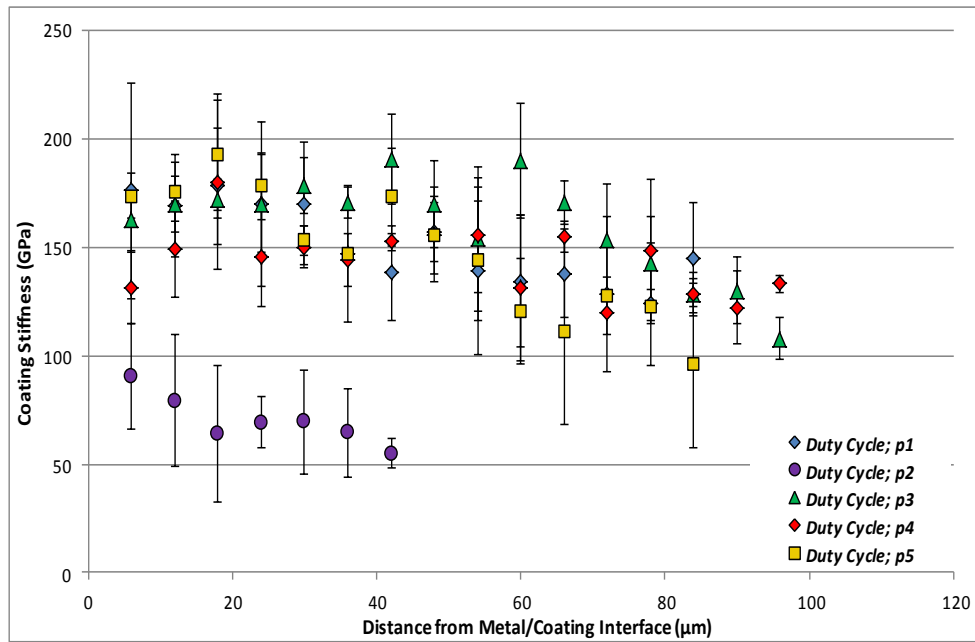
Figure 7.25 - Local stiffness distribution across coating PEO coating thicknesses for the different duty cycles; p_1, p_2, p_3, p_4 and p_5 respectively.

Furthermore, figure 7.25 shows that the highest value of stiffness measured for coating grown under p_1, p_2, p_3 and p_4 conditions was found approximately 18 - 20 μm distance from the metal/coating interface. This is consistent with there being middle denser region which contains larger amounts of high temperature phases.

Based on the analysis above, it can be noticed that coating quality (i.e. level of coating porosity, microcracks and the intrinsic stresses) and distribution throughout the structure may have the predominant effect on the mechanical properties of foams. Other factors such as coating thickness and phase composition are also evidently important but their effects may be less, especially when coatings produced under similar processing conditions (e.g. processing time and electrolyte composition etc.). The key requirement is to have good quality coating; this cannot easily be compensated for by increasing coating thickness. This has been evident in coatings

produced under duty cycles p_2 and p_5 where, in both cases, coating penetration into the foam interior was found to be very low, as shown in figure 7.17. Furthermore, coating grown under duty cycle p_2 has the lowest hardness and modulus, 7.7 GPa and 84 GPa, as compared to the other coatings. Although the average coating thickness was measured at 60 μm, the effect on foam specific strength is lower than that, for example, found with the coating grown under p_4 conditions with an average coating thickness of 45 μm (see table 7.6). For coatings produced under p_5 condition, the coating thickness and coating growth rate were the highest, averaging at 85 μm and 2.13 μm min^{-1} respectively, but the effect on foam yield stress and specific strength is not substantial (see figure 7.18, 7.20 and table 7.6). This effect can be explained by the fact that for coatings grown under condition p_2, the short anodic (positive bias) current of ON time duration (1.1 ms) does not allow for enough aluminium to be oxidized, and as this was followed by the longest OFF time (0.4 ms, see figure 7.16 and table 7.5), means that the effect is greater. On the other hand, the long ON time with the cathodic (negative bias) current allows liberation of more gaseous products (H_2 and O_2), as seen in the reactions below. The hydrogen (H_2) released is expected to form bubble-like or larger defect features within the coating layer, suggesting that oxygen or hydrogen can be evolved from near the substrate. The half-reactions occurring as result of anodic and cathodic current at the anode and cathode are shown respectively as follows:

$$Al \rightarrow Al^{3+} + 3e^- \qquad\qquad (7.1)$$
$$2OH^- + 2e \rightarrow \uparrow H_2 + O^{2-} \qquad\qquad (7.2)$$

This can be also observed for coatings produced under p_5 condition, where the longest ON time (2.25 ms) in cathode (negative bias) current aids the formation of these features within the coating, but a smaller amount of these cavities was observed. This was due, at least partly, to the sufficient time for aluminium to be oxidized by the anodic current (longer pulse ON time in the negative bias).

Jaspard-Mécuson et al. [141] recently reported some work on the effect of different positive to negative charge ratios on macroscopic properties PEO coatings. This work showed that with higher negative charge quantity than the positive one, a consistent thicker coating with no large defects can be formed. The process was shown to deliver no damaging stronger discharges and has been termed as a "soft

sparking"[141]. This effect, however, can only be achieved for processing time of longer than 40 - 50 minutes. Below this time, there is no such effect. In the present work, the processing time has been 40 minutes, and so a comparison may not be applicable.

For duty cycle p_4, although coating thickness and growth rate were the lowest in comparison with the other conditions, as seen in table 7.6 and figure 7.18, coating distribution inside the foam was found to be almost uniform (see figure 7.17) and the nanoindentation analysis showed that this coating has, although not the highest values, the least variation in hardness and modulus (see average values in table 7.7 and figure 7.24), which can be directly interpreted by the fact that this coating contains a smaller amount of porosity and microcracks. Moreover, during the nanoindentation test, it was noticed that only fewer indents were not successful because of porosity or a crack whilst this effect was reported more with the other coatings. The effect of these two parameters (coating uniformity and quality) can be seen in the increase in foam specific strength (5.5 MPa g^{-1} cm^{-3}), which was higher than, for example, the specific strength found for coating grown under p_2 condition (5.2 MPa g^{-1} cm^{-3}), especially when taking into account the increase in absolute density after coating of foams (see table 7.6).

7.3. The effect of Time on Duty Cycle p_4 Condition

This fourth process optimisation step was carried out specifically for duty cycle p_4 because under this condition coating distribution was found to be uniform throughout the foam structure and there was less scatter in the data obtained during the nanoindentation tests of the coating. Therefore, it was deemed to be important to investigate the effect of processing time using duty cycle p_4 condition to find out how this would affect coating quality and penetration. The processing times chosen for this part were denoted as t_4, t_5 and t_6 as shown in table 7.8. Foam samples (similar to those shown in figure 7.2) produced by the new developed infiltration rig shown in figure 4.4, in chapter 4, were used for this part of the present work.

Table 7.8 - Different PEO coating processing variables adopted at different stages in this work for coating of open cell aluminium foams. In this optimization stage, different processing times are used to produce coatings under duty cycle p_4 conditions.

Optimization Stage	Processing Variables	Treatment	Variations			Invariables
			Processing time (min)			Frequency at 250 Hz
First	**Time**	t_1	20			
		t_2	40			
		t_3	80			
			Pulse frequency (Hz)			Processing time of 40 minutes, **(t_2)**.
Second	**Frequency**	f_1	50			
		f_2	250			
		f_3	1250			
		f_4	6250			
			δ_+^{on} %	δ_-^{on} %	$\delta_{+/-}^{off}$ %	Processing time of 40 minutes / pulse frequency at 250 Hz, **($t_2 f_2$)**
Third	**Duty Cycles**	p_1	32.5	50	17.5	
		p_2	27.5	50	22.5	
		p_3	35	50	15	
		p_4	32.5	25	42.5	
		p_5	32.5	56.25	11.25	
			Processing time (min)			Processing time of 40 minutes / pulse frequency at 250 Hz/ using on/off ratio 4, ($t_2 f_2 p_4$)
Fourth	**Duty Cycle, ratio 4, p_4**	t_4	20			
		t_5	60			
		t_6	80			

Figure 7.26 - Example stress–strain curves for different PEO coated samples using duty cycle p_4 and different processing times (20, 40, 60 and 80 minutes), as compared to uncoated sample of replicated foam tested in compression.

Compression tests were performed on the coated foam samples and typical stress-strain curves are shown in figure 7.26 in comparison with untreated foam. It can be seen that there is continuous increase in foam strength and specific strength as shown in table 7.9. For the specific strength, there is a steady and continuous increase by around 0.9 MPa g^{-1} cm^{-3}, after each treatment of 20, 40, 60 and 80 minutes.

Table 7.9 – Average compression test results for the different types of PEO treated foams as well as thicknesses of coating applied, absolute density change, and other mechanical properties.

Foam	Duty Cycle	Treatment Time (min)	Volume Averaged, t (µm)	Absolute Density after Coating, (increase) $g\ cm^{-3}$		Yield Stress σ, MPa	Specific Strength σ/ρ, MPa $g^{-1}\ cm^{-3}$	Energy Absorbed, W (J/cm^3)
Replicated (1.6 mm pores)		**None**	0	1.03±0.0	(+0.0)	2.2±0.4	2.2	1.74±0.4
	p_4	20	19.4	1.15±0.02	(+0.03)	5.4±0.5	4.6	3.0±0.1
		40	45	1.12±0.03	(+0.07)	6.2± 0.3	5.5	3.0±0.2
		60	38	1.2±0.01	(+0.09)	7.7±0.7	6.4	3.4±0.1
		80	55	1.24±0.03	(+0.12)	9±1.3	7.3	3.8±0.2

This may indicate that coating quality has not been affected by the long processing time of 80 minutes. During the first processing stage, though, the use of longer treatment time in the t_3 condition (80 minutes treatment) did not improve the foams properties and the average yield stress and the specific strength were almost the same as those samples treated under t_2 conditions (40 minutes processing time) as shown in table 6.2 and figure 6.7 in chapter 6. Thus, the benefit is obtained for p_4 conditions as the quality of the coating is improved.

Comparison between the increase in absolute density (g cm^{-3}) after coatings using different duty cycles and duty cycle p_4 with 20, 40, 60 and 80 minutes treatment times is shown in figure 7.27. It can be noticed that the increase in coated foam density for the longest treatment time for duty cycle p_4 (80 minutes resulted in 0.11 g cm^{-3} increase) is far less than any other treatment condition with a processing time of 40 minutes only (values measured in the range of 0.18 – 0.34 g cm^{-3}).
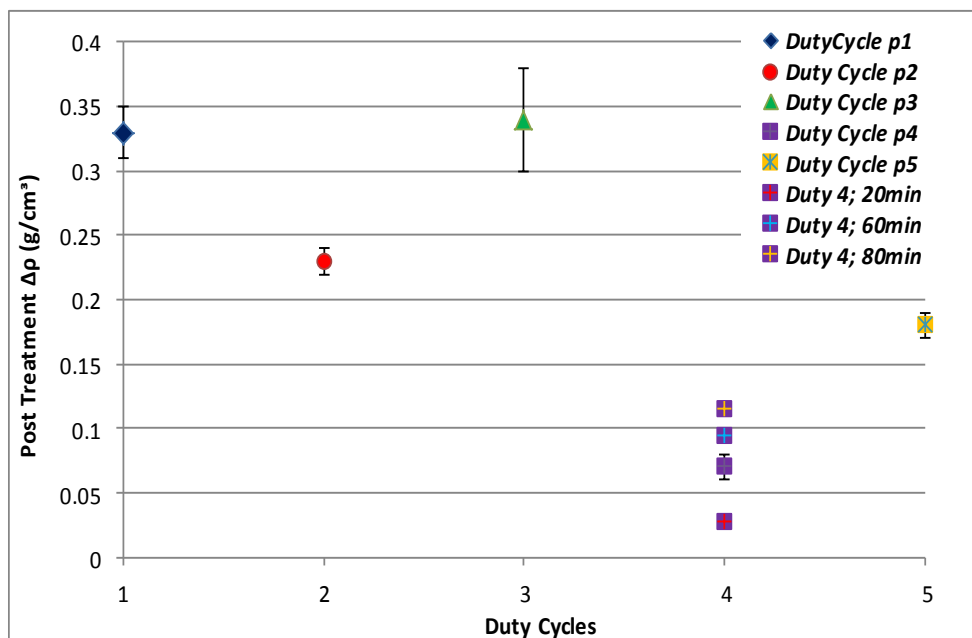
Figure 7.27 - Effect of using different processing times of 20, 60 and 80 minutes for duty cycle p_4 on the absolute density change Δρ of foams during PEO treatments. Comparison between density increase for other different duty cycles (p_1, p_2, p_3 and p_5 conditions) and duty p_4 is also included.

Comparison between coated foams yield stresses using different duty cycles p_1, p_2, p_3 and p_5 and duty cycle p_4 with 20, 40, 60 and 80 minutes treatment times is shown in figure 7.28.
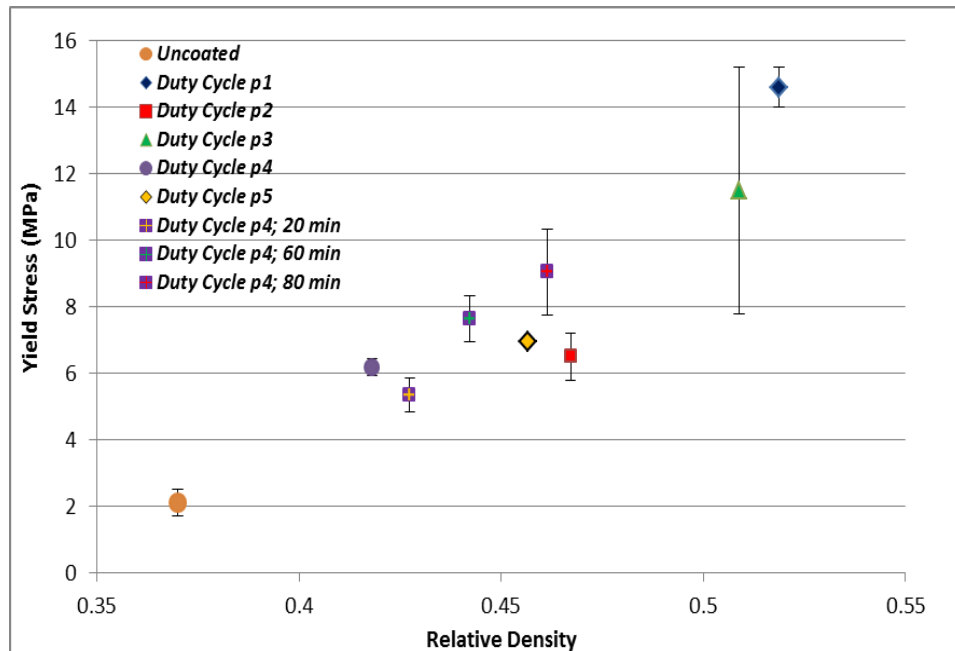
Figure 7.28 – Comparison showing the effect of using different duty cycles and duty cycle p_4 with 20, 60 and 80 minutes treatment times during PEO treatments of foams on increase in their yield stress. The graph represents the yield stress as function of foams relative densities. Error bars are standard deviation obtained from duplicate tests.

It can be seen that there are gradual improvements in achieving strength increase at the lowest cost of density increase which is presented by the foams treated at duty cycle p_4 for the different times. Because of the difference in processing times for duty cycle p_4 condition, an alternative measure of the ratio of the increase in foam strength per unit weight of coating should be considered and this is discussed in detail in the following section 7.4.

Typical scanning areas on the different coating cross-sections for this analysis are shown in figure 7.29. EDS analysis of these coatings shows that there is a trend of increasing silicon content with increasing processing times, as shown in figure 7.30.
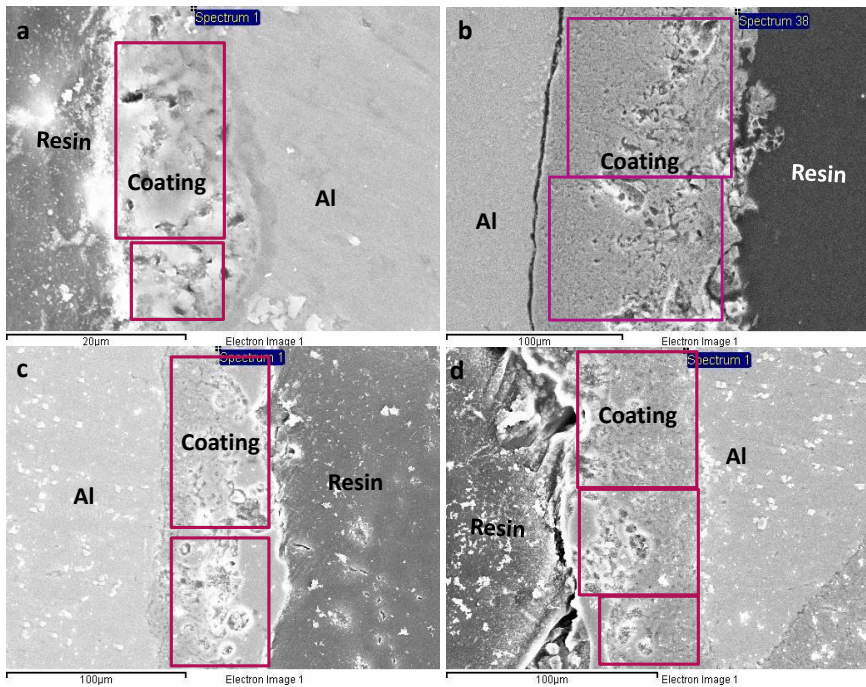
Figure 7.29 - SEM micrographs obtained during the EDS analysis of coating cross-sections produced at different treatment times of a) 20, b) 40, c) 60 and d) 80 minutes) using p_4 condition.

The content of Si reached 10 % for coatings produced at 60 and 80 minutes, but there has been associated negative effect on the foams mechanical properties, as was the case, for instance, for coating produced under f_4 and possibly p_2 conditions where possible effect of 10 % Si content has been observed. This leads to the possibility that the assumption made previously that when silicon content reaches 10 % or more, it will negatively affect the coating may not be correct. It may rather be that coatings that already contain large amount of porosity will be more affected by silicate phases. Kalkanci and Kurnaz [115] pointed out that glassy phase, found to form in coatings containing 6.1 - 7.85 % Si, fills the pores on the coating surface, leaving behind distributed occluded pores within the coating. Coating produced under p_4 condition has been found to contain the least amount of porosity, as compared with coatings grown under other conditions, which was evident from the nanoindentation results shown in figure 7.24 and 7.25, where less variation was observed.
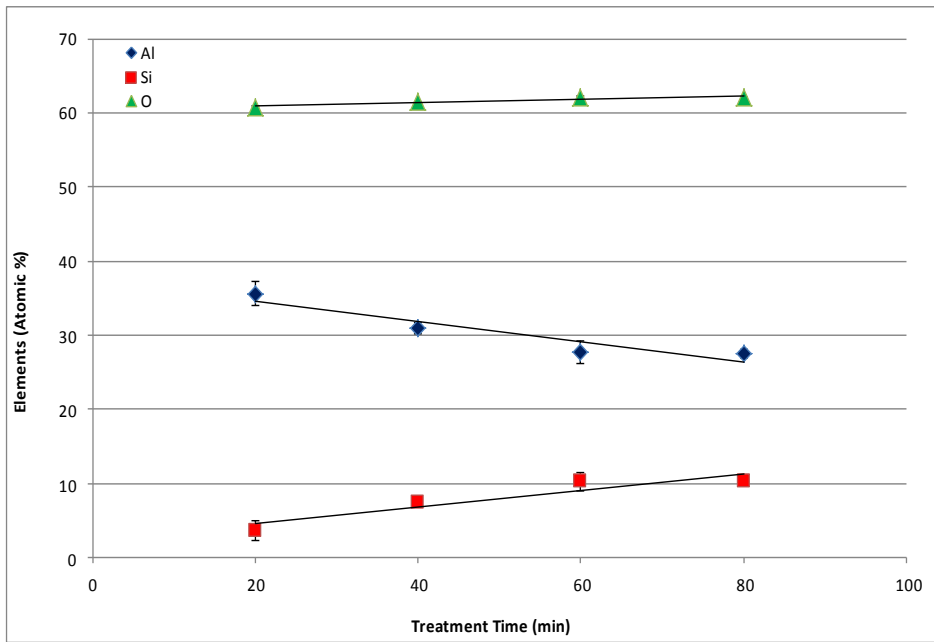
Figure 7.30 - Effect of different treatment times on levels of PEO coatings main elements. Coatings formed using current pulse adopted at 250Hz using duty cycle p_4. Note that line of best fit is used

According to the above analysis, it can be pointed out that PEO coatings structure and penetration into the foams interior are largely influenced by the current distribution which affects current density on the inner and outer surfaces. The general effect of different current distributions during PEO processing on irregular shaped samples has been previously investigated [94, 124, 126]. Current distribution is affected by the geometry of the sample under treatment, and it is found that the current density is higher at the edges and corners than in the middle regions of a sample. This may explain why the thickness of oxide layer increases in these regions, which causes the resistance of the coating to be higher than elsewhere. Due to such high resistance and high current concentration, coatings in these regions may experience the formation of some structural defects and cracks, due to strong discharge penetration into the coating and this ultimately results in current redistribution.

Deep into the foam structure, current distribution is more likely to be affected by internal edges and the enclosed spaces and this leads to low or no current density at the inner surfaces. The current distribution has been found to be affected by surface potential distribution, which can be due to electrolyte resistance, resistance polarisation of the oxide layer and concentration polarization and shielding by

gaseous products [142]. The sum of these differing resistances can be shown schematically in figure 7.31, as follows:
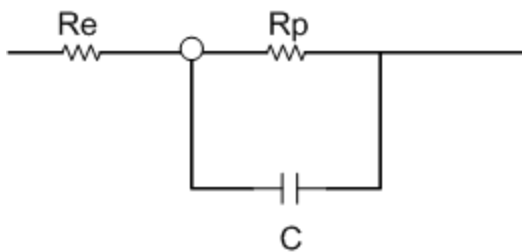
Figure 7.31 – schematic diagram showing the electrolyte resistance (Rp), polarization resistance (Rp) and the resistance provided by the dielectric, oxide film formed, (C), which contribute to the change in current distribution on the treated sample during PEO process [143].

The capacitance, C (C/V) of an oxide layer of a given thickness can be calculated from the following formula [144]:

$$C = \frac{\varepsilon_r \, \varepsilon_0 \quad A}{t} \qquad (7.3)$$

where ε_r is the permittivity of the dielectric (F m^{-1}) (the oxide film), ε_0 is the permittivity of vacuum, and is = 8.855 x 10^{-12} (F m^{-1}), A is the surface area of the dielectric and t is the thickness of the dielectric. It is therefore expected that the capacitance of the PEO coating will be higher in a porous material than in a dense one with coatings of the same thickness (t), as the surface area (A) for porous metals is higher. This has been shown experimentally for both foam and dense aluminium in work by Yerokhin, et al. [143].

The effect of current redistribution and the resultant current density can be shown in figure 7.32. At the beginning of the process, the increase in voltage leads to small increase in current (region A, figure 7.32), however, after reaching sufficient critical voltage, the oxide layer breaks down (point B).
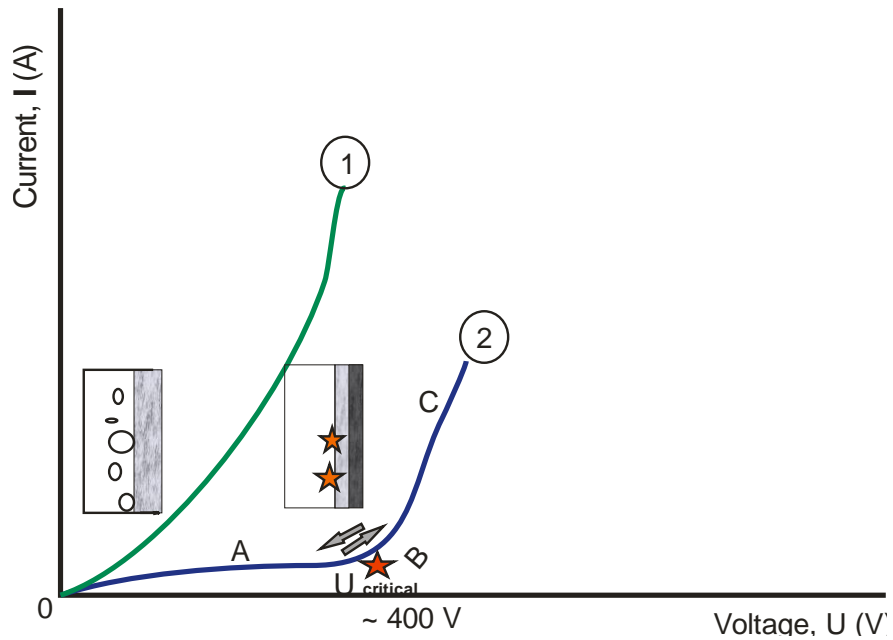
Figure 7.32 - Schematic diagram (after ref. [7]) of two different current-voltage characteristics for the PEO process with 1) showing reactions occurring in the near-electrode area and (2) in the dielectric oxide film on the electrode surface. Point B represents the critical voltage beyond which the oxide film formed initially breaks down.

This results in the formation of micro-discharges, distributing on the surface of the treated sample and aiding the processes (melting, re-melting and ejection of molten metal e.g. Al) of PEO coatings (region C). Due to the effects of differing resistances (electrolyte, dielectric coating, holes and edge effects, break down of the coating etc), voltage and current drop, resulting in current redistribution, C ↔ A (from region C to region A). This effect will be more pronounced and frequent in the treatment of irregular shaped samples, which contain more holes and edges. Even though coating growth continues due to an increase in the size and intensity of the micro-discharges, coating penetration into the pores will always be interrupted by the change in current density distribution and the resistances encountered from different systems.

7.4. General Discussions of Optimization Process

This section highlights the impact of the current work in improving foams mechanical properties, where a comparison is made between the properties of the PEO coated foams and foams coated by other materials and techniques. It should be noted that materials with high strength and low weight would be the most attractive for many applications. This means that the weight-specific property is of great interest, which can be calculated by the strength or stiffness divided by the density [12]. It has been shown that that metallic foams possess higher values of these properties than some bulk metals [12], and increasing these further will be advantageous for different applications. Furthermore, the weight-specific strength of coated foams have been quantified [83] by calculating both the increase in foam properties after application of different coatings and the corresponding increase in foams absolute density as follows :

$$\Delta\sigma = \sigma_{coating}^{foam} - \sigma_{Al}^{foam} \qquad (7.4)$$

$$\Delta\rho = \rho_{coating}^{foam} - \rho_{Al}^{foam} \qquad (7.5)$$

Therefore the specific strengths (σ/ρ), the increase in foam strength (Δσ) and foams density (Δρ) of the different coated foams in the present study and other work [1, 84, 85] are recorded in table 7.10 and figure 7.33 respectively.

Table 7.10 - Effects of different applied coatings on specific strength, strength increase, density increase and specific increase in foam strength of open cell aluminium foams from the present and 3 other works [1, 84, 85].

| Source | Technique/ Types of Coating | Variables | | σ/ρ (MPa g^{-1} cm^{-3}) | $\Delta\sigma$ (MPa) | $\Delta\rho$ (g cm$^{-)3}$ |
		Variable	Values			
Lausic et al. 2012	Electrodeposition/ Ni	Coating Thickness	24.2 µm	10.8	3.9	0.28
			39.4 µm	11.5	5.7	0.41
			46.2 µm	12.3	7.1	0.49
			55.8 µm	13.1	8.6	0.56
			71.9 µm	14.6	12.6	0.76
Bouwhuis et al. 2009	Electrodeposition/ Ni	Coating Thickness	25.6 µm	5.8	1.6	0.29
			39 µm	7	2.9	0.41
			47.3 µm	6	2.96	0.52
			56.7 µm	6.3	3.69	0.6
			72.3 µm	6.7	5.28	0.8
Boonyongmaneerat et al. 2008	Electrodeposition/ Ni-W	Processing Time	60 min	12.2	3	0.2
			180 min	9.7	5	0.5
			180 min	9.6	9	0.98
The present Work	PEO/Ceramic	Processing Time ($t_1 - t_3$)	20 min	5	2.1	0.1
			40 min	8.6	8.1	0.3
			80 min	7.5	8.1	0.5
		Pulse Frequency ($f_1 - f_4$)	50 Hz	3.6	2	0.21
			250 Hz	7.6	8.9	0.43
			1250 Hz	6.2	4.9	0.14
			6250 Hz	3.6	1.8	0.07
		Duty Cycles ($p_1 - p_5$)	Ratio 1	10.5	12.4	0.33
			Ratio 2	5.2	4.3	0.23
			Ratio 3	8.4	9.3	0.34
			Ratio 4	5.5	4	0.07
			Ratio 5	5.7	4.8	0.18
		Processing Time on Ratio 4 (p_4)	20 min	4.6	2.7	0.03
			60 min	6.4	5.45	0.1
			80 min	7.3	6.85	0.12

As it can be seen, the optimized PEO coatings improved the foam's specific strength in all conditions examined. For instance, the highest increase in strength $\Delta\sigma$ of 12.4 MPa alongside with an increase in density $\Delta\rho$ of 0.33 g cm^{-3} was obtained for foam coated under processing conditions of (t_2 f_2 p_1); that is 40 minutes treatment time, 250Hz pulse frequency and duty cycle 1, resulting in the highest overall specific strength of 10.5 MPa g^{-1} cm^{-3}. This value is ~ 377 % greater than that obtained for unprocessed foam with specific strength of ~ 2.2 MPa g^{-1} cm^{-3}. In the study of electrodepositing nanocrystalline Ni-W alloy [1] with the thinnest coating applied (~

10 μm) to the foams, the maximum effective specific strength recorded was ~ 12.2 MPa g^{-1} cm^{-3}, as compared to a value of ~ 9.1 MPa g^{-1} cm^{-3} for an uncoated foam sample. Further increases in coating thickness (~ 30 μm) resulted in a very small increment in specific strength, as result of a large increase in density that accompanied the strength increase. Moreover, when applying nanocrystalline Ni to aluminium foams [83], the specific strength increased from 6.43 to 6.7 MPa g^{-1} cm^{-3} after applying the thickest layer ~ 72.3 μm. Following the work in ref.[83], a recent study [84] reported a maximum increase in specific strength of coated foam from a value of 6.6 MPa g^{-1} cm^{-3}, when uncoated, to 14.6 MPa g^{-1} cm^{-3}, which resulted from the application of 72 μm thick n-Ni coating. The maximum increase in specific strength from previous work is estimated to be ≤ 120 % relative to that of uncoated foams of their type. The increase in specific strength for the present coated foams is much higher (~ 377 %). This implies that for applications where weight-specific properties matter, properties such as density and adhesion of the coating materials (which are found to be very good for PEO coatings) are as crucial as other properties like stiffness and hardness. For example, the density of plasma electrolytic oxide coating on open cell aluminium foam was estimated to be 2.6 g cm^{-3} [96], although a value of 2.88 g cm^{-3} has been measured [140] for a denser PEO coating on aluminium alloy. Both values, however, are still lower than a value of 3.8 g cm^{-3} expected for fully dense alumina. The difference is attributed to large amount of porosity contained within the coatings formed [104]. These values are much lower as compared to other coatings used for foams; with densities of the Ni–13W and Ni–20W (at.%) alloys = 10.8 and 11.7 g cm^{-3} while the Ni coatings have density of ~ 8.9 g cm^{-3} [1, 83].

Comparison between the strength increases and density increases calculated for the different coated foams is shown in figure 7.33, which illustrates the benefits of the application of PEO coatings on open cell aluminium foams as compared to other work mentioned above. This can be shown following eq. 7.4 and 7.5 respectively. In the present study, this was calculated as $\Delta\sigma = \sigma_{PEO/Al}^{foam} - \sigma_{Al}^{Foam}$, for strength increase, and $\Delta\rho = \rho_{PEO/Al}^{Foam} - \rho_{Al}^{Foam}$ for density increase.
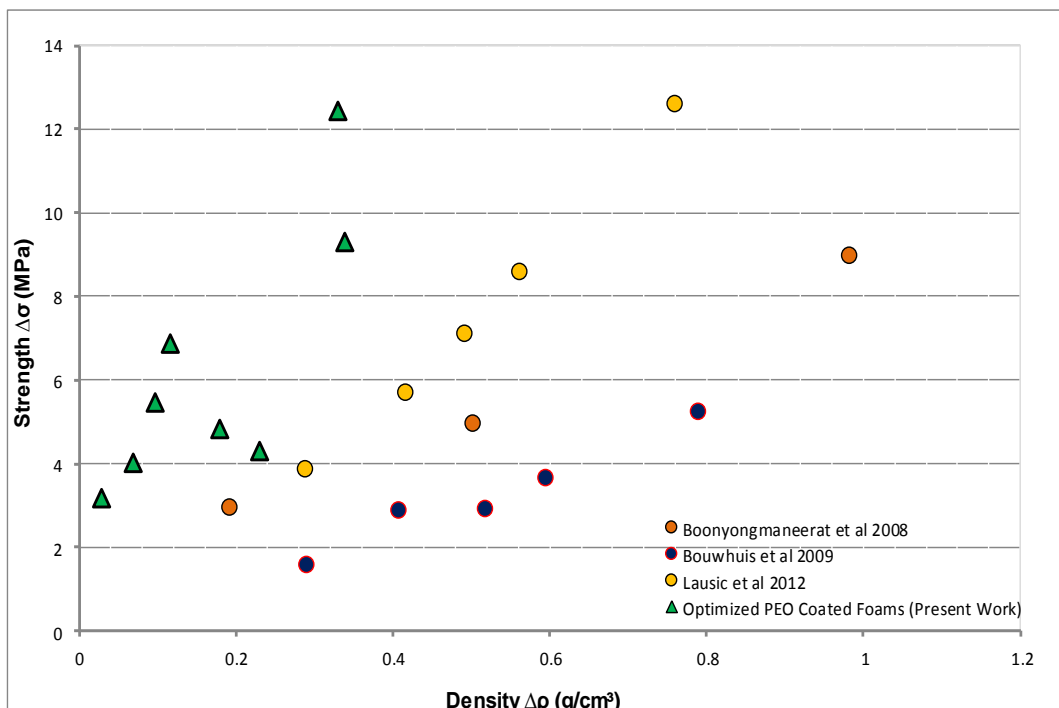
Figure 7.33 - Experimentally measured strength increase $\Delta\sigma$ plotted against density increase $\Delta\rho$ for coated open cell aluminium foams from the present work and 3 other different studies [1, 84, 85].

It can be seen that, for all PEO coated foams in the present study, large strength increase may be accomplished with lesser increase in foam density (all data are located farthest to left), as compared other coated aluminium foams. It can be further noted that large improvements in achieving strength increase at the lowest cost of density increase are presented with foams treated under (t_2 f_2 p_4) processing conditions, and with the effect of time on duty cycle p_4 the effect is even greater (these data are shown in figure 7.33).

Most work on PEO has focused on aluminum alloys. This has been the case since these alloys are, along with other several different alloys (e.g. Ti, Mg), used as components in many different fields of industries, including aerospace, automobile, and so on. Therefore, the aim was to enhance the surface and mechanical properties of these materials further by the applications of such technique. This project, on the other hand, is investigating the effects of this technique on pure aluminum (99.8 % Al) and Duocel foams (6101 alloy).

For aluminum alloys, elements such as Cu, Si, Mn, Mg, are the main alloy additions, and the effects of these elements on the metallurgical side of the coating morphologies and microstructure must be taken into account if the impact of current

work is to be transferred to aluminum alloys. As explained in chapter 3, aluminum alloying element such as Cu and Mg can significantly increase the amount of crystalline metastable phase of γ-Al_2O_3, and thermodynamically stable α–Al_2O_3 phase in the PEO coatings formed.

Chapter 8: Conclusions

In this work, Plasma Electrolytic Oxidation (PEO) coating treatments have been applied to open cell foams, with the aim to improve foam mechanical properties. The PEO process can be manipulated, using different parameters, such that a range of coating morphologies, thicknesses and mechanical properties can be achieved. The process was carried out in pulsed bipolar (PBP) current mode and optimized coating conditions were achieved after four different development steps. As detailed in table 4.3 in chapter 4, in the first stage, different processing times were used under processing conditions termed as t_1, t_2 and t_3 (20, 40 and 80 minutes respectively). In the second processing stage, different pulse frequencies under conditions named as f_1, f_2, f_3, and f_4 (50, 250, 1250 and 6250 Hz respectively) were used at a processing time of 40 minutes. Different duty cycles; namely p_1, p_2, p_3, p_4 and p_5 (different ON/OFF durations in a 250 Hz cycle and 40 minute processing time ($t_2 f_2$)) were used in the third PEO processing stage. In stage 4 conditions, further experiments were carried out on coatings produced under $t_2 f_2 p_4$ conditions to investigate the effects of different processing times denoted as t_4, t_5 and t_6 (20, 60 and 80 minutes) on coating deposition rate, microstructure and the foam mechanical properties. Coatings grown under these processing conditions were found to be of a good quality (containing smaller density of defects such as microcracks and probably lower intrinsic stresses), and to have low but well distributed coating thicknesses. These coatings had the greatest effect on foams in terms of strength increase ($\Delta\sigma$) compared to density increase ($\Delta\rho$).

The overall conclusion is that the PEO coating process may be successfully applied to open cell aluminium foams processed using different methods (the investment casting and the replication process), including those where the connection between cells is limited due to high foam density. The effect penetrates into the foam structure, even of relatively low porosity foams, and produces coating, albeit with diminishing thickness further into the structure. In all cases, the application of a low thickness coating leads to improved yield strength, specific strength and energy absorption capability; although this improvement is not maintained as thicker coatings are applied, particularly for low density foams tested in tension. This is

attributed to the conversion of large proportions of the metal to ceramic coating, which displays brittle fracture, and the greater defect concentrations in thicker coated layers. The greatest improvements in foam properties are obtained with the higher density replicated foams, which still retain a substantial ductile core to all of the struts.

The elastic modulus of the coated Duocel foams was improved, however a higher rate of damage and smaller strain to failure were observed for the thickest coating, resulting from t_3 condition. This is likely to be caused by, as is the case for the plastic properties, degradation of the coating properties at high thickness due to increased defect density as well as by general embrittlement of the associated composite foam material.

Analytical models examined to explain the effect of coatings on foam Young's modulus are based on the change in EI of the structural elements (assumed to be the struts), which can be simply calculated for different cross sectional shapes as appropriate. Such models have been compared to the data captured here and data from the literature on open cell metal foams with surface coatings. It was shown in general that the data are better described by models arising from the Gibson-Ashby regular structure, especially when using circular cross-section for beam stiffness analysis, whereas the random fibre array models (appropriate for very low density structure) underestimate the behaviour, although it should be noted that both models capture the trend of the continuous increase in foam stiffness with coating thickness.

PEO pulse frequency influences coating thickness, porosity and the measured mechanical properties. The major effect on coating hardness and elastic modulus as well as on the strength and stiffness of the coated foams is associated with the volume fraction of coating porosity. The optimum frequency was found to be 250Hz, where the yield stress, specific strength and energy absorbed increases are larger than ~ 400 , 250, and 150 % respectively, at a cost of 43% increase in density.

The effect of using different duty cycles (associated with the ON and OFF times in each cycle in the current pulse frequency used) results in different coating morphology, thickness, distribution and deposition rate. Very fast coating growth rate has been shown to be not always beneficial, whereas low coating growth rate (achieved using shorter ON and longer OFF durations in the positive and negative bias) may be useful for the formation of good quality coatings (containing less

microcracks and intrinsic stresses), with potential for close to uniform distribution of coating into the foam interior.

It is observed that coatings containing larger amount of porosity and microcracks are more likely to be affected by the higher Si content (10 wt. % or more), and the effect of this trend is shown in the reduction of the specific mechanical properties of coated foams. This is more evident with frequency change (i.e. f_4) and likely to be duty cycle change (specifically p_2).

The evaluation concerning the strength increase ($\Delta\sigma$) against density increase ($\Delta\rho$) of the coated foams was carried out and a comparison using this criterion with other coated open cell aluminium foams demonstrates that the benefits of PEO coatings to metal foams are greater than those shown by other metal foams coated by different techniques (the greatest improvements in achieving strength increase at the lowest cost of density increase are presented with foams treated under duty cycle p_4 conditions with the different times). The primary reason for this is that the oxide ceramic coatings formed on foams have, as well as the low density, excellent mechanical properties and good adhesion to the substrate. These properties have been improved by the PEO optimization process carried out in the present work.

Finally, the above discussion on manipulating particular parameters of the PEO process gives clear insights into the understanding of how these oxide ceramic layers can be formed evenly in the foam interior, which is essential for optimisation of the treatment process for porous metals. The present results elucidate characteristics of oxide film formation on small scale structural features (steps, pits, concave and convex surfaces, etc) that exist within the foam pores. These will be particularly important for development of new PEO-based surface treatment routines for porous and complex shape components that would allow further enhancement of their performance.

9. References

[1]   Y. Boonyongmaneerat, C. A. Schuh, and D. C. Dunand, "Mechanical properties of reticulated aluminum foams with electrodeposited Ni–W coatings," *Scripta Materialia,* vol. 59, pp. 336-339, 2008.

[2]   B. A. Bouwhuis, T. Ronis, J. L. McCrea, G. Palumbo, and G. D. Hibbard, "Structural nanocrystalline Ni coatings on periodic cellular steel," *Composites Science and Technology,* vol. 69, pp. 385-390, 2009.

[3]   F. Diologent, R. Goodall, and A. Mortensen, "Surface oxide in replicated microcellular aluminium and its influence on the plasticity size effect," *Acta Materialia,* vol. 57, pp. 286-294, 2009.

[4]   M. Suralvo, B. Bouwhuis, J. L. McCrea, G. Palumbo, and G. D. Hibbard, "Hybrid nanocrystalline periodic cellular materials," *Scripta Materialia,* vol. 58, pp. 247-250, 2008.

[5]   J. Banhart, "Manufacture, characterisation and application of cellular metals and metal foams," *Progress in Materials Science,* vol. 46, pp. 559-632, 2001.

[6]   Y. Conde, J. F. Despois, R. Goodall, A. Marmottant, L. Salvo, C. San Marchi, and A. Mortensen, "Replication Processing of Highly Porous Materials," *Advanced Engineering Materials,* vol. 8, pp. 795-803, 2006.

[7]   Yerokhin A. L, Nie X, Leyland A, Matthews A, Dowey S J., "Plasma electrolysis for surface engineering," *Surface and Coatings Technology,* vol. 122, pp. 73-93, 1999.

[8]   R. Goodall, A. Marmottant, L. Salvo, and A. Mortensen, "Spherical pore replicated microcellular aluminium: Processing and influence on properties," *Materials Science and Engineering: A,* vol. 465, pp. 124-135, 2007.

[9]   L. J. Gibson, "Mechanical behavior of metallic foams," *Annual Review of Materials Science,* vol. 30, pp. 191-227, 2000.

[10]   R. Goodall, *Metallic Foams and Sponges* vol. 2: in press, 2013.

[11]   J. Banhart, "Metal foams: Production and stability," *Advanced Engineering Materials,* vol. 8, pp. 781-794, 2006.

[12]   A. G. E. M.F. Ashby, N.A. Fleck, L.J., Gibson J.W. Hutchinson, H.N.G. Wadley, *Metal foams: A design guide*. Boston (MA): Butterworth- Heinemann 2000.

[13]   J. Banhart, "Manufacturing routes for metallic foams," *JOM,* vol. 52, pp. 22-27, 2000.

[14]   J. F. Despois, Y. Conde, C. San Marchi, and A. Mortensen, "Tensile Behaviour of Replicated Aluminium Foams," *Advanced Engineering Materials,* vol. 6, pp. 444-447, 2004.

[15]   C. San Marchi and A. Mortensen, "Deformation of open-cell aluminum foam," *Acta Materialia,* vol. 49, pp. 3959-3969, 2001.

[16]   Q. Fabrizio, A. Boschetto, L. Rovatti, and L. Santo, "Replication casting of open-cell AlSi7Mg0.3 foams," *Materials Letters,* vol. 65, pp. 2558-2561, 2011.

[17]   F. Diologent, R. Goodall, and A. Mortensen, "Creep of aluminium–magnesium open cell foam," *Acta Materialia,* vol. 57, pp. 830-837, 2009.

[18]   F. Diologent, E. Combaz, V. Laporte, R. Goodall, L. Weber, F. Duc, and A. Mortensen, "Processing of Ag–Cu alloy foam by the replication process," *Scripta Materialia,* vol. 61, pp. 351-354, 2009.

[19]   A.-E. Belhadj, S.-A. Kaoua, M. Azzaz, J. D. Bartout, and Y. Bienvenu, "Elaboration and characterization of metallic foams based on tin–lead," *Materials Science and Engineering: A,* vol. 494, pp. 425-428, 2008.

[20]   M. P. Staiger, I. Kolbeinsson, N. T. Kirkland, T. Nguyen, G. Dias, and T. B. F. Woodfield, "Synthesis of topologically-ordered open-cell porous magnesium," *Materials Letters,* vol. 64, pp. 2572-2574, 2010.

[21]   N. T. Kirkland, I. Kolbeinsson, T. Woodfield, G. J. Dias, and M. P. Staiger, "Synthesis and properties of topologically ordered porous magnesium," *Materials Science and Engineering: B,* vol. 176, pp. 1666-1672, 2011.

[22] S. R. Casolco, G. Dominguez, D. Sandoval, and J. E. Garay, "Processing and mechanical behavior of Zn–Al–Cu porous alloys," *Materials Science and Engineering: A,* vol. 471, pp. 28-33, 2007.

[23] G. Bertolino, P. A. Larochette, E. M. Castrodeza, C. Mapelli, A. Baruj, and H. E. Troiani, "Mechanical properties of martensitic Cu–Zn–Al foams in the pseudoelastic regime," *Materials Letters,* vol. 64, pp. 1448-1450, 2010.

[24] E. M. Castrodeza, C. Mapelli, M. Vedani, S. Arnaboldi, P. Bassani, and A. Tuissi, "Processing of shape memory CuZnAl open-cell foam by molten metal infiltration," *Journal of Materials Engineering and Performance,* vol. 18, pp. 484-489, 2009.

[25] E. M. Castrodeza and C. Mapelli, "Processing of brass open-cell foam by silica-gel beads replication," *Journal of Materials Processing Technology,* vol. 209, pp. 4958-4962, 2009.

[26] R. Prieto, E. Louis, and J. M. Molina, "Fabrication of mesophase pitch-derived open-pore carbon foams by replication processing," *Carbon,* vol. 50, pp. 1904-1912, 2012.

[27] J. F. Despois, A. Marmottant, Y. Conde, R. Goodall, L. Salvo, C. S. Marchi, and A. Mortensen, "Microstructural tailoring of open-pore microcellular aluminium by replication processing," vol. 512, ed, 2006, pp. 281-288.

[28] J. F. Despois, A. Marmottant, L. Salvo, and A. Mortensen, "Influence of the infiltration pressure on the structure and properties of replicated aluminium foams," *Materials Science and Engineering A,* vol. 462, pp. 68-75, 2007.

[29] R. Goodall, J. F. Despois, A. Marmottant, L. Salvo, and A. Mortensen, "The effect of preform processing on replicated aluminium foam structure and mechanical properties," *Scripta Materialia,* vol. 54, pp. 2069-2073, 2006.

[30] R. Goodall and A. Mortensen, "Microcellular aluminium? - Child's play!," *Advanced Engineering Materials,* vol. 9, pp. 951-954, 2007.

[31] G. Zaragoza and R. Goodall, "Metal Foams with Graded Pore Size for Heat Transfer Applications," *Advanced Engineering Materials,* pp. n/a-n/a, 2012.

[32] D. R. Lide, *CRC handbook of chemistry and physics : A ready-reference book of chemical and physical data.* Boca Raton: CRC Press, 2001.

[33] A. H. Brothers, R. Scheunemann, J. D. DeFouw, and D. C. Dunand, "Processing and structure of open-celled amorphous metal foams," *Scripta Materialia,* vol. 52, pp. 335-339, 2005.

[34] X. Wei, J. H. Chen, and L. H. Dai, "Energy absorption mechanism of open-cell Zr-based bulk metallic glass foam," *Scripta Materialia,* vol. 66, pp. 721-724, 2012.

[35] Y. Boonyongmaneerat and D. C. Dunand, "Ni-Mo-Cr Foams Processed by Casting Replication of Sodium Aluminate Preforms," *Advanced Engineering Materials,* vol. 10, pp. 379-383, 2008.

[36] K. P. Dharmasena and H. N. G. Wadley, "Electrical conductivity of open-cell metal foams," *Journal of Materials Research,* vol. 17, pp. 625-631, 2002.

[37] Y. Y. Zhao and D. X. Sun, "A novel sintering-dissolution process for manufacturing Al foams," *Scripta Materialia,* vol. 44, pp. 105-110, 2001.

[38] Q. Z. Wang, C. X. Cui, S. J. Liu, and L. C. Zhao, "Open-celled porous Cu prepared by replication of NaCl space-holders," *Materials Science and Engineering: A,* vol. 527, pp. 1275-1278, 2010.

[39] H. Bafti and A. Habibolahzadeh, "Production of aluminum foam by spherical carbamide space holder technique-processing parameters," *Materials & Design,* vol. 31, pp. 4122-4129, 2010.

[40] B. Jiang, N. Q. Zhao, C. S. Shi, and J. J. Li, "Processing of open cell aluminum foams with tailored porous morphology," *Scripta Materialia,* vol. 53, pp. 781-785, 2005.

[41] W. Niu, C. Bai, G. Qiu, and Q. Wang, "Processing and properties of porous titanium using space holder technique," *Materials Science and Engineering: A,* vol. 506, pp. 148-151, 2009.

[42] A. Mansourighasri, N. Muhamad, and A. B. Sulong, "Processing titanium foams using tapioca starch as a space holder," *Journal of Materials Processing Technology,* vol. 212, pp. 83-89, 2012.

[43] A. Jinnapat and A. Kennedy, "The Manufacture and Characterisation of Aluminium Foams Made by Investment Casting Using Dissolvable Spherical Sodium Chloride Bead Preforms," *Metals,* vol. 1, pp. 49-64, 2011.

[44] A. Jinnapat and A. Kennedy, "Characterisation and Mechanical Testing of Open Cell Al Foams Manufactured by Molten Metal Infiltration of Porous Salt Bead Preforms: Effect of Bead Size," *Metals,* vol. 2, pp. 122-135, 2012.

[45] A. Jinnapat and A. R. Kennedy, "The manufacture of spherical salt beads and their use as dissolvable templates for the production of cellular solids via a powder metallurgy route," *Journal of Alloys and Compounds,* vol. 499, pp. 43-47, 2010.

[46] D. T. Queheillalt, D. D. Hass, D. J. Sypeck, and H. N. G. Wadley, "Synthesis of open-cell metal foams by templated directed vapor deposition," *Journal of Materials Research,* vol. 16, pp. 1028-1036, 2001.

[47] M. F. A. L.G. Gibson, *Cellular Solids: Structure and Properties.* London, UK: the University of Cambridge Press, 1997.

[48] E. Andrews, W. Sanders, and L. J. Gibson, "Compressive and tensile behaviour of aluminum foams," *Materials Science and Engineering: A,* vol. 270, pp. 113-124, 1999.

[49] Z. G. Xu, J. W. Fu, T. J. Luo, and Y. S. Yang, "Effects of cell size on quasi-static compressive properties of Mg alloy foams," *Materials & Design,* vol. 34, pp. 40-44, 2012.

[50] E. W. Andrews, J. S. Huang, and L. J. Gibson, "Creep behavior of a closed-cell aluminum foam," *Acta Materialia,* vol. 47, pp. 2927-2935, 1999.

[51] R. Edwin Raj, V. Parameswaran, and B. S. S. Daniel, "Comparison of quasi-static and dynamic compression behavior of closed-cell aluminum foam," *Materials Science and Engineering: A,* vol. 526, pp. 11-15, 2009.

[52] A. Paul and U. Ramamurty, "Strain rate sensitivity of a closed-cell aluminum foam," *Materials Science and Engineering: A,* vol. 281, pp. 1-7, 2000.

[53] V. Gergely and B. Clyne, "The FORMGRIP Process: Foaming of Reinforced Metals by Gas Release in Precursors," *Advanced Engineering Materials,* vol. 2, pp. 175-178, 2000.

[54] V. Gergely, D. C. Curran, and T. W. Clyne, "The FOAMCARP process: foaming of aluminium MMCs by the chalk-aluminium reaction in precursors," *Composites Science and Technology,* vol. 63, pp. 2301-2310, 2003.

[55] M. F. Ashby, "The properties of foams and lattices," *Philosophical Transactions of the Royal Society A: Mathematical, Physical and Engineering Sciences,* vol. 364, pp. 15-30, 2006.

[56] M. F. Ashby, A. G. Evans, N. A. Fleck, L. J. Gibson, J. W. Hutchinson, and H. N. G. Wadley, "Chapter 4 - Properties of metal foams," in *Metal Foams*, ed Burlington: Butterworth-Heinemann, 2000, pp. 40-54.

[57] K. Y. G. McCullough, N. A. Fleck, and M. F. Ashby, "Uniaxial stress–strain behaviour of aluminium alloy foams," *Acta Materialia,* vol. 47, pp. 2323-2330, 1999.

[58] E. Koza, M. Leonowicz, S. Wojciechowski, and F. Simancik, "Compressive strength of aluminium foams," *Materials Letters,* vol. 58, pp. 132-135, 2004.

[59] L. Babout, E. Maire, J. Y. Buffière, and R. Fougères, "Characterization by X-ray computed tomography of decohesion, porosity growth and coalescence in model metal matrix composites," *Acta Materialia,* vol. 49, pp. 2055-2063, 2001.

[60] H. Bart-Smith, A. F. Bastawros, D. R. Mumm, A. G. Evans, D. J. Sypeck, and H. N. G. Wadley, "Compressive deformation and yielding mechanisms in cellular Al alloys determined using X-ray tomography and surface strain mapping," *Acta Materialia,* vol. 46, pp. 3583-3592, 1998.

[61] Q. Zhang, P. D. Lee, R. Singh, G. Wu, and T. C. Lindley, "Micro-CT characterization of structural features and deformation behavior of fly ash/aluminum syntactic foam," *Acta Materialia,* vol. 57, pp. 3003-3011, 2009.

[62] J. Zhou, P. Shrotriya, and W. O. Soboyejo, "Mechanisms and mechanics of compressive deformation in open-cell Al foams," *Mechanics of Materials,* vol. 36, pp. 781-797, 2004.

[63] M. S. Aly, "Tensile properties of open-cell nickel foams," *Materials & Design,* vol. 31, pp. 2237-2240, 2010.

[64] M. Shehata Aly, "Fracture of open-cell nickel foams under quasi-static tensile loading," *Journal of Materials Engineering and Performance,* vol. 19, pp. 1306-1310, 2010.

[65] M. Shehata Aly, A. Almajid, S. Nakano, and S. Ochiai, "Fracture of open cell copper foams under tension," *Materials Science and Engineering: A,* vol. 519, pp. 211-213, 2009.

[66] K. Stöbener, D. Lehmhus, M. Avalle, L. Peroni, and M. Busse, "Aluminum foam-polymer hybrid structures (APM aluminum foam) in compression testing," *International Journal of Solids and Structures,* vol. 45, pp. 5627-5641, 2008.

[67] L. Vendra and A. Rabiei, "Evaluation of modulus of elasticity of composite metal foams by experimental and numerical techniques," *Materials Science and Engineering: A,* vol. 527, pp. 1784-1790, 2010.

[68] J. F. Despois, R. Mueller, and A. Mortensen, "Uniaxial deformation of microcellular metals," *Acta Materialia,* vol. 54, pp. 4129-4142, 2006.

[69] D. P. Kou, J. R. Li, J. L. Yu, and H. F. Cheng, "Mechanical behavior of open-cell metallic foams with dual-size cellular structure," *Scripta Materialia,* vol. 59, pp. 483-486, 2008.

[70] E. Amsterdam, J. T. M. De Hosson, and P. R. Onck, "On the plastic collapse stress of open-cell aluminum foam," *Scripta Materialia,* vol. 59, pp. 653-656, 2008.

[71] E. Amsterdam, J. H. B. de Vries, J. T. M. De Hosson, and P. R. Onck, "The influence of strain-induced damage on the mechanical response of open-cell aluminum foam," *Acta Materialia,* vol. 56, pp. 609-618, 2008.

[72] E. Amsterdam, H. van Hoorn, J. T. M. De Hosson, and P. R. Onck, "The Influence of Cell Shape Anisotropy on the Tensile Behavior of Open Cell Aluminum Foam," *Advanced Engineering Materials,* vol. 10, pp. 877-881, 2008.

[73] C. San Marchi, J. F. Despois, and A. Mortensen, "Uniaxial deformation of open-cell aluminum foam: The role of internal damage," *Acta Materialia,* vol. 52, pp. 2895-2902, 2004.

[74] E. Amsterdam, P. R. Onck, and J. T. M. De Hosson, "Fracture and microstructure of open cell aluminum foam," *Journal of Materials Science,* vol. 40, pp. 5813-5819, 2005.

[75] P. S. Liu, "Tensile fracture behavior of foamed metallic materials," *Materials Science and Engineering A,* vol. 384, pp. 352-354, 2004.

[76] A. Fuganti, L. Lorenzi, A. G. Hanssen, and M. Langseth, "Aluminium foam for automotive applications," *Advanced Engineering Materials,* vol. 2, pp. 200-204, 2000.

[77] J. A. Reglero, M. A. Rodríguez-Peárez, E. Solórzano, and J. A. de Saja, "Aluminium foams as a filler for leading edges: Improvements in the mechanical behaviour under bird strike impact tests," *Materials and Design,* vol. 32, pp. 907-910, 2011.

[78] T. G. Nieh, K. Higashi, and J. Wadsworth, "Effect of cell morphology on the compressive properties of open-cell aluminum foams," *Materials Science and Engineering: A,* vol. 283, pp. 105-110, 2000.

[79] P. R. Onck, E. W. Andrews, and L. J. Gibson, "Size effects in ductile cellular solids. Part I: Modeling," *International Journal of Mechanical Sciences,* vol. 43, pp. 681-699, 2001.

[80] X.-q. Cao, Z.-h. Wang, H.-w. Ma, L.-m. Zhao, and G.-t. Yang, "Effects of cell size on compressive properties of aluminum foam," *Transactions of Nonferrous Metals Society of China,* vol. 16, pp. 351-356, 2006.

[81]   M. S. Aly, "Behavior of closed cell aluminium foams upon compressive testing at elevated temperatures: Experimental results," *Materials Letters,* vol. 61, pp. 3138-3141, 2007.

[82]   Y. Xiang and J. J. Vlassak, "Bauschinger and size effects in thin-film plasticity," *Acta Materialia,* vol. 54, pp. 5449-5460, 2006.

[83]   B. A. Bouwhuis, J. L. McCrea, G. Palumbo, and G. D. Hibbard, "Mechanical properties of hybrid nanocrystalline metal foams," *Acta Materialia,* vol. 57, pp. 4046-4053, 2009.

[84]   Lausic A. T, Bouwhuis B. A, McCrea J. L, Palumbo G, Hibbard G. D., "Mechanical anisotropy in electrodeposited nanocrystalline metal/metal composite foams," *Materials Science and Engineering: A,* vol. 552, pp. 157-163, 2012.

[85]   B. A. Bouwhuis, E. Bele, and G. D. Hibbard, "Metal/metal nanocrystalline cellular composites," 2009, pp. 63-73.

[86]   E. Bele, B. A. Bouwhuis, and G. D. Hibbard, "Failure mechanisms in metal/metal hybrid nanocrystalline microtruss materials," *Acta Materialia,* vol. 57, pp. 5927-5935, 2009.

[87]   L. M. Gordon, B. A. Bouwhuis, M. Suralvo, J. L. McCrea, G. Palumbo, and G. D. Hibbard, "Micro-truss nanocrystalline Ni hybrids," *Acta Materialia,* vol. 57, pp. 932-939, 2009.

[88]   T. G. Nieh, J. H. Kinney, J. Wadsworth, and A. J. C. Ladd, "Morphology and Elastic Properties of Aluminum Foams Produced by a Casting Technique," *Scripta Materialia,* vol. 38, pp. 1487-1494, 1998.

[89]   L. J. Gibson, "Modelling the mechanical behavior of cellular materials," *Materials Science and Engineering: A,* vol. 110, pp. 1-36, 1989.

[90]   A. E. Markaki and T. W. Clyne, "Magneto-mechanical stimulation of bone growth in a bonded array of ferromagnetic fibres," *Biomaterials,* vol. 25, pp. 4805-4815, 2004.

[91]   J. S. Huang and L. J. Gibson, "Elastic moduli of a composite of hollow spheres in a matrix," *Journal of the Mechanics and Physics of Solids,* vol. 41, pp. 55-75, 1993.

[92]   L. P. Lefebvre, J. Banhart, and D. C. Dunand, "Porous metals and metallic foams: Current status and recent developments," *Advanced Engineering Materials,* vol. 10, pp. 775-787, 2008.

[93]   K. Mohan, T. H. Yip, S. Idapalapati, and Z. Chen, "Impact response of aluminum foam core sandwich structures," *Materials Science and Engineering: A,* vol. 529, pp. 94-101, 2011.

[94]   W.-C. Gu, G.-H. Lv, H. Chen, G.-L. Chen, W.-R. Feng, and S.-Z. Yang, "PEO protective coatings on inner surface of tubes," *Surface and Coatings Technology,* vol. 201, pp. 6619-6622, 2007.

[95]   D. Djozan and M. Amir-Zehni, "Anodizing of inner surface of long and small-bore aluminum tube," *Surface and Coatings Technology,* vol. 173, pp. 185-191, 2003.

[96]   C. S. Dunleavy, J. A. Curran, and T. W. Clyne, "Plasma electrolytic oxidation of aluminium networks to form a metal-cored ceramic composite hybrid material," *Composites Science and Technology,* vol. 71, pp. 908-915, 2011.

[97]   J. Liu, X. Zhu, Z. Huang, S. Yu, and X. Yang, "Characterization and property of microarc oxidation coatings on open-cell aluminum foams," *Journal of Coatings Technology Research,* vol. 9, pp. 357-363, 2012.

[98]   Y. Jiang, Y. Zhang, Y. Bao, and K. Yang, "Sliding wear behaviour of plasma electrolytic oxidation coating on pure aluminium," *Wear,* vol. 271, pp. 1667-1670, 2011.

[99]   X. Shi-Gang, S. Li-Xin, Z. Rong-Gen, and H. Xing-Fang, "Properties of aluminium oxide coating on aluminium alloy produced by micro-arc oxidation," *Surface and Coatings Technology,* vol. 199, pp. 184-188, 2005.

[100]   M. Boinet, S. Verdier, S. Maximovitch, and F. Dalard, "Plasma electrolytic oxidation of AM60 magnesium alloy: Monitoring by acoustic emission technique. Electrochemical properties of coatings," *Surface and Coatings Technology,* vol. 199, pp. 141-149, 2005.

[101] A. L. Yerokhin , X. Nie, A. Leyland, A. Matthews "Characterisation of oxide films produced by plasma electrolytic oxidation of a Ti–6Al–4V alloy," *Surface and Coatings Technology,* vol. 130, pp. 195-206, 2000.

[102] C. S. Dunleavy, I. O. Golosnoy, J. A. Curran, and T. W. Clyne, "Characterisation of discharge events during plasma electrolytic oxidation," *Surface and Coatings Technology,* vol. 203, pp. 3410-3419, 2009.

[103] Y. Guan, Y. Xia, and G. Li, "Growth mechanism and corrosion behavior of ceramic coatings on aluminum produced by autocontrol AC pulse PEO," *Surface and Coatings Technology,* vol. 202, pp. 4602-4612, 2008.

[104] J. A. Curran and T. W. Clyne, "Thermo-physical properties of plasma electrolytic oxide coatings on aluminium," *Surface and Coatings Technology,* vol. 199, pp. 168-176, 2005.

[105] A. L. Yerokhin, A. Shatrov, V. Samsonov , P. Shashkov , A. Pilkington , A. Leyland , A. Matthews., "Oxide ceramic coatings on aluminium alloys produced by a pulsed bipolar plasma electrolytic oxidation process," *Surface and Coatings Technology,* vol. 199, pp. 150-157, 2005.

[106] Y. Guangliang, L. Xianyi, B. Yizhen, C. Haifeng, and J. Zengsun, "The effects of current density on the phase composition and microstructure properties of micro-arc oxidation coating," *Journal of Alloys and Compounds,* vol. 345, pp. 196-200, 2002.

[107] W. Xue, Z. Deng, Y. Lai, and R. Chen, "Analysis of Phase Distribution for Ceramic Coatings Formed by Microarc Oxidation on Aluminum Alloy," *Journal of the American Ceramic Society,* vol. 81, pp. 1365-1368, 1998.

[108] Y. H. T. D T Asquith , C X Wong, J R Yates ,A Matthews , AL Yerokhin "The evaluation of throwing power in electrodeposition," in *17th European conference on fracture, ECF 17*, Brno, Czech Republic, 2008, pp. 2105–2111.

[109] A. V. Engel, "Current distribution and throwing power in electrolytes [11]," *Nature,* vol. 146, p. 66, 1940.

[110] G. E. Gardam, "The evaluation of throwing power in electrodeposition," *Transactions of the Faraday Society,* vol. 34, pp. 698-711, 1938.

[111] R. H. U. Khan, A. Yerokhin, X. Li, H. Dong, and A. Matthews, "Surface characterisation of DC plasma electrolytic oxidation treated 6082 aluminium alloy: Effect of current density and electrolyte concentration," *Surface and Coatings Technology,* vol. 205, pp. 1679-1688, 2010.

[112] R. H. U. Khan, A. L. Yerokhin, T. Pilkington, A. Leyland, and A. Matthews, "Residual stresses in plasma electrolytic oxidation coatings on Al alloy produced by pulsed unipolar current," *Surface and Coatings Technology,* vol. 200, pp. 1580-1586, 2005.

[113] X. Nie, A. Leyland, H. W. Song, A. L. Yerokhin, S. J. Dowey, and A. Matthews, "Thickness effects on the mechanical properties of micro-arc discharge oxide coatings on aluminium alloys," *Surface and Coatings Technology,* vol. 116-119, pp. 1055-1060, 1999.

[114] W.-C. Gu, G.-H. Lv, H. Chen, G.-L. Chen, W.-R. Feng, and S.-Z. Yang, "Characterisation of ceramic coatings produced by plasma electrolytic oxidation of aluminum alloy," *Materials Science and Engineering: A,* vol. 447, pp. 158-162, 2007.

[115] H. Kalkanci and S. C. Kurnaz, "The effect of process parameters on mullite-based plasma electrolytic oxide coatings," *Surface and Coatings Technology,* vol. 203, pp. 15-22, 2008.

[116] A. L. S. Yerokhin, L. O. Gurevina, N. L. Leyland, A. Pilkington, A. Matthews, A., "Discharge characterization in plasma electrolytic oxidation of aluminium," *Journal of Physics D: Applied Physics,* vol. 36, pp. 2110-2120, 2003.

[117] J. Tian, Z. Luo, S. Qi, and X. Sun, "Structure and antiwear behavior of micro-arc oxidized coatings on aluminum alloy," *Surface and Coatings Technology,* vol. 154, pp. 1-7, 2002.

[118] W. W. Xue, C. Li, Y. Deng, Z. Chen, R. Zhang, T., "Effect of microarc discharge surface treatment on the tensile properties of Al-Cu-Mg alloy," *Materials Letters,* vol. 56, pp. 737-743, 2002.

[119] G. Alcalá, S. Mato, P. Skeldon, G. E. Thompson, A. B. Mann, H. Habazaki, and K. Shimizu, "Mechanical properties of barrier-type anodic alumina films using nanoindentation," *Surface and Coatings Technology,* vol. 173, pp. 293-298, 2003.

[120] J. J. Mecholsky, R. W. Rice, and S. W. Freiman, "Prediction of Fracture Energy and Flaw Size in Glasses from Measurements of Mirror Size," *Journal of the American Ceramic Society,* vol. 57, pp. 440-443, 1974.

[121] S. M. Wiederhorn, "BRITTLE FRACTURE AND TOUGHENING MECHANISMS IN CERAMICS," *Annual Review of Materials Science,* vol. 14, pp. 373-403, 1984.

[122] J. L. Xu, F. Liu, F. P. Wang, D. Z. Yu, and L. C. Zhao, "Formation of Al2O3 coatings on NiTi alloy by micro-arc oxidation method," *Current Applied Physics,* vol. 9, pp. 663-666, 2009.

[123] V. Raj and M. Mubarak Ali, "Formation of ceramic alumina nanocomposite coatings on aluminium for enhanced corrosion resistance," *Journal of Materials Processing Technology,* vol. 209, pp. 5341-5352, 2009.

[124] J. Sun, Y. Han, and K. Cui, "Microstructure and apatite-forming ability of the MAO-treated porous titanium," *Surface and Coatings Technology,* vol. 202, pp. 4248-4256, 2008.

[125] Y. Yan, J. Sun, Y. Han, D. Li, and K. Cui, "Microstructure and bioactivity of Ca, P and Sr doped TiO 2 coating formed on porous titanium by micro-arc oxidation," *Surface and Coatings Technology,* vol. 205, pp. 1702-1713, 2010.

[126] Y.-P. Sun and K. Scott, "An analysis of the influence of mass transfer on porous electrode performance," *Chemical Engineering Journal,* vol. 102, pp. 83-91, 2004.

[127] E. E. Underwood, *Quantitative stereology*: Addison-Wesley, 1970.

[128] E. Arlt, "The influence of an increasing particle coordination on the densification of spherical polders," *Acta Metallurgica,* vol. 30, pp. 1883-1890, 1982.

[129] J. F. Despois and A. Mortensen, "Permeability of open-pore microcellular materials," *Acta Materialia,* vol. 53, pp. 1381-1388, 2005.

[130] N. Dukhan and C. A. Minjeur Ii, "A two-permeability approach for assessing flow properties in metal foam," *Journal of Porous Materials,* vol. 18, pp. 417-424, 2011.

[131] M. Medraj, E. Baril, V. Loya, and L. P. Lefebvre, "The effect of microstructure on the permeability of metallic foams," *Journal of Materials Science,* vol. 42, pp. 4372-4383, 2007.

[132] R. K. Iler, *The Chemistry of silica: solubility, polymerization, colloid and surface properties and biochemistry of silica*. New York:: John Wiley and Sons, 1979.

[133] T. D. Tonyan and L. J. Gibson, "Strengthening of cement foams," *Journal of Materials Science,* vol. 27, pp. 6379-6386, 1992.

[134] M. F. Ashby, *Materials selection in mechanical design*, 3rd Edition ed.: Butterworth-Heinemann, 2005.

[135] H. F. Cheng and F. S. Han, "Compressive behavior and energy absorbing characteristic of open cell aluminum foam filled with silicate rubber," *Scripta Materialia,* vol. 49, pp. 583-586, 2003.

[136] Z. Wang, H. Ma, L. Zhao, and G. Yang, "Studies on the dynamic compressive properties of open-cell aluminum alloy foams," *Scripta Materialia,* vol. 54, pp. 83-87, 2006.

[137] J. R. Davis, J. R. Davis, Associates, and A. S. M. I. H. Committee, *Aluminum and aluminum alloys*. Materials Park, OH: ASM International, 1993.

[138] R. Goodall, J.-F. Despois, A. Marmottant, L. Salvo, and A. Mortensen, "The effect of preform processing on replicated aluminium foam structure and mechanical properties," *Scripta Materialia,* vol. 54, pp. 2069-2073, 2006.

[139] J. M. Wheeler, J. A. Curran, and S. Shrestha, "Microstructure and multi-scale mechanical behavior of hard anodized and plasma electrolytic oxidation (PEO) coatings on aluminum alloy 5052," *Surface and Coatings Technology,* vol. 207, pp. 480-488, 2012.

[140] S.-G. Xin, L.-X. Song, R.-G. Zhao, and X.-F. Hu, "Composition and thermal properties of the coating containing mullite and alumina," *Materials Chemistry and Physics,* vol. 97, pp. 132-136, 2006.

[141] F. Jaspard-Mécuson, T. Czerwiec, G. Henrion, T. Belmonte, L. Dujardin, A. Viola, and J. Beauvir, "Tailored aluminium oxide layers by bipolar current adjustment in the Plasma Electrolytic Oxidation (PEO) process," *Surface and Coatings Technology,* vol. 201, pp. 8677-8682, 2007.

[142] A. L. Yerokhin , E. Parfenov, A. Matthews "Throwing power studies of PEO process," presented at the Euromat 2011, Montpellier, France, 2011.

[143] A.L. Yerokhin, E. Parfenov, A. Matthews "Modelling of PEO using FR data," presented at the Euromat 2009, Glasgow, UK, 2009.

[144] H. Nishiyama and M. Nakamura, "Capacitance of a strip capacitor," *Components, Hybrids, and Manufacturing Technology, IEEE Transactions on,* vol. 13, pp. 417-423, 1990.

10. Appendix
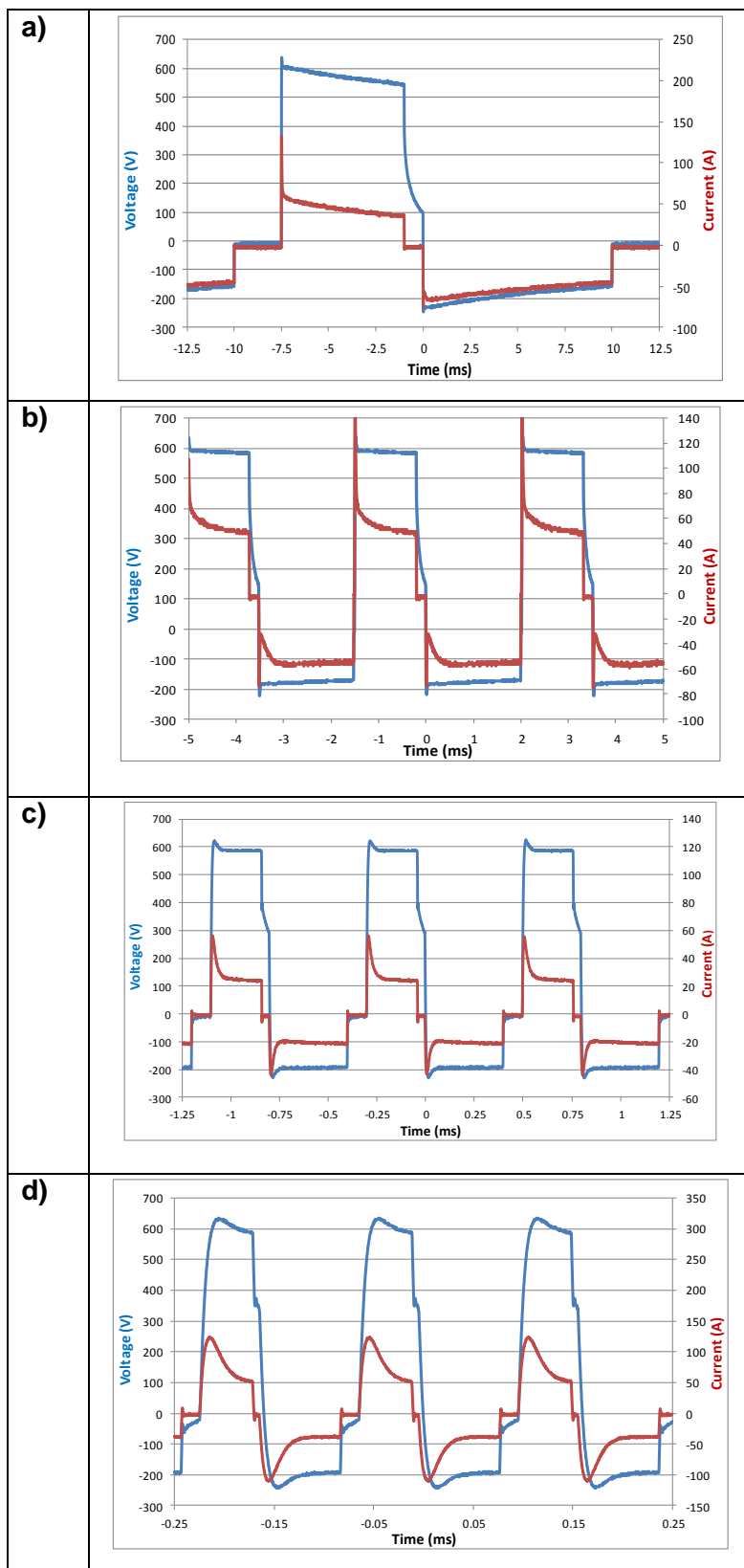
Figure 10.1 - Current and voltage waveforms for frequency of a) 50, b) 250, c) 1250 and d) 6250Hz in PBC mode during PEO processing of open cell aluminium foams used in this work.
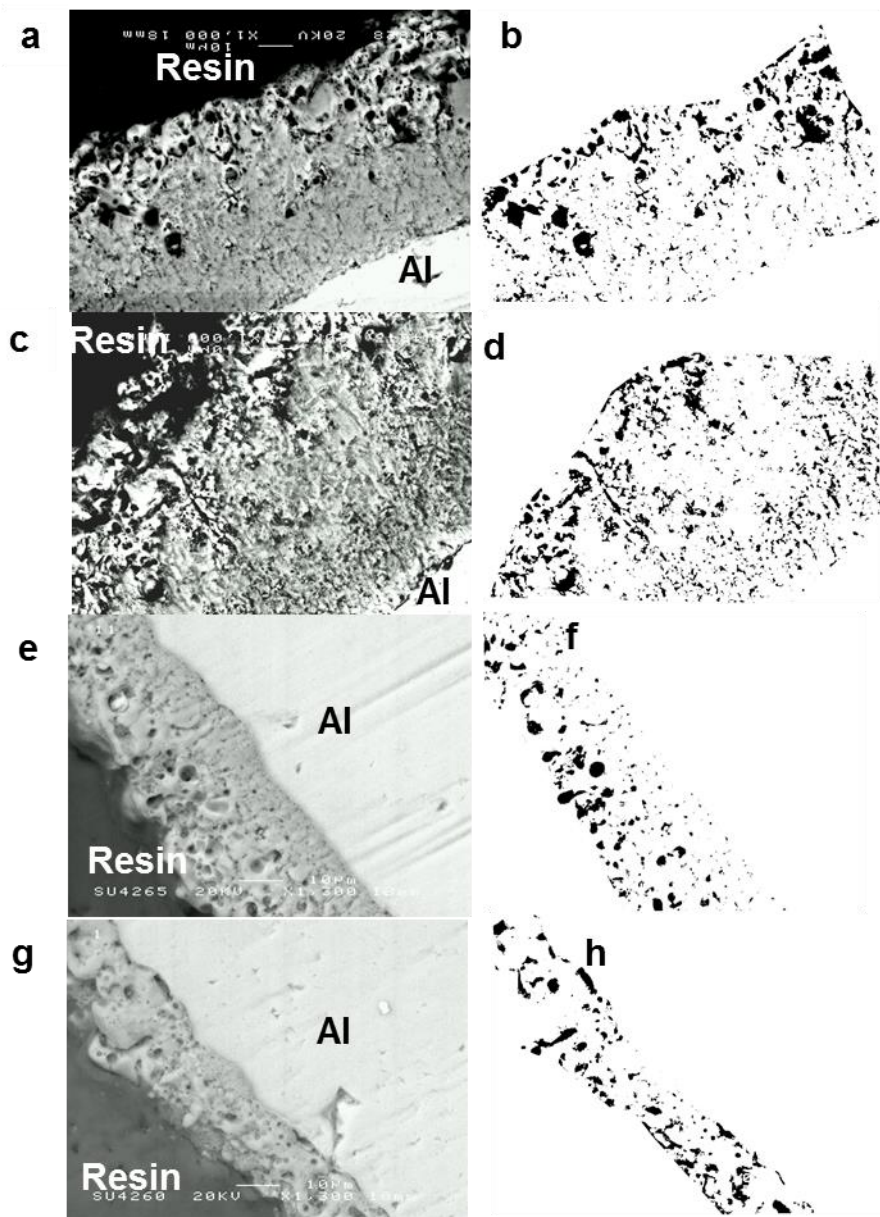
Figure 10.2 - Representative Backscatter SEM images for coatings produced with a) 50, c) 250, e) 1250 and g) 6250Hz, before and after applying threshold to these images (b, d, f, and h). Pores can be visually seen in Mask images (b, d, f, and h) produced by the ImageJ software.
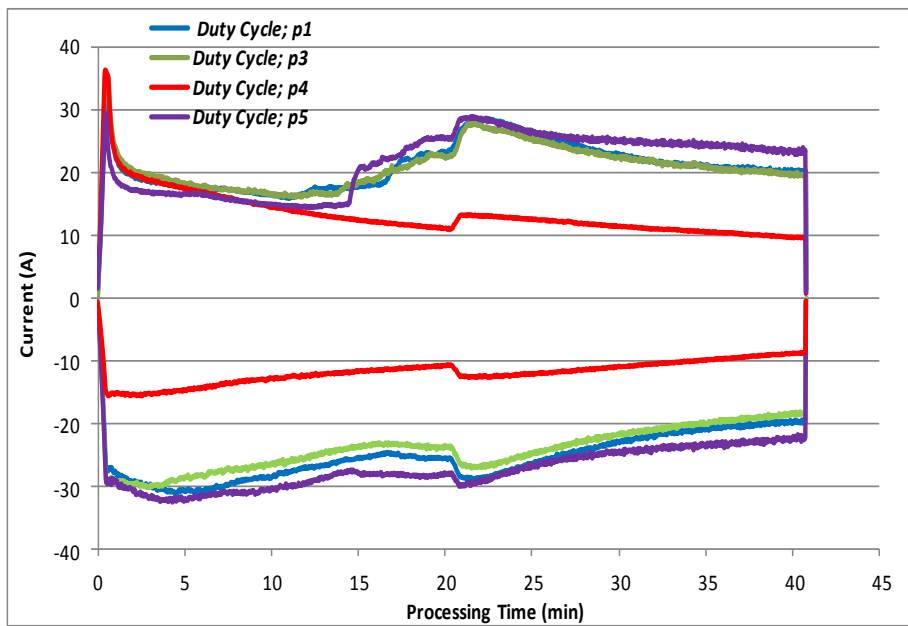
Figure 10.3 - Evolution of current during PEO processing of open cell aluminium foams using 250Hz frequency but with different duty cycles (on/off ratio in positive and negative bias) of p_1, p_3, p_4 and p_5 conditions. Data for p_2 condition is not available sue to system error during processing of data.